From synergy to inhibition: Effects of multi-component solutions on the crystallization of divalent carbonates in natural and synthetic environments

A thesis presented to Trinity College Dublin, the University of Dublin for the degree of Doctor of Philosophy in Geology, in the School of Natural Sciences.

Under the supervision of Dr. Juan Diego Rodríguez-Blanco

2024

Niamh Frances Siglinde Faulkner

Trinity College Dublin
Coláiste na Tríonóide, Baile Átha Cliath
The University of Dublin

iCRAG
SFI RESEARCH CENTRE IN APPLIED GEOSCIENCES

Geological Survey
Suirbhéireacht Gheolaíochta
Ireland | Éireann

Declaration:

I declare that this thesis has not been submitted as an exercise for a degree at this or any other university and it is entirely my own work.

I agree to deposit this thesis in the University's open access institutional repository or allow the Library to do so on my behalf, subject to Irish Copyright Legislation and Trinity College Library conditions of use and acknowledgement.

Niamh Faulkner

September 2023

ABSTRACT

The understanding of the processes governing the mechanisms, kinetics, and pathways of carbonate crystallization is crucial in the context of carbon capture and storage through mineralization. However, uncertainty still exists about the precise nature of how minerals, specifically carbonates, form and how specific factors (e.g., foreign ions, supersaturation and temperature) affect their kinetics and mechanisms of formation. By understanding the mechanisms, kinetics and pathways of carbonate formation and transformation, we gain the foundational knowledge in order to control the crystallisation and stability of carbonates. Prior to this study, the influence of ions on carbonate formation was predominantly limited to single ions. The aim of this thesis is to examine the effects of multi-component solutions on the crystallization of common divalent carbonates, in both synthetic and natural polymineralic systems.

Using a combination of *in situ* crystallisation, microscopic, solid-state and spectroscopic techniques, including UV-Vis spectrophotometry, scanning electron microscopy and powder X-ray diffraction we carried out a comprehensive exploration of the impact of foreign ions on the kinetics and mechanisms governing divalent (Ca, Sr, Ba) carbonates crystallisation, leveraging in situ experiments. Following this, our focus shifted towards the captivating evolution of a complex divalent (Ca, Mg, Fe) carbonate natural cement, which crystallized during an in-situ basalt carbonate mineralization process. These main variables taken into consideration included: i) the ions' ratio and concentration in solution; ii) the saturation state within aqueous solutions; iii) the dehydration of divalent (e.g., Ca^{2+}, Mg^{2+}, Sr^{2+}, Ba^{2+}) ions; iv) variations in the ionic radii of these divalent cations; v) the effects of the differing coordination numbers of these divalent cations among carbonate types.

This thesis has demonstrated that the synergistic influence of ions significantly diverges from their individual effects, thereby offering profound insights into the impacts of multi-component solutions on natural and synthetic carbonate crystallisation. By seamlessly integrating homogeneous nucleation experiments, mineral replacement reactions, and meticulous (high-

resolution) examinations of naturally carbonated basalts, alongside geochemical modelling, we have achieved a profound mechanistic insight into carbonate formation. This newfound knowledge holds the key to regulating the kinetics and mechanisms of carbonate formation, whether in the context of field-based geological processes or industrial carbon capture and storage (CCS) applications.

Acknowledgements

The work described in this thesis was funded by a research grant from the Science Foundation Ireland Centre for Research in Applied Geosciences and Geological Survey Ireland under the iCRAG/SFI-GSI: Environmental Geoscience Programme (TARGET-CCS; rodrigjd-SFI-17/RC-PhD/3481).

First and foremost, to my steadfast supervisor Juan Diego Rodríguez-Blanco, a huge thank you for all your support, advice and patience as I figured this all out. Thank you for sharing all your knowledge and time throughout my experience as an undergraduate and postgraduate at TCD. I truly couldn't have hoped for more dedicated or good-humoured guidance and assistance.

I would like to thank everyone who has offered technical assistance and advice during my PhD., including Robbie Goodhue and special thank you to my fellow members of the carbonate REEsearch group. Thank you to Quentin Crowely, Nancy Riggs and Micha Ruhl for wonderful memories teaching the Spain fieldtrip. Of course a huge thank you to Francis Hendron for always having the postgrad's best interests at heart, this place is going to fall apart without you.

Thank you to everyone who made my time aboard the RV Celtic Explorer during the PORO-CLIM expedition so memorable, including Ben Couvin and Mathew Allison. The outreach programme we developed and ran was the highlight of my PhD.

I would like to thank everyone that offered me support and advice in Trinity Student Counselling Service, especially Sheila Devane for your invaluable support.

I count myself extremely lucky in life to be surrounded by such a wonderful support network of friends and family, all of whom have contributed immensely to keeping me sane throughout this. To my skipper Ian Bowring and all my salty Springer crewmates, thank you for providing me with haven to escape the trials and tribulations of PhD life. To my Meme Queens, Bronwyn and Emma Mallon, thank you for keeping me laughing throughout. To my partner in ~~crime~~ geology,

Maeve Murphy Quinlan, who'd have thought it all those years ago trekking in Villamanín that we'd both be foolhardy enough to go get a degree in this.

Thank you to Erica Krueger for not letting me quit to start a bakery, for being my companion in Guinness, simply put I would not have finished this without you.

Thanks to my fabulous friends who were there to go for a swim, a pint, a walk, a coffee, to listen to me rant, to give me a hug and keep me laughing, in no particular order, Jasmine Blenkins O'Callaghan, Éilis Brennan, Art Coyne, Robin Keane, Sadhbh Sheeran, Zoe Roseby, Lydia Whittaker, Blanka Kovacs, Neil Dunne, Lily Guinness, Alice Bowen, and Josune Portillo. To Nicole Cosgrove and Alex Bowring, your friendship is invaluable, thank you.

To Elliot Carter, an extra special thank you for all your support, advice and patience. You are a true gem.

To my amazing family, for showering me in love and support, a huge thank you to my siblings Olivia, Paddy, Jessye and Finlay. Lastly and most importantly to my wonderful parents, Mary and Andrew, who have been my biggest supporters, thank you for your constant encouragement and support in so many ways.

Illegitimi non carborundum

PREFACE

This thesis is presented in paper format with each of the three substantive research chapters forming a self-contained manuscript that have been published in or prepared for submission to peer-reviewed academic journals, as well as a general introduction to the topic and general conclusions of this work. The thesis is laid out in the following manner:

Chapter 1. Contains a general introduction to the topics of this thesis topic, including the climate background, as well as carbonate and the kinetics and mechanisms of carbonate crystallisation. Additionally it discusses the carbonate mineralisation of basalt, highlighting the importance of having a better understanding of the kinetics and mechanisms of carbonate formation in order to successfully store carbon via carbonate mineralisation of basalt.

Chapter 2. Contains the research aims and objectives of this project, including the three main research questions of the thesis. Additionally, it contains specific research aims and objectives for the individual manuscripts.

Chapter 3 (Paper 1) was first submitted to the ACS journal "Crystal Growth and Design" in March 2023. My supervisor Dr. Juan Diego Rodríguez-Blanco is listed as an author on the paper. He offered comments on the paper and helped with editing. Supporting information for this manuscript is presented in appendix A.

Chapter 4 (Paper 2) is a manuscript in preparation submit to an international peer-reviewed journal. The manuscript is authored by N. Faulkner, my supervisor Dr. Juan Diego Rodríguez-Blanco, who offered comments and helped with experimental design; fellow students within my research group helped with some sampling, Luca Terribili, Andrea Pierozzi and Adrienn Szucs. Supporting information for this manuscript is presented in appendix B.

Chapter 5 (Paper 3) is a manuscript in preparation to submit to an international peer-reviewed journal. The manuscript is authored by N. Faulkner, my supervisor Dr. Juan Diego

Rodríguez-Blanco, who collected the samples from Svalbard in 2009 during the AMASE exhibition and conducted analysis on the samples, as well advising and editing the manuscript. Dr. Elliot Carter advised and edited the manuscript. Fellow students within my research group helped with some data reduction: Adrienn Szucs, Melanie Maddin and Luca Terribili. Supporting information for this manuscript is presented in appendix C.

Chapter 6. Contains general conclusions of this thesis as a whole.

Appendices A, **B** and **C** are included containing figures and text supplementary to those presented in the main body of the manuscript.

Table of Contents

List of Figures

List of Tables

ABBREVIATIONS

ACC	Amorphous calcium carbonate
AMASE	Arctic Mars Analogue Svalbard Expedition
BBF	Breibogen-Bockfjorden Fault
BDL	Below detection limit
BSE	Back Scattered Electrons
BVC	Bockfjord Volcanic Complex
CCS	Carbon Capture and Storage
CDR	Carbon Dioxide Removal
CIT	Citrate
GHG	Greenhouse gas
IAP	Ion Activity Product
K_{sp}	Solubility Product
PDF	Pair Distribution Function
PILP	Polymer induced liquid precursor
PETM	Palaeocene-Eocene Thermal Maximum
PPL	Plane-polarised light
SEM	Scanning Electron Microscopy
SEM-CL	Scanning Electron Microscopy Cathodoluminescence
SEM-EDS	Scanning Electron Microscopy- Energy Dispersive Spectroscopy
SI	Saturation index, defined as the base-10 logarithm of the saturation state Ω
XP	Crossed polars
XRD	X-Ray Diffraction

Chapter 1.

INTRODUCTION

1.1. THE ROLE OF CARBON DIOXIDE IN THE CLIMATE CRISIS

The climate crisis is the largest threat to life on Earth, driven by high rates of anthropogenic greenhouse gas (GHG) production, notably carbon dioxide (CO_2). The increased rates of carbon dioxide in the atmosphere have already contributed to the increased severity and occurrence of extreme climatic events. For example, in 2023 alone globally we have experienced record breaking hottest months, with July 2023 as hottest month on record ever since 1880 (O'Shea and NASA, 2023). Here in Ireland, July 2023 was also the wettest month on record (based on digitised data back to 1940; Met Éireann, 2023).

The aim of the Paris Agreement (2015) is to limit the global average warming to below 2 °C, with a focus on a 1.5 °C warming threshold (United Nations, 2015). The Intergovernmental Panel on Climate Change's (IPCC) Fifth Assessment Report (AR5) reported that in order to limit global temperature rise to less than 2 °C the maximum level atmospheric CO_2 of 450 ppm is limited by 2100 (IPCC, 2014). According to Haszeldine *et al.* (2018) "staying within that limit means that global emissions need to reduce at about 3% yr^{-1} from now (37 Gt CO_2 yr^{-1}) to a net balance of zero around 2050."

The recent IPCC Sixth Assessment Report (AR6; IPCC, 2023) revealed the grim climate realities that we are facing due the devastating consequences of rising greenhouse gas (GHG) emissions. The average global temperature has already increased by 1.1 °C since pre-industrial values and is set to continue rising; the likelihood of reaching or surpassing 1.5 °C between 2021 and 2040 is over 50% (IPCC, 2023). Note, when referring to pre-industrial values CO_2 values value of ~280 ppm

was chosen (Etheridge *et al.*, 1996). For context, the National Oceanic and Atmospheric Administration's (NOAA) Mauna Loa Atmospheric Baseline Observatory measured the highest recorded peak of atmospheric CO_2 in May 2023, 424 ppm, since monitoring began in May 1974 (National Oceanic and Atmospheric Administration, 2023).

According to Marland *et al.* (2007) since 1751 the estimated input of CO_2 emissions to the atmosphere is 315 Gt C. When you compare that to the current global emissions rate of just over 40 Gt C per year (Lawrence *et al.*, 2018), to the overall emissions value for the past 300 years there has been a steep increase in CO_2 emissions, which started around the 1900s.

Approximately half the annual anthropogenic CO_2 emissions are being absorbed by terrestrial and marine ecosystems (Cox *et al.*, 2000; Oelkers and Cole, 2008). The atmosphere and ocean CO_2 exchange is very fast. The increased amount of CO_2 has already started to affect the ocean chemistry via ocean acidification. Haugan and Drange (1996) state that compared to pre-industrial values, the ocean's surface water pH has already decreased by 0.1 units. The increasing trend of ocean acidification could see the pH decrease by as much as 0.3 to 0.4 units by the end of the century (Orr *et al.*, 2005). Ocean acidification has serious implications on carbonate secreting organisms, e.g. molluscs, corals and foraminifera, and the larger ocean ecosystem. Ocean acidification causes perturbations in the bicarbonate (HCO_3^-) and carbonic acid (H_2CO_3) equilibrium, which in turn results in the undersaturation of oceanic calcite and aragonite worldwide (IPCC, 2018; Mele *et al.*, 2023). The ramifications of ocean acidification are huge on biomineralizing species, of which calcium-bearing minerals account for roughly 50% of all known biominerals, with calcium carbonate being the most abundant biomineral composition, both in terms of taxa abundance and quantity formed (Lowenstam and Weiner, 1989). Disturbances to the carbon cycle, resulting in ocean acidification, has been linked to the "big five" extinction events, including the Palaeocene-Eocene thermal maximum (PETM), which resulted in major extinctions in calcifying benthic foraminifera (Pelejero *et al.* 2010).

In order to accomplish the goal of limited warming, the Paris Agreement (United Nations, 2015) recommends efforts "to achieve a balance between anthropogenic emissions by sources and removals by sinks of greenhouse gases in the second half of this century". The International Energy

Agency (IEA) has estimated that to comply with the Paris Agreement and limit global warming to within 2 °C by 2050 a minimum of 15-20% of global CO_2 emission reduction will need to result from CCS. This means that at least 6000 Mt CO_2 yr^{-1} will need to be sequestered (International Energy Agency, 2013). The removal of greenhouse gases will require carbon capture and storage (CCS) and carbon dioxide removal (CDR) technologies.

CCS involves the injection of CO_2 into geological formations, which is usually referred to as *in-situ* storage (IPCC, 2005). *In situ* storage can result in structural or mineral trapping, due to the carbonation of silicate rocks. While *in situ* carbonation involves injection underground, *ex-situ* carbonation occurs in a "chemical processing plant after mining and pre-treating the silicates" (IPCC, 2005). The by-products of *ex-situ* carbonation are then either re-used in construction or in mine reclamation, this is an example of CCU (carbon capture and utilisation).

1.2. CARBONATES: CRYSTALLISATION & MECHANISMS

1.2.1 CARBONATE TYPES

Carbonate minerals consist of a carbonate ion, CO_3^{2-} and a metal cation. Of the anhydrous carbonates there are two distinct isomorphous groups, calcite-type and aragonite-type. These groups are divided as a consequence of the ionic radius of the metal cation. Calcite-type have ionic radii of ≤ 1 Å, whereas aragonite-type carbonates have ionic radii ≥ 1 Å. Calcite-type minerals possess the ability to integrate both calcium (Ca) and magnesium (Mg) ions within their structures. The ionic radius of Ca^{2+} in calcite-type carbonates is 1.00 Å (coordination 6), whereas the ionic radius of Ca^{2+} in aragonite-type carbonates is 1.18 Å (coordination 9), which is why $CaCO_3$ can be both calcite and aragonite type (Shannon and IUCr, 1976; Speer, 1983). The rhombohedral calcite-type carbonates include calcite ($CaCO_3$), magnesite ($MgCO_3$), siderite ($FeCO_3$) and rhodochrosite ($MnCO_3$) (Reeder, 1983a). The four naturally occurring orthorhombic divalent carbonate group, also known as aragonite-

type carbonates are aragonite ($CaCO_3$), strontianite ($SrCO_3$), Witherite ($BaCO_3$) and cerucite ($PbCO_3$) (Speer, 1983). The ability of polymorphic calcium carbonate to precipitate as coordination 6 calcite and coordination 9 aragonite is what also allows living organisms to create very strong skeletons and shells via targeted crystallisation of both polymorphs during biomineralization processes.

1.2.2 CRYSTALLISATION MECHANISMS

By understanding the mechanisms, kinetics and pathways of carbonate formation and transformation, we gain the foundational knowledge in order to control the formation and stability of carbonates. This knowledge is essential, understanding the mechanisms at the nanoscale is key to targeting the crystallisation of carbonates during CCS to optimise the process.

Within the carbonate minerals there is a wide variety in mechanisms and kinetics of mineral carbonates formation. These include i) crystallisation from an amorphous precursor, ii) multistage dissolution and precipitation via intermediate phases, iii) spherulitic growth, iv) Ostwald ripening and v) pseudomorphic transformation and replacement. For example, within the Ca, Ca-Mg and REE carbonate systems:

- The **Ca carbonate system**: calcite crystallisation pathways are complex and multifarious. It can form from amorphous calcium carbonate (ACC) via intermediate vaterite or aragonite (Rodriguez-Blanco *et al.* 2011, 2012, 2017; Bots *et al.*, 2012), through pseudomorphic transformation of ikaite (Besselink *et al.*, 2017). ACC transforms extremely fast (<2 min at 25° C) to crystalline $CaCO_3$ polymorphs (Rodriguez-Blanco *et al.*, 2011). The transformation to vaterite occurs through a sequence of three stages: Initially, ACC is disordered and hydrated, subsequently undergoing a rapid transition to a dehydrated and more ordered ACC state. Concurrently, vaterite begins to form through spherulitic growth. In the next phase, ACC dissolves and reprecipitates as vaterite, driven by a reduction in the supersaturation of the solution specifically with respect to vaterite. Next Ostwald ripening of the vaterite particles occurs (Bots *et al.*, 2012; Rodriguez-Blanco *et al.* 2017). Vaterite then slowly dissolves and recrystallises as calcite. Besselink *et al.* (2017) stresses the

importance of understanding of $CaCO_3$ crystallization pathways, as they determine the polymorph selection, size, shape, crystallinity and properties of the final thermodynamically stable $CaCO_3$ phase (calcite) which is dependent on the one or more metastable precursor(s).

- The **Ca-Mg carbonates**: Monohydrocalcite is a carbonate that forms in Mg-rich environments. Like calcium carbonate it crystallises via stages. This starts with highly supersaturated solutions from which a Mg-bearing, ACC precursor precipitates. Mg-ACC then precipitates to monohydrocalcite via two stages of dissolution and reprecipitation, stage three and four consist of Oswald ripening (Rodriguez-Blanco, *et al.*, 2014). Similarly, dolomite crystallises via a poorly-ordered Mg-rich precursor (Mg-ACC, where Mg/Ca≈1) but requires high temperatures (T> 60 ˚C) to form (Rodriguez-Blanco *et al.* 2015).
- **Rare earth carbonates** (e.g., La and Nd carbonates): Rare earth carbonate compounds can also crystallise from hydrous amorphous precursors, via spherulitic growth or pseudomorphic replacement, by following multiple crystallisation pathways (Rodriguez-Blanco *et al.*, 2014; Vallina *et al.*, 2014, 2015; Szucs *et al.*, 2021, 2022).

Carbonate crystallisation mechanisms and pathways are very sensitive to many parameters, including temperature, pressure, pH, and the presence of foreign ions or impurities. For example:

- **Temperature:** The transformation of ACC to calcium carbonate polymorphs is affected by temperature. Typically it transforms to calcite via intermediate vaterite at low temperatures (<30 °C) and via aragonite at higher temperatures (>60 °C) (Ogino *et al.*, 1987; Rodriguez-Blanco *et al.*, 2017).
- **Inorganics:** The effects of adding Mg^{2+} has been well studied for the calcium carbonate system. Mg^{2+} is known inhibit $CaCO_3$ crystallisation, increasing the lifetime of amorphous calcium carbonate (ACC), (Loste *et al.*, 2003; Rodríguez-Blanco *et al.*, 2012). Mg^{2+} inhibits $CaCO_3$ crystallisation, due to the dehydration of the Mg^{2+} ion from solution prior to incorporation into the growing $CaCO_3$ crystals (Nielsen *et al.*, 2016).

- **pH**: Rodriguez-Blanco *et al.* (2012) and Tobler *et al.* (2016) showed that small variations in pH can considerably alter the crystallisation rates and pathways of ACC. Tobler *et al.* (2016) showed that the lifetime of ACC was extended by increasing the pH, which then favoured the transformation of ACC directly to calcite (pH 12.7), without the intermediate vaterite.
- **Organics:** The effects of organics in the crystallisation of $CaCO_3$ polymorphs can be very complex and depending on chemistry of the organic molecule involved (functional group), concentration of organic in solution, organic/water ratio, among others. For example, using calcium carbonate solutions with alcohol (e.g., ethanol, isopropanol) favours aragonite precipitation (Sand *et al.*, 2012b). However, in the presence of citrate, ACC directly crystallizes to calcite, with no intermediate vaterite (Tobler *et al.*, 2015).

1.3. CARBON CAPTURE AND STORAGE VIA CARBONATE MINERALISATION

Carbon capture and storage (CCS) technology is widely recognised and endorsed for the mitigation of anthropogenic CO_2 emissions (IPCC, 2005; Benson and Cole, 2008; Oelkers and Cole, 2008; Schrag, 2009; International Energy Agency, 2013; Williamson, 2016; Snæbjörnsdóttir *et al.*, 2020; English and English, 2022). There are various types of geological carbon storage: physical trapping; solubility trapping and mineral trapping.

Mineral trapping is a CCS method whereby CO_2 is fixed into inorganic carbonate minerals via the reaction of CO_2 and metal-oxide bearing silicate phases IPCC (2005). When injected CO_2 is dissolved in water it can expressed by the chemical reaction:

$$CO_2(g) + H_2O \leftrightarrow H_2CO_3 \leftrightarrow HCO_3^- + H^+ \leftrightarrow \ CO_3^{2-} + 2H^+$$

in which the dissolved CO_2 becoming dissociated into bicarbonate or carbonate aqueous species (Knauss *et al.*, 2005). It results in increased acidity of the groundwater (decrease in pH from near

neutral to around 4), also increasing the solubility of minerals in the host rock (Xu *et al.*, 2004). Due to this acidification process, ions from the primary silicate phases are released to the aqueous solution as the host rock starts to dissolve, so the concentration of ionic species in water increases. The interaction of these species with the carbonate ions can result in the formation of secondary carbonate phases (Xu *et al.*, 2004; IPCC, 2005; Benson and Cole, 2008). Mineral trapping is the most permanent form of geological storage (Gunter *et al.*, 2005; IPCC, 2005). Gunter *et al.* (1997) states that Ca, Mg and Fe carbonates are predicted to be the primary minerals that store CO_2

The kinetics, mechanism and pathways of these reactions are dependent on the compositions of both the injected fluid and the host rock. According to the IPCC (2005) the reactions between dissolved CO_2 and host rock phases can vary depending on the host rock composition. Carbonates can dissolve rapidly in a matter of days, whereas silicate minerals can dissolve extremely slowly (100s-1000s years). Pauwels *et al.* (2007) also highlights this issue with the length of time it takes for primary phases to be dissolved, stating that a main factor for long term geologic carbon storage is the reactivity of the host rocks. Ideal reservoirs are large, with highly reactive phases and high percentage of porosity to allow the rapid kinetics of formation of secondary carbonate minerals. The process of geological CCS requires a large amount of reservoir rock, according to the IPCC (2005), i.e., "to fix a tonne of CO_2 requires about 1.6 to 3.7 tonnes of rock".

Flood basalts have been proposed as great potential repository for CCS as an alternative to the conventional sedimentary reservoirs due to several advantages:

i. Basalt contains roughly 25 wt% Ca, Mg and Fe oxides, as well as ample amounts of other cations, including Al^{3+} and Na^{+}. (Schaef *et al.*, 2010; Gislason and Oelkers, 2014; Gislason *et al.*, 2014);
ii. Basaltic rocks are highly reactive to CO_2-containing fluids, more so than sedimentary rocks, meaning the cations in basalt are rapidly available to form carbonate minerals (Rosenbauer *et al.*, 2012; Gislason and Oelkers, 2014);
iii. Their abundance on the Earth's surface, basalts make up ~5% of the continental crust, and considerable amount of the oceanic crust. (Schaef *et al.*, 2010; Gislason and Oelkers, 2014).

According to Archer (2005) and Snæbjörnsdóttir *et al.* (2014, 2017) offshore basaltic CCS in the mid-ocean ridges theoretically has the potential to store all the CO_2 from burning of all fossil fuel on Earth (~5000 Gt C).

The CarbFix Project, Iceland, is an active carbon capture and storage facility, permanently storing CO_2 vis carbonate mineralisation of basalt (Snæbjörnsdóttir *et al.*, 2014, 2020; Matter *et al.*, 2016). The project uses the CO_2 which is a by-product of the geothermal energy production from the Hellisheidi geothermal power plant in SW Iceland. Iceland is an ideal area for basaltic CCS as the island made of ~90% basaltic rocks (Snæbjörnsdóttir *et al.*, 2014). The plant produces up to 60,000 tons of CO_2 per year, which is derived from magma a few km below the site (Gislason *et al.*, 2010). Since injection began in 2014 over 70,000 tons of CO_2 have been mineralised (Snæbjörnsdóttir *et al.*, 2021) and have recently began a pilot injection using CO_2 dissolved in seawater (Voigt *et al.*, 2021). The success of the CarbFix project demonstrates the feasibility of carbon capture and storage via basaltic mineralisation as a tool for the remediation of anthropogenic CO_2 emissions.

1.4. SCOPE OF THIS PHD THESIS

This doctoral dissertation represents a comprehensive exploration into the impact of multi-component aqueous solutions on the intricate crystallization mechanisms governing the formation of ubiquitous divalent carbonates. The majority of previous studies in this domain have primarily concentrated on the influence of carbonate crystallization using single specific ions or organic molecules as opposed to considering the intricate interplay of multiple components in solution. This investigation encompasses both experimental studies and observations within natural systems, including synthetic and naturally occurring polymineralic systems. In particular, chapter 3 aims to determine the combined influence of organic (CIT) and inorganics (Mg^{2+} and SO_4^{2-}) on crystallisation pathways and growth kinetics of $CaCO_3$. Chapter 4 aims to examine the mechanisms behind the replacement of a calcite-type carbonate (calcite) by aragonite types (strontianite and witherite). Lastly chapter 5 examines the influence of the geochemistry of the host rock during the *in situ* carbonation of

basalt, from the Sverrefjellet volcano in Svalbard, a natural analogue of basaltic carbon capture and storage. Through these investigations, this work contributes valuable insights to the understanding of complex carbonate crystallization processes in diverse environmental contexts (biomineralization processes, carbon capture and storage via mineral carbonation) or during the industrial synthesis of carbonate solids.

1.5 REFERENCES

Archer, D. (2005) ‘Fate of fossil fuel CO2 in geologic time’, Journal of Geophysical Research C: Oceans. doi: 10.1029/2004JC002625.

Benson, S. M. and Cole, D. R. (2008) ‘CO2 sequestration in deep sedimentary formations’, Elements, 4(5), pp. 325–331. doi: 10.2113/gselements.4.5.325.

Besselink, R. et al. (2017) ‘How short-lived ikaite affects calcite crystallization’, Crystal Growth and Design. American Chemical Society, 17(12), pp. 6224–6230. doi: 10.1021/acs.cgd.7b00743.

Bots, P. et al. (2012) ‘Mechanistic insights into the crystallization of amorphous calcium carbonate (ACC)’, Crystal Growth and Design, 12(7), pp. 3806–3814. doi: 10.1021/cg300676b.

Cox, P. M. et al. (2000) ‘Acceleration of global warming due to carbon-cycle feedbacks in a coupled climate model’, Nature, 408, pp. 184–187. doi: 10.1038/35041539.

English, J. M. and English, K. L. (2022) ‘An Overview of Carbon Capture and Storage and its Potential Role in the Energy Transition’, First Break. European Association of Geoscientists & Engineers, 40(4), pp. 35–40. doi: 10.3997/1365-2397.FB2022028.

Etheridge, D. M. et al. (1996) ‘Natural and anthropogenic changes in atmospheric CO2 over the last 1000 years from air in Antarctic ice and firn’, Journal of Geophysical Research: Atmospheres. John Wiley & Sons, Ltd, 101(D2), pp. 4115–4128. doi: 10.1029/95JD03410.

Gislason, S. and Oelkers, E. (2014) ‘Carbon Storage in Basalt’, Science, 334, pp. 373–374.

Gislason, S. R. et al. (2010) ‘Mineral sequestration of carbon dioxide in basalt: A pre-injection overview of the CarbFix project’, International Journal of Greenhouse Gas Control, 4(3), pp. 537–545. doi: 10.1016/j.ijggc.2009.11.013.

Gislason, S. R. et al. (2014) ‘Rapid solubility and mineral storage of CO2 in basalt’, in Energy Procedia. Elsevier Ltd, pp. 4561–4574. doi: 10.1016/j.egypro.2014.11.489.

Gunter, W. D., Mavor, M. J. and Robinson, J. R. (2005) 'CO2 storage and enhanced methane production: Field testing at Fenn-Big Valley, Alberta, Canada, with application', in Greenhouse Gas Control Technologies. Elsevier Ltd, pp. 413–421. doi: 10.1016/B978-008044704-9/50042-2.

Gunter, W. D., Wiwehar, B. and Perkins, E. H. (1997) 'Aquifer disposal of CO2-rich greenhouse gases: Extension of the time scale of experiment for CO2-sequestering reactions by geochemical modellingEinlagerung von CO2-Treibhaus-Gasen in einem Aquifer: Erweiterung des Zeitma�stabes von Experimenten von CO2-Aufnahme-Reaktionen durch geochemische Modellierung', Mineralogy and Petrology. Springer Science and Business Media LLC, 59(1–2), pp. 121–140. doi: 10.1007/bf01163065.

Haszeldine, R. S. et al. (2018) 'Negative emissions technologies and carbon capture and storage to achieve the Paris Agreement commitments', Philosophical Transactions of the Royal Society A: Mathematical, Physical and Engineering Sciences, 376(2119). doi: 10.1098/rsta.2016.0447.

Haugan, P. M. and Drange, H. (1996) 'Effects of CO2 on the ocean environment', Energy Conversion and Management. doi: 10.1016/0196-8904(95)00292-8.

International Energy Agency (2013) Technology roadmap - Carbon capture and Storage, Technology Roadmap Carbon Capture and Storage. doi: 10.1007/SpringerReference_7300.

IPCC (2005) IPCC Special Report on Carbon dioxide Capture and Storage, Working Group III of the Intergovernmental Panel on Climate Change. Edited by Prepared by Working Group III of the Intergovernmental Panel on Climate Change et al. Cambridge, United Kingdom and New York, NY, USA: Cambridge University Press. doi: 10.1021/es200619j.

IPCC (2014) Climate Change 2014 Synthesis Report - IPCC, Climate Change 2014: Synthesis Report. Contribution of Working Groups I, II and III to the Fifth Assessment Report of the Intergovernmental Panel on Climate Change. doi: 10.1017/CBO9781107415324.

IPCC (2018) Special Report on Global Warming of 1.5C, Global Warming of 1.5 °C: An IPCC Special Report on the impacts of global warming of 1.5°C above pre-industrial levels and related

global greenhouse gas emission pathways, in the context of strengthening the global response to the threat of climate change.

IPCC (2023) Climate Change 2023: Synthesis Report. Contribution of Working Groups I, II and III to the Sixth Assessment Report of the Intergovernmental Panel on Climate Change. Edited by P. Arias et al. Geneva, Switzerland. doi: 10.59327/IPCC/AR6-9789291691647.

Knauss, K. G., Johnson, J. W. and Steefel, C. I. (2005) 'Evaluation of the impact of CO2, co-contaminant gas, aqueous fluid and reservoir rock interactions on the geologic sequestration of CO2', Chemical Geology, 217(3-4 SPEC. ISS.), pp. 339–350. doi: 10.1016/j.chemgeo.2004.12.017.

Lawrence, M. G. et al. (2018) 'Evaluating climate geoengineering proposals in the context of the Paris Agreement temperature goals', Nature Communications. Nature Publishing Group. doi: 10.1038/s41467-018-05938-3.

Loste, E. et al. (2003) 'The role of magnesium in stabilising amorphous calcium carbonate and controlling calcite morphologies', Journal of Crystal Growth. North-Holland, 254(1–2), pp. 206–218. doi: 10.1016/S0022-0248(03)01153-9.

Lowenstam, H. A. and Weiner, S. (1989) 'On Biomineralization', On Biomineralization. Oxford University Press. doi: 10.1093/OSO/9780195049770.001.0001.

Marland, G., Boden, T. and Andres, R. (2007) Global, regional, and national CO2 emissions. In: Trends: A Compendium of Data on Global Change. Carbon Dioxide Information Analysis Center, Oak Ridge National Laboratory, U.S. Department of Energy, Oak Ridge, TN, USA,.

Matter, J. M. et al. (2016) 'Rapid carbon mineralization for permanent disposal of anthropogenic carbon dioxide emissions', Science. American Association for the Advancement of Science, 352(6291), pp. 1312–1314. doi: 10.1126/science.aad8132.

Mele, I. et al. (2023) 'Ocean acidification, warming and feeding impacts on biomineralization pathways and shell material properties of Magallana gigas and Mytilus spp.', Marine Environmental Research. Elsevier, 186, p. 105925. doi: 10.1016/J.MARENVRES.2023.105925.

Met Éireann (2023) July 2023: Provisionally Ireland's wettest July on record.

National Oceanic and Atmospheric Administration (2023) Broken record: Atmospheric carbon dioxide levels jump again.

Nielsen, M. R. et al. (2016) 'Inhibition of Calcite Growth: Combined Effects of Mg2+ and SO42-', Crystal Growth and Design. American Chemical Society, 16(11), pp. 6199–6207. doi: 10.1021/acs.cgd.6b00536.

O'Shea, C. and NASA (2023) 'NASA Clocks July 2023 as Hottest Month on Record Ever Since 1880'.

Oelkers, E. H. and Cole, D. R. (2008) 'Carbon dioxide sequestration: A solution to a global problem', Elements, 4(5), pp. 305–310. doi: 10.2113/gselements.4.5.305.

Ogino, T., Suzuki, T. and Sawada, K. (1987) 'The formation and transformation mechanism of calcium carbonate in water', Geochimica et Cosmochimica Acta, 51(10), pp. 2757–2767. doi: 10.1016/0016-7037(87)90155-4.

Orr, J. C. et al. (2005) 'Anthropogenic ocean acidification over the twenty-first century and its impact on calcifying organisms', Nature. doi: 10.1038/nature04095.

Pauwels, H. et al. (2007) 'Chemistry of fluids from a natural analogue for a geological CO2 storage site (Montmiral, France): Lessons for CO2-water-rock interaction assessment and monitoring', Applied Geochemistry, 22(12), pp. 2817–2833. doi: 10.1016/j.apgeochem.2007.06.020.

Pelejero, C., Calvo, E. and Hoegh-Guldberg, O. (2010) 'Paleo-perspectives on ocean acidification', Trends in Ecology and Evolution, pp. 332–344. doi: 10.1016/j.tree.2010.02.002.

Reeder, R. J. (1983) 'Chapter 1. Crystal Chemistry Of The Rhombohedral Carbonates', Carbonates. De Gruyter, pp. 1–48. doi: 10.1515/9781501508134-005.

Rodriguez-Blanco, J. D. et al. (2012) 'The role of pH and Mg on the stability and crystallization of amorphous calcium carbonate', in Journal of Alloys and Compounds. doi: 10.1016/j.jallcom.2011.11.057.

Rodriguez-Blanco, Juan Diego et al. (2014) ' The role of REE 3+ in the crystallization of lanthanites ', Mineralogical Magazine. Mineralogical Society, 78(6), pp. 1373–1380. doi: 10.1180/minmag.2014.078.6.03.

Rodriguez-Blanco, Juan Diego. et al. (2014) 'The role of Mg in the crystallization of monohydrocalcite', Geochimica et Cosmochimica Acta. Pergamon, 127, pp. 204–220.

Rodriguez-Blanco, J. D., Sand, K. K. and Benning, L. G. (2017) 'ACC and Vaterite as Intermediates in the Solution-Based Crystallization of CaCO3', in New Perspectives on Mineral Nucleation and Growth. doi: 10.1007/978-3-319-45669-0_5.

Rodriguez-Blanco, J. D., Shaw, S. and Benning, L. G. (2011) 'The kinetics and mechanisms of amorphous calcium carbonate (ACC) crystallization to calcite, via vaterite.', Nanoscale, 3(1), pp. 265–271. doi: 10.1039/c0nr00589d.

Rodriguez-Blanco, J. D., Shaw, S. and Benning, L. G. (2015) 'A route for the direct crystallization of dolomite', American Mineralogist. Walter de Gruyter GmbH, 100(5–6), pp. 1172–1181. doi: 10.2138/am-2015-4963.

Rosenbauer, R. J. et al. (2012) 'Carbon sequestration via reaction with basaltic rocks: Geochemical modeling and experimental results', Geochimica et Cosmochimica Acta, 89, pp. 116–133. doi: 10.1016/j.gca.2012.04.042.

Sand, K. K. et al. (2012) 'Crystallization of CaCO 3 in water-Alcohol mixtures: Spherulitic growth, polymorph stabilization, and morphology change', Crystal Growth and Design, 12(2), pp. 842–853. doi: 10.1021/cg2012342.

Schaef, H. T., McGrail, B. P. and Owen, A. T. (2010) 'Carbonate mineralization of volcanic province basalts', International Journal of Greenhouse Gas Control, 4(2), pp. 249–261. doi: 10.1016/j.ijggc.2009.10.009.

Schrag, D. P. (2009) 'Onshore geologic storage of CO2', Science, pp. 1656–1658. doi: 10.1126/science.1175677.

Shannon, R. D. and IUCr (1976) 'Revised effective ionic radii and systematic studies of interatomic distances in halides and chalcogenides', urn:issn:0567-7394. International Union of Crystallography, 32(5), pp. 751–767. doi: 10.1107/S0567739476001551.

Snæbjörnsdóttir, S. et al. (2014) 'CO 2 storage potential of basaltic rocks in Iceland and the oceanic Ridges', in Energy Procedia. Elsevier Ltd, pp. 4585–4600. doi: 10.1016/j.egypro.2014.11.491.

Snæbjörnsdóttir, S. et al. (2017) 'The chemistry and saturation states of subsurface fluids during the in situ mineralisation of CO2 and H2S at the CarbFix site in SW-Iceland', International Journal of Greenhouse Gas Control. Elsevier Ltd, 58, pp. 87–102. doi: 10.1016/j.ijggc.2017.01.007.

Snæbjörnsdóttir, S. Ó. et al. (2020) 'Carbon dioxide storage through mineral carbonation', Nature Reviews Earth & Environment. Springer Science and Business Media LLC, 1(2), pp. 90–102. doi: 10.1038/s43017-019-0011-8.

Snæbjörnsdóttir, S. Ó. et al. (2021) 'Protecting Our Climate by Turning CO2 Into Stone', Frontiers for Young Minds. Frontiers Media SA, 9. doi: 10.3389/FRYM.2021.579895.

Speer, J. A. (1983) 'Chapter 5. CRYSTAL CHEMISTRY and PHASE RELATIONS of ORTHORHOMBIC CARBONATES', in De Gruyter (ed.) Carbonates. De Gruyter, pp. 145–190. doi: 10.1515/9781501508134-009.

Szucs, A. M. et al. (2021) 'Reaction Pathways toward the Formation of Bastnäsite: Replacement of Calcite by Rare Earth Carbonates', Crystal Growth and Design. American Chemical Society, 21, pp. 512–527. doi: 10.1021/acs.cgd.0c01313.

Szucs, Adrienn Maria et al. (2022) ‘Targeted Crystallization of Rare Earth Carbonate Polymorphs at Hydrothermal Conditions via Mineral Replacement Reactions’, Global Challenges. John Wiley & Sons, Ltd, p. 2200085. doi: 10.1002/GCH2.202200085.

Tobler, D. J. et al. (2015) ‘Citrate effects on amorphous calcium carbonate (ACC) structure, stability, and crystallization’, Advanced Functional Materials. Wiley-VCH Verlag, 25(20), pp. 3081–3090. doi: 10.1002/adfm.201500400.

Tobler, D. J. et al. (2016) ‘Effect of pH on Amorphous Calcium Carbonate Structure and Transformation’, Crystal Growth and Design. doi: 10.1021/acs.cgd.6b00630.

United Nations (2015) ‘Adoption of the Paris Agreement’, Conference of the Parties on its twenty-first session

Vallina, B. et al. (2014) ‘The effect of heating on the morphology of crystalline neodymium hydroxycarbonate, NdCO3OH’, Mineralogical Magazine. Cambridge University Press, 78(6), pp. 1391–1397. doi: 10.1180/MINMAG.2014.078.6.05.

Vallina, B. et al. (2015) ‘The role of amorphous precursors in the crystallization of La and Nd carbonates’, Nanoscale. Royal Society of Chemistry, 7(28), pp. 12166–12179. doi: 10.1039/c5nr01497b.

Voigt, M. et al. (2021) ‘An experimental study of basalt–seawater–CO2 interaction at 130 °C’, Geochimica et Cosmochimica Acta. Pergamon, 308, pp. 21–41. doi: 10.1016/j.gca.2021.05.056.

Williamson, P. (2016) ‘Scrutinize CO2 removal methods’, Nature, 22(3), pp. 153–155.

Xu, T., Apps, J. A. and Pruess, K. (2004) ‘Numerical simulation of CO2 disposal by mineral trapping in deep aquifers’, Applied Geochemistry, 19(6), pp. 917–936. doi: 10.1016/j.apgeochem.2003.11.003.

Chapter 2.

RESEARCH AIMS & OBJECTIVES

2.1 RESEARCH AIMS

This research focuses on the kinetics and mechanisms of divalent carbonate mineralisation. Through the synthesis of carbonate minerals under the influence multi-component solutions and the analysis of carbonate cements on geological samples, this research presents further insights into the conditions required for carbonate formation in the context of biomineralization, industrial $CaCO_3$ production and carbon capture and storage (CCS) in basaltic reservoirs.

During the last two centuries the atmospheric concentrations of CO_2 have increased from 278 ppm (1750) to over 420 ppm (2023) (Stein and National Oceanic and Atmospheric Administration, 2022). Scientific research has demonstrated that the ideal method for long-term storage of carbon underground is CCS via mineral trapping (IPCC, 2005). This also means that it is essential to optimise the existing methods or develop new carbon capture and storage strategies to reach the targets established by the IPCC panel (IPCC, 2018). However, these optimisation methods are not easy because of the heterogeneous nature of the geologic environment, the composition of water and the complex and multi-stage crystallisation mechanisms of minerals, including carbonate minerals. We do not have an in-depth mechanistic understanding of how minerals, specifically carbonates, form and how specific factors (e.g., foreign ions, supersaturation, temperature, pressure) affect their kinetics and mechanisms of formation. If we can understand the role of all these factors in CCS, it would be easier to control the formation of C-bearing minerals and therefore improve CCS methods.

CCS in basalt has proven very efficient at rapidly storing CO_2 as carbonate via mineral trapping, which is the most stable method of CO_2 storage over geological time. This is due to the abundance of ions like Mg^{2+}, Ca^{2+}, Al^{3+}, Fe^{2+} and Na^{+} in basalt, the high reactivity to CO_2-containing

fluids and their abundance on the Earth's surface. The CarbFix Project has shown that in less than two years post injection 95% of the CO_2 injected was mineralised into carbonates (Matter *et al.*, 2016) which is exponentially quicker than mineralization rates in conventional CCS. Also, the injection of seawater into basaltic reservoirs can be more cost and efficient than fresh water, and which could lead to a substantial reduction in the large infrastructure costs for undertaking carbon capture and storage capture and storage activities (Voigt *et al.*, 2021). CarbFix's CO_2SeaStone project, has highlighted the need to understand the combined influence of common seawater ions such as, Na^+, Cl^-, Ca^{2+}, Mg^{2+}, SO_4^{2-}, on the formation of carbonates. By understanding the combined role of foreign ions in these reactions and the mechanisms by which these carbonates form, as well as their kinetics of formation, we could target the formation of stable C-bearing minerals during field-based or industry-based CCS processes.

The contributions made here have wide applicability. This research aims to extend our understanding about carbonate formation and mechanisms in relation to CO_2 sequestration, as well as biomineralisation process, industrial applications and wider carbonate geochemistry.

The overall goal of this thesis is to examine the effects of multi-component solutions on the crystallization of divalent carbonates experimentally and within natural systems. This is approached in three ways: Influences of carbonate crystallisation; carbonate mineral replacement reactions; carbonate crystallisation and replacement processes in natural analogues of basaltic CCS.

This thesis will address 3 central questions:

1) What is the combined influence of a multicomponent solutions on $CaCO_3$ crystallisation?
2) Does Ca^{2+} influence the mechanisms of calcite replacement by aragonite type carbonates?
3) How does the geochemistry of the host basalt influence the resulting carbonate cements?

2.2 RESEARCH OBJECTIVES

The objectives of this research are threefold:

This research follow the formation pathways of calcium carbonate ($CaCO_3$) crystallisation from a multicomponent solution of known inhibitors. Through UV-Vis spectrophotometry the mechanisms and kinetics quantifies the reaction rates.

I hypothesise that the combination of common seawater ions and inorganics will reveal a more complex formation pathway than reported in single ion studies (e.g., Astilleros *et al.*, 2000; Davis, Dove and De Yoreo, 2000; Wasylenki *et al.*, 2005; Nehrke *et al.*, 2007; Sugiura *et al.*, 2013, 2019; Füger *et al.*, 2019). $CaCO_3$ crystallisation was followed *in situ* using UV-Vis spectrophotometry. $CaCO_3$ characterisation will be undertaken using powder X-ray diffraction (XRD) in the Geology laboratories in Trinity College Dublin (TCD) and scanning electron microscopy (SEM) imaging will be conducted in the Centre for Microscopy and Analysis (CMA) laboratories in TCD.

Using homogeneous nucleation and heterogeneous nucleation experiments, this research assesses the replacement of rhombohedral calcite with orthorhombic carbonates strontianite ($SrCO_3$) and witherite ($BaCO_3$) across ambient and hydrothermal conditions. For this study, it was of interest to investigate the influence of Ca^{2+} on the $BaCO_3$ and $SrCO_3$.

I hypothesise that calcite replacement by $SrCO_3$ and $BaCO_3$ occurs initially by an aragonite type surface precipitation on the calcite crystal and that Ca^{2+} influence (inhibits) $SrCO_3$ and $BaCO_3$ crystallisation in homogeneous nucleation experiments. $BaCO_3$ and $SrCO_3$ crystallisation was followed *in situ* using UV-Vis spectrophotometry. $BaCO_3$ and $SrCO_3$ characterisation was undertaken using powder XRD in the Geology laboratories in TCD and SEM imaging will be conducted in the CMA laboratories in TCD.

By examining carbonate rims and cements from basaltic samples from the Sverrefjellet volcano, Svalbard (Norway), this study aims to contribute to this growing area of CCS via mineral carbonation research by exploring the *in situ* carbonisation basaltic rocks as a natural analogue for basaltic CCS projects, i.e. CarbFix (Matter *et al.*, 2009; Gíslason *et al.*, 2018).

I hypothesise the geochemistry of the host rock influences the crystallisation of carbonate cements. Phase characterisation, of both the carbonate rims and the basaltic portion of the sample was

undertaken using powder XRD in the Geology laboratories in TCD and SEM including energy dispersive spectroscopy (EDS) and cathodoluminescence (CL), imaging will be conducted in the CMA laboratories in TCD.

2.3 REFERENCES

Gíslason, S. R. et al. (2018) 'A brief history of CarbFix: Challenges and victories of the project's pilot phase', Energy Procedia. Elsevier, 146, pp. 103–114. doi: 10.1016/J.EGYPRO.2018.07.014.

IPCC (2005) IPCC Special Report on Carbon dioxide Capture and Storage, Working Group III of the Intergovernmental Panel on Climate Change. Edited by Prepared by Working Group III of the Intergovernmental Panel on Climate Change et al. Cambridge, United Kingdom and New York, NY, USA: Cambridge University Press. doi: 10.1021/es200619j.

IPCC (2018) Special Report on Global Warming of 1.5C, Global Warming of 1.5 °C: An IPCC Special Report on the impacts of global warming of 1.5°C above pre-industrial levels and related global greenhouse gas emission pathways, in the context of strengthening the global response to the threat of climate change.

Matter, J. M. et al. (2009) 'Permanent Carbon Dioxide Storage into Basalt: The CarbFix Pilot Project, Iceland', in Energy Procedia, pp. 3641–3646. doi: 10.1016/j.egypro.2009.02.160.

Matter, J. M. et al. (2016) 'Rapid carbon mineralization for permanent disposal of anthropogenic carbon dioxide emissions', Science. American Association for the Advancement of Science, 352(6291), pp. 1312–1314. doi: 10.1126/science.aad8132.

Stein, T. and National Oceanic and Atmospheric Administration (2022) Carbon dioxide now more than 50% higher than pre-industrial levels | National Oceanic and Atmospheric Administration.

Voigt, M. et al. (2021) 'An experimental study of basalt–seawater–CO2 interaction at 130 °C', Geochimica et Cosmochimica Acta. Pergamon, 308, pp. 21–41. doi: 10.1016/j.gca.2021.05.056.

Chapter 3.

Synergistic effects of Mg^{2+}, SO_4^{2-} and citrate ions on $CaCO_3$ crystallisation inhibition

Authors: Niamh Faulkner and Juan Diego Rodríguez-Blanco

Journal: Crystal Growth and Design

Publication Status: In review (submitted March 7th 2023; resubmitted July 18th 2023)

Author Contributions: N. Faulkner conducted all analyses, wrote the manuscript and produced all figures and tables. J.D Rodríguez-Blanco advised and edited the manuscript.

Synergistic effects of Mg^{2+}, SO_4^{2-} and citrate ions on $CaCO_3$ crystallisation inhibition

3.1 ABSTRACT

The formation pathways of $CaCO_3$ from solution in the presence of three combined foreign ions (Mg^{2+}, SO_4^{2-} and citrate) have been followed in situ using a combination of UV-Vis spectrophotometry, powder X-ray diffraction and scanning electron microscopy. Most studies focus on the effects of these single ions in the crystallisation of $CaCO_3$, however, our understanding of their combined effects is scarce. The crystallisation in these multicomponent solutions reveals an intricate scenario, as the concentration of ions, ratio and formation of complexes prior to the nucleation of $CaCO_3$ influence the initial reactive fluid saturation state and affect the kinetics and mechanisms of crystal growth, polymorph selection and crystal morphology. The combination of two or three ions results in the crystallisation of mainly aragonite, with multiple variations depending on the ion concentrations and ratios prior to the nucleation of the first solid phase. In all cases the combination of ions slowed down the crystallisation rates and influenced the morphology of the primary solids, predominantly via the adsorption of inhibitors to specific crystallographic faces. These complex crystallisation pathways of $CaCO_3$ from multicomponent solutions provide insights into the mechanisms controlling biomineralization and abiotic $CaCO_3$ formation during industrial synthesis or carbon capture and storage processes.

3.2 INTRODUCTION

Calcium carbonate is one of the most abundant minerals in the sedimentary record, forming both abiotically and through biomineralization processes. It plays a vital role in the global carbon cycle (Mabry and Mondal, 2011; Washbourne *et al.*, 2015; Pogge von Strandmann *et al.*, 2019; Osman *et al.*, 2020; Portugal *et al.*, 2020) and is found throughout in many different environments

(from caves, lakes and seawater to soils and hot springs). Calcium-bearing minerals account for roughly 50% of all known biominerals, with calcium carbonate being the most abundant biomineral, both in terms of taxa abundance and quantity formed (Lowenstam and Weiner, 1989).

$CaCO_3$ formation is also of industrial importance, as it has a key role in the production of solids with targeted compositions, structures, sizes, shapes and surface properties across a range of industrial applications. These include the targeted synthesis of $CaCO_3$ for use as fillers to improve mechanical properties of plastics (Thenepalli *et al.*, 2015); there is widespread use in the pharmaceutical industry, including $CaCO_3$ based drugs delivery systems (Wei *et al.*, 2008; Feng *et al.*, 2022) and as antiacids (Fu *et al.*, 2022); $CaCO_3$ is used as a remediation tool for concrete (Bang *et al.*, 2010) and in contaminated soils for bioremediation (Zeng *et al.*, 2016); and in $CaCO_3$ based energy storage systems (Khosa *et al.*, 2019).

Due to the widespread natural occurrence and importance of $CaCO_3$ in industrial applications, most of the studies of $CaCO_3$ nucleation and growth have focused on its crystallisation mechanisms and kinetics, both abiotically and during biomineralisation processes. In particular, during the last decades there have been a large number of experimental studies examining the influence of divalent (e.g., Mg^{2+}, Sr^{2+}, Ba^{2+}, Cd^{2+}, SO_4^{2-}) and trivalent (e.g., REE^{3+}, PO_4^{3-}) ions (Astilleros *et al.*, 2000; Davis *et al.*, 2000; Wasylenki *et al.*, 2005; Nehrke *et al.*, 2007; Sugiura *et al.*, 2013, 2019; Füger *et al.*, 2019), as well as organics (e.g., citrate, alcohols, proteins) (Sand *et al.*, 2012a; Tobler *et al.*, 2014; Montanari *et al.*, 2017) on calcium carbonate formation and trace chemistry, most of them showing an overall inhibition effect on $CaCO_3$ growth kinetics. Investigating the influence of ions like Na^+, Cl^-, SO_4^{2-} and Mg^{2+}, is of interest, as they are the most abundant ions in seawater and they are known to affect the polymorph selection and crystal chemistry of abiotic and biotic $CaCO_3$ during geologic times (Sandberg, 1983; Wilkinson *et al.*, 1984; Zhuravlev and Wood, 2009; Bots *et al.*, 2011). For example, the Mg:Ca ratio of 5.2 in modern seawater results in $CaCO_3$ precipitating as aragonite in marine environment (Sun *et al.*, 2015). Sulphate, at 28 mM is the second most common anion in seawater (Canfield and Farquhar, 2009) and is commonly incorporated into biominerals, amounting to around 2% of all $CaCO_3$ biominerals, including brachiopod shells and corals (Cusack *et al.*, 2008;

Balthasar and Cusack, 2015) and it is known to play a key role in the switch from calcite to aragonite seas (Bots et al., 2011).

Notably, the individual effects of Mg^{2+} and SO_4^{2-} on $CaCO_3$ crystallisation are well documented, such as inhibiting $CaCO_3$ crystallisation, reduction of crystallisation rates and polymorph control (Nancollas and Reddy, 1971; Berner, 1975; Reddy and Nancollas, 1976; Busenberg and Niel Plummer, 1985; Zhang *et al.*, 2007; Zhu *et al.*, 2022). Mg^{2+} is known inhibit $CaCO_3$ crystallisation, increasing the lifetime of amorphous calcium carbonate (ACC), as reported both in abiotic (Loste *et al.*, 2003; Rodriguez-Blanco *et al.*, 2012) and biotic processes (e.g. (Raz *et al.*, 2003; Politi *et al.*, 2010; Foran *et al.* 2013). In laboratory-based experiments SO_4^{2-} has been shown to influence the kinetics and mechanisms of $CaCO_3$ crystallisation in both homogeneous, (Bots *et al.*, 2011) and heterogeneous nucleation, with almost a 90% reduction in the nucleation rate (Zhu *et al.*, 2021). However, there is a knowledge gap on the combined effects of Mg^{2+} and SO_4^{2-} on $CaCO_3$. Experimental research has shown that $MgSO_4$ can be used to produce specific aragonite morphologies (Hu *et al.*, 2008) and that the presence of SO_4^{2-} results in the inhibition of calcite nucleation and growth more efficiently than Mg^{2+} individually (Nielsen *et al.*, 2016). Experimental results agree with atomistic simulations that show that SO_4^{2-} forms ion pairs with Mg^{2+} and promote the low-temperature formation of Mg-bearing carbonates (Zhang *et al.*, 2019; Toroz *et al.*, 2021, 2022).

In seawater, biogenic $CaCO_3$ regularly forms in the presence of and is influenced by biomolecules. As such, the role of biomolecules on $CaCO_3$ has been studied to a great extent (e.g., Meldrum and Hyde, (2001); Raz *et al.* (2003); Henriksen *et al.* (2004); Meldrum (2013); Hodson *et al.* (2015); Patwardhan and Staniland, (2019) and Mercedes-Martín *et al.* (2022)). These studies are also of great industrial importance, as the organics can be used to produce $CaCO_3$ polymorphs with targeted morphologies and shapes (e.g., Didymus *et al.*, 1993; Moore *et al.*, 2004; Sand *et al.*, 2012b; Gopi *et al.*, 2013; Ma *et al.*, 2015) or to prevent scale formation (e.g., molecules like (poly)acrylic acid and (poly)aspartic acid, among others, are widely used scale inhibitors in washing machines and in oil and gas fields; (Liu *et al.*, 2011; Al-Hamzah *et al.*, 2014; Zahlan *et al.*, 2019). Two important

inhibitors that are commonly studied by industry are citric acid and triphosphate (Gebauer *et al.*, 2009).

Citric acid, or its deprotonated form citrate (CIT, $C_3H_5O(COO)_3^{3-}$), has been linked to biomineralization processes (Sato *et al.*, 2011) as it is an intermediate in the tricarboxylic acid cycle that can form during glycolysis. It has three carboxyl groups and one hydroxylic group and can form complexes with Ca^{2+} in water at medium and high pH (Westin and Rasmuson, 2005). CIT has been shown to stabilise ACC (Tobler *et al.*, 2015) and also inhibits $CaCO_3$ crystallisation due to the complexing with Ca^{2+} ions forming calcium citrate, resulting in decreases in both free Ca^{2+} ion activity and $CaCO_3$ saturation levels, thus affecting the morphology and polymorph selection of $CaCO_3$ (Westin and Rasmuson, 2005; Gebauer *et al.*, 2009; Montanari *et al.*, 2017).

While numerous laboratory-based studies have quantified the effects of individual elements on $CaCO_3$ crystallisation, detailed kinetic studies with multi-component solutions (e.g., seawater; Zuddas *et al.* (2003) and Lopez, *et al.*(2009)) are scarce, but they are urgently needed to understand the complex interaction of multiple inorganics and organics during the early stages of nucleation and growth of carbonate minerals in seawater, or during complex industrial $CaCO_3$ synthesis. To the best of our knowledge, the authors believe this is the first laboratory-based study to quantify the effects of a multicomponent system, comprising both biomolecules and common seawater divalent ions on the crystallisation of $CaCO_3$ at low supersaturation conditions and ambient (21 °C) temperature. Understanding the effect of solutions containing different ions simultaneously provides a key insight into the formation mechanics, morphologies, surface properties and stabilities of $CaCO_3$ biominerals, allowing us to mimic conditions closer to biomineralisation, as well as offering insight into mineral-fluid interactions for industrial and environmental applications, from the synthesis of nanoparticles for environmental purposes (Kezuka *et al.*, 2019; Dang and Xu, 2022) to the injection of CO_2-charged seawater into basaltic reservoirs for carbon capture and storage (CCS) (Voigt *et al.*, 2021).

Building on works such as Nielsen *et al.* (2016) and Montanari *et al.* (2017), (see Appendix A1), in this study we have followed an incremental approach and gradual progression to study the combined effects of Mg^{2+} and SO_4^{2-} and citrate ions on the crystallization of $CaCO_3$ at varying

concentrations and ambient conditions. We predict that the combined influence of Mg^{2+} and SO_4^{2-} and citrate ions will have a larger impact on $CaCO_3$ crystallisation kinetics, e.g. longer induction times, than each ion's individual influence. Second, we speculate that the combination of certain ions will have a stronger influence than others (e.g., Mg^{2+} + CIT > SO_4^{2-} + CIT). Third, we envisage that changing the concentration of each ion will directly correlate to changes in crystallisation kinetic parameters. For this purpose we have targeted the concentrations of Ca^{2+} and CO_3^{2-} below the solubility of amorphous calcium carbonate to determine the impact of these ions in combination on the early stages of crystallisation of $CaCO_3$ directly from aqueous solutions. We used UV-Vis spectrophotometry to monitor the crystallization of $CaCO_3$ *in situ* and real time. Initially, we focused on the pure system to establish a baseline reference point. After we examined the individual and combined influence of Mg^{2+} and SO_4^{2-}, then with the addition of CIT. This allowed us to i) quantify the kinetics of crystallisation, ii) investigate any changes in $CaCO_3$ morphology and iii) infer crystallisation mechanisms.

Our investigation demonstrates that even minor modifications in the chemical composition of a multi-component solution can exert a significant influence on the kinetics of $CaCO_3$ crystallization, the selection of polymorphs, and the morphology of the primary crystalline solids. This understanding of the impact of the solution matrix on the crystallization mechanism during the early stages of mineral formation is of paramount importance for gaining insights into biomineralization processes and for effectively controlling the properties, particle size, and shape of solids during industrial synthesis of $CaCO_3$.

3.3 METHODS

3.3.1 CaCO3 synthesis and crystallisation

The effects of Mg^{2+} and SO_4^{2-} (alone and in combination) on $CaCO_3$ crystallization were studied at ambient temperature (21 °C). To examine the effect Mg^{2+} and $MgSO_4$, 4 mM aqueous solutions of $CaCl_2$ with different concentrations of Mg^{2+} or $MgSO_4$ (1, 5, 10, 15 and 20 mM) were added to a 4 mM solution of Na_2CO_3. For the effect SO_4^{2-} experiments different concentrations of

SO_4^{2-} (1, 5, 10, 15 and 20 mM) were added to a 4 mM solution of Na_2CO_3 and combined with aqueous solutions of 4 mM $CaCl_2$. Ambient temperature was chosen as it is close to the average seawater temperature, 20 °C (Roemmich, 2014).

In order to gain a comprehensive understanding of the impact of these ions on the kinetics, mechanisms, polymorph selection, and crystal morphology of $CaCO_3$ formation, it was crucial to conduct experiments encompassing a range of values. Concentrations of the Ca^{2+} and CO_3^{2-} bearing solutions were selected using similar concentrations previously reported Montanari *et al.* (2017). These concentrations were selected for three main reasons, first is to ensure that $CaCO_3$ forms by a homogeneous nucleation process (avoiding surface precipitation processes, e.g., on the walls of the cuvettes/reactors). The second advantage of using these concentrations is to ensure that crystallisation happens below the solubility of ACC, compared to, for example, Tobler *et al.* (2015) who used solutions with concentrations of 13 mM to produce ACC. Third, the subsequent effect of concentration on the supersaturation levels was also taken into account to avoid too long (hours) induction times and crystallisation rates in the pure system, in line with Montanari *et al.* (2017), who showed the inverse relationship between the saturation index (SI) of the solution and the induction time for $CaCO_3$ polymorphs (Appendix A2). The selection and concentration of additives was done to mimic concentrations in seawater and other environments with different $Ca/Mg/SO_4$ ratios (rivers, estuaries, industrial production of $CaCO_3$), for example the modern Ca/Mg ratio of seawater is 5.2 (Sun *et al.*, 2015) and river water is 0.54 (Murray, 2004) and the current sulphate concentration in seawater is 28 mM (Canfield and Farquhar, 2009). Also, these values are similar to previous $CaCO_3$ crystallisation experiments used by Bots *et al.*, (2011); Nielsen *et al.* (2016); Montanari *et al.* (2017) and Zhu *et al.* (2021).

The solutions were prepared using reagent grade chemicals: calcium chloride ($CaCl_2$: VWR Chemicals, 99.5% purity), sodium carbonate (Na_2CO_3: Acros Organics, 99.5% purity), magnesium chloride ($MgCl_2$: Merck KGaA), magnesium sulphate ($MgSO_4$: Alfa Aesar), sodium sulphate (Na_2SO_4) and ultrapure deionized water (Milli-Q; specific resistivity >18 MΩ cm^{-1}). Following these first experiments, the combined effects of citrate (CIT) and Mg^{2+} and/or SO_4^{2-} on $CaCO_3$ were

investigated. Various citrate concentrations (0.1, 0.5, 1.0 mM) were combined with 10 mM Mg^{2+} and/or SO_4^{2-} to examine the combined effects of these ions on $CaCO_3$ crystallisation. CIT values were selected because they span over one order of magnitude, with another value (0.5 mM) in between the max and min limits. Solutions of Na_2CO_3 and CIT (Sodium citrate tribasic dihydrate: $HOC(COONa)(CH_2COONa)_2 \cdot 2H_2O$: Sigma Aldrich, ≥99.0% purity) were mixed with $CaCl_2$ containing Mg^{2+} and/or SO_4^{2-}. In the case of the effect of combined SO_4^{2-} + CIT, solutions of 4 mM Na_2CO_3, 10 mM Na_2SO_4 and CIT were combined with a 4 mM $CaCl_2$ solution. Hereby the experiments with various molarities of $Mg^{2+}/SO_4^{2}/MgSO_4$ and their effect on $CaCO_3$ will be known as *round 1 experiments* and the experiments with the addition of citrate will be known as *round 2 experiments*.

The saturation indices of aragonite, calcite and vaterite were calculated with the hydrogeochemical code PHREEQC (Parkhurst and Appelo, 1999) using the minteq.v4 database (Allison, *et al.,* 1991).

The saturation index (SI) is defined as:

$$SI = Log\,(\frac{IAP}{K_{sp}})$$

Where IAP represents the ion activity product and K_{sp} represents the solubility product of the mineral phase.

All crystallisation reactions were followed using time-resolved UV-Vis spectrophotometry, examining the change in solution absorbance (turbidity), after the methods of Tobler *et al.* (2014; 2015). This involved mixing equal volumes (1 mL) of a 4 mM Na_2CO_3 solution and a 4 mM $CaCl_2$ solution, containing varying Mg^{2+} and/or SO_4 concentrations. The UV-Vis spectrophotometer (OceanOptics) measured turbidity at a wavelength of 450 nm and the solutions were constantly stirred. UV-Vis spectrophotometry was used to monitor the in situ change in crystallisation rates as a function of turbidity. The experiments ran until the absorbance (i.e. turbidity) profile reached a

plateau, figure 1. The solutions were then vacuum filtered and washed with isopropanol and dried, following the method of Rodriguez-Blanco *et el.* (2008). Each experiment was repeated up to three times. Further details about the sample cell design and experimental conditions are given in the Appendix A3 and A4.

In order to obtain enough sample for characterization with powder-XRD and SEM it was necessary to run complimentary large batch experiments (1 L total volume), at the same concentrations and conditions alongside the UV-vis spectrophotometry experiments. This method of scaling up was done according to the procedures of Van Driessche *et al.* (2012); Vallina *et al.* (2015); Montanari *et al.* (2017) and Mulders *et al.* (2021).

The $CaCO_3$ polymorphs produced in the experiments were identified using a powder XRD Bruker D5000 powder X-ray diffractometer (Cu Kα radiation, 0.02° $step^{-1}$ from 5 to 50° 2θ at 0.15° min^{-1}). Phase identification was carried out using Diffract Suite EVA software from Bruker in combination with the Powder Data File (PDF-4, The International Centre for Diffraction Data). Pattern-matching refinement and determination of the relative proportions of the precipitated $CaCO_3$ polymorphs were carried out with the Rietveld refinement software TOPAS (Coelho *et al.*, 2011). The quantitative XRD errors uniformly remained below 1–2 wt %, requiring no additional data pre-processing such as normalization. Further details about the limitations of phase identification are presented in Appendix A5.

In the samples containing calcite that formed in the presence of Mg^{2+}, the Mg content was calculated using the equation after Arvidson and Mackenzie (1999):

$$X_{(MgCO_3)} = -3.6393 d_{(10\bar{1}4)} + 11.0405$$

Where $X_{(MgCO3)}$ represents the mole percent $MgCO_3$ in the calcite $d_{(10\bar{1}4)}$ represents the d-spacing of the $\{10\bar{1}4\}$ Bragg peak.

Samples were examined and imaged using a scanning electron microscope (Tescan MIRA XMU FE-SEM) to determine the morphology and sizes of the $CaCO_3$ polymorphs. The SEM operated

under high vacuum conditions, at 5 kV with a MD SE (in-lens) detector in Ultra high resolution mode. Samples were mounted on SEM mounts and gold coated (5 nm).

3.3.2 Kinetic data analysis

Following the method of Montanari *et al.* (2017) the normalized turbidity profiles were fitted to the Johnson-Mehl-Avrami-Kolmogorov particle nucleation model (Kolmogorov, 1937; Johnson and Mehl, 1939; Avrami, 1940), based on the Avrami equation (Avrami, 1940):

$$\alpha = 1 - e^{-(k\cdot(t-t_{ind}))^n}$$

Where *a* represents the degree of the reaction (normalised turbidity data), t_{ind} is the induction time, the time between solution mixing *t* and the onset of nucleation, *k* is the rate of crystallisation, and *n* is the Avrami constant (Avrami, 1940).

Rewriting the Avrami Equation gives:

$$-ln\,ln(1-y) = n\,ln\,k + n\,ln\,\mathrm{t}$$

The reaction with kinetics that conform to this equation give a straight line when $-ln\,ln(1-y)$ is plotted against *ln* t (Putnis, 1992; Xia *et al.*, 2009). The empirical parameter n value is given by the value of the slope, which is used to compare reaction mechanisms. The intercept on the y axis gives the value of n *ln* k, by which the k value can be determined.

3.4 RESULTS

3.4.1 Turbidity experiments

The addition of SO_4^{2-} and/or Mg^{2+}, as well as the combination of the divalent ions with CIT, influenced both the nucleation and growth of $CaCO_3$ from solution. All the kinetic data results are presented numerically in Table 3.1 and Table 3.2. In general, the inhibition increased with higher concentrations of dopant and was the most significant when divalent ions were combined with citrate. This inhibition was represented by i) increased induction time, ii) changes in turbidity profile shape and iii) reduced crystallisation rates.

Delays to $CaCO_3$ crystallisation were observed in all tested conditions, this induction period (t_{ind}) varied with inhibitor added and increased with inhibitor concentration. In the absence of foreign ions, the induction time of pure $CaCO_3$ was 31 seconds and the primary crystallisation process was completed after 360 seconds (Figure 3.1). Representative normalized turbidity obtained during $CaCO_3$ crystallisation for *round 1* and *round 2* experiments are shown in Figure 3.2 and Figure 3.3, respectively. Overall, a positive correlation was found between inhibitor concentration and induction times across the experiments.

In *round 1* there is a wide range in the influence on the induction time, the general pattern of influence on induction time increased in the order SO_4^{2-} < $MgSO_4$ <Mg^{2+} (Figure 3.2). The addition of SO_4^2 resulted in the shortest delays, ranging from 38 seconds (1 mM) to 301 seconds (20 mM). Between 1- 15 mM SO_4^{2-}, relative to the pure system t_{ind}, the addition of SO_4^{2-} resulted in an average increase of induction time of 77%. Compared to the behaviour of SO_4^{2-}, we observed a stronger increase in the induction time when Mg^{2+} was added to the system. This effect increased with increased Mg^{2+} molarity, especially in the experiments with ≥15 mM of Mg^{2+}. Induction times ranged from 45 seconds (1 mM) to 414 seconds (20 mM), which was the longest delay to induction observed in *Round 1* experiments. At lower concentrations (≤ 10 mM), the combination of Mg with SO_4 resulted in the largest delays to induction, up to 160 seconds (5 mM $MgSO_4$), after which Mg^{2+} (≥ 15 mM) had the stronger influence.

The addition of CIT in *round 2* experiments **(**Figure 3.3) had a stronger influence on induction times, compared to the *round 1* experiments, which became more pronounced with increased CIT molarity. Similar to the *round 1* experiments, this influence was ion specific and followed a general pattern of influence on induction time that increased in the order CIT + SO_4^{2-} < CIT + $MgSO_4$ < CIT + Mg^{2+}.

There was little difference between induction time values from the *round 1* experiments with SO_4^{2-} and the *round 2* experiments combination of SO_4^{2-} and CIT. Similar to *round 1*, these induction times were the shortest in the *round 2* experiments, with the largest delay of 5 minutes (0.5 mM CIT). The combination of CIT + $MgSO_4$ resulted in longer induction times than the *round 1* results. Compared to the *round 1* experiment (10 mM $MgSO_4$) the addition of $MgSO_4$ and 0.1 mM and 0.5 mM CIT resulted in increased induction rates of 15.8 and 26.3 minutes respectively (an increase of 3 orders of magnitude and 4 orders of magnitude respectively). However, at the maximum CIT value (1.0 mM) the induction dropped to only 7.4 minutes. The largest increase of the induction period was observed in the CIT + Mg^{2+} experiments. These increases were substantially higher compared to the *round 1* experiments without CIT (1.2 minutes), ranging from 12 minutes (0.1 mM CIT), 49 minutes (0.5 mM CIT) and 118 minutes (1.0 mM CIT). The Mg^{2+} + CIT experiments are the best example of the positive correlation between inhibitor concentration and induction times (R^2 = 0.99052).

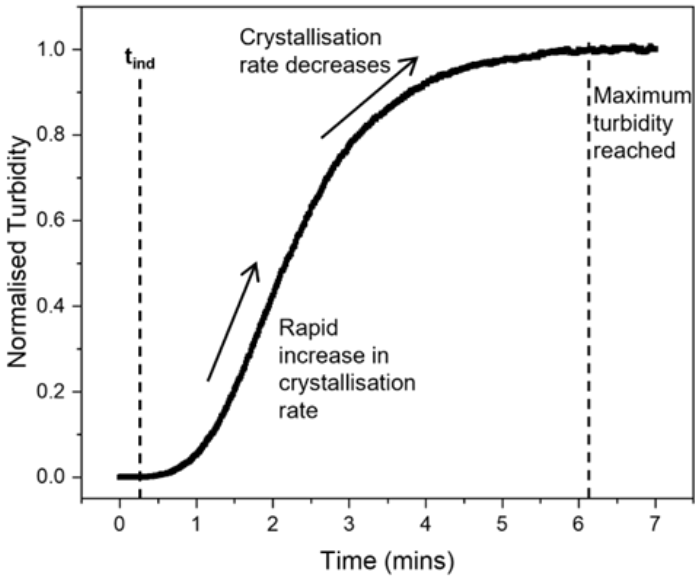

Figure 3.1: Normalized turbidity profile for the pure system after mixing two solutions of 4 mM Na_2CO_3 and 4 mM $CaCl_2$. t_{ind} denotes the induction time and the onset of $CaCO_3$ crystallisation. The crystallisation rate, k, initial increases rapidly, following a decrease until it plateaus as maximum turbidity is reached.

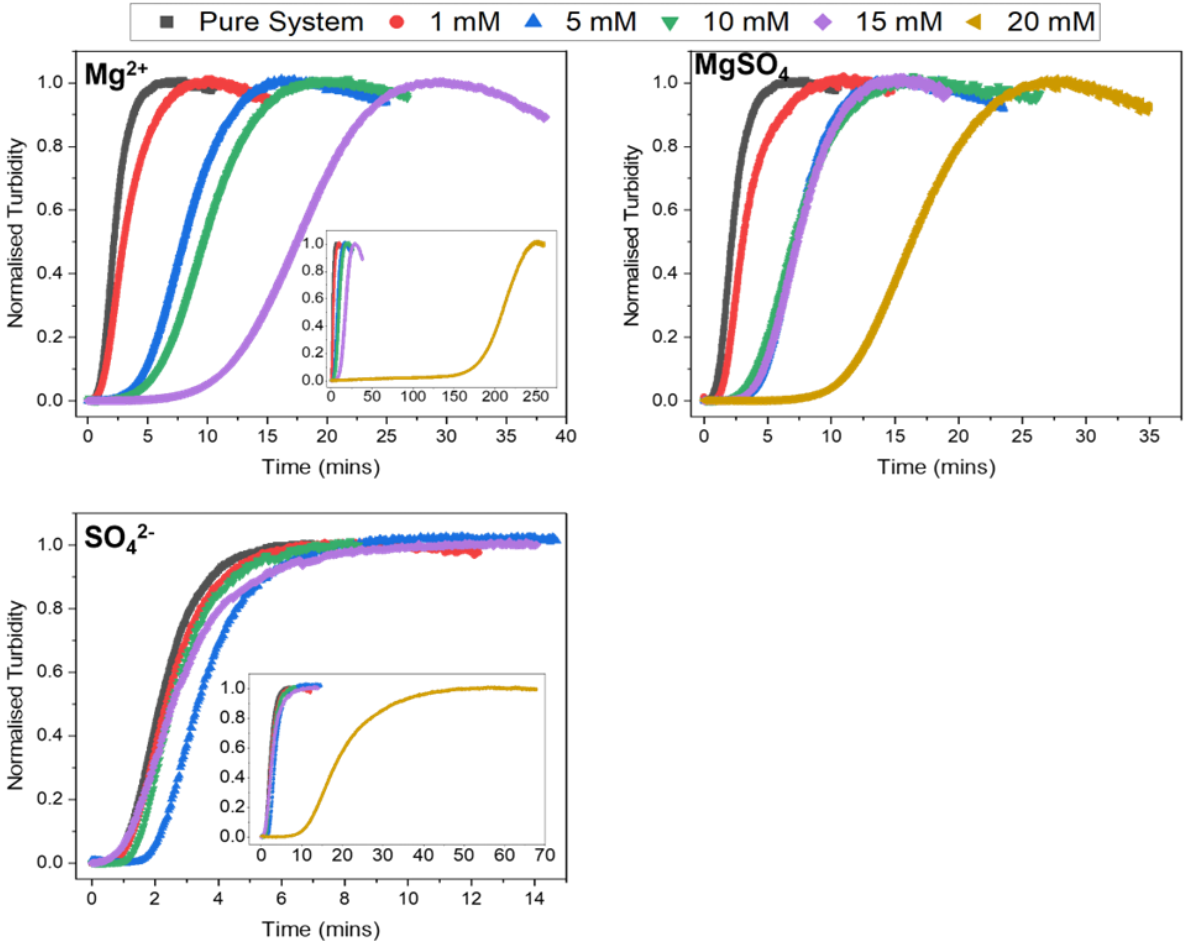
Pure System
1 mM
5 mM
10 mM
15 mM
20 mM
Mg2+
MgSO4
SO4 2-
Normalised Turbidity
Time (mins)

Figure 3.2: Round 1 $CaCO_3$ crystallisation experiments monitored by UV-vis spectrophometry, normalized turbidity plots. Top right: Mg^{2+} system. Inset: full experiment demonstrating the increase in induction time with 20 mM Mg^{2+} compared to the lower molarity experiments. Top left: $MgSO_4$ system. Bottom SO_4^{2-} system. Inset: full experiment demonstrating the increase in induction time with 20 mM SO_4^{2-} compared to the lower molarity experiments. Symbols refer to the same ion molarity in experiments: Pure system (■); 1mM (●); 5 mM (▲); 10 mM (▼); 15 mM (◆); 20 mM (◀).

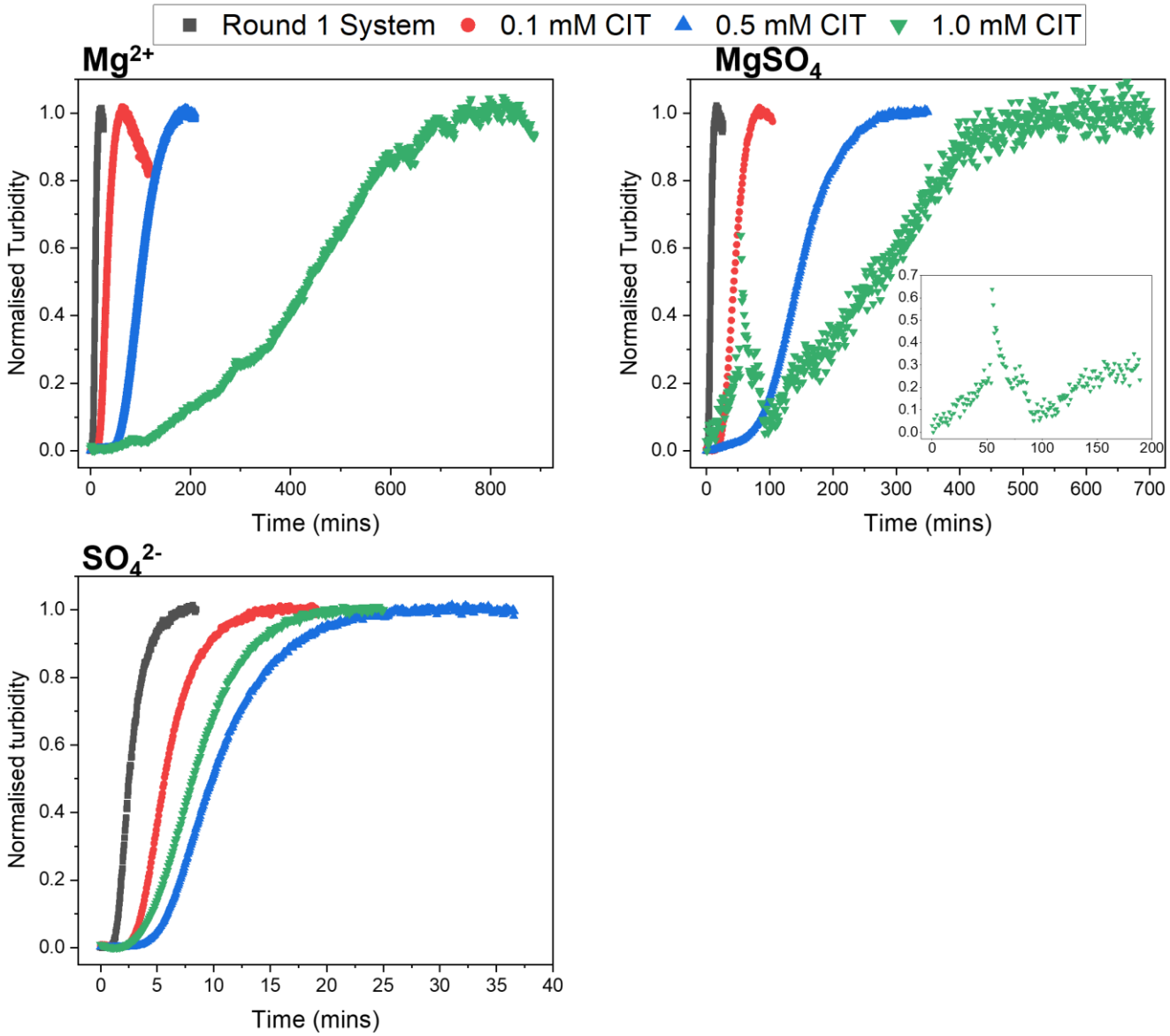
Round 1 System
0.1 mM CIT
0.5 mM CIT
1.0 mM CIT
Mg2+
Normalised Turbidity
Time (mins)
MgSO4
Normalised Turbidity
Time (mins)
SO4 2-
Normalised turbidity
Time (mins)

Figure 3.3: Round 2 normalized turbidity plots, monitoring the combined effect of ions (10 mM of the round 1 ion) and various citrate concentrations. Top left: Mg^{2+} and CIT system. Top right: $MgSO_4$ and CIT system. Inset transient phase. Bottom: SO_4^{2-} and CIT system. Symbols refer to the same ion molarity in experiments: turbidity profile of round 1 experiments, 10 mM of the examined inhibitor (■); + 0.1 mM CIT (●); + 0.5 mM CIT (▲); + 1.0 mM CIT (▼).

	Concentration (mM)	JMAK model fit		Saturation Index			Phase	
		t_{ind} (sec)	k ($x10^{-3}$ s^{-1})$_a$	Calcite	Aragonite	Vaterite	Dominant	Minor
	Pure System	31	6.84	2.16	2.01	1.58	CC (96%)	VAT (4%)
+ Mg^{2+}	1	45	4.68	2.13	1.98	1.55	ARG (64%)	VAT (34%); CC (2%)
	5	85	1.89	2.02	1.87	1.44	ARG (98%)	CC (2%)
	10	72	1.55	1.92	1.77	1.34	ARG (100%)	
	15	248	0.88	1.83	1.68	1.25		
	20	414	0.07	1.76	1.61	1.18		CC (<1%)
+ $MgSO_4$	1	48	4.81	2.12	1.97	1.54	ARG (66%)	VAT (28%); CC (6%)
	5	160	2.10	1.99	1.84	1.41	ARG (78%)	VAT (18%); CC (>4%)
	10	116	2.07	1.87	1.72	1.29	ARG (94%)	CC (5%): VAT (>1%)
	15	140	2.03	1.78	1.63	1.2	ARG (97%)	VAT (3%)
	20	300	0.94	1.7	1.55	1.12	ARG (93%)	VAT (7%)
+ SO_4^{2-}	1	38	6.16	2.14	1.99	1.56	VAT (92%)	CC (8%)
	5	80	4.39	2.07	1.92	1.49	VAT (95%)	CC (5%)
	10	56	5.99	2.00	1.85	1.42	VAT(94%)	ARG (2%); CC (<1%)
	15	46	5.50	1.94	1.79	1.36	VAT (92%)	ARG (8%)

	20	396	0.81	1.89	1.74	1.31	VAT (97%)	ARG (3%)

Table 3.1: Data Collected from round 1 turbidity experiments. Phases wt % determined with XRD, CC, calcite; ARG, aragonite, VAT, vaterite. Saturation Indices values from PHREEQC. [a] Extracted from JMAK n ~ 1.

	CIT concentration (mM)	JMAK model fit		Saturation Index			Phase	
		t_{ind} (min)	k ($x10^6$ s^{-1})$_a$	Calcite	Aragonite	Vaterite	Dominant	*Minor*
+ 10 mM Mg^{2+}	0	1.20	1545.48	1.92	1.77	1.34	ARG 100%	
	0.1	12	447.15	1.91	1.76	1.33		
	0.5	49	152.50	1.9	1.75	1.33		
	1	118	25.43	1.8	1.74	1.32		
+ 10 mM $MgSO_4$	0	1.90	2065.94	1.87	1.72	1.29	ARG (94%)	CC (5%); VAT (>1%)
	0.1	15.75	337.23	1.87	1.72	1.29	ARG 100%	
	0.5	26.25	104.36	1.86	1.71	1.28		
	1	7.35	45.82	1.85	1.7	1.27		
+ 10 mM SO_4^{2-}	0	0.93	5985.35	2.00	1.85	1.42	VAT (94%)	ARG (2%); CAL (<1%)
	0.1	2.73	2619.21	1.99	1.84	1.41	VAT (84%)	CAL (16%)
	0.5	5.00	1493.81	1.96	1.81	1.38	CAL (100%)	
	1	4.10	1764.80	1.9	1.75	1.32		

Table 3.2: Data collected from round 2 turbidity experiments. Phases wt % determined with XRD, CC, calcite; ARG, aragonite, VAT, vaterite. Saturation Indices values from PHREEQC. [a] Extracted from JMAK n ~ 1.

Compared to the pure system (Figure 3.1), the addition of ions caused changes to the normalized turbidity profile's shape, resulting in an increase in time to reach plateau (i.e., maximum turbidity) and a decrease in the turbidity profile slope. A general trend of decrease in the profile slope angle with increasing ion/inhibitor concentration was observed. The change in the profile shape was more profound in *round 2* experiments, following the addition of CIT. The most striking change in profile shape occurred in the $MgSO_4$ + 1.0 mM CIT, where a transient increase and decrease in absorbance took place between 1 and 90 minutes after solution mixing. This indicates a potential short-lived (~7 min) transient metastable phase that formed before the main crystallisation curve (inset Figure 3.3).

Results summarised in Table 3.1 and Table 3.2 confirm an overall trend of increasing ion concentration increases the induction time (t_{ind}), decreasing in the slope of the absorbance profile which corresponds with reductions in crystallisation rates (*k*). Overall, a negative correlation was found between inhibitor concentration and crystallization rates across the experiments. The influence is heightened with the addition of CIT into the system. Changes in crystallisation rates (*k*) were quantified using the JMAK model. Representative examples of fits of the turbidity profile data to the equation are provided in the supporting information (Appendix: A9)

The influence on the crystallisation rates (*k*) in *round 1* is ion and concentration dependent, with crystallization rates decreasing in the order SO_4^{2-} < $MgSO_4$ <Mg^{2+} (Figure 3.4). The addition 1-15 mM of SO_4^{2-} had minimal effects on the *k* rate, the highest concentration (20 mM) demonstrated 88% reduction in the *k* rate (0.81×10^{-3} s^{-1}) compared to the pure system. Similar to SO_4^{2-}, the highest concentration (20 mM) of $MgSO_4$ resulted in 86% reduction in the *k* rate (0.94×10^{-3} s^{-1}) compared to the pure system. At lower $MgSO_4$ concentrations there is an initial in a drop in *k* rates (1- 5 mM), followed by a plateau (5- 15 mM). The largest reduction in crystallisation rates (*k*) was observed in the Mg^{2+} system, which were the lowest at every examined concentration in the *round 1* experiments. The largest reduction was observed at 20 mM Mg^{2+}, which was two orders of magnitude less than the pure system (0.07×10^{-3} s^{-1}).

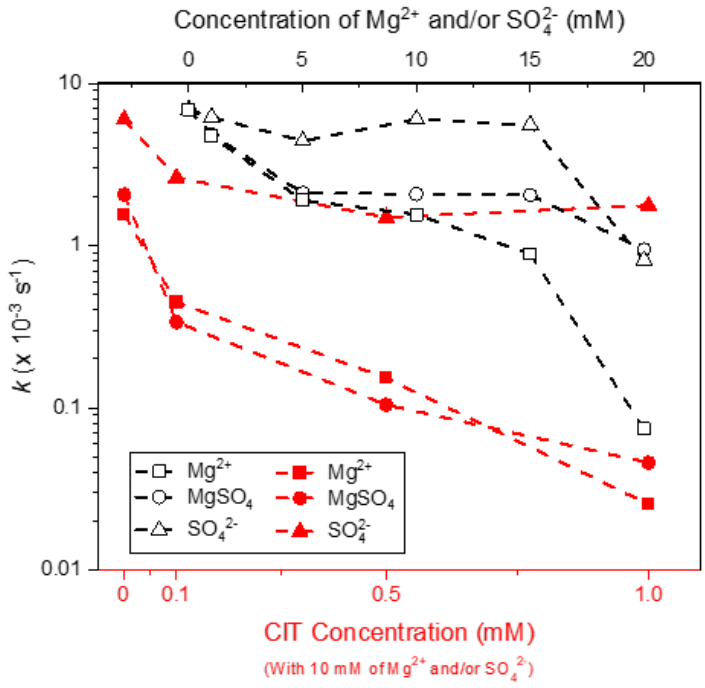

Figure 3.4: Crystallisation rate (k) as a function of concentration. Round 1 experiments are represented by black empty symbols, the top axis corresponding to round 2 concentrations. Round 2 experiments are represented by red solid symbols and corresponding concentrations on the bottom axis.

Significant reductions in crystallization rates were observed in *round 2* experiments compared to *round 1*. Similarly, the influence on the crystallisation rates (*k*) in *round 2* is ion and concentration dependent, demonstrating an overall negative correlation, except crystallization rates decreases in the order SO_4^{2-} <Mg^{2+}≤ $MgSO_4$ **(**Figure 3.4). The CIT + SO_4^{2-} experiments were the quickest (orders of magnitude faster than CIT + Mg^{2+}/$MgSO_4$), with an average 67% reduction in *k* rates compared to those without CIT (10 mM SO_4^{2-}). Interestingly there is a slight increase in *k* between 0.5 mM (1493.81 x 10^{-6} s^{-1}) and 1.0 mM CIT (1764.80 x 10^{-6} s^{-1}), which is associated with a phase change from vaterite to calcite. Both CIT + Mg^{2+} and CIT + $MgSO_4$ resulted in drastic reductions in crystallisation rate, compared to *round 1* (10 mM Mg^{2+}/$MgSO_4$), with an average reduction of 87% and 92% in *k* respectively. Even at the lowest CIT concentration (0.1 mM) the reductions are large, 447.15 x 10^{-6} s^{-1} (CIT + Mg^{2+}) and 337.23 x 10^{-6} s^{-1} (CIT + $MgSO_4$). The retarding influence of CIT + Mg^{2+} and CIT + $MgSO_4$ on crystallisation rate is similar across all concentrations.

3.4.2 $CaCO_3$ composition & morphology

The addition of dopants had a strong influence in the polymorph selection of the primary $CaCO_3$ phases crystallised after solution mixing (Figure 3.5 and Figure 3.6). In *round 1 experiments*, increased concentrations of SO_4^{2-} resulted in the preferential crystallisation of vaterite over the other anhydrous $CaCO_3$ polymorphs. While at lower molarities (1 to 5 mM) some (<10%) calcite formed, above 10 mM SO_4^{2-} most $CaCO_3$ consisted of vaterite with minor aragonite (<3%) and traces of calcite, the latter two becoming less abundant or absent at higher SO_4^{2-} concentrations. In contrast, the addition of Mg^{2+} or $MgSO_4$ favoured aragonite formation. At concentrations higher than 1 mM Mg^{2+} aragonite became the most abundant phase, followed by vaterite and calcite, but the former became the only phase precipitating at Mg^{2+} concentrations ≥10 mM. Similarly, at 1-10 mM $MgSO_4$ all three polymorphs were present, with aragonite the most abundant, followed by vaterite and calcite and increased $MgSO_4$ concentration the abundance of calcite and vaterite decreased. In particular, at 10 mM $MgSO_4$ the sum of vaterite and calcite was <10 wt %. At ≥15 mM $MgSO_4$ calcite was not detected and <10% of vaterite precipitated.

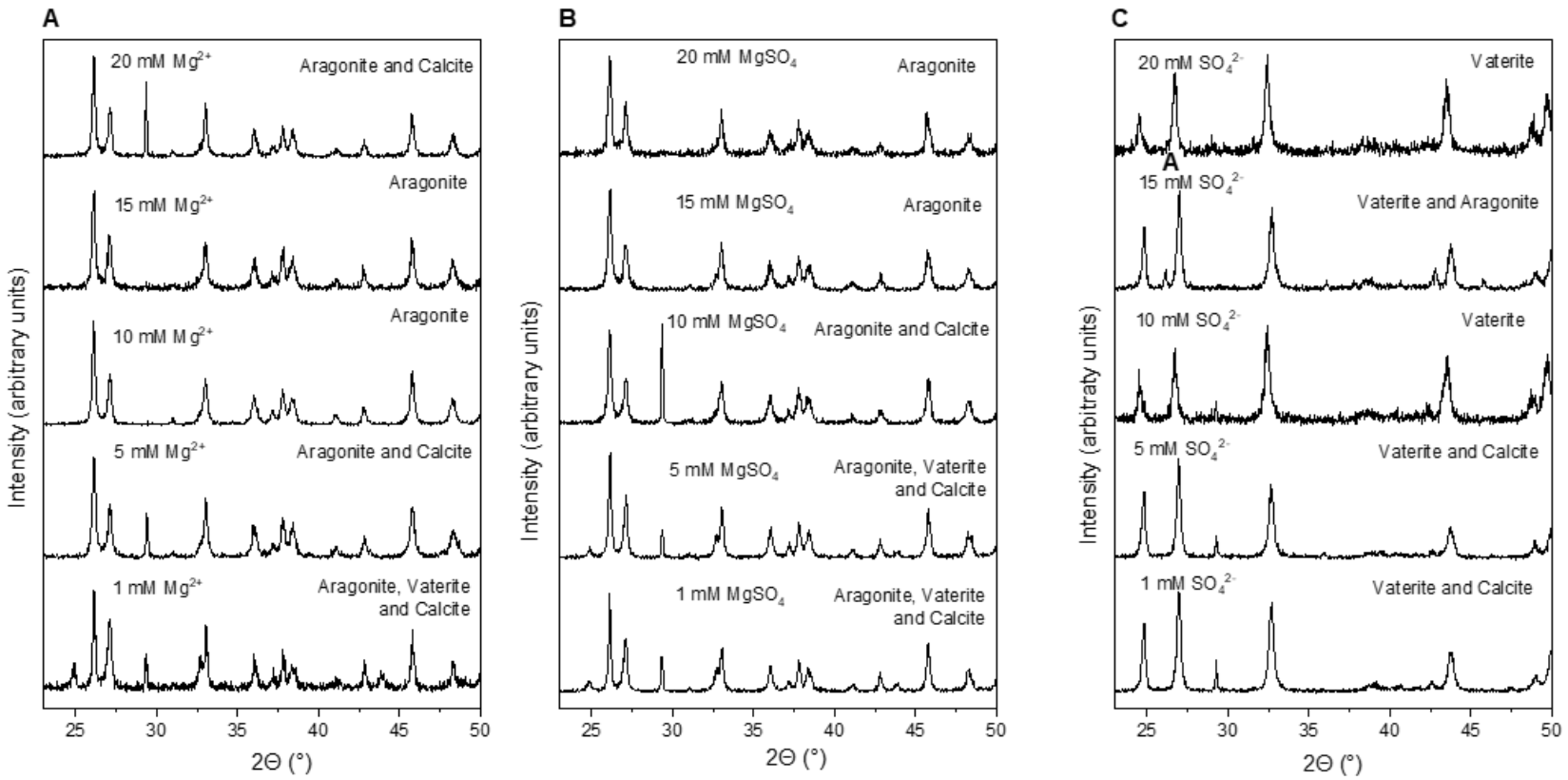

Figure 3.5: Powder XRD patterns of Round 1 experiments. A) Mg^{2+} system, B) $MgSO_4$ system C) SO_4^{2-} system. For phase wt % values see Table 3.1.

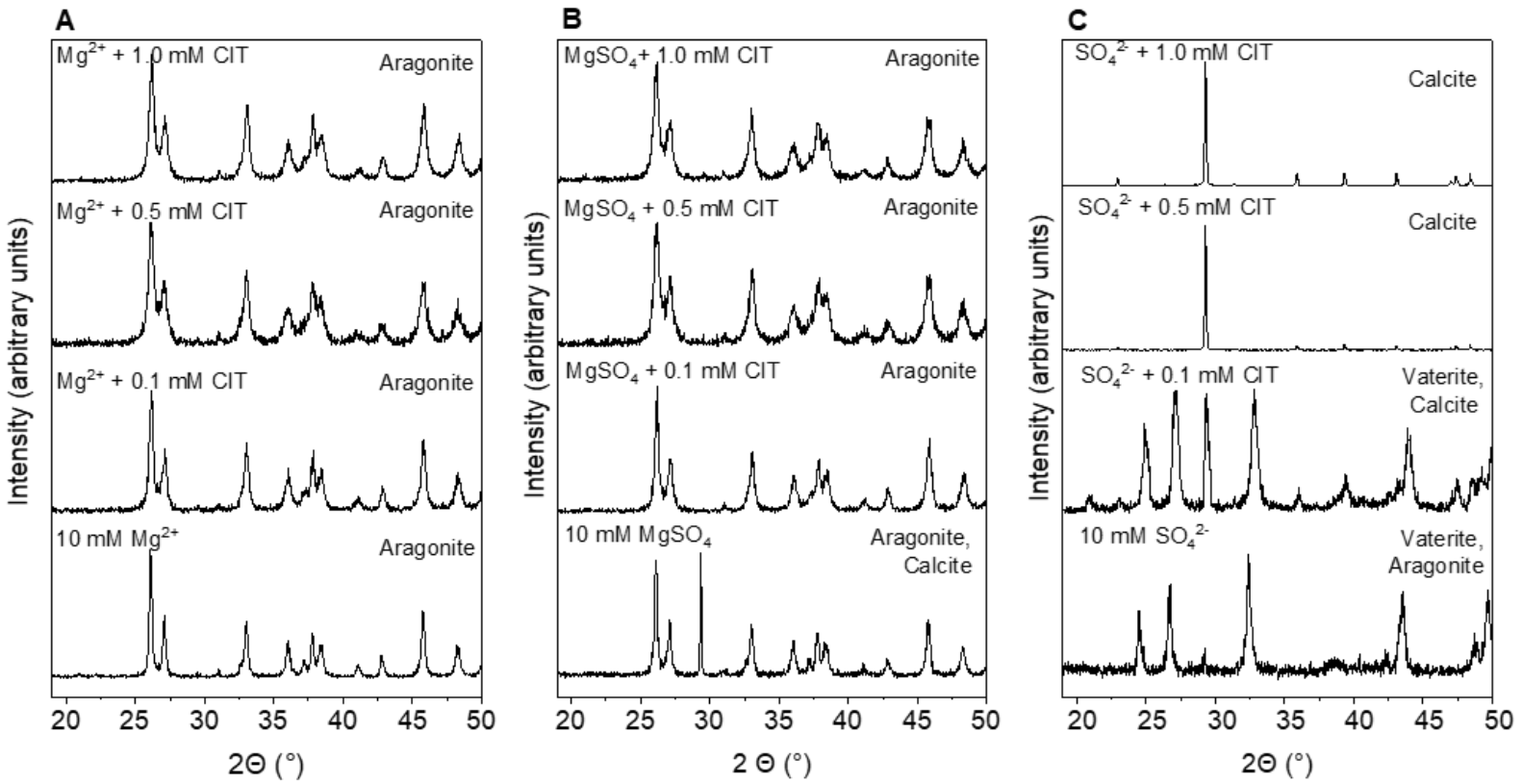

Figure 3.6: Powder XRD patterns of Round 2 experiments. A) Mg^{2+} and CIT system. B) $MgSO_4$ and CIT system, C) SO_4^{2-} and CIT system. The bottom XRD pattern denotes the round 1 turbidity data (10 mM of the examined inhibitor). For phase wt% values see Table 3.2.

Round two experiments showed similar results with one exception: in the CIT + SO_4^{2-} experiments the dominant $CaCO_3$ polymorph was calcite, with some vaterite. At 10 mM SO_4^{2-} + 0.1 mM CIT the dominant phase was vaterite (84%) with minor calcite (15%), but at higher CIT concentrations the only detected phase was calcite. In the Mg^{2+} and $MgSO_4$ experiments with citrate, only aragonite was detected at all examined CIT molarities (Figure 3.6).

All the calcite samples (8 in total) that precipitated following the addition of Mg^{2+} or $MgSO_4$ did not produce any Mg-bearing calcite, as the unit cell parameters were the same compared to pure calcite. The calculation of the mol% of $MgCO_3$ after Arvidson and Mackenzie (1999), revealed values of <0.1 mol %.

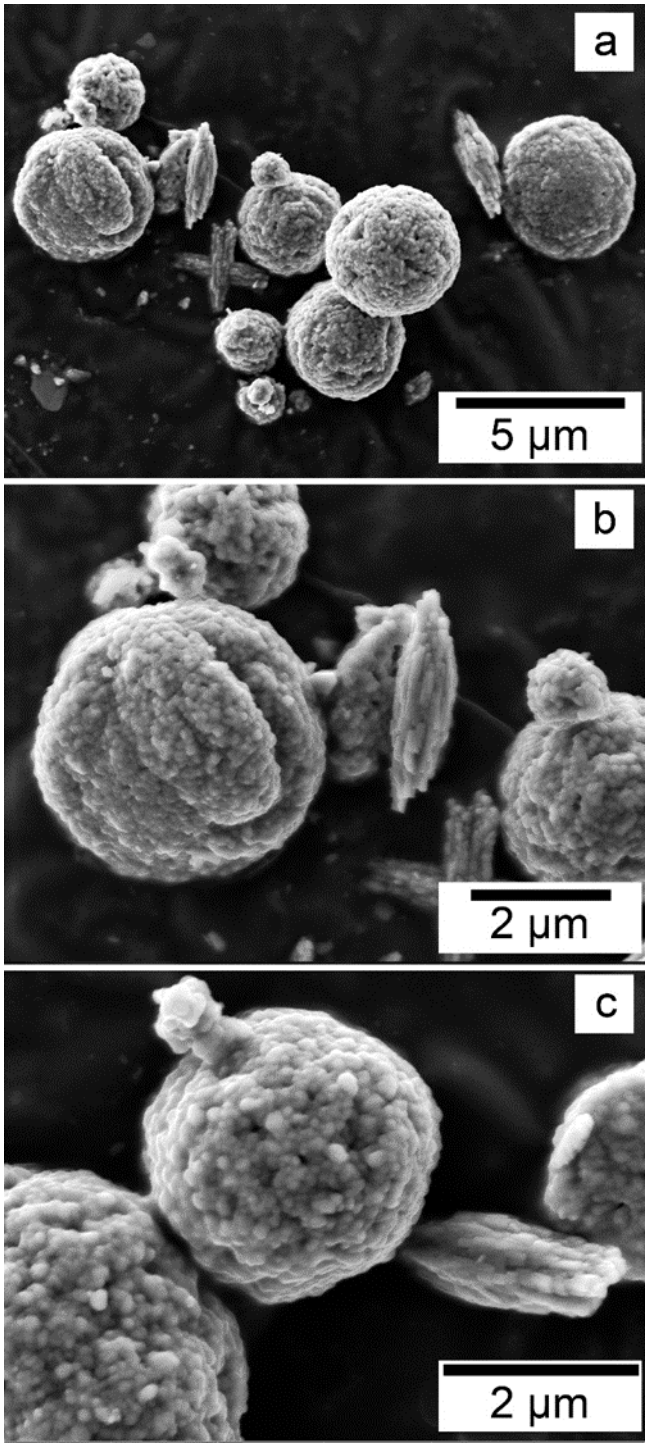

Figure 3.7: SEM images of $CaCO_3$ from round 1, SO_4^{2-} system. At higher concentrations of SO_4^{2-} spindle aggregates start forming within the spherules (a). Close up of spindle aggregate within the vaterite spherule, with prolate spheroid and cruciform aragonite (b). Classic vaterite spherules, shown with prolate spheroid aragonite (c).

The morphologies of $CaCO_3$ polymorphs were strongly affected by the foreign ions used in our experiments. While vaterite always showed spherulitic morphology in all experiments (Figure 3.12), the morphologies of aragonite and calcite were dependent on the concentration of the ion(s) in solution. In particular, aragonite crystals in *round 1 experiments* varied from acicular clusters, bows, to prolate spheroids and hedgehog pseudo-hexagons (large clusters radiating from a common centre) at the highest $MgSO_4$ molarities (Figure 3.8 and Figure 3.9). Citrate also influenced the aragonite morphology, which was different compared to the *round 1 experiments*, forming twinned crystals, rosettes, and pseudo hexagons, as well as globular, cauliflower like, aggregates (Figure 3.10 and Figure 3.11). These aggregates were ~2 μm wide and consisted of nanoparticles with sizes <100 nm.

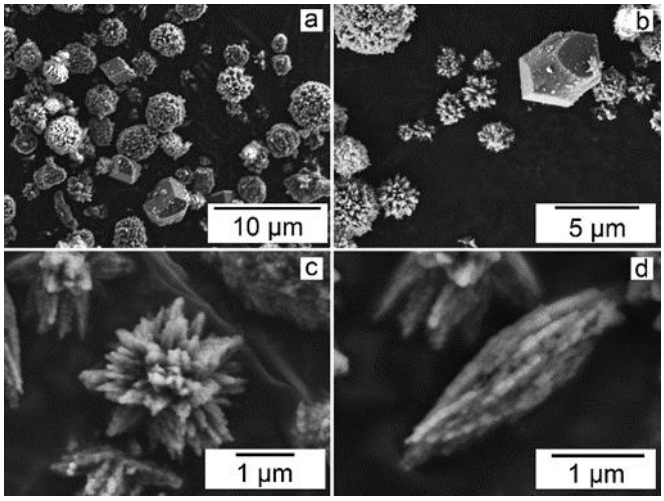

Figure 3.8: SEM images of $CaCO_3$ from round 1 Mg^{2+} system, revealing the variety of morphologies present in the sample, consisting of aragonite and elongated calcite (a and b) Aragonite showed various forms including pseudo-spherules that radiate from the centre (c) and prolate spheroids (d).

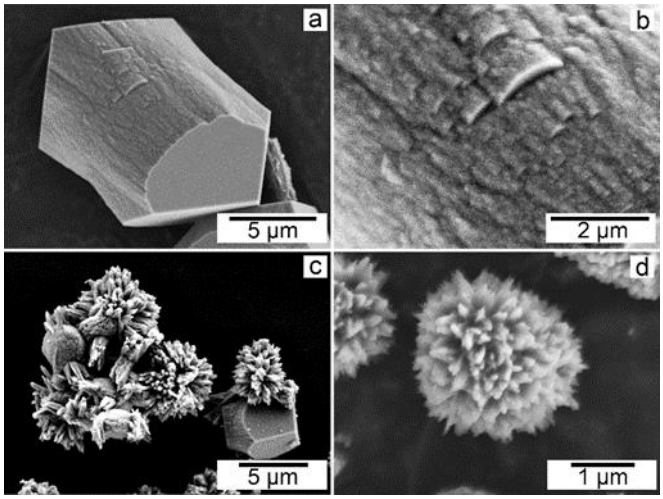

Figure 3.9: SEM images of $CaCO_3$ from round 1 $MgSO_4$ system. Calcite is elongated along the $\{10\bar{1}0\}$ *face (a), close up of step edges on the calcite faces (b). Classical vaterite spherules surrounded by aragonite exhibiting a range of morphologies (c) and close up of stellate aragonite (d).*

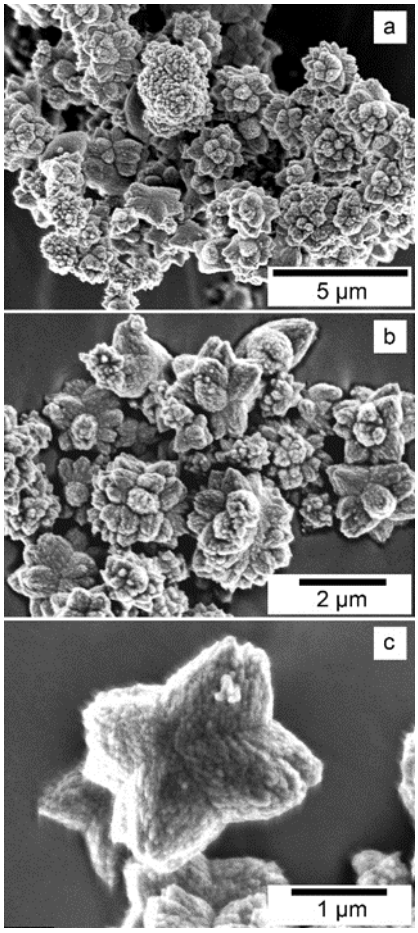

Figure 3.10: SEM images of $CaCO_3$ from round 2, Mg^{2+} and CIT system. Aragonite exhibits different morphology to round 1 aragonites (see figure 3.7). Aragonite exhibiting globular, cauliform and twinned morphologies (a and b). Close up of twinned aragonite forming star shapes (c).

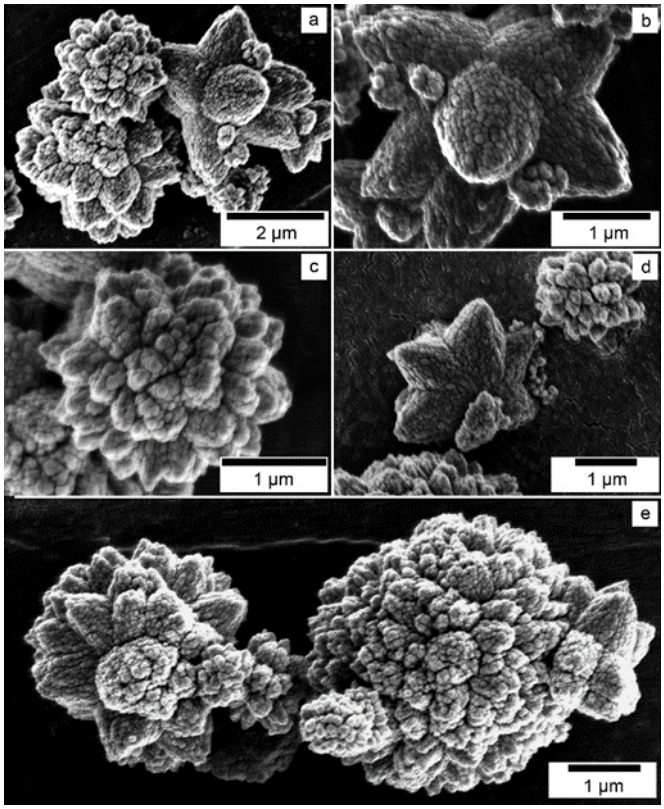

Figure 3.11: SEM images of $CaCO_3$ from round 2 $MgSO_4$ and CIT system. Aragonite exhibits similar morphology to Mg^{2+} and CIT system aragonites (see figure 3.10). Star shape, twinned aragonite (b and d), cauliform morphology (c).

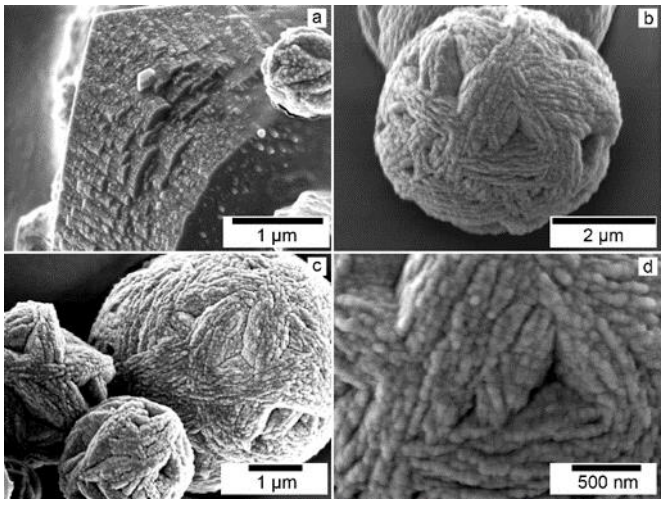

Figure 3.12: SEM images of $CaCO_3$ from round 2 SO_4^{2-} and CIT system. Step edges on calcite along the $\{10\bar{1}0\}$ face (a). Vaterite spherules with spindle aggregates arranged in pseudo-hexagonal symmetry (b, c and d), resulting in rosette forms.

In the case of calcite, the pure system calcite exhibited classic rhombohedral morphology, but the increase of Mg^{2+} and $MgSO_4$ molarities was translated into elongated crystals exhibiting growth steps along the elongated rough crystal faces (Figure 3.9). This same shapes was observed in the samples produced with SO_4^{2-} + CIT (Figure 3.12) and they are similar to the morphologies reported by (Meldrum and Hyde, 2001; Montanari *et al.*, 2017), showing calcite crystals elongated along the *c* axis.

In summary, the influence of the additives affected the kinetics of crystallisation, the resulting polymorph and the morphology of the crystals. Inhibition increased with higher concentrations of dopant and was the most significant when ions were combined with citrate. In general, there was trend to aragonite crystallisation, which exhibited a different range of morphologies between samples formed in the presence or absence of citrate ions.

3.5 DISCUSSION

The effect of Mg^{2+}, SO_4^{2-} and CIT, both alone and in combination, on $CaCO_3$ was investigated by monitoring the time-dependent changes in solution turbidity using UV-Vis spectrophotometry. Although some particles may have formed before the first increase in absorbance, we assume that the nucleation of $CaCO_3$ started at the onset of the absorbance process. This absorbance behaviour was consistent for all experiments, so the error in this assumption would be proportional for all experiments regardless the chemistry of the aqueous solution. Similarly, we assumed the point where the absorbance reached a maximum corresponds to the situation where equilibrium had been reached with respect to the primary crystallised $CaCO_3$ solid(s).

3.5.1 Mechanisms of Crystallisation and the effect of foreign ions

Our results reveal that the mechanisms and kinetics of $CaCO_3$ crystallisation are influenced both alone and in combination, by Mg^{2+}, SO_4^{2-} and CIT (Table 3.1 and Table 3.2). The resulting normalised turbidity profiles highlight the influence i.e., changes in growth rate and mechanism of crystallisation of $CaCO_3$ nucleation and growth, indicating that these effects differ based on the concentrations of the initial reactive aqueous solutions (Figure 3.2 and Figure 3.3). These profiles reveal that the degree of the inhibition is dependent on two factors: (i) The presence of the inhibitors and (ii) their concentration.

An evolution of crystallisation mechanisms following the addition of inhibitors occurred, initial nucleation-controlled growth followed by ripening. The presence of spherulitic vaterite in certain experiments (most notably the SO_4 experiments) and aragonite indicates spherulitic growth (nucleation-controlled) mechanism (Andreassen, 2005; Andreassen *et al.*, 2010; Beck and Andreassen, 2010; Rodriguez-Blanco *et al*. 2017). The supersaturation required for spherulitic growth is high (SI > 2-3) (Gránásy *et al.*, 2005; Beck and Andreassen, 2010). In our experiments, most saturation indices (SI) values for the $CaCO_3$ polymorphs before the onset of crystallisation are between 1 and 2 (Table 3.1 and Table 3.2) showing that these levels of supersaturation are significantly high enough to promote spherulitic growth. After this initial spherulitic growth, the

formation of the solid phases decreases the concentrations of Ca^{2+} and CO_3^{2-} ions in solution, triggering a change in the crystallisation mechanism, which would be consistent with classical growth or ripening (Rodriguez-Blanco *et al.* 2017). Similar multistage crystallisation has been observed using UV-Vis spectrophotometry in both calcium carbonates (Montanari *et al.*, 2017) and iron carbonates (Mulders *et al.*, 2021).

In the JMAK particle nucleation model the slope of the curves allowed us to obtain crystallisation rates (Tobler *et al.*, 2015; Montanari *et al.*, 2017; Mulders *et al.*, 2021). When fitting the normalised turbidity profiles to the JMAK model using a single *n* value for the whole profile there R^2 value obtained was not high (< 70 %); however, it was possible to fit all turbidity profiles to at least two different *n* and *k* values and obtain R^2 values higher than >97%. These results show that the crystallisation reaction follows a multi-stage pathway with at least two different mechanisms of crystallisation that resulted in different growth rates of $CaCO_3$. As a result, the first section is fitted to n ~4 and the second is fitted using n ~1 (see Appendix A9 for representative fits).

All the tested inhibitors decreased the rate of crystallisation and this decrease is proportional to the concentration of inhibitor(s). The individual effects of the examined additives have been demonstrated in previous studies, i.e., Mg^{2+} delays crystallisation (Berner, 1975; Davis *et al.*, 2000; Rodriguez-Blanco *et al.*, 2015; Nielsen *et al.*, 2016) and Nielsen *et al.* (2016) showed that SO_4^{2-} enhances the inhibiting effects of Mg^{2+}. We expected the combined influence of $MgSO_4$>Mg^{2+}, however the individually Mg^{2+} resulted in longer induction times, especially at 20 mM, and slower crystallisation rates. When $MgSO_4$ and CIT were combined in the *round 2* experiments resulted in $MgSO_4$>Mg^2.

The addition of CIT significantly altered the crystallisation rates, *round 2* values (x 10^{-6} s^{-1}) are ~ 3 orders of magnitude slower than the *round 1* rates (x 10^{-3} s^{-1}). The inhibiting effect of CIT has been explained as the formation of Ca-CIT ion pairs (Westin and Rasmuson, 2005; Gebauer *et al.*, 2009; Montanari *et al.*, 2017). When examining the influence of CIT/Ca on the $CaCO_3$ crystallisation rate Montanari *et al.* (2017) found that the addition of 1.0 mM CIT resulted in *k* rate of 227 x 10^{-3} s^{-1}; this rate is faster than any of the crystallisation rates from this study. In comparison, the combination

of 1.0 mM and 10 mM Mg^{2+} drastically reduces the crystallisation by 3 orders of magnitude, to 25 x 10^{-6} s^{-1}. A similar effect was observed with the addition of $MgSO_4$. This highlights the synergistic influence is more complex than the individual.

There are significant variations between the induction times, this range is observed between the additive types, with some causing longer delays i.e. Mg^{2+}>SO_4^{2-}, as well as within the individual experiments as a result of concentration (Appendix A7). Induction times ranging from less than a minute (no inhibitors) to several hours (high concentrations of inhibitors, especially Mg combined with and CIT).

While there are overall correlations between ion concentration and the kinetic parameters, induction time (positive) and crystallisation rate (negative), the relationships do not progress linearly (Figure 3.4). For example, in the *round 1* experiments in all cases the induction times a longer at 5 mM than at 10 mM. In the SO_4^{2-} system the induction time is longer at 5 mM (80 seconds) than at 10 mM (56 seconds) and the crystallisation rate is slower at 5 mM (4.39 x 10^{-3} s^{-1}) than at 10 mM (5.99 x 10^{-3} s^{-1}). This phenomenon is also observed in the *round 2* experiment with SO_4^{2-}, where SO_4^{2-} + 0.5 mM CIT has a slower *k* rate and longer t_{ind} than the maximum CIT concentration. Changes in phases occur are associated with these non-linear experiments. For example, <10 mM SO_4^{2-} minor calcite forms, whereas minor aragonite forms at higher concentrations. It is possible that there is a higher barrier at the lower concentration, i.e., the barrier to calcite precipitation increases with SO_4^{2-} concentration up to threshold of 10 mM, at which point it is preferential to precipitate aragonite, which is not as impeded as calcite and can form faster.

In all experiments, at the onset of crystallisation the turbidity starts to increase. While the turbidity profiles exhibit typical sigmoidal shape, changes in profile shape were observed following the addition of inhibitors. The decrease in profile slope as the inhibitor concentration increases was observed and has been interpreted as representing a decrease in nucleation rate (Wang *et al.*, 2012; Tobler *et al.*, 2014, 2015; Montanari *et al.*, 2017; Mulders *et al.*, 2021). Interesting at the highest concentration of CIT + $MgSO_4$ (1.0 mM CIT + 10 mM $MgSO_4$) there is a significant change in profile shape, showing a transient precursory phase that has a lifetime of 90 minutes (Figure 3.3, $MgSO_4$

inset). It is worth noting that no other experiment exhibited a transient phase. All samples obtained during this time did not show the presence of any solid phase, but the lifetime of this transient phase seems to be linked to the formation of solid $CaCO_3$, as it starts breaking down just before the onset of aragonite nucleation. We interpret this as a transient, dense liquid phase, similar to ACC, containing CIT. However, ACC is ruled out as the solutions saturation state is below ACC solubility. Other transient liquid precursors, such as polymer-induced liquid precursors (PILP), which are "transient states in non-classical crystallisation" (Sugawara-Narutaki, *et al*., 2021) have been observed in the presence of acidic polypeptides during $CaCO_3$ synthesis (Gower and Tirrell, 1998; Gower, 2008; Schenk *et al.*, 2013). They are of interest in the field of biomineralisation, due to the role that acidic macromolecules play during crystallisation, notably on morphological controls (Cheng *et al.*, 2007). However, further investigation into this transient phase is beyond the scope of this study.

Saturation state of the initial reactive solution influences the resulting phase. The saturation index values calculated for aragonite are lower with increased amounts of CIT compared to the pure system or experiments made in the absence of this organic, this in part due to the chelating nature of CIT (Gebauer *et al.*, 2008; Tobler *et al.* 2015), which binds to Ca^{2+} and Mg^{2+} ions, forming Ca-(CIT) and Mg-(CIT) complexes. These CIT complexes reduce the activity of the free Ca^{2+} and Mg^{2+} ions in solution (Appendix A6), reducing the supersaturation of the $CaCO_3$ polymorphs, in agreement with Tobler *et al.* (2015), who demonstrated that increasing CIT decreases the amount of precipitated ACC and calcite. In our experiments, the longer induction times (i.e., longer nucleation times) and the decrease in the slopes of the turbidity profiles (i.e., slower growth kinetics) with increased CIT concentrations are consistent with this decrease in supersaturation due to the formation of Ca-CIT and Mg-CIT complexes before the onset of the crystallisation process.

3.5.2 Polymorph selection and crystal morphology:

$CaCO_3$ polymorph selection was influenced by the addition of inhibitors. The saturation indices derived from PHREEQC suggest that at all examined molarities the solution is supersaturated for the three $CaCO_3$ polymorphs (Table 3.1 and Table 3.2). However the three polymorphs did not always precipitate, a result of a nucleation barrier resulting from the presence of the inhibitors, which in

combination and at high concentrations inhibited the nucleation of vaterite and calcite therefore promoting the crystallisation of aragonite. The extent of the influence of the inhibitors varied, depending on whether it was a single inhibitor or combined effects. Across both *round 1* and *round 2* experiments the inhibition effects were amplified with increased inhibitor molarity, in line with results observed in previous studies (Tobler *et al.*, 2015; Nielsen *et al.*, 2016; Montanari *et al.*, 2017). In the case of *round 2* experiments CIT was a dominant inhibitor. Previous studies have shown that the examined ions and organics influence the polymorph selection of $CaCO_3$: Mg^{2+} promotes the crystallisation of aragonite (Lippmann, 1973; Berner, 1975; Loste *et al.*, 2003) over calcite and vaterite, while SO_4^{2-} tends to stabilise vaterite (Han and Aizenberg, 2003; Raz *et al.*, 2003; Hu *et al.*, 2008; Fernández-Díaz *et al.* 2010). However, in combination Mg^{2+} has the stronger influence over SO_4^{2-}, and aragonite crystallisation is promoted over calcite and vaterite (Hu *et al.*, 2008). CIT has been shown to favour the precipitation of calcite (Kitano and Hood, 1965; Westin and Rasmuson, 2005). In general all experiments with Mg^{2+}, including those in combination with SO_4^{2-} and CIT, promoted aragonite formation (Figure 3.5 and Figure 3.6). SO_4^{2-} on its own promoted primary vaterite formation, however, when combined with Mg^{2+} or CIT, the latter two had a stronger influence than SO_4^{2-}. The combination of CIT and SO_4^{2-} favoured calcite over vaterite, highlighting the stronger influence that CIT plays over SO_4^{2-}. Similarly SO_4^{2-} had a minor influence when combined with Mg^{2+}.

Morphology

The addition of inhibitors also influenced the morphologies of aragonite, vaterite and calcite. Morphologies varied depending on the additive and concentration, in some instances the combination of ions resulted in different morphologies than the individual ion. Both aragonite and vaterite displayed a range of spherulitic growth morphologies, including the "non-classical" such as cauliflower-like, stellate, bows and pseudo hexagonal aragonite (Chakrabarty and Mahapatra, 1999; Sand *et al.*, 2012b, 2012a) as well as vaterite rosettes, similar to gypsum desert rose (Gehrke *et al.*, 2005; Niedermayr, Köhler and Dietzel, 2013; Trushina *et al.*, 2014; Hargis *et al.*, 2021). This diversity of spherulitic growth morphologies can be a result of many factors, like the interaction of foreign ions with mineral surfaces, the supersaturation levels and the temperature (Vallina *et al.*,

2014, 2015; Rodriguez-Blanco *et al*., 2017). Also, it is well know that in most biomineralisation processes biomolecules play a vital role in the polymorph selection and the resulting crystal morphologies (Meldrum, 2013). While the individual influence of ions like Mg^{2+} and SO_4^{2-} and organic additives like CIT on $CaCO_3$ crystallisation in abiotic and biotic environments is well recognised, their combined influence on $CaCO_3$ morphology is not as established. Many studies suggest that organic molecules can bind to specific crystal planes during growth, either promoting or inhibiting growth long those planes, and controlling the resulting morphology (e.g., the mollusc *Atrina rigida* and the sea urchin *Paracentrotus lividus;* Albeck *et al*. 2009).

A. Aragonite

Aragonite exhibited an assortment of morphologies, influenced by both ions (singular and combined) and concentrations. For example, with SO_4^{2-}: at 15 mM it formed prolate spheroids, consisting of nanoparticles of aragonite, whereas at 20 mM SO_4^{2-} aragonite became acicular, with long narrow needles radiating from a common centre (Figure 3.7). Changes in morphology occurred also with changes in $MgSO_4$ molarity (Figure 3.9). At lower molarity aragonite exhibited various morphologies, predominantly stellate acicular clusters that radiated from a common centre, as well as prolate spheroids and bows. At higher molarities aragonite was predominantly hedgehog-like pseudo-hexagons. CIT influenced the aragonite morphology, which were different compared to the *round 1* experiments ($CaCO_3$ + $Mg/MgSO_4$ systems) and consisted of rosettes and pseudo hexagons, usually twinned (Sand *et al.*, 2012a) as well as globular, cauliflower-like crystals (Figure 3.10 and Figure 3.11). Some of these morphologies are similar to the "unconventional" morphologies observed by Chakrabarty and Mahapatra, (1999) in synthetic aragonite produced from highly concentrated (1 M) solutions.

B. Vaterite

The "pure system" vaterite consisted of near spherical spherulites, with the addition of SO_4^{2-} the vaterite appeared to form spindle aggregates within the spherules (Figure 3.7). This type of morphology became more defined with the combination SO_4^{2-} + CIT, displaying pseudo-hexagonal

symmetry, resembling rosettes, similar to gypsum desert roses (Figure 3.12). These vaterite morphologies were described by Gehrke et al. (2005) as 6-fold symmetry rosettes with mesocrystals, consisting of truncated hexagonal crystalline platelets, a feature that can be usually observed when examined at the micrometre scale using electron diffraction (Trushina *et al.*, 2014). Similar morphologies were reported by (Niedermayr *et al.*, 2013), obtained by using poly-aspartic acid. Certain ions such as NH_4^+ and acids are known to strongly influence the morphology of vaterite, promoting the formation of hexagonal plate-like, rosettes and flower-like vaterite (Gehrke *et al.*, 2005; Pouget *et al.*, 2010; Guan *et al.*, 2018). Jiang *et al*. (2017) and Seknazi *et al*. (2019) produced vaterite which demonstrated chirality when grown in the presence of aspartic acid, suggesting a change in its growth mechanism because of the formation of bonds between aspartic acid and the Ca-carboxylate groups (Jiang *et al.* 2017). Li and Wu (2009) observed this in rosette calcite, where growth of faces occurs at certain angles around the nuclei "due to repulsive interactions between the polymers adsorbed on the blocked surfaces". We propose a similar mechanism in which the combination of SO_4^{2-} + CIT would adsorb to the crystal surface, blocking these sites, promoting vicinal faces to grow, forming rosettes.

C. Calcite

Compared to the pure system, where calcite usually exhibits classic rhombohedral morphology, calcite developed elongated shapes (Figure 3.9 and Figure 3.12) in the presence of inhibitors (Mg^{2+}, $MgSO_4$, CIT + SO_4), similar to the morphologies reported by Meldrum and Hyde (2001); Kralj *et al.*, (2004); Nielsen *et al.*, (2016); and Montanari *et al.*, (2017) that show calcite elongated along the *c*-axis. This elongation is explained as a result of the adsorption of the inhibitors onto the $\{10\bar{1}4\}$ crystallographic face during the solution-surface interaction, strongly inhibiting or fully blocking the growth of new units along this face and promoting of growth step edges on the vicinal $\{10\bar{1}0\}$ face. Meldrum and Hyde (2001) stated that when combined with organic additives Mg^{2+} results in the adsorption on specific crystal faces altering the morphology. The calcite crystals that were elongated in the presence of CIT suggest that either the CIT was responsible for the growth inhibition of the

{$10\bar{1}4$} faces, as seen in (Nielsen *et al.*, 2016), or the combination of CIT + SO_4^{2-} had this effect on calcite nucleation and growth (Figure 3.12).

3.5.3 Implications:

From the turbidity and batch experiments it is evident that the use of multicomponent solutions in $CaCO_3$ crystallisation has revealed a very complex evolution compared to single solution experiments. The combination of inhibitors and concentration influences the initial reactive fluid saturation state and poisons crystal nucleation and growth, and this in turn affects the kinetics and mechanisms of crystallisation, as well as the resulting $CaCO_3$ polymorph. The effect that organics such as CIT can have on polymorph selection and crystallisation kinetics and mechanics is strong. However, this effect is reinforced by the presence of Mg^{2+} and is translated into changes in the crystallisation pathways and crystal morphologies. This study shows that small variations in ratio or concentration of common ions in seawater combined with the presence of common organics in biomineralization can have a drastic effect in the mechanisms and kinetics of crystallisation and the morphology of the primary solid. These different mechanisms of crystallisation and kinetics of growth and growth morphology can have strong influence in the geochemistry of the forming rock during abiotic and biotic mineralisations, including the industrial crystallisation of $CaCO_3$. For example, the understanding of the combined effects of common seawater ions, at ambient temperature and under environmentally relevant conditions can provide insight into the $CaCO_3$ crystallisation mechanisms and kinetics during seawater injections into basaltic reservoirs (Voigt *et al.*, 2021). This can be highly relevant when CO_2-charged seawater is used during basaltic carbon capture and storage (e.g., pilot project, CO_2SeaStone, at the CarbFix facilities in Iceland). A report produced by Grand View Research (2022) states that the global market for $CaCO_3$ in 2021 was an estimated $42.5 billion USD, which is projected to rise over the next 10 years. The $CaCO_3$ global market covers a range of industries, including paper, painting, plastics and coatings. These industries require $CaCO_3$ with specific particle size and surface properties which can be obtained by using facile experimental protocols that can target the size and morphology of $CaCO_3$ solids using environmentally clean multicomponent solutions.

3.6 CONCLUSIONS

By studying the influence alone and in combination this study sheds light on the delicate controls of $CaCO_3$, demonstrating that even minor changes to the solution chemistry (ions and concentrations) can have a large influence on the kinetics and mechanisms of $CaCO_3$ formation. The effects of each ion are not uniform, with Mg^{2+} having greater influence over SO_4^{2-}. The individual effects are often overridden by the more potent ones when combined, e.g., while SO_4^{2-} individually stabilises vaterite and has little effect on the kinetic parameters, when combined with Mg^{2+} aragonite is promoted over vaterite, and when combined with CIT calcite is promoted.

This study demonstrates the complexity of $CaCO_3$ formation pathways from multicomponent solutions containing common inorganics (Mg^{2+} and SO_4^{2-}) and organics (CIT). The concentration of the inhibitors affects the formation of $CaCO_3$ i) by inhibiting $CaCO_3$ nucleation and decreasing the rate of crystallisation; ii) by influencing the primary polymorph (the combination of all ions promoted the formation of aragonite over calcite and vaterite, though vaterite was promoted in the presence of SO_4^{2}). iii) by controlling the morphology of crystals, promoting the formation of vaterite and aragonite spherulites and the growth of $\{10\bar{1}0\}$ faces and the elongation along the *c*-axis in calcite.

This understanding of the complex system of $CaCO_3$ formation from multicomponent solutions provides insights into mechanisms controlling biomineralization, the targeting of specific morphologies for industry as well as the fate of injected seawater during CCS.

3.7 REFERENCES

Al-Hamzah, A. A. et al. (2014) 'Inhibition by poly(acrylic acid) and morphological changes in calcium carbonate and calcium carbonate/calcium sulfate crystallization on silica fibers', Industrial and Engineering Chemistry Research. American Chemical Society, 53(21), pp. 8793–8803. doi: 10.1021/IE500911G/ASSET/IMAGES/LARGE/IE-2014-00911G_0015.JPEG.

Albeck, S., Addadi, L. and Weiner, S. (2009) 'Regulation of Calcite Crystal Morphology by Intracrystalline Acidic Proteins and Glycoproteins', http://dx.doi.org/10.3109/03008209609029213. Taylor & Francis, 35(1–4), pp. 365–370. doi: 10.3109/03008209609029213.

Allison, J. D., Brown, D. S. and Novo-Gradac, K. J. (1991) MINTEQA2/PRODEFA2, A Geochemical Assessment Model for Environmental Systems: Version 3·0 Users' Manual. Athens, GA: Environmental Research Laboratory, Office of Research and Development U.S. Environmental Protection Agency.

Andreassen, J. P. (2005) 'Formation mechanism and morphology in precipitation of vaterite—nano-aggregation or crystal growth?', Journal of Crystal Growth. North-Holland, 274(1–2), pp. 256–264. doi: 10.1016/J.JCRYSGRO.2004.09.090.

Andreassen, J. P. et al. (2010) 'Investigations of spherulitic growth in industrial crystallization', Chemical Engineering Research and Design. Elsevier, 88(9), pp. 1163–1168. doi: 10.1016/J.CHERD.2010.01.024.

Arvidson, R. S. and Mackenzie, F. T. (1999) 'The dolomite problem; control of precipitation kinetics by temperature and saturation state', American Journal of Science. American Journal of Science, 299(4), pp. 257–288. doi: 10.2475/AJS.299.4.257.

Astilleros, J. M. et al. (2000) 'The effect of barium on calcite {1014} surfaces during growth', Geochimica et Cosmochimica Acta. Pergamon, 64(17), pp. 2965–2972. doi: 10.1016/S0016-7037(00)00405-1.

Avrami, M. (1939) 'Rate of Nucleation in Condensed Systems The', Free Energy of a Nonuniform System. I. Interfacial Free Energy The Journal of Chemical Physics, 7, p. 258. doi: 10.1063/1.1750380.

Avrami, M. (1940) 'Rate of Nucleation in Condensed Systems The Journal of Chemical Physics', Heterogeneous Nucleation The Journal of Chemical Physics, 8, p. 198. doi: 10.1063/1.1750631.

Balthasar, U. and Cusack, M. (2015) 'Aragonite-calcite seas—Quantifying the gray area', Geology. GeoScienceWorld, 43(2), pp. 99–102. doi: 10.1130/G36293.1.

Bang, S. S. et al. (2010) 'Microbial calcite, a bio-based smart nanomaterial in concrete remediation', http://dx.doi.org/10.1080/19475411003593451. Taylor & Francis , 1(1), pp. 28–39. doi: 10.1080/19475411003593451.

Beck, R. and Andreassen, J. P. (2010) 'Spherulitic growth of calcium carbonate', Crystal Growth and Design. American Chemical Society, 10(7), pp. 2934–2947. doi: 10.1021/CG901460G/ASSET/IMAGES/LARGE/CG-2009-01460G_0003.JPEG.

Berner, R. A. (1975) 'The role of magnesium in the crystal growth of calcite and aragonite from sea water', Geochimica et Cosmochimica Acta. Pergamon, 39(4), pp. 489–504. doi: 10.1016/0016-7037(75)90102-7.

Bots, P. et al. (2011) 'The role of SO4 in the switch from calcite to aragonite seas', Geology. GeoScienceWorld, 39(4), pp. 331–334. doi: 10.1130/G31619.1.

Busenberg, E. and Niel Plummer, L. (1985) 'Kinetic and thermodynamic factors controlling the distribution of SO32− and Na+ in calcites and selected aragonites', Geochimica et Cosmochimica Acta. Pergamon, 49(3), pp. 713–725. doi: 10.1016/0016-7037(85)90166-8.

Canfield, D. E. and Farquhar, J. (2009) 'Animal evolution, bioturbation, and the sulfate concentration of the oceans', Proceedings of the National Academy of Sciences of the United States of America. National Academy of Sciences, 106(20), pp. 8123–8127. doi: 10.1073/PNAS.0902037106/SUPPL_FILE/SD1.XLS.

Chakrabarty, D. and Mahapatra, S. (1999) 'Aragonite crystals with unconventional morphologies', Journal of Materials Chemistry. The Royal Society of Chemistry, 9(11), pp. 2953–2957. doi: 10.1039/A905407C.

Cheng, X. et al. (2007) 'Biomimetic synthesis of calcite films by a polymer-induced liquid-precursor (PILP) process: 1. Influence and incorporation of magnesium', Journal of Crystal Growth. North-Holland, 307(2), pp. 395–404. doi: 10.1016/J.JCRYSGRO.2007.07.006.

Coelho, A. A. et al. (2011) 'The TOPAS symbolic computation system', Powder Diffraction. Cambridge University Press, 26(S1), pp. S22–S25. doi: 10.1154/1.3661087.

Cusack, M. et al. (2008) 'Micro-XANES mapping of sulphur and its association with magnesium and phosphorus in the shell of the brachiopod, Terebratulina retusa', Chemical Geology. Elsevier, 253(3–4), pp. 172–179. doi: 10.1016/J.CHEMGEO.2008.05.007.

Dang, H. and Xu, Z. (2022) 'Mg-calcite CaCO3 particle: Rapid synthesis and application in fabrication of environmentally friendly hydrophobic polyurethane sponge for oil–water separation', Journal of Environmental Chemical Engineering. Elsevier, 10(5), p. 108280. doi: 10.1016/J.JECE.2022.108280.

Davis, K. J., Dove, P. M. and De Yoreo, J. J. (2000) 'The role of Mg2+ as an impurity in calcite growth', Science. American Association for the Advancement of Science, 290(5494), pp. 1134–1137. doi: 10.1126/SCIENCE.290.5494.1134/ASSET/89670F6A-D97B-4EC0-A9C0-F2D4E39F1798/ASSETS/GRAPHIC/SE4308963004.JPEG.

Didymus, J. M. et al. (1993) 'Influence of low-molecular-weight and macromolecular organic additives on the morphology of calcium carbonate', Journal of the Chemical Society, Faraday Transactions. The Royal Society of Chemistry, 89(15), pp. 2891–2900. doi: 10.1039/FT9938902891.

Van Driessche, A. E. S. et al. (2012) The Role and Implications of Bassanite as a Stable Precursor Phase to Gypsum Precipitation Downloaded from.

Feng, Z. et al. (2022) 'Industrially synthesized biosafe vaterite hollow CaCO3 for controllable delivery of anticancer drugs', Materials Today Chemistry. Elsevier, 24, p. 100917. doi: 10.1016/J.MTCHEM.2022.100917.

Foran, E., Weiner, S. and Fine, M. (2013) 'Biogenic Fish-gut Calcium Carbonate is a Stable Amorphous Phase in the Gilt-head Seabream, Sparus aurata', Scientific Reports 2013 3:1. Nature Publishing Group, 3(1), pp. 1–5. doi: 10.1038/srep01700.

Fu, J., Leo, C. P. and Show, P. L. (2022) 'Recent advances in the synthesis and applications of pH-responsive CaCO3', Biochemical Engineering Journal. Elsevier, 187, p. 108446. doi: 10.1016/J.BEJ.2022.108446.

Füger, A. et al. (2019) 'Effect of growth rate and pH on lithium incorporation in calcite', Geochimica et Cosmochimica Acta. Pergamon, 248, pp. 14–24. doi: 10.1016/J.GCA.2018.12.040.

Gebauer, D. et al. (2009) 'The Multiple Roles of Additives in CaCO3 Crystallization: A Quantitative Case Study', Advanced Materials. John Wiley & Sons, Ltd, 21(4), pp. 435–439. doi: 10.1002/ADMA.200801614.

Gebauer, D., Völkel, A. and Cölfen, H. (2008) 'Stable prenucleation calcium carbonate clusters', Science. American Association for the Advancement of Science , 322(5909), pp. 1819–1822. doi: 10.1126/SCIENCE.1164271/SUPPL_FILE/GEBAUER_SOM.PDF.

Gehrke, N. et al. (2005) 'Superstructures of calcium carbonate crystals by oriented attachment', Crystal Growth and Design. American Chemical Society , 5(4), pp. 1317–1319. doi: 10.1021/CG050051D/SUPPL_FILE/CG050051DSI20050523_122939.PDF.

Gopi, S., Subramanian, V. K. and Palanisamy, K. (2013) 'Aragonite–calcite–vaterite: A temperature influenced sequential polymorphic transformation of CaCO3 in the presence of DTPA', Materials Research Bulletin. Pergamon, 48(5), pp. 1906–1912. doi: 10.1016/J.MATERRESBULL.2013.01.048.

Gower, L. A. and Tirrell, D. A. (1998) 'Calcium carbonate films and helices grown in solutions of poly(aspartate)', Journal of Crystal Growth. North-Holland, 191(1–2), pp. 153–160. doi: 10.1016/S0022-0248(98)00002-5.

Gower, L. B. (2008) 'Biomimetic model systems for investigating the amorphous precursor pathway and its role in biomineralization', Chemical Reviews, 108(11), pp. 4551–4627. doi: 10.1021/CR800443H.

Gránásy, L. et al. (2005) 'Growth and form of spherulites', Physical Review E - Statistical, Nonlinear, and Soft Matter Physics. American Physical Society, 72(1), p. 011605. doi: 10.1103/PHYSREVE.72.011605/FIGURES/11/MEDIUM.

Grand View Research (2022) Calcium Carbonate Market Size, Share & Trends Analysis Report By Application (Paper, Plastics, Paints & Coatings, Adhesives & Sealants), By Region, And Segment Forecasts, 2022 - 2030.

Guan, Y. et al. (2018) 'Controlled Synthesis and Microstructure of Metastable Flower-Like Vaterite', Materials. Multidisciplinary Digital Publishing Institute (MDPI), 11(11). doi: 10.3390/MA11112300.

Hargis, C. W. et al. (2021) 'Calcium Carbonate Cement: A Carbon Capture, Utilization, and Storage (CCUS) Technique', Materials 2021, Vol. 14, Page 2709. Multidisciplinary Digital Publishing Institute, 14(11), p. 2709. doi: 10.3390/MA14112709.

Henriksen, K. et al. (2004) 'Coccolith biomineralisation studied with atomic force microscopy', Palaeontology. John Wiley & Sons, Ltd, 47(3), pp. 725–743. doi: 10.1111/J.0031-0239.2004.00385.X.

Hodson, M. E. et al. (2015) 'Biomineralisation by earthworms - An investigation into the stability and distribution of amorphous calcium carbonate', Geochemical Transactions. BioMed Central Ltd., 16(1), pp. 1–16. doi: 10.1186/S12932-015-0019-Z/FIGURES/7.

Hu, Z. et al. (2008) 'Synthesis of needle-like aragonite from limestone in the presence of magnesium chloride', Journal of Materials Processing Technology. Elsevier, 209(3), pp. 1607–1611. doi: 10.1016/J.JMATPROTEC.2008.04.008.

Jiang, W. et al. (2017) 'Chiral acidic amino acids induce chiral hierarchical structure in calcium carbonate', Nature Communications 2017 8:1. Nature Publishing Group, 8(1), pp. 1–13. doi: 10.1038/ncomms15066.

Johnson, P. F. and Mehl, R. F. (1939) 'Reaction Kinetics in Processes of Nucleation and Growth.', Transactions of the American Institute of Mining and Metallurgical Engineers, (135), pp. 416–442.

Kezuka, Y. et al. (2019) 'Synthesis of Tunable-Aspect-Ratio Calcite Nanoparticles via Mg2+ Doping', Crystal Growth and Design. American Chemical Society, 19(11), pp. 6784–6791. doi: 10.1021/ACS.CGD.9B01196/ASSET/IMAGES/LARGE/CG9B01196_0006.JPEG.

Khosa, A. A. et al. (2019) 'Technological challenges and industrial applications of CaCO3/CaO based thermal energy storage system – A review', Solar Energy. Pergamon, 193, pp. 618–636. doi: 10.1016/J.SOLENER.2019.10.003.

Kitano, Y. and Hood, D. W. (1965) 'The influence of organic material on the polymorphic crystallization of calcium carbonate', Geochimica et Cosmochimica Acta. Pergamon, 29(1), pp. 29–41. doi: 10.1016/0016-7037(65)90075-X.

Kolmogorov, A. N. (1937) 'On the statistical theory of the crystallisation of metals', Bull. Acad. Sci. USSR, Math, 1(3), pp. 355–259.

Kralj, D. et al. (2004) 'Effect of Inorganic Anions on the Morphology and Structure of Magnesium Calcite', Chemistry - A European Journal. John Wiley & Sons, Ltd, 10(7), pp. 1647–1656. doi: 10.1002/CHEM.200305313.

Li, W. and Wu, P. (2009) 'Biomimetic synthesis of monodisperse rosette-like calcite mesocrystals regulated by carboxymethyl cellulose and the proposed mechanism : An unconventional

rhombohedra-stacking route', CrystEngComm. The Royal Society of Chemistry, 11(11), pp. 2466–2474. doi: 10.1039/B901580A.

Lippmann, F. (1973) Sedimentary Carbonate Minerals. 1st edn. Berlin, Heidelberg: Springer Berlin Heidelberg. doi: 10.1007/978-3-642-65474-9.

Liu, Z. et al. (2011) 'Synthesis and scale inhibitor performance of polyaspartic acid', Journal of Environmental Sciences. Elsevier, 23(SUPPL.), pp. S153–S155. doi: 10.1016/S1001-0742(11)61100-5.

Lopez, O., Zuddas, P. and Faivre, D. (2009) 'The influence of temperature and seawater composition on calcite crystal growth mechanisms and kinetics: Implications for Mg incorporation in calcite lattice', Geochimica et Cosmochimica Acta. Pergamon, 73(2), pp. 337–347. doi: 10.1016/J.GCA.2008.10.022.

Loste, E. et al. (2003) 'The role of magnesium in stabilising amorphous calcium carbonate and controlling calcite morphologies', Journal of Crystal Growth. North-Holland, 254(1–2), pp. 206–218. doi: 10.1016/S0022-0248(03)01153-9.

Lowenstam, H. A. and Weiner, S. (1989) 'On Biomineralization', On Biomineralization. Oxford University Press. doi: 10.1093/OSO/9780195049770.001.0001.

Ma, X. et al. (2015) 'Gelatin intervened synthesis of calcite cocoon-like microparticles assembled with small rhombohedra at low temperature', http://dx.doi.org/10.1179/1743676115Y.0000000033. Taylor & Francis, 115(1), pp. 1–5. doi: 10.1179/1743676115Y.0000000033.

Mabry, J. C. and Mondal, K. (2011) 'Magnesian calcite sorbent for carbon dioxide capture', http://dx.doi.org/10.1080/09593330.2010.486843. TF , 32(1), pp. 55–67. doi: 10.1080/09593330.2010.486843.

Meldrum, F. C. (2013) 'Calcium carbonate in biomineralisation and biomimetic chemistry', International Materials Reviews . Taylor & Francis, 48(3), pp. 187–224. doi: 10.1179/095066003225005836.

Meldrum, F. C. and Hyde, S. T. (2001) 'Morphological influence of magnesium and organic additives on the precipitation of calcite', Journal of Crystal Growth. North-Holland, 231(4), pp. 544–558. doi: 10.1016/S0022-0248(01)01519-6.

Mercedes-Martín, R. et al. (2022) 'Effects of salinity, organic acids and alkalinity on the growth of calcite spherulites: Implications for evaporitic lacustrine sedimentation', The Depositional Record. John Wiley & Sons, Ltd, 8(1), pp. 143–164. doi: 10.1002/DEP2.136.

Montanari, G. et al. (2017) 'Impact of citrate ions on the nucleation and growth of anhydrous CaCO3', Crystal Growth and Design. American Chemical Society, 17(10), pp. 5269–5275. doi: 10.1021/acs.cgd.7b00796.

Moore, L., Hopwood, J. D. and Davey, R. J. (2004) 'Unusual morphological and microstructural features of synthetic calcite induced by acrylate/styrene copolymers', Journal of Crystal Growth. North-Holland, 261(1), pp. 93–98. doi: 10.1016/J.JCRYSGRO.2003.09.013.

Mulders, J. J. P. A., Tobler, D. J. and Oelkers, E. H. (2021) 'Siderite nucleation pathways as a function of aqueous solution saturation state at 25 °C', Chemical Geology. Elsevier, 559, p. 119947. doi: 10.1016/J.CHEMGEO.2020.119947.

Murray, J. W. (2004) What controls the composition of riverwater and seawater: equilibrium versus kinetic ocean. Oceanography 400 — Autumn 2006, Chemical Oceanography Lecture Notes, E-Publishing Inc., University of Washington.

Nancollas, G. H. and Reddy, M. M. (1971) 'The crystallization of calcium carbonate. II. Calcite growth mechanism', Journal of Colloid and Interface Science. Academic Press, 37(4), pp. 824–830. doi: 10.1016/0021-9797(71)90363-8.

Nehrke, G. et al. (2007) 'Dependence of calcite growth rate and Sr partitioning on solution stoichiometry: Non-Kossel crystal growth', Geochimica et Cosmochimica Acta. Pergamon, 71(9), pp. 2240–2249. doi: 10.1016/J.GCA.2007.02.002.

Niedermayr, A., Köhler, S. J. and Dietzel, M. (2013) 'Impacts of aqueous carbonate accumulation rate, magnesium and polyaspartic acid on calcium carbonate formation (6–40 °C)', Chemical Geology. Elsevier, 340, pp. 105–120. doi: 10.1016/J.CHEMGEO.2012.12.014.

Nielsen, M. R. et al. (2016) 'Inhibition of Calcite Growth: Combined Effects of Mg2+ and SO42-', Crystal Growth and Design. American Chemical Society, 16(11), pp. 6199–6207. doi: 10.1021/acs.cgd.6b00536.

Osman, A. I. et al. (2020) 'Recent advances in carbon capture storage and utilisation technologies: a review', Environmental Chemistry Letters 2020 19:2. Springer, 19(2), pp. 797–849. doi: 10.1007/S10311-020-01133-3.

Parkhurst, D. L. and Appelo, C. A. J. (1999) 'User's guide to PHREEQC (Version 2): A computer program for speciation, batch-reaction, one-dimensional transport, and inverse geochemical calculations', Water-Resources Investigations Report. doi: 10.3133/WRI994259.

Patwardhan, S. V and Staniland, S. S. (2019) 'Biomineralisation: how Nature makes nanomaterials', Green Nanomaterials: From bioinspired synthesis to sustainable manufacturing of inorganic nanomaterials. IOP Publishing. doi: 10.1088/978-0-7503-1221-9CH6.

Pogge von Strandmann, P. A. E. et al. (2019) 'Rapid CO 2 mineralisation into calcite at the CarbFix storage site quantified using calcium isotopes', Nature Communications. Nature Publishing Group, 10(1). doi: 10.1038/s41467-019-10003-8.

Politi, Y. et al. (2010) 'Role of magnesium ion in the stabilization of biogenic amorphous calcium carbonate: A structure-function investigation', Chemistry of Materials. American Chemical Society, 22(1), pp. 161–166. doi: 10.1021/CM902674H/SUPPL_FILE/CM902674H_SI_001.PDF.

Portugal, C. R. M. e. et al. (2020) 'Microbiologically Induced Calcite Precipitation biocementation, green alternative for roads – is this the breakthrough? A critical review', Journal of Cleaner Production. Elsevier, 262, p. 121372. doi: 10.1016/J.JCLEPRO.2020.121372.

Pouget, E. M. et al. (2010) 'The development of morphology and structure in hexagonal vaterite', Journal of the American Chemical Society. American Chemical Society, 132(33), pp. 11560–11565. doi: 10.1021/JA102439R/SUPPL_FILE/JA102439R_SI_005.MPG.

Putnis, A. (1992) Introduction to mineral sciences. 1st edn. Cambridge University Press.

Raz, S. et al. (2003) 'The Transient Phase of Amorphous Calcium Carbonate in Sea Urchin Larval Spicules: The Involvement of Proteins and Magnesium Ions in Its Formation and Stabilization', Advanced Functional Materials. John Wiley & Sons, Ltd, 13(6), pp. 480–486. doi: 10.1002/ADFM.200304285.

Reddy, M. M. and Nancollas, G. H. (1976) 'The crystallization of calcium carbonate: IV. The effect of magnesium, strontium and sulfate ions', Journal of Crystal Growth. North-Holland, 35(1), pp. 33–38. doi: 10.1016/0022-0248(76)90240-2.

Rodriguez-Blanco, J. D. et al. (2012) 'The role of pH and Mg on the stability and crystallization of amorphous calcium carbonate', in Journal of Alloys and Compounds. doi: 10.1016/j.jallcom.2011.11.057.

Rodriguez-Blanco, J. D., Sand, K. K. and Benning, L. G. (2017) 'ACC and Vaterite as Intermediates in the Solution-Based Crystallization of CaCO3', in New Perspectives on Mineral Nucleation and Growth. doi: 10.1007/978-3-319-45669-0_5.

Rodriguez-Blanco, J. D., Shaw, S. and Benning, L. G. (2008) 'How to make "stable" ACC: protocol and preliminary structural characterization', Mineralogical Magazine. doi: 10.1180/minmag.2008.072.1.283.

Rodriguez-Blanco, J. D., Shaw, S. and Benning, L. G. (2015) 'A route for the direct crystallization of dolomite', American Mineralogist. Walter de Gruyter GmbH, 100(5–6), pp. 1172–1181. doi: 10.2138/am-2015-4963.

Roemmich, D. (2014) Voyager: How Long until Ocean Temperature Goes up a Few More Degrees? |, Scripps Institution of Oceanography.

Sand, K. K. et al. (2012a) 'Aragonite growth in water-alcohol mixtures: Classical or nonclassical crystallization?', Materials Research Society Symposium Proceedings, 1419, pp. 7–13. doi: 10.1557/opl.2012.885.

Sand, K. K. et al. (2012b) 'Crystallization of CaCO 3 in water-Alcohol mixtures: Spherulitic growth, polymorph stabilization, and morphology change', Crystal Growth and Design, 12(2), pp. 842–853. doi: 10.1021/cg2012342.

Sandberg, P. A. (1983) 'An oscillating trend in Phanerozoic non-skeletal carbonate mineralogy', Nature 1983 305:5929. Nature Publishing Group, 305(5929), pp. 19–22. doi: 10.1038/305019a0.

Sato, A. et al. (2011) 'Glycolytic intermediates induce amorphous calcium carbonate formation in crustaceans', Nature Chemical Biology 2011 7:4. Nature Publishing Group, 7(4), pp. 197–199. doi: 10.1038/nchembio.532.

Schenk, A. S. et al. (2013) 'Polymer-induced liquid precursor (PILP) phases of calcium carbonate formed in the presence of synthetic acidic polypeptides—relevance to biomineralization', Faraday Discussions. The Royal Society of Chemistry, 159(0), pp. 327–344. doi: 10.1039/C2FD20063E.

Seknazi, E. et al. (2019) 'Incorporation of organic and inorganic impurities into the lattice of metastable vaterite', Inorganic Chemistry Frontiers. The Royal Society of Chemistry, 6(10), pp. 2696–2703. doi: 10.1039/C9QI00849G.

Sugawara-Narutaki, A., Nakamura, J. and Ohtsuki, C. (2021) 'Polymer-induced liquid precursors (PILPs) and bone regeneration', Bioceramics. Elsevier, pp. 391–398. doi: 10.1016/B978-0-08-102999-2.00017-X.

Sugiura, Y. et al. (2013) 'Acceleration and inhibition effects of phosphate on phase transformation of amorphous calcium carbonate into vaterite', American Mineralogist. Walter de Gruyter GmbH, 98(1), pp. 262–270. doi: 10.2138/AM.2013.4212/MACHINEREADABLECITATION/RIS.

Sugiura, Y. et al. (2019) 'PO4 adsorption on the calcite surface modulates calcite formation and crystal size', American Mineralogist. De Gruyter Open Ltd, 104(10), pp. 1381–1388. doi: 10.2138/AM-2019-7015/MACHINEREADABLECITATION/RIS.

Sun, W. et al. (2015) 'Nucleation of metastable aragonite CaCO 3 in seawater', Proceedings of the National Academy of Sciences of the United States of America. National Academy of Sciences, 112(11), pp. 3199–3204. doi: 10.1073/PNAS.1423898112/SUPPL_FILE/PNAS.1423898112.SAPP.PDF.

Thenepalli, T. et al. (2015) 'A strategy of precipitated calcium carbonate (CaCO3) fillers for enhancing the mechanical properties of polypropylene polymers', Korean Journal of Chemical Engineering 2015 32:6. Springer, 32(6), pp. 1009–1022. doi: 10.1007/S11814-015-0057-3.

Tobler, D. J. et al. (2014) 'The Effect of Aspartic Acid and Glycine on Amorphous Calcium Carbonate (ACC) Structure, Stability and Crystallization', Procedia Earth and Planetary Science. Elsevier BV, 10, pp. 143–148. doi: 10.1016/j.proeps.2014.08.047.

Tobler, D. J. et al. (2015) 'Citrate effects on amorphous calcium carbonate (ACC) structure, stability, and crystallization', Advanced Functional Materials. Wiley-VCH Verlag, 25(20), pp. 3081–3090. doi: 10.1002/adfm.201500400.

Toroz, D. et al. (2021) 'New insights into the role of solution additive anions in Mg2+ dehydration: implications for mineral carbonation', CrystEngComm. The Royal Society of Chemistry, 23(28), pp. 4896–4900. doi: 10.1039/D1CE00052G.

Toroz, D. et al. (2022) 'A Database of Solution Additives Promoting Mg2+Dehydration and the Onset of MgCO3Nucleation', Crystal Growth and Design. American Chemical Society, 22(5), pp. 3080–3089. doi: 10.1021/ACS.CGD.1C01525/ASSET/IMAGES/LARGE/CG1C01525_0005.JPEG.

Trushina, D. B. et al. (2014) 'CaCO3 vaterite microparticles for biomedical and personal care applications', Materials Science and Engineering: C. Elsevier, 45, pp. 644–658. doi: 10.1016/J.MSEC.2014.04.050.

Vallina, B. et al. (2014) 'The effect of heating on the morphology of crystalline neodymium hydroxycarbonate, NdCO3OH', Mineralogical Magazine. Cambridge University Press, 78(6), pp. 1391–1397. doi: 10.1180/MINMAG.2014.078.6.05.

Vallina, B. et al. (2015) 'The role of amorphous precursors in the crystallization of La and Nd carbonates', Nanoscale. Royal Society of Chemistry, 7(28), pp. 12166–12179. doi: 10.1039/c5nr01497b.

Voigt, M. et al. (2021) 'An experimental study of basalt–seawater–CO2 interaction at 130 °C', Geochimica et Cosmochimica Acta. Pergamon, 308, pp. 21–41. doi: 10.1016/j.gca.2021.05.056.

Wang, Y. W. et al. (2012) 'In Situ Study of the Precipitation and Crystallization of Amorphous Calcium Carbonate (ACC)', Crystal Growth and Design. American Chemical Society, 12(3), pp. 1212–1217. doi: 10.1021/CG201204S.

Washbourne, C. L. et al. (2015) 'Rapid removal of atmospheric CO2 by urban soils', Environmental Science and Technology. American Chemical Society, 49(9), pp. 5434–5440. doi: 10.1021/ES505476D/SUPPL_FILE/ES505476D_SI_001.PDF.

Wasylenki, L. E. et al. (2005) 'Nanoscale effects of strontium on calcite growth: An in situ AFM study in the absence of vital effects', Geochimica et Cosmochimica Acta. Pergamon, 69(12), pp. 3017–3027. doi: 10.1016/J.GCA.2004.12.019.

Wei, W. et al. (2008) 'Preparation of hierarchical hollow CaCo3 particles and the application as anticancer drug carrier', Journal of the American Chemical Society. American Chemical Society, 130(47), pp. 15808–15810. doi: 10.1021/JA8039585/SUPPL_FILE/JA8039585_SI_001.PDF.

Westin, K.-J. and Rasmuson, Å. C. (2005) 'Crystal growth of aragonite and calcite in presence of citric acid, DTPA, EDTA and pyromellitic acid', Journal of Colloid and Interface Science. Academic Press, 282(2), pp. 359–369. doi: 10.1016/j.jcis.2004.03.029.

Wilkinson, B. H., Buczynski, C. and Owen, R. M. (1984) 'Chemical control of carbonate phases; implications from Upper Pennsylvanian calcite-aragonite ooids of southeastern Kansas', Journal of

Sedimentary Research. GeoScienceWorld, 54(3), pp. 932–947. doi: 10.1306/212F853A-2B24-11D7-8648000102C1865D.

Xia, F. et al. (2009) 'Mechanism and kinetics of pseudomorphic mineral replacement reactions: A case study of the replacement of pentlandite by violarite', Geochimica et Cosmochimica Acta. Pergamon, 73(7), pp. 1945–1969. doi: 10.1016/J.GCA.2009.01.007.

Zahlan, H. et al. (2019) 'Synthesis of Poly (Citric Acid-Co-Glycerol) and Its Application as an Inhibitor of CaCO3 Deposition', Materials 2019, Vol. 12, Page 3800. Multidisciplinary Digital Publishing Institute, 12(22), p. 3800. doi: 10.3390/MA12223800.

Zeng, W.-A. et al. (2016) Effect of calcium carbonate on cadmium and nutrients uptake in tobacco (Nicotiana tabacum L.) planted on contaminated soil - PubMed, Journal of Environmental Biology.

Zhang, P., Tweheyo, M. T. and Austad, T. (2007) 'Wettability alteration and improved oil recovery by spontaneous imbibition of seawater into chalk: Impact of the potential determining ions Ca2+, Mg2+, and SO42−', Colloids and Surfaces A: Physicochemical and Engineering Aspects. Elsevier, 301(1–3), pp. 199–208. doi: 10.1016/J.COLSURFA.2006.12.058.

Zhang, X. et al. (2019) 'Interatomic potentials of Mg ions in aqueous solutions: structure and dehydration kinetics', European Journal of Mineralogy. GeoScienceWorld, 31(2), pp. 275–287. doi: 10.1127/EJM/2019/0031-2815.

Zhu, Y. et al. (2021) 'Sulfate-Controlled Heterogeneous CaCO3Nucleation and Its Non-linear Interfacial Energy Evolution', Environmental Science and Technology. American Chemical Society, 55(16), pp. 11455–11464. doi: 10.1021/ACS.EST.1C02865/ASSET/IMAGES/MEDIUM/ES1C02865_M004.GIF.

Zhu, Y. et al. (2022) 'Process-Specific Effects of Sulfate on CaCO3Formation in Environmentally Relevant Systems', Environmental Science and Technology. American Chemical Society, 56(12), pp. 9063–9074. doi: 10.1021/ACS.EST.1C08898/ASSET/IMAGES/LARGE/ES1C08898_0006.JPEG.

Zhuravlev, A. Y. and Wood, R. A. (2009) 'Controls on carbonate skeletal mineralogy: Global CO2 evolution and mass extinctions', Geology. GeoScienceWorld, 37(12), pp. 1123–1126. doi: 10.1130/G30204A.1.

Zuddas, P., Pachana, K. and Faivre, D. (2003) 'The influence of dissolved humic acids on the kinetics of calcite precipitation from seawater solutions', Chemical Geology. Elsevier, 201(1–2), pp. 91–101. doi: 10.1016/S0009-2541(03)00230-4.

Chapter 4.

Mechanistic insights into the formation of aragonite-type carbonates: the role of Ca^{2+} in the crystallisation of strontianite and witherite

Authors: Niamh Faulkner, Juan Diego Rodríguez-Blanco, Luca Terribili, Andrea Pierozzi and Adrienn Szucs.

Publication Status: Unpublished

Author Contributions: N. Faulkner conducted UV- Vis spectrophometry, sample synthesis and XRD analyses, wrote the manuscript and produced all figures and tables. J.D Rodríguez-Blanco advised and edited the manuscript. L. Terribili and A. Pierozzi collected XRD and SEM data and assisted with sample preparation. A Szucs assisted with sample preparation and collected XRD data.

Mechanistic insights into the formation of aragonite-type carbonates: the role of Ca^{2+} in the crystallisation of strontianite and witherite

4.1 ABSTRACT

This study investigates the transformation of calcite to aragonite-type carbonates, specifically witherite ($BaCO_3$) and strontianite ($SrCO_3$), under ambient to low hydrothermal conditions (21 to 80°C). The host grains are replaced via the pseudomorphic replacement of calcite by witherite and strontianite, occurring primarily through a dissolution-precipitation mechanism. The extent of this transformation is found to be significantly influenced by several key factors, including the composition of the aqueous solution, the grain size of the initial calcite, and the temperature and pH of the system.

Furthermore, we explore the role of Ca^{2+} ions in the formation of $BaCO_3$ and $SrCO_3$ from aqueous solutions *in situ* using UV-Vis spectrophotometry. Our results demonstrate that Ca^{2+} ions exert an inhibiting effect on the nucleation and growth of these aragonite-type carbonates. This inhibition is attributed to multiple factors, including the presence of hydration barriers, differences in coordination numbers between $^{VI}Ca^{2+}$ and $^{IX}Ba^{2+}/^{XI}Sr^{2+}$, and the high supersaturation levels during the crystallization process.

The solid samples were studied with a combination of powder X-ray diffraction, scanning electron microscopy. Results from both the homogeneous and heterogeneous nucleation experiments highlight that the influence of aqueous Sr and Ba is not uniform. In summary, this study provides valuable insights into the kinetics and mechanisms of calcite transformation to witherite and strontianite under ambient low hydrothermal conditions.

4.2 INTRODUCTION

Witherite ($BaCO_3$) and strontianite ($SrCO_3$) are isostructural carbonates. Along with aragonite ($CaCO_3$) and cerucite ($PbCO_3$) they make the four naturally occurring orthorhombic divalent carbonate group, also known as aragonite-type carbonates (Speer, 1983). Synthetic isostructural carbonates include radium carbonate ($RaCO_3$) (Speer, 1983) and europium (II) carbonate (EuCO3) (Mayer *et al*., 1964). Of the anhydrous carbonates there are two distinct isomorphous groups. These groups are divided as a consequence of the ionic radius of the metal cation. Calcite-type have ionic radii of < 1 Å, whereas aragonite-type carbonates have ionic radii > 1 Å. The ionic radius of Ca^{2+} in calcite-type carbonates is 1.00 Å (coordination 6), whereas the ionic radius of Ca^{2+} in aragonite-type carbonates is 1.18 Å (coordination 9), which is why $CaCO_3$ can be both calcite and aragonite type (Shannon and IUCr, 1976; Speer, 1983). The ability of polymorphic calcium carbonate to precipitate as coordination 6 calcite and coordination 9 aragonite is what also allows living organism to create very strong skeletons and shells via biomineralization processes by crystallising both polymorphs (Morse and Mackenzie, 1990).

The calcite group is characterised as rhombohedral, whereas the aragonite type are orthorhombic (Dana, 1932). Orthorhombic carbonates belongs to the space group *Pmcn* (witherite: a = 5.3126 Å, b = 8.8958 Å, and c = 6.4284 Å; strontianite: a = 5.090 Å, b = 8.358 Å, and c = 5.997 Å), whereas rhombohedral carbonates such as calcite belong to the space group *R3c* (De Villiers, 1971). Orthorhombic carbonates form twins that are pseudo-hexagonal in character (Dana, 1932). However, the high temperature cubic forms of Ba and Sr carbonates have structures related to $NaCl_2$, where Ba and Sr occupy the Na-sites and CO_3 occupies the Cl-sites (Lander, 1949; Speer, 1983).

Witherite's crystal structure was initially established by Colby and LaCoste, (1933) and later updated/refined by others (De Villiers, 1971; Holl *et al.*, 2000). At high temperature $BaCO_3$'s crystal structure evolves, from orthorhombic to hexagonal (803 °C) and cubic (976 °C) (Lander 1949). There is a high pressure polymorph, known as $BaCO_3$II (Lin and Liu, 1997), but unlike the high temperature

polymorphs, it still retains the same crystal structure. There is twinning on the unit prism {110}, cyclic and polysynthetic twinning, (110) : (110) 61.7° (Speer, 1983).

Witherite deposits are scarce and associated with low temperature hydrothermal veins (Mavromatis *et al.*, 2016), it is the second most common barium ore, after Barite ($BaSO_4$). It can be a gangue mineral associated with barite and galena (PbS), Dana (1932). Deposits include its type locality, Alston Moor, Cumbria (England); Cave-in-Rock, Illinois (USA); and in lower Cambrian stratiform deposits in the Qinling region, (southwestern China), which has some of the world's largest witherite deposits. (Pi *et al.*, 2014). Other industrial applications for witherite include glassware and ceramics, rat poison and hardening steel.

Strontianite's crystal structure was first identified by Zachariasen (1928) and subsequently refined (De Villiers, 1971; Jarosch and Heger, 1988). Lander (1949) found that the structure of $SrCO_2$ changed from orthorhombic to hexagonal at 912 °C, as well as reporting the existence of a high temperature cubic polymorph. Like other aragonite type carbonates, there is twinning on the unit prism {110}, cyclic and polysynthetic twinning, (110) : (110) 62.5° (Speer, 1983).

Similar to witherite, strontianite forms as low hydrothermal deposits, these deposits include the type locality Strontian (Scotland), Cave-in Rock, Illinois (USA) and Sierra Mojada, (Mexico) and is often found associated with celestine, $SrSO_4$ (Helz and Holland, 1965; Garcia-Guinea *et al.*, 2009). Strontianite is used in the production of coloured glass, paint, for television tubes, for strontium oxide and in ferrite magnets for small DC motors (Erdemoğlu and Canbazoğlu, 1998). The solubility of strontianite and witherite has been studied across a range of conditions/parameters (Helz and Holland, 1965; Busenberg *et al.*, 1984; Busenberg and Plummer, 1986).

Ionic radii of divalent cations is responsible for the formation of solid solutions between isostructural carbonates, (Mg^{2+}= 0.72 Å, Ca^{2+} = 1.00 Å, Sr^{2+} = 1.18 Å, Ba^{2+} = 1.35 Å, (Shannon, 1976)). Generally if the difference between ionic radii is ≥ 0.11 Å then there's a miscibility gap between end members, ≤ 0.11 Å results in solid solutions, i.e. $CaCO_3$- $MgCO_3$ (Reeder, 1983b). Solid solutions between $BaCO_3$ and $CaCO_3$ are also known, as well as the complete solid solutions between

$BaCO_3$ and $SrCO_3$. The $BaCO_3$ and $CaCO_3$ solid solution has miscibility gaps, and an intermediate phase, $BaCa(CO_3)_2$, and is restricted to below 10 mol % $CaCO_3$ in $BaCO_3$ and below 5 mol % $BaCO_3$ in $CaCO_3$ (Speer, 1983). The intermediate phase $BaCa(CO_3)_2$ has three polymorphs: Alstonite, barytocalcite and paralstonite (Baldasari and Speer, 1979; Speer, 1983; Spahr *et al.*, 2019; Chuliá-Jordán *et al.*, 2021). There is a solid solution between witherite and strontianite, as well as solid solutions between $CaCO_3$ and witherite, and $CaCO_3$ and strontianite. Studies on the $Ba_xSr_{1-x}CO_3$ solid solution have typical focused on isotopic fractionation (Böttcher *et al.*, 1997; Prieto *et al.*, 1997; Sánchez-Pastor *et al.*, 2011; Mavromatis *et al.*, 2016).

In the orthorhombic carbonates there are substitutions between the divalent cations Ca^{2+}, Sr^{2+}, Pb^{2+}, Ba^{2+} (with increasing ionic radius). Natural witherite often contains impurities including, $SrCO_3$, as much as 11 mol %, $CaCO_3$ and $MgCO_3$ as well as trace $PbCO_3$ (Speer, 1983; Busenberg and Plummer, 1986). A deposit of Sr-rich witherite from the Cassiar District, British Columbia (Canada) was reported to contain $Ba_{0.888}Sr_{0.112}CO_3$ and was associated with barite (Baldasari and Speer, 1979). Ca-rich witherite can be attributed to presence of calcite inclusions (Baldasari and Speer, 1979).. Natural witherite typically has considerable inclusions of Ca^{2+}, witherite from the Silurian Tonoloway Formation in Pennsylvania (USA) consists of $Sr_{0.729}Ca_{0.269}Ba_{0.002}CO_3$ (Speer, 1976). The Ba content in natural strontianite is usually very low, however one example of natural Ba-strontianite is from the Kola Alkaline Carbonatite Province (Russia) which contains 3.37 wt % BaO (Kapuston,1980) and (Speer, 1983).

Ba- Sr substitution is of interest in other minerals, not just in carbonates. The substitution of Sr and Ba in double perovskite oxides, e.g. $Ba_{2-x}Sr_xZnWO_6$, have been examined due to their range of industrial applications, e.g. solar cells, lasers, X-ray detectors (Alsabah *et al.*, 2017). Ba-Sr substitution also takes place within sulphates, there is $(Sr,Ba,Ra)SO_4$ solid solution series. Barite and Celestine are often found in association with Ba- Sr carbonates. (Kotelnikov *et al.*, 2000; Klinkenberg *et al.*, 2018; Weber *et al.*, 2018).

The effect of (aqueous) Sr^{2+} and Ba^{2+} on carbonates has been previously studied, as the relationship between Sr and Ca is of geologic and environmental importance. The Sr/Ca ratio for

palaeoseawater is obtained from (biogenic) carbonates it represents the exchange of ions between the continent and the oceans (Turekian, 1964). Wasylenki *et al.* (2005) found that at low concentrations Sr^{2+} promoted calcite growth, when Sr^{2+} is incorporated into growing calcite it thickens the terraces on the [104] plane. However, they found that at higher concentrations Sr^{2+} inhibits calcite growth, similarly to other alkaline-earth metal ions e.g. Mg^{2+} which can inhibit calcite growth (Nielsen *et al.*, 2016; Faulkner & Rodríguez-Blanco, *In revision*). Lindner *et al.* examined the influence of aqueous Ba^{2+} (2017) and Sr^{2+} (2019) on magnesite. They found little to no Ba^{2+} is incorporated into $MgCO_3$, favouring norsethite, $BaMg(CO_3)_2$ precipitation instead. They found that Sr^{2+} did not influence the growth, or step morphologies.

Diagenetic alterations of carbonates, notably aragonite and Mg-calcite to the more metastable calcite is pervasive in the geological record and is well recorded in the literature (Folk, 1964; Bathurst, 1972; Aissaoui, 1985; Bruni and Wenk, 1985, etc.), with recrystallisation occurring via dissolution-reprecipitation. Laboratory based studies have examined the alteration of biogenic aragonite (Pederson *et al.*, 2020) as well as examining the replacement reactions between rhombohedral and orthorhombic carbonates seeds. Using calcite (2021), aragonite and dolomite (2022) seeds in REE-bearing solutions under low temperature and hydrothermal conditions, Szucs *et al.* found that new phases formed as surface precipitates that partially or completely replace the host minerals. Yuan *et al.* (2016) and Kim *et al.* (2021) examined the replacement of calcium carbonate by aragonite-type carbonate, cerussite ($PbCO_3$) finding that the development of nanoporosity on the host crystal was critical for the replacement via dissolution-reprecipitation mechanisms. Recently Forjanes *et al.* (2022) found that dissolution-reprecipitation mechanisms result in the formation of "thin, cohesive, pseudomorphic shells of $SrCO_3$ and $BaCO_3$ on the surface of calcite" following the interaction of calcite crystals in Sr and Ba-bearing solutions. These thin precipitate layers effectively armoured the calcite, preventing further replacement of the crystal.

In order to better understand the kinetics and physicochemical aspects of the replacement reactions of calcite to aragonite type carbonates (namely. $BaCO_3$ and $SrCO_3$) this study aims to answer the following questions: What are the growth rates of $BaCO_3$ and $SrCO_3$ from solution? What

are the kinetics of calcite replacement by aragonite type carbonates? Does Ca^{2+} influence the formation of $BaCO_3$ and $SrCO_3$? Is Ca^{2+} incorporated into $BaCO_3$ and $SrCO_3$ during growth? Shedding light on these questions will allow an improved understanding of kinetics and mechanisms of replacement between calcite– and aragonite–type carbonate groups.

In this study we studied the influence of Ca^{2+} on the homogeneous nucleation of $BaCO_3$ and $SrCO_3$ from solution. We also quantified the kinetics of replacement of rhombohedral calcite with orthorhombic carbonates strontianite and witherite across ambient and low hydrothermal conditions. Understanding these replacement reactions can provide geologic insight into the transformation of carbonate to aragonites in mineral-fluid hydrothermal reactions during metamorphic processes.

4.3 METHODS

4.3.1 MINERAL SYNTHESIS AND CRYSTALLISATION

The synthesis of $BaCO_3$ and $SrCO_3$ followed two approaches, (i) homogeneous nucleation from aqueous solution and (ii) replacement reaction experiments (heterogeneous nucleation). Solutions were prepared using sodium carbonate (Na_2CO_3; Acros Organics, 99.5% purity), strontium chloride hexahydrate ($SrCl_2 \cdot 6H_2O$; Alfa Aesar, >99% purity), barium chloride dihydrate ($BaCl_2 \cdot 2H_2O$; J.T.Baker, 99.0 - 101.0%) and calcium chloride dihydrate ($CaCl_2 \cdot 2H_2O$; VWR Chemicals, 99.5% purity) and ultrapure deionized water (Milli-Q; specific resistivity >18 MΩ cm^{-1}). Solution concentrations are listed in Table 4.1.

4.3.1.1 HOMOGENEOUS NUCLEATION EXPERIMENTS

To examine the in situ formation of $BaCO_3$ and $SrCO_3$ at ambient temperature (21 °C), time resolved UV-vis spectrophotometry was used following the methods described by Tobler *et al.* (2014 and 2015). Absorbance as a function of time was measured at a fixed wavelength of 450 nm after Montanari *et al.,* (2017). For this 1 mL of Na_2CO_3 4 mM was added to the plastic cuvette in the UV-vis spectrophotometer (Ocean Optics), then 1 mL of $BaCl_2$ or $SrCl_2$ 4 mM was added. The solution

was constantly stirred using a magnetic stirrer. The experiments ran until maximum turbidity was achieved (i.e. a plateau of absorbance was reached). The effect of Ca^{2+} on the $BaCl_2$ and $SrCl_2$ was also examined. This was done by combining solutions of $BaCl_2$ ± $CaCl_2$ or $SrCl_2$ ± $CaCl_2$ with Na_2CO_3 as described above. The influence of Ca^{2+} was examined at various molarities (0.1- 4.0 mM). These concentrations were selected for to ensure $BaCO_3$ and $SrCO_3$ form by a homogeneous nucleation process (avoiding surface precipitation processes, e.g., on the walls of the cuvettes/reactors). The Ca^{2+} concentrations (Ca/Sr 0-100% and Ca/Ba 0-25%) were chosen to examine changes within the kinetics of $SrCO_3$ and $BaCO_3$ crystallisation, whilst limiting/avoiding the formation of calcite.

Complimentary large batch experiments (500 mL in total volume) were also carried out at the same concentrations and conditions alongside the UV-vis spectrophotometry experiments, in order to obtain suitable amounts of precipitates for analysis with powder X-ray diffraction (XRD) and scanning electron microscopy (SEM). The solutions were then vacuum filtered and washed with isopropanol and dried, following the method of Rodriguez-Blanco *et el.* (2008). This method of scaling up was done according to the procedures of Van Driessche *et al.* (2012); Vallina *et al.*(2015); Montanari *et al.*, (2017) and Mulders *et al.* (2021).

4.3.1.2 REPLACEMENT EXPERIMENTS

To examine the replacement of calcite by aragonite type minerals witherite and strontianite, the interaction of Ba and Sr bearing aqueous solutions (at various concentrations) with calcite was conducted across a range of temperatures. Two types of replacement rection experiments were conducted using different types of calcite (i) calcite powder (ii) calcite seeds.

For the calcite powder experiments 1 g (0.01 M) were placed in borosilicate glass batch reactors with an aqueous solution (125 mL) bearing $BaCl_2$, $SrCl_2$ (both 0.1 M). To examine the influence of temperature on the replacement reaction experiments were carried out at four different temperatures (21, 40, 60 and 90 °C). Solid samples were carefully extracted across regular time

intervals across a 5 day period, and dried in an oven at 30 °C during 30 mins, following the methods of Szucs *et al.* (2021). In the following description, these experiments are known as calcite powder replacement experiments.

For the calcite seeds experiments the experimental procedure consisted of placing 0.043 g (0.43 mM, ~30 seeds) of calcite crystals (Iceland spar variety), with crystal sizes of 0.5-1.0 mm, in reactors/autoclaves with aqueous solutions of $BaCl_2$ or $SrCl_2$ (both 100 mM) in order to examine replacement. Experiments were then carried out across a range of temperatures (7, 21, 35, 80 and 200 °C). As described above solid samples were carefully extracted across regular time intervals and placed in a 30 °C oven for 30 mins to dry. In the following description, these experiments are known as calcite seeds experiments.

4.3.2 PHREEQC

The saturation indices of strontianite, witherite, calcite were calculated with the hydrogeochemical code PHREEQC (Parkhurst and Appelo, 1999) using the LLNL database (Allison, *et al.*, 1991).

The saturation index (SI) is defined as:

$$SI = Log\,(\frac{IAP}{K_{sp}})$$

Where IAP represents the ion activity product and K_{sp} represents the solubility product of the mineral phase.

4.3.3 KINETIC DATA ANALYSIS

The turbidity data were normalised respective to maximum turbidity. For both the turbidity data (homogeneous nucleation) and the replacement reaction data the Johnson-Mehl-Avrami-Kolmogorov (JMAK) particle nucleation model, which is based on the Avrami equation (Avrami, 1941) was applied in order to retrieve mechanistic and kinetic data.

$$\alpha = 1 - e^{-(k\cdot(t-t_{ind}))^n}$$

Where *a* represents the degree of the reaction (normalised turbidity data), t_{ind} is the induction time, the time between solution mixing *t* and the onset of nucleation, *k* is the rate of crystallisation/reaction constant, and *n* is the Avrami constant (Avrami, 1939).

Rewriting the Avrami Equation gives:

$$-ln\,ln(1-y) = n\,ln\,k + n\,ln\,t$$

The reaction with kinetics that conform to this equation give a straight line when $-ln\,ln(1-y)$ is plotted against *ln* t (Putnis, 1992; Xia *et al.*, 2009). The empirical parameter n value is given by the value of the slope, which is used to compare reaction mechanisms. The intercept on the y axis gives the value of n *ln* k, by which the k value can be determined.

4.3.4 MINERAL CHARACTERISATION:

4.3.4.1 POWDER X-RAY DIFFRACTION

All samples were examined by powder X-ray diffraction (XRD) diffraction and by scanning electron microscopy (SEM) analyses. Samples were characterised by XRD to identify and quantify the newly formed crystalline compounds. Conventional XRD patterns were obtained using a powder XRD Bruker D5000 powder X-ray diffractometer (Cu Kα radiation, 0.02° $step^{-1}$ from 5 to 50° 2θ at 0.15° min^{-1}). Phase identification was carried out using DIFFRAC.EVA software from Bruker in combination with the Powder Data File (PDF-4, The International Centre for Diffraction Data). Pattern-matching refinement and quantification of crystalline phases were carried out with the Rietveld refinement software TOPAS (Coelho *et al.*, 2011). The quantitative XRD errors uniformly remained below 1–2 wt%, requiring no additional data pre-processing such as normalization.

4.3.4.2 SCANNING ELECTRON MICROSCOPY (SEM).

SEM was used to investigate any changes in crystal morphology or crystal overgrowths on calcite grains. Semi quantitative analysis using energy dispersive spectroscopy (SEM-EDS) was carried out to determine the Ca^{2+} composition of the newly formed phases. Samples mounted on SEM mounds and were gold coated (5 nm) and placed into the Tescan Mira4 Field Emission Scanning

Electron Microscope fitted with a backscattered electron (BSE) detector and two XMax 170 mm^2 Oxford Instruments EDS detectors running Oxford Instruments NanoAnalysis AZtecTimed analysis software. All analyses were performed using a beam current of 300 pA and an accelerating voltage of either 5 keV, for detailed imaging, or 20 kV, for EDS analysis.

4.4 RESULTS

4.4.1 Homogeneous crystallisation

The addition of Ca^{2+} influenced both the nucleation and growth of $BaCO_3$ and $SrCO_3$ from solution. All the kinetic data results are presented numerically in Table 4.1**.** In general, the inhibition increased with higher concentrations of dopant. This inhibition was reflected in i) increased induction times (t_{ind}) , ii) reduced crystallisation rates (*k*).

Effect of Ca^{2+} on $SrCO_3$ crystallisation

Representative normalized turbidity obtained during $SrCO_3$ crystallisation for each Ca^{2+} concentration is shown in Figure 4.1. Ca^{2+} has an inhibiting effect on $SrCO_3$ formation, as there is a significant increase in induction time by $\sim$2 orders of magnitude from the pure system (8 seconds) to Ca/Sr = 75% (100 seconds) and Ca/Sr = 100 % (180 seconds). Ca^{2+} also has a profound influence on the crystallisation rate, which reduces drastically with as little as 1 mM of Ca^{2+}, from the pure system at 2.51 x 10^{-2} s^{-1} down to 0.56 x 10^{-2} s^{-1}. The saturation indices (SI) derived from PHREEQC suggest that at all examined molarities the solution is supersaturated for both pure strontianite (SI= 3.15- 2.96) and calcite (SI= 1.5- 2), however, only at the highest concentration of Ca (Ca/Sr = 100%) did minor amounts of calcite (3%) precipitate. XRD analysis revealed that calcian-strontianite is the resulting phase in all Ca-bearing experiments Figure 4.2. The Ca-strontianite XRD Bragg peaks were broader than the pure strontianite and were displaced to higher 2Θ (°) values compared to pure strontianite, indicative of decrease of the size of the unit cell due to Ca incorporation. SEM images revealed that this Ca-bearing solid always showed spherulitic morphologies (Appendix B5). Energy dispersive

spectroscopy (EDS) microscopy was carried out on selective crystals to confirm the chemistry. The Ca content increases with increased Ca concentration in the starting solution, up to atom % 16.95, see analytical results in the Supporting Information section (Appendix B5).

		JMAK MODEL FIT			SATURATION INDEX $(SI)_c$			DOMINANT PHASE	PHASE % (TOPAS)
	Ca:Sr	t_{ind} $(sec)_a$	k $(x10^{-2}\ S^{-1})_b$	AVRAMI NUMBER (n)	WITHERITE	STRONTIANITE	CALCITE		
Effect of Ca^{2+} on $SrCO_3$	0 %	8	2.51	2.06		3.15		Strontianite	100
	25 %	23	0.69	2.36		3.1	1.57	Ca-Strontianite	100 (Sr 63%; Ca 37%)
	50 %	11	0.13	1.01		3.05	1.83	Ca-Strontianite	100 (Sr 66%; Ca 34%)
	75 %	100	0.4	5.51		3	1.97	Ca-Strontianite	100 (Sr 54%; Ca 46%)
	100 %	180	0.3	5.26		2.96	2.06	Ca-Strontianite	97 (Sr 54%; Ca 46%); 3% Cal
	Ca: Ba								
Effect of Ca^{2+} on $BaCO_3$	0%	7	3.1	2.30	2.48			Witherite	100
	2.5%	13	1.8	2.50	2.47		0.62	Ca-Witherite	100 (Ba 76%; Ca 23%)
	6.25%	60	0.22	2.20	2.47		1.01	Ca-Witherite	100
	12.5%	289	0.162	4.73	2.45		1.29	Ca-Witherite	100 (Ba 67%; Ca 33%)
	25%	360	0.126	5.75	2.42		1.58	Ca-Witherite	100 (Ba 85%; Ca 15%)

Table 4.1: Data collected from Turbidity experiments. Kinetic data from JMAK model fit a) Induction time (t_{ind}), b) crystallisation rate (k). c) Saturation Indices (SI) values calculated using PHREEQC for the initial solution composition, prior to $BaCO_3$ or $SrCO_3$ precipitation. Phases determined by XRD and Rietveld refinement.

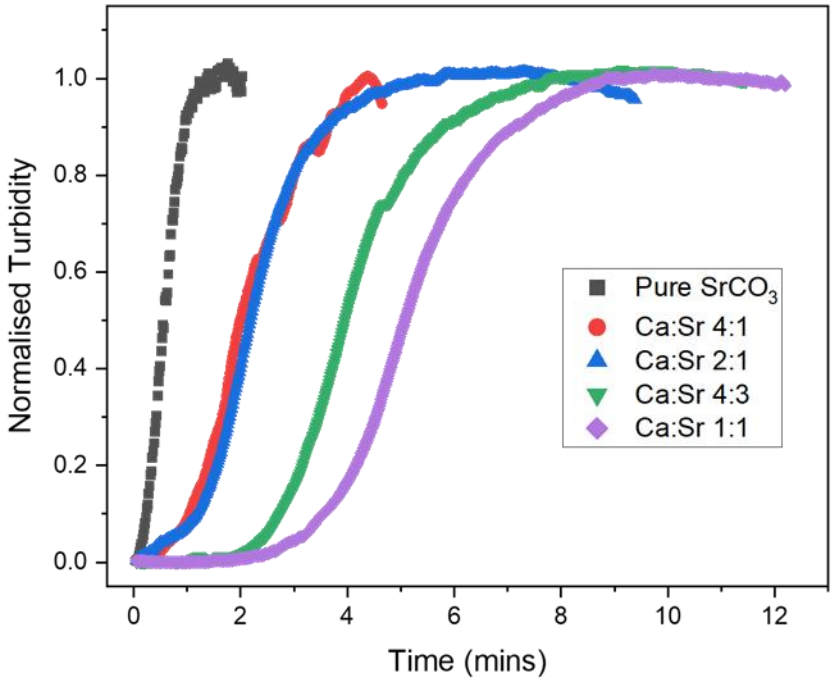

Figure 4.1: Influence of Ca^{2+} on $SrCO_3$ normalized turbidity plots. Crystallisation experiments monitored by UV-vis spectrophometry. Pure system (■); 1 mM (●); 2 mM (▲); 3 mM (▼); 4 mM (◆).

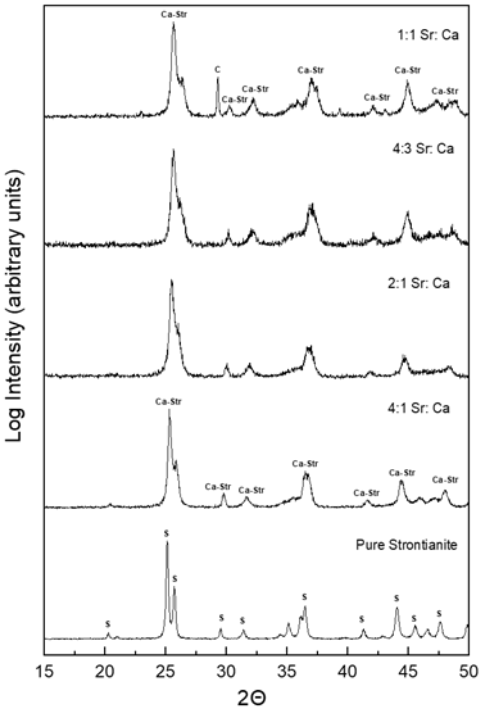

Figure 4.2: powdered XRD patterns obtained as products of the experiments carried out on the effect of Ca^{2+} on strontianite.

Effect of Ca^{2+} on $BaCO_3$ crystallisation

Representative normalized turbidity obtained during $BaCO_3$ crystallisation for each Ca^{2+} concentration is shown in Figure 4.3. Similar to the $SrCO_3$ turbidity experiments, the influence of Ca^{2+} on $BaCO_3$ is strong, however, this profound effect can be already seen at even lower molarities compared to the $Sr_{1-x}Ca_xCO_3$ experiments. This is particularly apparent with the increased induction time, at Ca/Ba= 25% the induction time is more than 50 times higher than the pure system, from 7 seconds to 6 minutes (360 seconds), an increase of ∼2 orders of magnitude. This is coupled with a significant drop in the crystallisation rates following the introduction of Ca^{2+}. From 3.1 x 10^{-2} s^{-1} in pure system, to 0.126 x 10^{-2} s^{-1} with the addition of 1 mM Ca^{2+}. The saturation indices derived from PHREEQC suggest that at all examined molarities the solution is supersaturated for pure witherite (SI ~ 2.4). While calcite is supersaturated at concentrations of > 0.25 mM Ca^{2+}, XRD analysis revealed that only calcian-witherite precipitated. The resulting XRD patterns for calcian-witherite are broader than pure witherite, and the peaks have also shifted to higher 2Θ (°) values, indicative of decrease of the size of the unit cell due to Ca^{2+} incorporation Figure 4.4.

The Ca^{2+} concentration also influenced the morphology of the witherite crystals. At the lowest concentrations (0.1 mM) witherite typically precipitated as bundles of needles, that radiate outward, forming branches and resembling a bow. Increasing the Ca^{2+} concentration caused the witherite to form rounder spherules, Figure 4.5. EDS microanalyses revealed that Ca content increased with concentration, up to atom% 4.75.

Results summarised in Table 4.1 and

Figure *4.6* confirm an overall positive correlation between Ca^{2+} concentration and the induction time (t_{ind}), as well as a decrease in the slope of the absorbance profile which corresponds to reductions of the crystallisation rates (k). Overall, the negative correlation between the Ca^{2+} concentration and crystallization rates (k) was quantified using the JMAK model. Representative examples of fits of the turbidity profile data to the equation are provided in the supporting information (B3 and B4).

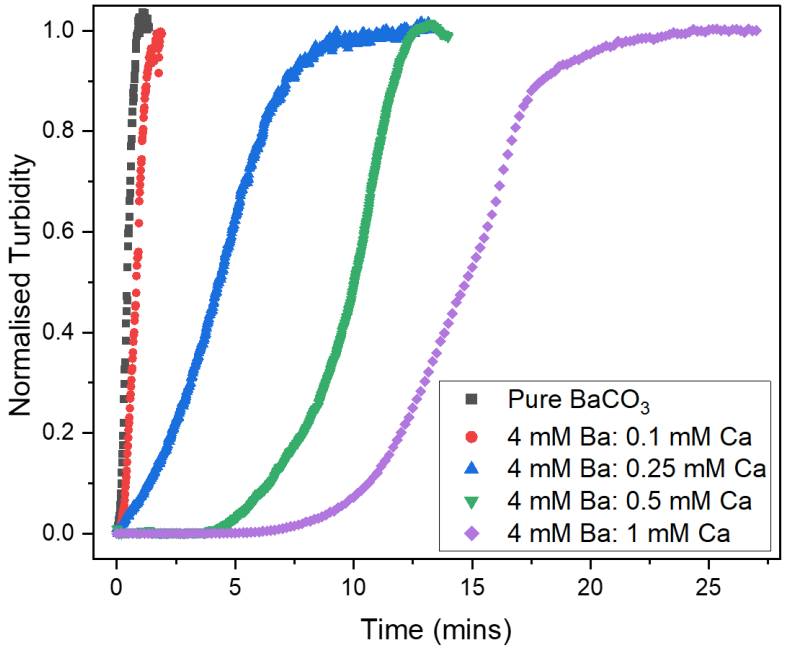

Figure 4.3: Influence of Ca^{2+} on $BaCO_3$ normalized turbidity plots. Crystallisation experiments monitored by UV-vis spectrophometry. Pure system (■); 0.1 mM (●); 0.25 mM (▲); 0.5 mM (▼); 1.0 mM (◆).

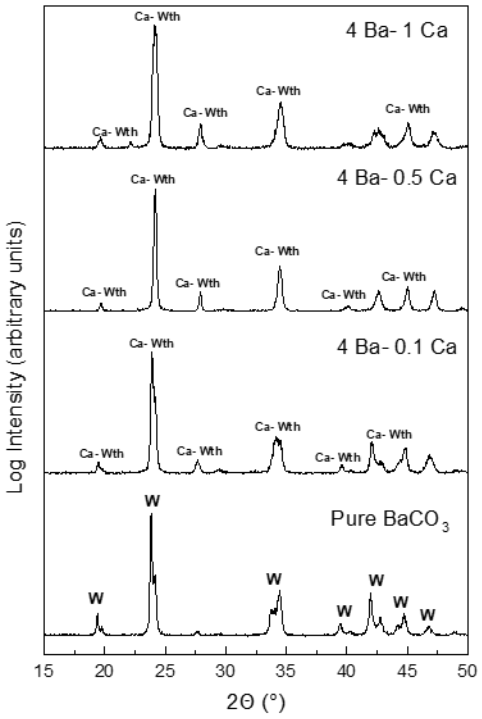

Figure 4.4: powdered XRD patterns obtained as products of the experiments carried out on the effect of Ca^{2+} on witherite.

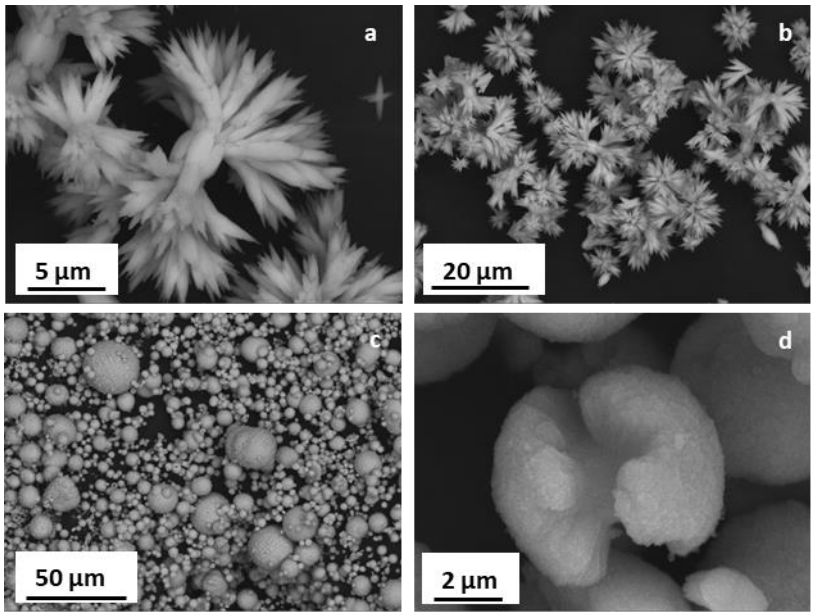

Figure 4.5: SEM images showing branching needles of witherite, 0.1 mM Ca (a and b) crystals evolve to rounder spherules with increased Ca content (c and d).

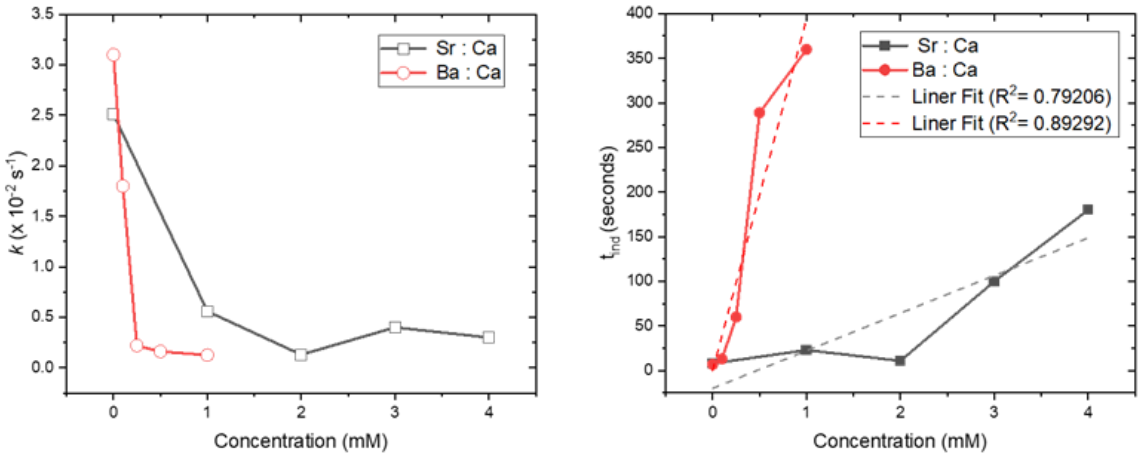

Figure 4.6: The influence of Ca^{2+} on crystallisation rate, k, (left) and induction time, t_{ind}, (right). There is an overall positive correlation between induction time and concertation, whereas there is a negative correlation between crystallisation rate and concertation.

4.4.2 Heterogeneous crystallisation: Calcite powder interaction with Ba- and Sr- bearing aqueous solutions.

The examination of the solid samples obtained from the interaction of calcite with Ba or Sr-bearing solutions resulted in partial or complete replacement of the host calcite with newly formed phases. The extent of the replacement reaction differed between the Ba and Sr experiments and with temperature.

Powder X-ray diffraction.

Characterisation with XRD allowed us to identify any newly formed secondary minerals, following the evolution of the carbonates as a function of time. Calcite and either calcian-witherite or calcian-strontianite were identified as the only phases present during the reaction period. XRD patterns are presented in Figure 4.7 and Figure 4.8 and all the experimental results are summarized in Table 4.2 and Table 4.3.

Rietveld refinement analysis revealed that wt% of witherite or strontianite increased with time relative to calcite, confirming that replacement reactions had occurred. Rietveld refinement confirmed that the kinetics of the replacement reactions were ion dependent, with >95 % replacement to $SrCO_3$ occurring at 21°C after 55 hours, whereas the maximum replacement by $BaCO_3$ reached only 60 wt% at 21 °C after 55 hours. Semiquantitative analysis revealed that the newly formed phases contained structural Ca.

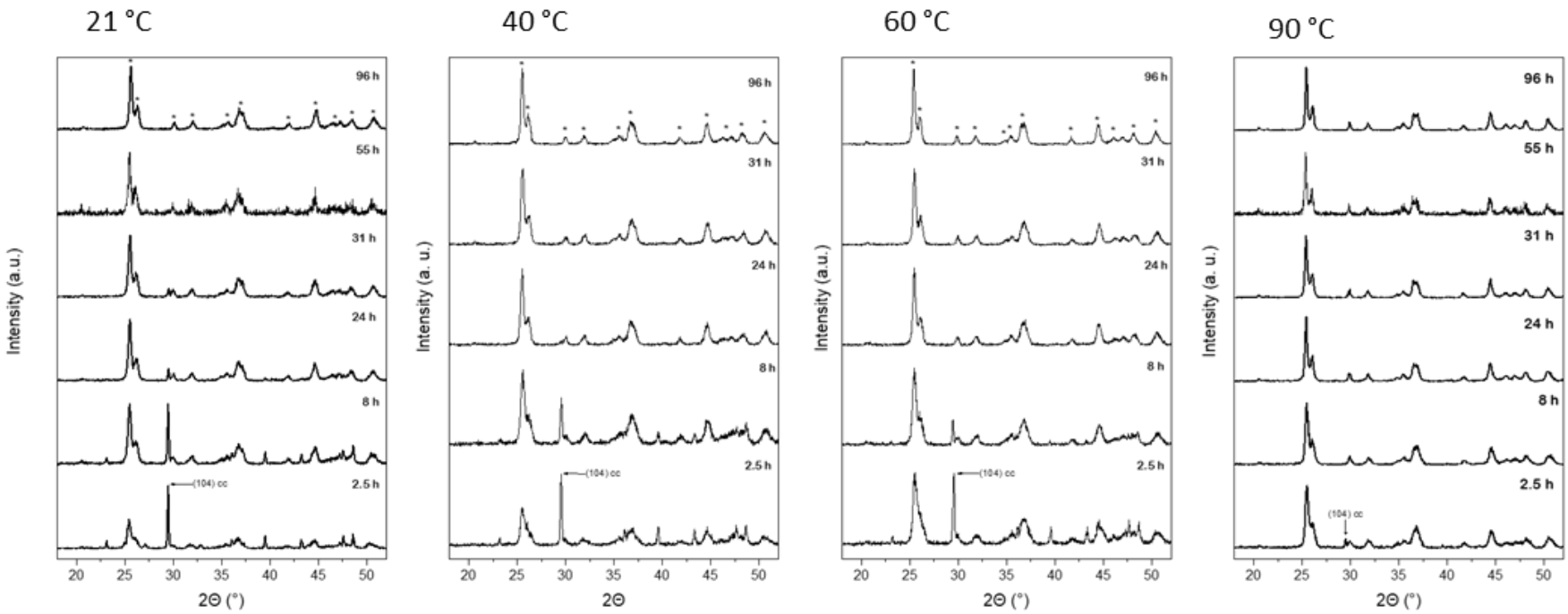

Figure 4.7: Powdered XRD patterns showing the replacement of calcite by (Ca)-strontianite carried out at 21, 40, 60 and 90 °C (left to right).

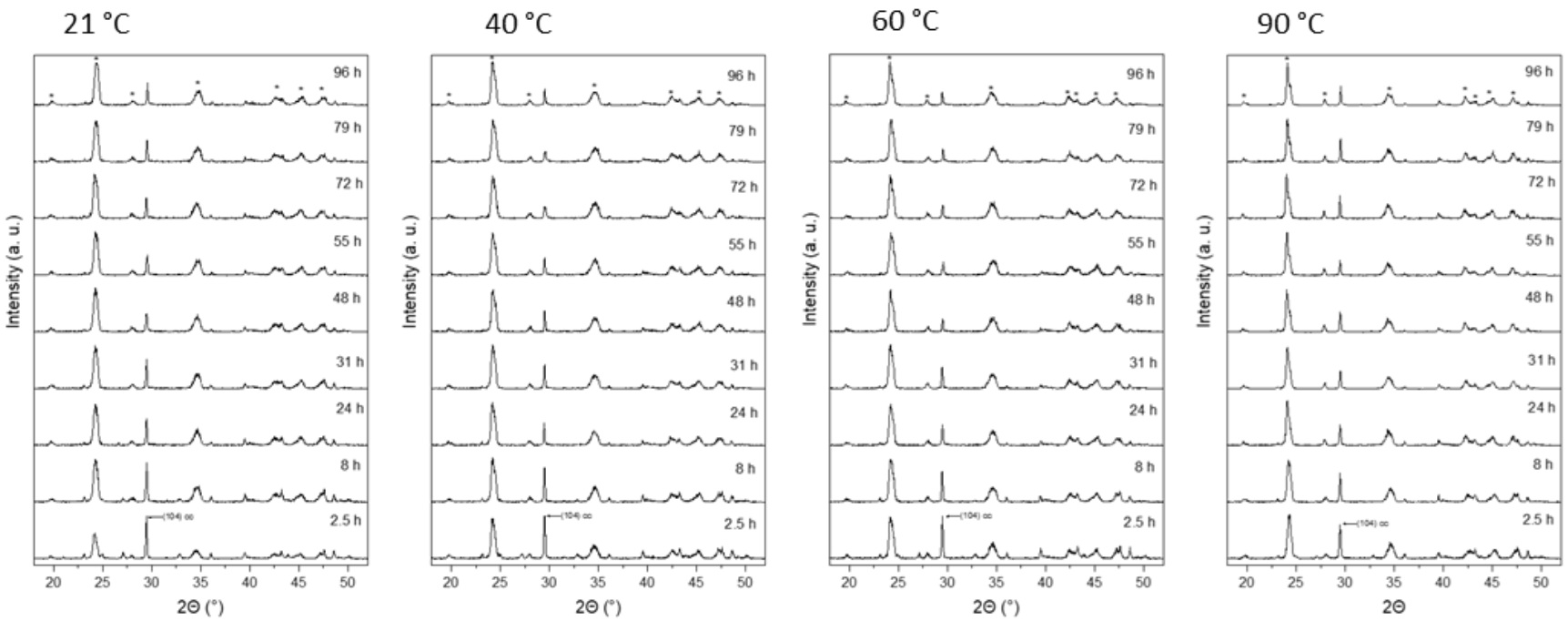

Figure 4.8: Powdered XRD patterns showing the replacement of calcite by (Ca)-witherite carried out at 21, 40, 60 and 90 °C (left to right).

	Time (hours)	% Phase consumed	Phase formed	Rate of transformation k ($x10^{-6}$ s^{-1})	Avrami constant n
21	2.5	57	(Ca)-Strontianite	8.1×10^{-5}	0.485
	8	75			
	24	95			
	31	96			
	55	99			
	96	98			
40	2.5	63	(Ca)-Strontianite	9.7×10^{-5}	0.620
	8	82			
	24	98			
	31	99			
	96	100			
60	2.5	72	(Ca)-Strontianite	2.6×10^{-4}	0.424
	8	95			
	24	98			
	31	97			
	96	100			
90	2.5	97	(Ca)-Strontianite	*	*
	8	98			
	24	100			

Table 4.2: Experimental conditions and identities of the strontianite formed during the interaction of calcite with strontium bearing aqueous solutions.

T °C	Time (hours)	% Phase consumed	Phase formed	Rate of transformation k ($x10^{-6}$ s^{-1})	Avrami constant n
21	2.5	35	(Ca)-Witherite	2.9×10^{-6}	0.217
	8	46			
	24	55			
	31	55			
	48	61			
	55	60			
	72	62			
	79	51			
	96	66			
40	2.5	57	(Ca)-Witherite	6.3×10^{-6}	0.064
	8	57			
	31	66			
	48	65			
	55	63			
	72	64			
	79	64			
	96	63			
60	2.5	48	(Ca)-Witherite	8.3×10^{-6}	0.181
	8	55			
	24	53			
	31	65			
	48	68			
	55	73			
	72	70			
	79	63			
	96	71			
90	2.5	49	(Ca)-Witherite	3.0×10^{-6}	0.093
	8	56			
	24	62			
	31	62			
	48	57			
	55	63			
	72	61			
	79	63			
	96	63			

Table 4.3: Experimental conditions and identities of the witherite formed during the interaction of calcite with barium bearing aqueous solutions

Quantitative kinetic studies

The *n* and *k* values, Table 4.2 and Table 4.3, obtained from the Avrami equation (Avrami, 1939) by plotting – *ln ln (1 – y)* against *ln t*, Figure 4.9 and Figure 4.10**,** provided insight into the reaction mechanisms, notably *k* which denotes the crystallisation rate. While the estimated *k* and *n* values provide primary information about kinetics of the crystallisation process, it is important to highlight the limitations. These data must be interpreted with caution because there are limited data points available to establish precise values for these experiments, especially for those with Sr-bearing solutions at 90 °C. Additional data points/research is needed to develop reliable data.

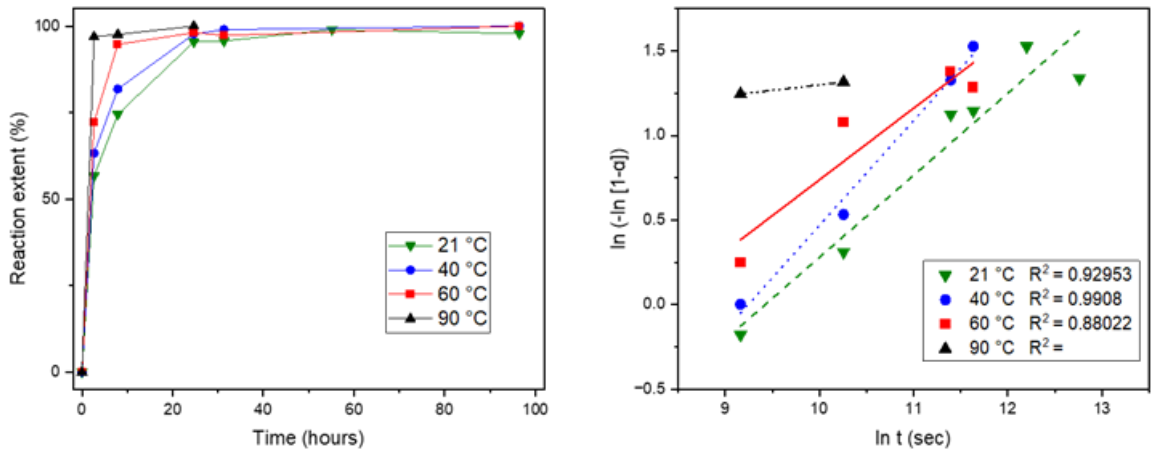

Figure 4.9: Reaction extent plotted against time (left) and the corresponding Avrami plot (right) for the replacement of calcite by strontianite experiment at 21, 40, 60 and 90 °C.

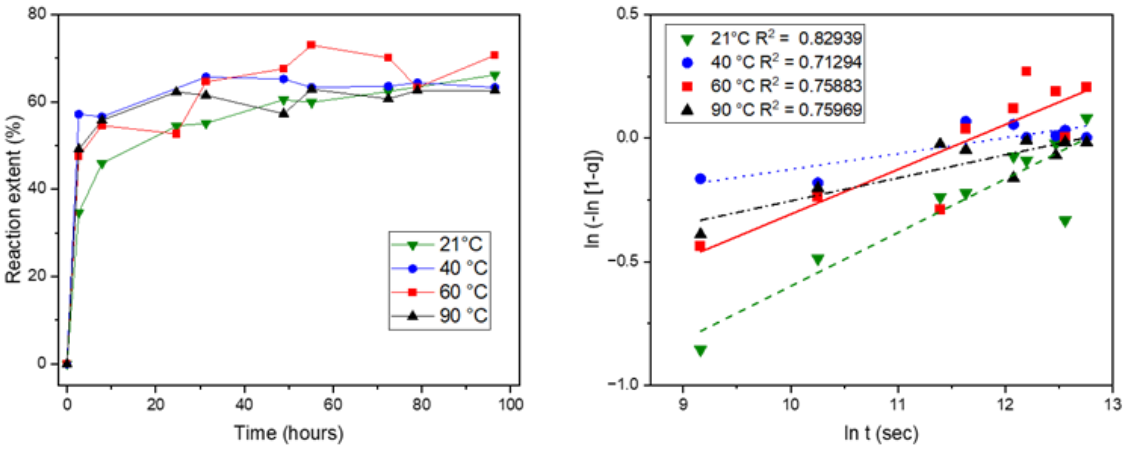

Figure 4.10: Reaction extent plotted against time (left) and the corresponding Avrami plot (right) for the replacement of calcite by witherite experiment at 21, 40, 60 and 90 °C.

Hydrogeochemical modelling from PHREEQC confirmed that during the interaction of calcite with Ba and Sr-bearing solutions, the aqueous solution became supersaturated with respect to pure witherite and strontianite, respectively (Appendix B6).

Scanning electron microscopy

The morphology of the solids revealed clear signs of calcite surface dissolution. The Ba-bearing experiments resulted in scattered crystals consisting of small blades or spindles that were protruding out from the calcite surface in the lower temperature experiments (21 and 40 °C), exhibiting a non-random orientation relative to the surface of the calcite host. At higher temperatures and after longer reaction times, bundles of twinned, bladed witherite grew, either partially or completely covering and replacing the calcite (Figure 4.11**)**. The Sr- bearing carbonates developed thin platy prisms that formed aggregates which either partially or completely replaced the calcite (Figure 4.12**)**. The original morphology and dimensions of the calcite grains were preserved, indicating pseudomorphic replacement. In most experiments the strontianite phases grew oriented to the calcite surface. After completion of the replacement reaction some of the newly formed crystals also showed random orientation relative to the calcite grain. Semi-quantitative SEM-EDS revealed the Ca^{2+} composition (Up to 6.77 atom% in witherite and up to 8.62 atom % in strontianite) of the newly formed phases.

The broadening and shift to higher 2theta values of the Bragg peaks observed in the XRD patterns indicated that incorporation of Ca^{2+} had occurred in both $SrCO_3$ and $BaCO_3$ samples.

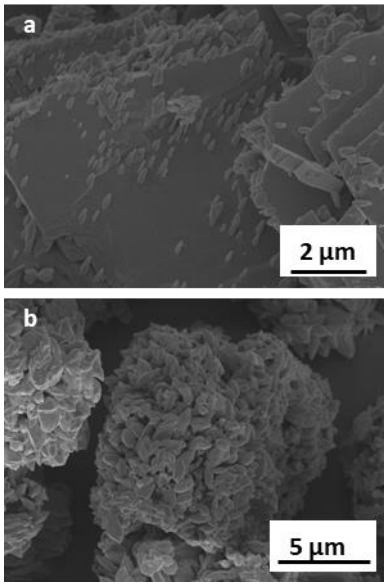

Figure 4.11: Calcite powder reacted with $BaCO_3$ bearing aqueous solutions. Very little surface precipitation at after 24 hours at 21°C (a). Witherite grew more, either partially or completely covering after 24 hours at 60 °C (b).

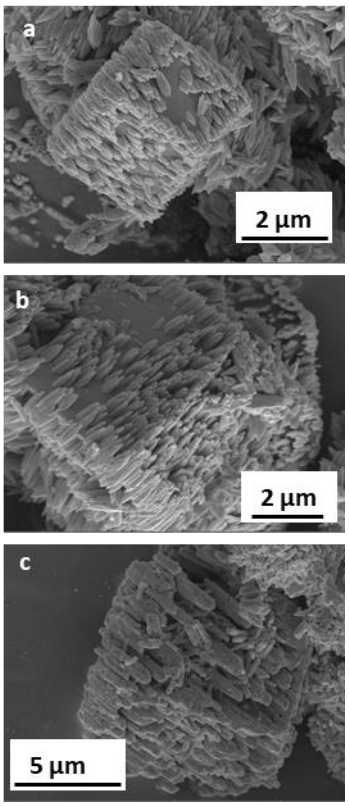

Figure 4.12: Calcite powder reacted with $SrCO_3$ bearing aqueous solutions. Surface precipitation at after 24 hours at 21°C (a), 60 °C (b) and 90 °C (c).

4.4.3 Heterogeneous crystallisation: Calcite seeds interaction with Ba- and Sr- bearing aqueous solutions.

The solid samples obtained from the interaction of calcite seeds and Ba- or Sr-bearing solutions revealed a partial replacement of the host calcite with newly formed phases. Initial observations in visible light through binocular lenses revealed a series of surface precipitates. Most notably, there were changes in the opacity and colour of the calcite seeds. Pre-reaction, the initial calcite seeds (Iceland spar variety) were colourless and transparent. After interactions with Sr- and Ba- bearing aqueous solutions, the calcite became increasingly translucent to opaque and yellow-ish, orangey-brown (Appendix B7).

SEM revealed the formation of a surface precipitate on the calcite seed experiments, forming clusters of aggregates dispersed on the calcite surface. Quickly (< 24 hours) the entire surface of the seeds was covered in surface precipitates, forming a thin crust. In the Sr-bearing experiments strontianite grew oriented relative to the calcite crystal faces, with the lower molarity experiments (5 mM) forming bundles of twinned, bladed crystals, whereas at higher molarities (50 mM) the surface of strontianite was acicular, forming aggregates that were radiating out from a central point. Although the SEM revealed secondary minerals present as surface precipitates on the calcite seeds, these surface precipitate crusts were very thin. As such characterisation and quantification of phases with XRD revealed that newly formed secondary minerals was very low ≤1 %.

4.5 DISCUSSION

Through a combination of crystallisation from solution and replacement experiments, we uncovered the crystallisation behaviour of strontianite and witherite in the presence of Ca^{2+} ions under low-hydrothermal conditions. This investigation into the behaviour of Ca^{2+} provided valuable insights into the kinetic and pathways of the process. In the turbidity experiments, homogenous nucleation occurred following the interaction of Ba^{2+} or Sr^{2+} (± Ca^{2+}) and CO_3^{2-}, resulting in the precipitation of (calcian-) witherite and (calcian-) strontianite. In the replacement experiments, the interaction of the carbonate host grain and the Ba- or Sr-bearing solution resulted in the initial dissolution of the host and the release of Ca^{2+} and CO_3^{2-} into the solutions. This resulted in allowing the CO_3^{2-} ions to interact with Ba^{2+} or Sr^{2+} ions which led to the formation of Ca-bearing witherite and strontianite precipitates on the surface of the host grain.

Our comprehension of the replacement reactions involving the transformation from calcite to aragonite-type carbonates (strontianite and witherite) requires an evaluation of the impact of Ca^{2+} on the homogeneous nucleation of $BaCO_3$ and $SrCO_3$ from solution.

4.5.1 HOMOGENEOUS NUCLEATION

Although some crystalline nanoparticles may have formed before the first increase in absorbance, we assume that the nucleation processes of $BaCO_3$ or $SrCO_3$ solids began at the onset of the absorbance process. As this absorbance behaviour was consistent for all experiments, the error in this assumption would be proportional for all experiments regardless the chemistry of the aqueous solution. Similarly, we assumed the point where the absorbance reached a maximum corresponds to the situation where equilibrium had been reached with respect to the primary crystallised $BaCO_3$ or $SrCO_3$ solid(s).

The inhibiting effect of Ca^{2+}

Plenty of research has gone into the examination of the influence of divalent (e.g., Mg^{2+}, Sr^{2+}, Ba^{2+}, Cd^{2+}, SO_4^{2-}) and trivalent (e.g., REE^{3+}, PO_4^{3-}) ions (Astilleros *et al.*, 2000; Davis *et al.*, 2000; Wasylenki *et al.*, 2005; Nehrke *et al.*, 2007; Sugiura *et al.*, 2013, 2019; Füger *et al.*, 2019) on $CaCO_3$ crystallisation mechanisms and kinetics. For example, the influence of Mg^{2+} is well documented, such as inhibiting calcite crystallisation, reduction of crystallisation rates and polymorph control of $CaCO_3$ (Nancollas and Reddy, 1971; Berner, 1975; Reddy and Nancollas, 1976; Busenberg and Niel Plummer, 1985; Zhang *et al.*, 2007; Zhu *et al.*, 2022); these effects have been explained as resulting from the dehydration of the Mg^{2+} ion. Whereas the influence of Ca^{2+} on other carbonates has not had as much attention. Berninger *et al.* (2016) found that while Ca^{2+} is incorporated into the growing $MgCO_3$ seeds, there is little to no noticeable effect on the growth rate, contrary to the inhibiting influence of Mg^{2+} on $CaCO_3$ growth.

Our results reveal that the kinetics of $BaCO_3$ and $SrCO_3$ crystallisation are inhibited by Ca^{2+} (Table 4.1). Across all the tested Ca^{2+} concentrations, the induction time (t_{ind}) increased and the rate of crystallisation (k) decreased. The resulting normalised turbidity profiles highlight the influence of the Ca^{2+} ion (Figure 4.1 and Figure 4.3). The decrease in profile slope as the increase of Ca^{2+} concentration coincided with an increase of the induction time (t_{ind}) and a decrease of the rate of

crystallisation (*k*). This change in profile can be interpreted as representing a decrease in nucleation rate (Wang *et al.*, 2012; Tobler *et al.*, 2014, 2015; Montanari *et al.*, 2017; Mulders *et al.*, 2021).

These results reveal that the degree of the inhibition is not identical between the strontianite and witherite. This becomes particularly apparent when considering variations in the induction times. The addition of 1.0 mM of Ca^{2+} (Ca/Sr or Ca/Ba = 25%) delays $SrCO_3$ induction by 23 seconds, whereas $BaCO_3$ is delayed by 6 minutes (360 seconds). Even when 4.0 mM of Ca^{2+} (Ca/Sr = 100%) is added the $SrCO_3$ the induction time is only 3 minutes. A similar influence is observed in the changes in crystallisation rate (*k*). The crystallisation rate at Ca/Sr = 25% is 0.69×10^{-2} s^{-1}, whereas at Ca/Ba = 25% *k* is 0.126×10^{-2} s^{-1}; Ca/Sr = 100% is 0.3×10^{-2} s^{-1}.

Morphology and growth mechanism

The saturation indices derived from PHREEQC (Appendix B6) suggest that in the $SrCO_3$ experiments at all examined molarities the aqueous solution is supersaturated with respect to strontianite (SI 2.96- 3.15) and calcite (SI 1.57- 2.06) immediately after mixing the solutions, however XRD revealed that minor calcite (3 %) only precipitated at Ca/Sr= 100%. The saturation indices calculated for strontianite are lower with increased amounts of Ca compared to the pure system. Calcian-strontianite formed, which was confirmed by XRD and energy dispersive spectroscopy (EDS) microanalysis of selected crystals. The content of Ca in the newly formed phases increased with Ca concentration in solution (up to atom % 16.95). In the $BaCO_3$ experiments solution is supersaturated with respect to witherite (SI 2.42- 2.48) at all examined molarities. Despite solutions being saturated with respect to calcite (SI = 1.01-1.58), at Ca/Ba >2.5%, no calcite precipitated, instead calcian-witherite formed. It is worth noting that as calcian-strontianite and calcian-witherite precipitated with varying Ca/Sr or Ca/Ba ratios, these minerals will have different solubility products compared to pure strontianite or witherite. As such our PHREEQC calculations should be viewed as approximations.

SEM images of the samples from the turbidity experiments revealed that Ca^{2+} concentration also influences the morphology of the crystals. This is particularly evident in the $BaCO_3$ experiments: At Ca/Ba = 2.5% witherite displays a branching needle morphology (Figure 4.5), as seen in other

aragonite-type carbonates (Gránásy *et al.*, 2005; Sand *et al.*, 2012b), whereby the early stages of growth happen via threadlike fibres along the c-axis, from a central "eye" structure in the core region, before splaying out into, like a bow. Similar morphologies have been observed in aragonite when doped with ethanol by Sand *et al.* (2012), they confirmed that the segments are composed of individual crystals. conclude that the were formed by spherulitic growth by classical, ion-by-ion attachment. The morphologies displayed are examples of the "category 2" spherulites described by Gránásy *et al.*, (2005). While the branching morphology of aragonite-type carbonate are not unique to a specific additive or set of conditions, we observed that with increased Ca^{2+} concentration the witherite becomes increasingly spherical during growth, and by Ca/Ba= 100% it forms fully developed spherules (Figure 4.5). We observed a decrease in the crystallite size of strontianite and witherite when crystallised in the presence of Ca, which is very consistent with spherulitic growth (Beck and Andreassen, 2010; Sand *et al.*, 2012b) . There seems to be an overall trend of negative correlation between Ca concentration and crystallite size. As most of these crystalline spherules consist of aggregates of nanocrystals, the small size of the individual units also affects their solubility, further highlighting the need to view the SI values from PHREEQC as approximations.

Spherulitic morphologies result from a nucleation-controlled growth process, and this spherulitic growth mechanism requires high supersaturation levels (SI > 2-3) (Gránásy *et al.*, 2005; Beck and Andreassen, 2010). Ripening occurs following the initial spherulitic growth, as the formation of the solid phases decreases the concentrations of Ba^{2+} or Sr^{2+} and CO_3^{2-} ions in solution.

Ca substitutions and phase relationships

The inhibiting effect of Ca^{2+} discussed here could be attributed to several factors. It could be the result of dehydration of the solvation shell, driven by the differences in ionic potential and changes in the coordination number of Ca^{2+}. Ca^{2+} is considered to have a 6-fold coordination number in water (Katz *et al.*, 1996; Baer and Mundy, 2016) and Sr^{2+} and Ba^{2+} in water have 8-fold coordination (Kerridge and Kaltsoyannis, 2011; Chaudhari *et al.*, 2015). Therefore, Ca^{2+} has a stronger hydration shell compared to Ba^{2+} and Sr^{2+}, due to higher ionic potential, i.e. the ionic

charge/ionic radii, ($^{VI}Ca^{2+}$ = 2 $Å^{-1}$; $^{IX}Sr^{2+}$= 1.69 $Å^{-1}$; $^{IX}Ba^{2+}$= 1.48 $Å^{-1}$). As a result the delayed precipitation of Ca-strontianite and Ca-witherite from solution is a consequence of the need to dehydrate $^{VI}Ca^{2+}$ from solution before incorporating into the crystalline solid. A similar effect is observed in the inhibition of $CaCO_3$ by $^{VI}Mg^{2+}$, driven by the stronger hydration shell of the $^{VI}Mg^{2+}$ ion (Berner, 1975; Davis *et al.*, 2000; Rodriguez-Blanco *et al.*, 2015; Nielsen *et al.*, 2016).. Differences in ionic potentials are driven by differences in the ionic radii between $^{VI}Ca^{2+}$, $^{IX}Sr^{2+}$ and $^{IX}Ba^{2+}$. The difference in ionic radii of $^{VI}Ca^{2+}$ and $^{IX}Sr^{2+}$ of is smaller than that of $^{VI}Ca^{2+}$ and $^{IX}Ba^{2+}$, which could explain the stronger inhibition effect seen in $BaCO_3$ even at lower molarities. Overall. these differences in the coordination number of Ca^{2+} compared to Sr^{2+}/Ba^{2+} may contribute to the inhibiting effect on $BaCO_3$ and $SrCO_3$ crystallisation. As Ca^{2+} is in coordination 6 ($^{VI}Ca^{2+}$, r = 1.00 Å) in aqueous solution (Katz *et al.*, 1996; Baer and Mundy, 2016) and Sr^{2+} and Ba^{2+} are in coordination 9 in strontianite and witherite, additionally to the dehydration process, the Ca^{2+} cation needs to increase its coordination from 6 to 9 ($^{IX}Ca^{2+}$, r= 1.18). Therefore this change in coordination will require additional energy, this being translated into prolonged reaction times.

4.5.2 REPLACEMENT REACTIONS

Following the examination of the effect of Ca^{2+} on $BaCO_3$ and $SrCO_3$, we examined the replacement reactions of calcite to strontianite and witherite. In aqueous solutions replacement results from a dissolution-precipitation reaction, which Carlson (1983b) summarised in the following steps: i) dissolution at surface of parent crystal, ii) nucleation of product crystal, iii) transport of complexes in solution and iv) precipitation at surface of product crystal. Transformation from calcite- to aragonite-type involves a change in crystal structure, from rhombohedral with 6-fold symmetry to orthorhombic with 9-fold symmetry. The combination of XRD and SEM data showed that the interaction of calcite with the Sr and Ba-bearing fluids is translated into a solution-mediated either partial or full pseudomorphic replacement of calcite by either strontianite or witherite.

Replacement reactions

Controls on replacement reactions have been reported in the literature, namely temperature, ionic radii of the replacing cation, the dissolution rate of the host mineral and the molar volumes of the new phases (Szucs *et al.*, 2021, 2022) as well as the fluid saturation state.

Saturation indices derived from PHREEQC show that when both the Ba- and Sr-bearing solutions are placed in contact with calcite at ambient temperature, they are already supersaturated for witherite (SI= 7.23) and strontianite (SI= 4.42). The saturation indices of the $BaCO_3$ and $SrCO_3$ phases are still positive even before equilibrium has been reached for calcite (e.g., $SI_{calcite} = -3$), see Appendix B6. This suggests that the formation of $BaCO_3$ and $SrCO_3$ can likely take place during the early stages of calcite dissolution. The observed replacements were centripetal (forming from the periphery inwards), resulting from a difference in solubility between the newly formed phase and the host mineral, the former being less soluble. (e.g., Szucs *et al.*, 2021).

The calcite powder experiments resulted in the full ($SrCO_3$) or partial ($BaCO_3$ up to 73% replaced) replacement of calcite after 96 hours. On the other hand, the calcite seed experiment led to the development of a surface crust of precipitates on the calcite, effectively armouring the host and halting any subsequent dissolution of the mineral. This highlights that another driving force of the replacement reaction is the size of the original host mineral. Forjanes *et al.*(2022) reported similar armouring of calcite with a thin layer of strontianite (< 40 μm thick) or witherite (~25 μm thick) that encased an unaltered calcite core, using large calcite crystals (2 × 3 × 3 mm), even after a prolonged period of time (up to 2 years). Szucs *et al.* (2022) speculated that the extent of the replacement could be a consequence of the grain size distribution of the host and therefore its surface area, having opted for small grain sizes (0.5- 1.0 mm).

The replacement reaction kinetics are strongly dependent on the pH of the solution and the dissolution rate of calcite. At ambient temperature the initial pH of the Sr- or Ba-bearing aqueous solutions are close to neutral ($BaCl_2$ pH ~ 6.96 and $SrCl_2$ pH ~ 6.95). The dissolution rate of calcite during the earliest stages of interaction with Sr or Ba solutions is approx. $10^{-10.2}$ mol cm^{-2} sec^{-1} (Chou

et al. (1989). After initial dissolution of calcite the systems evolves from pH 6.9 towards 8.1-8.2. This increase in pH would decrease the dissolution rate to approximately $10^{-10.4}$ mol cm^{-2} sec^{-1} (Chou *et al*. (1989). While the dissolution rate initially drives the replacement, the formation of the strontianite or witherite overgrowths will eventually prevent further calcite dissolution, as the calcite core becomes isolated from the solution.

At higher temperature experiments (up to 90 °C) the initial pH values slightly change ($BaCl_2$ pH ~ 6.86 and $SrCl_2$ pH ~ 6.86). While the dissolution kinetics will increase at higher temperatures (Sjöberg and Rickard, 1984; Naviaux *et al.*, 2019) calculations with PHREEQC show that the solubility of calcite is lower, which is translated into lower SI for the Sr/Ba-bearing carbonates.

Differences in the molar volumes of the host mineral and the newly forming mineral also play a crucial role in the replacement process. The molar volume of the newly forming minerals, strontianite (38.42 cm^3 mol^{-1}) and witherite (45.81 cm^3 mol^{-1}), is higher than calcite (36.90 cm^3 mol^{-1}). As a result, the replacement occurs via the formation of a compact crust overgrowth of carbonates with higher molar volumes, which progressively insulates the host from the surrounding aqueous solution. This decreases the rate of replacement, leading to a situation of partial equilibrium, wherein the host ends up completely isolated from the aqueous solution (Rodriguez-Blanco *et al*., 2008). If the molar volume of the overgrowth were lesser than that of the host, this would be translated into the generation of porosity (e.g., Etschmann *et al.*, 2014; Szucs *et al.*, 2023). It is important to note, the molar volumes of calcian-witherite and calcian-strontianite will be slightly different to the pure phases, however, existing bibliographic information on the molar volumes of the calcian types are scarce. The values will still be larger than that of calcite .

Calcite transformation to strontianite can be expressed as:

$$CaCO_3(s) + SrCl_2(aq) \rightarrow (Sr_xCa_{1-x})CO_3(s) + Cl^-(aq) + {Ca^{2+}}_x(aq)$$

Calcite transformation to witherite can be expressed as:

$$CaCO_3(s) + BaCl_2(aq) \rightarrow (Ba_xCa_{1-x})CO_3(s) + Cl^-(aq) + {Ca^{2+}}_x(aq)$$

Our results suggest that the extent and kinetics of the replacement reactions is dependent on the ionic radius, with smaller $^{IX}Sr^{2+}$ (r= 1.31) forming carbonates that replace calcite faster than $^{IX}Ba^{2+}$ (r= 1.47 Å) carbonates. Though initial replacement reactions occurred rapidly in both the Ba- and Sr-bearing solutions across all examined temperatures, the Sr-bearing solutions were particularly rapid after 2.5 hours. Temperature influenced extent of reaction with 57 wt%, 63 wt% and 72 wt% replacement by $SrCO_3$ occurring at 21, 40, and 60 °C respectively (). At 90 °C the replacement by $SrCO_3$ was nearly fully complete at 97 wt % (full replacement was observed under 24 hours).

In comparison, in the $BaCO_3$ system calcite had been replaced by up to 57% $BaCO_3$ after 2.5 hours. Temperature and time did not have the same influence on $BaCO_3$ precipitation as in the $SrCO_3$ experiments, the maximum $CaCO_3$ replaced by $BaCO_3$ was 70 wt% after 72 hours at 60 °C (Figure 4.10). Forjanes *et al.* (2022) similarly reported that regardless of Ba concentration, duration and temperature, XRD revealed the replacement of calcite by witherite resulted in less than 2.5 wt%; though they also found little influence regarding Sr-bearing solutions, with strontianite replacement accounting for > 3.5 wt%. As an analogue example, Szucs et al. (2022) found that temperature dictated the kinetics of the replacement reactions for REE-bearing carbonates: at ambient temperature (21 °C) there was a maximum of 10 wt% and 15 wt% replacement of dolomite and aragonite respectively. Under hydrothermal conditions (50 - 220 °C) full replacement reactions occurred, the replacement time decreasing with increasing temperature (from 56 days at 50 °C to 3 days at 220 °C).

Morphology and growth orientation/epitaxy

Regarding the morphology of the newly formed phases, twinning was observed in the samples, particularly in strontianite when the replacement reaction was fully complete and crystal orientation was random to the calcite grain, though this might be a result of twinning. Aragonite-type carbonates twinning occurs on the unit prism {110}, the angle $(1\bar{1}0):(110)$ is 62.5° for strontianite (Speer, 1983). Twinning was also observed by Forjanes *et al*. (2022).

SEM revealed the non-random orientation of strontianite and witherite on the calcite surface (Figure 4.11 and Figure 4.12), which is interpreted as an epitaxial overgrowth consistent with

Forjanes *et al.* (2022), who also observed surface precipitation of strontianite or witherite that was oriented relative to the calcite surface, describing the epitaxial growth as occurring parallel between $(10\bar{1}4)[010]_{\mathrm{cal}} \parallel (021)[100]_{\mathrm{str/wth}}$. The development of oriented epitactic overgrowths following the replacement of calcite by other carbonates that has been previously reported in the literature. When replacing calcite by cerussite ($PbCO_3$), Yuan *et al.* (2016) did not observe epitaxial growth on the calcite (104) surface, stating that instead cerussite formed through a dissolution-recrystallization mechanism. Kim *et al.* (2021) described the formation of a pseudomorphic shell (~ 5−10 μm thick) during the replacement of calcite and aragonite by cerussite. Szucs *et al.* (2021) reported oriented epitaxial of REE carbonates (kozoite) on the surface of calcite. While, Szucs *et al.* (2022) did not report any epitaxial overgrowth in REE carbonates following the replacement of dolomite or aragonite, they note that in the early stages of the experiments epitaxial overgrowths may have occurred prior to the full replacement, but were unable to observe this due fast kinetics of the replacement reaction. They also note that if they had they used larger calcite grains the formation of an overgrowth may have been more prominent.

The formation of an epitaxial crust ultimately prevents the further replacement of calcite, as it forms a stronger barrier between the calcite crystal and the aqueous solution, which in turn hinders the precipitation kinetics of the newly forming phases. The armouring of the calcite prevents further dissolution of the host, effectively cutting of the release of CO_3^{2-} ions into solution, thus limiting the precipitation of strontianite of witherite. Partial equilibrium between the armoured calcite and the aqueous solution develops at the later stages of the reaction as a result of the armouring. This partial equilibrium can be long lasting, as Forjanes *et al.* (2022) noted, with the crust being stable for up to 2 years.

4.6 CONCLUSIONS

This study demonstrates that the transformation of calcite-type to aragonite-type carbonates can take place at ambient to low hydrothermal conditions (21- 80 °C) via the interaction of calcite and Ba/Sr bearing aqueous solutions. The extent of the transformation from calcite to strontianite and witherite is dependent on i) the composition aqueous solution ii) grain size of the calcite iii) temperature and iv) pH of the system. Results from both the homogeneous and heterogeneous nucleation experiments highlight that the influence of aqueous Sr and Ba is not uniform.

By initially examining the influence of Ca^{2+} influence the formation of $BaCO_3$ and $SrCO_3$ we have gained a deeper understanding of the replacement reactions involving the transformation from calcite to aragonite-type carbonates. Examining the influence of Ca^{2+} has revealed that this ion has a similar (though not to the same extent) inhibiting effect on the crystallisation kinetics and mechanisms, due to its dehydration, as other alkaline earth metals, e.g., Mg^{2+}, has on $CaCO_3$. Differences in the coordination number of Ca, from coordination 6 in aqueous solution, to coordination 9 in aragonite-type carbonates further delayed crystallisation. The high supersaturation levels during the crystallisation from solution experiments are translated into the crystallisation of calcian-strontianite and calcian-witherite crystallise via spherulitic growth mechanism.

The pseudomorphic replacement of calcite to strontianite and witherite occurs via a dissolution-precipitation mechanism mediated by the aqueous solution and the formation of an oriented overgrowth, with a centripetal replacement front. The extent of replacement is dictated by grain size, with larger grains failing to be fully replaced due to the armouring of the grain with surface precipitates, isolating the unreacted calcite core and a state of partial equilibrium being reached. The speed of the replacement reaction by aragonite-type carbonate is dictated by the ionic radii and molar volume, with strontianite forming faster than witherite.

These results provide insights into the transform kinetics and mechanisms from calcite-type to aragonite-type carbonates. Hence this study has application across a range of geological applications,

including the use of Sr/Ca ratio as palaeothermometer for seawater temperature, as well as industrial (e.g., production of Sr ferrites, pyrotechnics, phosphors, ceramics…) applications.

4.7 REFERENCES

AISSAOUI, D. M. (1985) 'Botryoidal aragonite and its diagenesis', Sedimentology. John Wiley & Sons, Ltd, 32(3), pp. 345–361. doi: 10.1111/J.1365-3091.1985.TB00516.X.

Allison, J. D., Brown, D. S. and Novo-Gradac, K. J. (1991) MINTEQA2/PRODEFA2, A Geochemical Assessment Model for Environmental Systems: Version 3·0 Users' Manual. Athens, GA: Environmental Research Laboratory, Office of Research and Development U.S. Environmental Protection Agency.

Alsabah, Y. A. et al. (2017) 'Synthesis and Study of the Effect of Ba2+ Cations Substitution with Sr2+ Cations on Structural and Optical Properties of Ba2−xSrxZnWO6 Double Perovskite Oxides (x = 0.00, 0.25, 0.50, 0.75, 1.00)', Materials. Multidisciplinary Digital Publishing Institute (MDPI), 10(5). doi: 10.3390/MA10050469.

Astilleros, J. M. et al. (2000) 'The effect of barium on calcite {1014} surfaces during growth', Geochimica et Cosmochimica Acta. Pergamon, 64(17), pp. 2965–2972. doi: 10.1016/S0016-7037(00)00405-1.

Avrami, M. (1939) 'Rate of Nucleation in Condensed Systems The', Free Energy of a Nonuniform System. I. Interfacial Free Energy The Journal of Chemical Physics, 7, p. 258. doi: 10.1063/1.1750380.

Avrami, M. (1941) 'Rate of Nucleation in Condensed Systems The', Heterogeneous Nucleation The Journal of Chemical Physics, 9, p. 198. doi: 10.1063/1.1750872.

Baer, M. D. and Mundy, C. J. (2016) 'Local Aqueous Solvation Structure Around Ca2+ during Ca2+···Cl- Pair Formation', Journal of Physical Chemistry B. American Chemical Society, 120(8), pp. 1885–1893. doi: 10.1021/ACS.JPCB.5B09579/ASSET/IMAGES/LARGE/JP-2015-09579N_0003.JPEG.

Baldasari, A. and Speer, J. A. (1979) 'Witherite composition, physical properties, and genesis', American Mineralogist , 64(7–8), pp. 724–747.

Bathurst, R. G. C. (1972) Carbonate Sediments and Their Diagenesis. 2nd edn. Elsevier.

Beck, R. and Andreassen, J. P. (2010) 'Spherulitic growth of calcium carbonate', Crystal Growth and Design. American Chemical Society, 10(7), pp. 2934–2947. doi: 10.1021/CG901460G/ASSET/IMAGES/LARGE/CG-2009-01460G_0003.JPEG.

Berner, R. A. (1975) 'The role of magnesium in the crystal growth of calcite and aragonite from sea water', Geochimica et Cosmochimica Acta. Pergamon, 39(4), pp. 489–504. doi: 10.1016/0016-7037(75)90102-7.

Berninger, U. N. et al. (2016) 'On the effect of aqueous Ca on magnesite growth – Insight into trace element inhibition of carbonate mineral precipitation', Geochimica et Cosmochimica Acta. Pergamon, 178, pp. 195–209. doi: 10.1016/J.GCA.2016.01.019.

Böttcher, M. E. et al. (1997) 'Characterization of synthetic BaCO3 – SrCO3 (witherite-strontianite) solid-solutions by Fourier transform infrared spectroscopy', European Journal of Mineralogy. Schweizerbart'sche Verlagsbuchhandlung, 9(3), pp. 519–528.

Bruni, S. F. and Wenk, H. R. (1985) 'Replacement of aragonite by calcite in sediments from the San Cassiano Formation (Italy)', Journal of Sedimentary Research. GeoScienceWorld, 55(2), pp. 159–170. doi: 10.1306/212F8652-2B24-11D7-8648000102C1865D.

Busenberg, E. and Niel Plummer, L. (1985) 'Kinetic and thermodynamic factors controlling the distribution of SO32− and Na+ in calcites and selected aragonites', Geochimica et Cosmochimica Acta. Pergamon, 49(3), pp. 713–725. doi: 10.1016/0016-7037(85)90166-8.

Busenberg, E. and Plummer, L. N. (1986) 'The solubility of BaCO3(cr) (witherite) in CO2-H2O solutions between 0 and 90°C, evaluation of the association constants of BaHCO3+(aq) and BaCO30(aq) between 5 and 80°C, and a preliminary evaluation of the thermodynamic properties of Ba2+(aq)', Geochimica et Cosmochimica Acta. Pergamon, 50(10), pp. 2225–2233. doi: 10.1016/0016-7037(86)90077-3.

Busenberg, E., Plummer, L. N. and Parker, V. B. (1984) 'The solubility of strontianite (SrCO3) in CO2-H2O solutions between 2 and 91°C, the association constants of SrHCO+3(aq) and SrCO03(aq) between 5 and 80°C, and an evaluation of the thermodynamic properties of Sr2+(aq) and SrCO3(cr) at 25°C and 1 atm total pressure', Geochimica et Cosmochimica Acta. Pergamon, 48(10), pp. 2021–2035. doi: 10.1016/0016-7037(84)90383-1.

Carlson, W. D. (1983) 'The POLYMORPHS of CaCO3 and the ARAGONITE - CALCITE TRANSFORMATION ', in Reeder, R. J. (ed.) Carbonates. De Gruyter, pp. 191–226. doi: 10.1515/9781501508134-010/HTML.

Chaudhari, M. I., Soniat, M. and Rempe, S. B. (2015) 'Octa-Coordination and the Aqueous Ba2+ Ion', Journal of Physical Chemistry B. American Chemical Society, 119(28), pp. 8746–8753. doi: 10.1021/ACS.JPCB.5B03050/ASSET/IMAGES/MEDIUM/JP-2015-030507_0007.GIF.

Chou, L., Garrels, R. M. and Wollast, R. (1989) 'Comparative study of the kinetics and mechanisms of dissolution of carbonate minerals', Chemical Geology. Elsevier, 78(3–4), pp. 269–282. doi: 10.1016/0009-2541(89)90063-6.

Chuliá-Jordán, R. et al. (2021) 'Crystal Structure of BaCa(CO3)2 Alstonite Carbonate and Its Phase Stability upon Compression', ACS Earth and Space Chemistry. American Chemical Society, 5(5), pp. 1130–1139. doi: 10.1021/ACSEARTHSPACECHEM.1C00032/SUPPL_FILE/SP1C00032_SI_001.PDF.

Coelho, A. A. et al. (2011) 'The TOPAS symbolic computation system', Powder Diffraction. Cambridge University Press, 26(S1), pp. S22–S25. doi: 10.1154/1.3661087.

Colby, M. Y. and LaCoste, L. J. . B. (1933) 'The Crystal Structure of Cerussite', Zeitschrift für Kristallographie - Crystalline Materials. De Gruyter (O), 84(1–6), pp. 299–309. doi: 10.1524/ZKRI.1933.84.1.299.

Dana, E. S. (1932) Dana's Textbook of Mineralogy . 4th edn. Edited by W. . Ford. New York: John Wiley and Sons.

Davis, K. J., Dove, P. M. and De Yoreo, J. J. (2000) 'The role of Mg2+ as an impurity in calcite growth', Science. American Association for the Advancement of Science, 290(5494), pp. 1134–1137. doi: 10.1126/SCIENCE.290.5494.1134/ASSET/89670F6A-D97B-4EC0-A9C0-F2D4E39F1798/ASSETS/GRAPHIC/SE4308963004.JPEG.

Van Driessche, A. E. S. et al. (2012) The Role and Implications of Bassanite as a Stable Precursor Phase to Gypsum Precipitation Downloaded from.

Erdemoğlu, M. and Canbazoğlu, M. (1998) 'The leaching of SrS with water and the precipitation of SrCO3 from leach solution by different carbonating agents', Hydrometallurgy. Elsevier, 49(1–2), pp. 135–150. doi: 10.1016/S0304-386X(98)00018-8.

Etschmann, B. et al. (2014) 'Grain boundaries as microreactors during reactive fluid flow: Experimental dolomitization of a calcite marble', Contributions to Mineralogy and Petrology. Springer Verlag, 168(2), pp. 1–12. doi: 10.1007/S00410-014-1045-Z/FIGURES/8.

Folk, R. L. (1964) 'Recrystallisation of ancient limestones', AAPG Bulletin. GeoScienceWorld, 48(4), pp. 525–526. doi: 10.1306/BC743C61-16BE-11D7-8645000102C1865D.

Forjanes, P. et al. (2022) 'Formation of Strontianite and Witherite Cohesive Layers on Calcite Surfaces for Building Stone Conservation', Crystal Growth & Design. American Chemical Society (ACS), 22, p. 6428. doi: 10.1021/ACS.CGD.2C00383/ASSET/IMAGES/MEDIUM/CG2C00383_M001.GIF.

Füger, A. et al. (2019) 'Effect of growth rate and pH on lithium incorporation in calcite', Geochimica et Cosmochimica Acta. Pergamon, 248, pp. 14–24. doi: 10.1016/J.GCA.2018.12.040.

Garcia-Guinea, J. et al. (2009) 'Luminescence of Strontianite (SrCO3) from Strontian (Scotland, UK)', Radiation Measurements. Pergamon, 44(4), pp. 338–343. doi: 10.1016/J.RADMEAS.2009.03.018.

Gránásy, L. et al. (2005) 'Growth and form of spherulites', Physical Review E - Statistical, Nonlinear, and Soft Matter Physics. American Physical Society, 72(1), p. 011605. doi: 10.1103/PHYSREVE.72.011605/FIGURES/11/MEDIUM.

Helz, G. R. and Holland, H. D. (1965) 'The solubility and geologic occurrence of strontianite', Geochimica et Cosmochimica Acta, 29(12), pp. 1303–1315. doi: 10.1016/0016-7037(65)90008-6.

Holl, C. M. et al. (2000) 'Compression of witherite to 8 GPa and the crystal structure of BaCO3II', Physics and Chemistry of Minerals 2000 27:7. Springer, 27(7), pp. 467–473. doi: 10.1007/S002690000087.

Holland, H. D. et al. (1963) 'The coprecipitation of Sr+2 with aragonite and of Ca+2 with strontianite between 90° and 100°C', Geochimica et Cosmochimica Acta. Pergamon, 27(9), pp. 957–977. doi: 10.1016/0016-7037(63)90105-4.

Jarosch, D. and Heger, G. (1988) 'Neutron diffraction investigation of strontianite, SrCO3', Bulletin de Minéralogie. Persée - Portail des revues scientifiques en SHS, 111(2), pp. 139–142. doi: 10.3406/BULMI.1988.8078.

Katz, A. K. et al. (1996) 'Calcium ion coordination: A comparison with that of beryllium, magnesium, and zinc', Journal of the American Chemical Society. American Chemical Society , 118(24), pp. 5752–5763. doi: 10.1021/JA953943I/SUPPL_FILE/JA5752A.PDF.

Kerridge, A. and Kaltsoyannis, N. (2011) 'The coordination of Sr2+ by hydroxide: a density functional theoretical study', Dalton Transactions. The Royal Society of Chemistry, 40(42), pp. 11258–11266. doi: 10.1039/C1DT10883B.

Kim, Y. et al. (2021) 'Replacement of Calcium Carbonate Polymorphs by Cerussite', ACS Earth and Space Chemistry. American Chemical Society. doi: 10.1021/ACSEARTHSPACECHEM.1C00177/ASSET/IMAGES/LARGE/SP1C00177_0006.JPEG.

Klinkenberg, M. et al. (2018) 'The solid solution–aqueous solution system (Sr,Ba,Ra)SO4 + H2O: A combined experimental and theoretical study of phase equilibria at Sr-rich compositions', Chemical Geology. Elsevier, 497, pp. 1–17. doi: 10.1016/J.CHEMGEO.2018.08.009.

Kotelnikov, A. R. et al. (2000) 'Experimental study of celestite-barite solid solution', Geochemistry International, 38(12), pp. 1286–1293.

Lander, J. J. (1949) 'Polymorphism and Anion Rotational Disorder in the Alkaline Earth Carbonates', The Journal of Chemical Physics. American Institute of PhysicsAIP, 17(10), p. 892. doi: 10.1063/1.1747083.

Lin, C. C. and Liu, L. G. (1997) 'High pressure phase transformations in aragonite-type carbonates', Physics and Chemistry of Minerals 1997 24:2. Springer, 24(2), pp. 149–157. doi: 10.1007/S002690050028.

Lindner, M. et al. (2017) 'On the effect of aqueous barium on magnesite growth – A new route for the precipitation of the ordered anhydrous Mg-bearing double carbonate norsethite', Chemical Geology. Elsevier, 460, pp. 93–105. doi: 10.1016/J.CHEMGEO.2017.04.019.

Lindner, M. et al. (2019) 'On the effect of aqueous strontium on magnesite growth', Chemical Geology. Elsevier, 510, pp. 1–9. doi: 10.1016/j.chemgeo.2019.02.002.

Mavromatis, V. et al. (2016) 'Barium isotope fractionation during witherite (BaCO3) dissolution, precipitation and at equilibrium', Geochimica et Cosmochimica Acta. Pergamon, 190, pp. 72–84. doi: 10.1016/J.GCA.2016.06.024.

Mayer, I., Levy, E. and Glasner, A. (1964) 'The crystal structure of EuSO4 and EuCO3', Acta Crystallographica. International Union of Crystallography, 17(8), pp. 1071–1072. doi: 10.1107/S0365110X64002699.

Montanari, G. et al. (2017) 'Impact of citrate ions on the nucleation and growth of anhydrous CaCO3', Crystal Growth and Design. American Chemical Society, 17(10), pp. 5269–5275. doi: 10.1021/acs.cgd.7b00796.

Morse, J. W. and Mackenzie, F. T. (1990) Geochemistry of sedimentary carbonates / John W. Morse, Fred T. Mackenzie., Geochemistry of sedimentary carbonates. Elsevier; Developments in Sedimentology, 48. doi: 10.1016/0016-7037(93)90401-h.

Mulders, J. J. P. A., Tobler, D. J. and Oelkers, E. H. (2021) 'Siderite nucleation pathways as a function of aqueous solution saturation state at 25 °C', Chemical Geology. Elsevier, 559, p. 119947. doi: 10.1016/J.CHEMGEO.2020.119947.

Nancollas, G. H. and Reddy, M. M. (1971) 'The crystallization of calcium carbonate. II. Calcite growth mechanism', Journal of Colloid and Interface Science. Academic Press, 37(4), pp. 824–830. doi: 10.1016/0021-9797(71)90363-8.

Naviaux, J. D. et al. (2019) 'Temperature dependence of calcite dissolution kinetics in seawater', Geochimica et Cosmochimica Acta. Pergamon, 246, pp. 363–384. doi: 10.1016/J.GCA.2018.11.037.

Nehrke, G. et al. (2007) 'Dependence of calcite growth rate and Sr partitioning on solution stoichiometry: Non-Kossel crystal growth', Geochimica et Cosmochimica Acta. Pergamon, 71(9), pp. 2240–2249. doi: 10.1016/J.GCA.2007.02.002.

Nielsen, M. R. et al. (2016) 'Inhibition of Calcite Growth: Combined Effects of Mg2+ and SO42-', Crystal Growth and Design. American Chemical Society, 16(11), pp. 6199–6207. doi: 10.1021/acs.cgd.6b00536.

Parkhurst, D. L. and Appelo, C. A. J. (1999) 'User's guide to PHREEQC (Version 2): A computer program for speciation, batch-reaction, one-dimensional transport, and inverse geochemical calculations', Water-Resources Investigations Report. doi: 10.3133/WRI994259.

Pederson, C. L. et al. (2020) 'Variation in the diagenetic response of aragonite archives to hydrothermal alteration', Sedimentary Geology. Elsevier, 406, p. 105716. doi: 10.1016/J.SEDGEO.2020.105716.

Pi, D. H. et al. (2014) 'Depositional environments for stratiform witherite deposits in the Lower Cambrian black shale sequence of the Yangtze Platform, southern Qinling region, SW China:

Evidence from redox-sensitive trace element geochemistry', Palaeogeography, Palaeoclimatology, Palaeoecology. Elsevier, 398, pp. 125–131. doi: 10.1016/J.PALAEO.2013.09.029.

Prieto, M. et al. (1997) 'Nucleation, growth, and zoning phenomena in crystallizing (Ba,Sr)CO3, Ba(SO4,CrO4), (Ba,Sr)SO4, and (Cd,Ca)CO3 solid solutions from aqueous solutions', Geochimica et Cosmochimica Acta. Pergamon, 61(16), pp. 3383–3397. doi: 10.1016/S0016-7037(97)00160-9.

Putnis, A. (1992) Introduction to mineral sciences. 1st edn. Cambridge University Press.

Reddy, M. M. and Nancollas, G. H. (1976) 'The crystallization of calcium carbonate: IV. The effect of magnesium, strontium and sulfate ions', Journal of Crystal Growth. North-Holland, 35(1), pp. 33–38. doi: 10.1016/0022-0248(76)90240-2.

Reeder, R. J. (1983) 'Chapter 1. CRYSTAL CHEMISTRY of the RHOMBOHEDRAL CARBONATES', in Carbonates: Mineralogy and Chemistry. 11th edn. Reviews in Mineralogy, Mineralogical Society of America, Chantilly, Virginia, pp. 1–48. doi: 10.1515/9781501508134-005.

Rodriguez-Blanco, J. D., Sand, K. K. and Benning, L. G. (2017) 'ACC and Vaterite as Intermediates in the Solution-Based Crystallization of CaCO3', in New Perspectives on Mineral Nucleation and Growth. doi: 10.1007/978-3-319-45669-0_5.

Rodriguez-Blanco, J. D., Shaw, S. and Benning, L. G. (2008) 'How to make "stable" ACC: protocol and preliminary structural characterization', Mineralogical Magazine. doi: 10.1180/minmag.2008.072.1.283.

Rodriguez-Blanco, J. D., Shaw, S. and Benning, L. G. (2015) 'A route for the direct crystallization of dolomite', American Mineralogist. Walter de Gruyter GmbH, 100(5–6), pp. 1172–1181. doi: 10.2138/am-2015-4963.

Sánchez-Pastor, N. et al. (2011) 'Raman Study of Synthetic Witherite–Strontianite Solid Solutions', https://doi.org/10.1080/00387010.2011.610409. Taylor & Francis Group , 44(7–8), pp. 500–504. doi: 10.1080/00387010.2011.610409.

Sand, K. K. et al. (2012a) 'Aragonite growth in water-alcohol mixtures: Classical or nonclassical crystallization?', Materials Research Society Symposium Proceedings, 1419, pp. 7–13. doi: 10.1557/opl.2012.885.

Sand, K. K. et al. (2012b) 'Crystallization of CaCO 3 in water-Alcohol mixtures: Spherulitic growth, polymorph stabilization, and morphology change', Crystal Growth and Design, 12(2), pp. 842–853. doi: 10.1021/cg2012342.

Shannon, R. D. and IUCr (1976) 'Revised effective ionic radii and systematic studies of interatomic distances in halides and chalcogenides', urn:issn:0567-7394. International Union of Crystallography, 32(5), pp. 751–767. doi: 10.1107/S0567739476001551.

Sjöberg, E. L. and Rickard, D. T. (1984) 'Temperature dependence of calcite dissolution kinetics between 1 and 62°C at pH 2.7 to 8.4 in aqueous solutions', Geochimica et Cosmochimica Acta. Pergamon, 48(3), pp. 485–493. doi: 10.1016/0016-7037(84)90276-X.

Spahr, D. et al. (2019) 'A new BaCa(Co3)2 polymorph', Acta Crystallographica Section B: Structural Science, Crystal Engineering and Materials. International Union of Crystallography, 75(3), pp. 291–300. doi: 10.1107/S2052520619003238/RA5050ISUP2.RTV.

Speer, J. A. (1976) 'Pennsylvania Minerals: II. Strontianite', The Mineralogical Record, 7(2), pp. 69–71.

Speer, J. A. (1983) 'Chapter 5. CRYSTAL CHEMISTRY and PHASE RELATIONS of ORTHORHOMBIC CARBONATES', in De Gruyter (ed.) Carbonates. De Gruyter, pp. 145–190. doi: 10.1515/9781501508134-009.

Sugiura, Y. et al. (2013) 'Acceleration and inhibition effects of phosphate on phase transformation of amorphous calcium carbonate into vaterite', American Mineralogist. Walter de Gruyter GmbH, 98(1), pp. 262–270. doi: 10.2138/AM.2013.4212/MACHINEREADABLECITATION/RIS.

Sugiura, Y. et al. (2019) 'PO4 adsorption on the calcite surface modulates calcite formation and crystal size', American Mineralogist. De Gruyter Open Ltd, 104(10), pp. 1381–1388. doi: 10.2138/AM-2019-7015/MACHINEREADABLECITATION/RIS.

Szucs, A. M. et al. (2021) 'Reaction Pathways toward the Formation of Bastnäsite: Replacement of Calcite by Rare Earth Carbonates', Crystal Growth and Design. American Chemical Society, 21, pp. 512–527. doi: 10.1021/acs.cgd.0c01313.

Szucs, A. M. et al. (2023) 'The role of nanocerianite (CeO2) in the stability of Ce carbonates at low-hydrothermal conditions', RSC Advances. The Royal Society of Chemistry, 13(10), pp. 6919–6935. doi: 10.1039/D3RA00519D.

Szucs, Adrienn Maria et al. (2022) 'Targeted Crystallization of Rare Earth Carbonate Polymorphs at Hydrothermal Conditions via Mineral Replacement Reactions', Global Challenges. John Wiley & Sons, Ltd, p. 2200085. doi: 10.1002/GCH2.202200085.

Tobler, D. J. et al. (2014) 'The Effect of Aspartic Acid and Glycine on Amorphous Calcium Carbonate (ACC) Structure, Stability and Crystallization', Procedia Earth and Planetary Science. Elsevier BV, 10, pp. 143–148. doi: 10.1016/j.proeps.2014.08.047.

Tobler, D. J. et al. (2015) 'Citrate effects on amorphous calcium carbonate (ACC) structure, stability, and crystallization', Advanced Functional Materials. Wiley-VCH Verlag, 25(20), pp. 3081–3090. doi: 10.1002/adfm.201500400.

Turekian, K. K. (1964) 'The marine geochemistry of strontium', Geochimica et Cosmochimica Acta. Pergamon, 28(9), pp. 1479–1496. doi: 10.1016/0016-7037(64)90163-2.

Vallina, B. et al. (2015) 'The role of amorphous precursors in the crystallization of La and Nd carbonates', Nanoscale. Royal Society of Chemistry, 7(28), pp. 12166–12179. doi: 10.1039/c5nr01497b.

De Villiers, J. P. R. (1971) 'Crystal Structures of Aragonite, Strontianite, and Witherite | American Mineralogist | GeoScienceWorld', American Mineralogist, 56(5–6), pp. 758–767.

Wang, Y. W. et al. (2012) 'In Situ Study of the Precipitation and Crystallization of Amorphous Calcium Carbonate (ACC)', Crystal Growth and Design. American Chemical Society, 12(3), pp. 1212–1217. doi: 10.1021/CG201204S.

Wasylenki, L. E. et al. (2005) 'Nanoscale effects of strontium on calcite growth: An in situ AFM study in the absence of vital effects', Geochimica et Cosmochimica Acta. Pergamon, 69(12), pp. 3017–3027. doi: 10.1016/J.GCA.2004.12.019.

Weber, J. et al. (2018) 'Unraveling the Effects of Strontium Incorporation on Barite Growth - In Situ and Ex Situ Observations Using Multiscale Chemical Imaging', Crystal Growth and Design. American Chemical Society, 18(9), pp. 5521–5533. doi: 10.1021/ACS.CGD.8B00839/SUPPL_FILE/CG8B00839_SI_003.AVI.

Xia, F. et al. (2009) 'Mechanism and kinetics of pseudomorphic mineral replacement reactions: A case study of the replacement of pentlandite by violarite', Geochimica et Cosmochimica Acta. Pergamon, 73(7), pp. 1945–1969. doi: 10.1016/J.GCA.2009.01.007.

Yuan, K. et al. (2016) 'Replacement of calcite (CaCO3) by Cerussite (PbCO3)', Environmental Science and Technology. American Chemical Society, 50(23), pp. 12984–12991. doi: 10.1021/ACS.EST.6B03911/ASSET/IMAGES/LARGE/ES-2016-03911T_0007.JPEG.

Zachariasen, W. H. (1928) ' Untersuchungen über die Kristallstruktur von Sesquioxyden und Verbindungen ABO3', in Skrifter utgitt av det Norske Videnskaps-Akademi i Oslo. 1st edn, pp. 1–165.

Zhang, P., Tweheyo, M. T. and Austad, T. (2007) 'Wettability alteration and improved oil recovery by spontaneous imbibition of seawater into chalk: Impact of the potential determining ions Ca2+, Mg2+, and SO42−', Colloids and Surfaces A: Physicochemical and Engineering Aspects. Elsevier, 301(1–3), pp. 199–208. doi: 10.1016/J.COLSURFA.2006.12.058.

Zhu, Y. et al. (2022) ‘Process-Specific Effects of Sulfate on CaCO3Formation in Environmentally Relevant Systems’, Environmental Science and Technology. American Chemical Society, 56(12), pp. 9063–9074. doi: 10.1021/ACS.EST.1C08898/ASSET/IMAGES/LARGE/ES1C08898_0006.JPEG.

Chapter 5.

New insights into the textural and chemical evolution during natural carbonation processes at Sverrefjellet volcano, Svalbard

Authors: Niamh Faulkner, Juan Diego Rodríguez-Blanco, Adrienn Szucs, Elliot Carter, Melanie Maddin and Luca Terribili

Publication Status: Unpublished

Author Contributions: N. Faulkner conducted data analysis, wrote the manuscript and produced all figures and tables. Samples were collected by J.D Rodríguez-Blanco during the Arctic Mars Analogue Svalbard Expedition (AMASE) in 2009. J.D Rodríguez-Blanco prepared samples, collected optical microscopy data, conducted XRD and SEM, SEM-CL analyses, advised and edited the manuscript. E. Carter advised and edited the manuscript. A. Szucs, M. Maddin and L. Terribili carried out data reduction.

New insights into the textural and chemical evolution during natural carbonation processes at Sverrefjellet volcano, Svalbard

5.1 ABSTRACT

This study investigates the influence of host rock geochemistry and the evolution of carbonate cements during the carbonation of basaltic rocks from the Sverrefjellet volcano in Svalbard. The correlation of petrography, XRD results, SEM, cathodoluminescence and, major elemental compositional data provides insight into the mechanisms behind carbonation sequence. In this way, a better understanding of sample composition, influence of the basaltic host rock, sample history and environmental conditions during the carbonation processes can be inferred.

The carbonate cements are composed of calcite-type carbonates falling within the magnesite-calcite-siderite compositional range. Distinct stages of carbonation are observed in the cements, coinciding with a crystal chemistry evolution from calcian proto-dolomite to Ca-poor magnesite and ultimately to a mixture of Fe-rich carbonates (siderite) and non-carbonate cements.

The results highlight the profound influence of the host rock's geochemistry on the composition and progression of carbonate cements. As the carbonation process progresses away from the basalt host rock, shifts in the cation composition within the carbonate minerals are observed, showing an evolution in the Ca/Mg ratio toward magnesite. Notably, the dissolution of Mg-rich phases, such as forsterite and enstatite, leads to Mg becoming the dominant cation in the forming carbonates. The carbonation conditions at Sverrefjellet provide a natural analogue for anthropogenic CCS via mineralisation like the CarbFix project, Iceland, which primarily yields calcite as the main carbonate phase. In contrast, Sverrefjellet displays a predominance of magnesite-rich carbonates. This is indicative of higher-temperature conditions, that allow for magnesium dehydration from solution prior to its incorporation into growing crystals. These findings contribute valuable insights to the field of

CCS and enhance our understanding of carbonate mineralization processes in geological environments.

5.2 INTRODUCTION

The archipelago of Svalbard lies between 74° and 81° N, and 10° and 35° E. It comprises several islands, of which the largest is Spitsbergen, followed by Nordaustlandet and Edgeøya. The archipelago has enticed numerous geologists due to the availability of rocks spanning from the Palaeoproterozoic to the Neogene, in a near complete succession. Currently ~60 % of the land area of Svalbard is covered by glaciers (Elvevold *et* al., 2007). Harland (1997) provides an extensive account of the geology of Svalbard. The basement ranges from Precambrian to Silurian in age, and has undergone periods of deformation and metamorphism, including during the Caledonian orogeny. According to Elvevold *et al*. (2007) the island of Spitsbergen was named in 1596 by Willem Barents, due to the sharp jagged peaks of the basement rocks.

In north-western Spitsbergen there are three Quaternary volcanic centres in the Bockfjorden area, Sverrefjellet, Sigurdfjell and Halvdanpiggen. The area has some of the largest and richest sources of xenoliths in the world, with abundant examples from both the upper mantle and lower continental crust (Amundsen *et al.*, 1987), hosted in alkali basalts. The basalts are also associated with several types of carbonates. Mantle derived carbonate inclusions occur in xenoliths as Mg-Fe-rich carbonate globules (Amundsen, 1987; Steele *et al.*, 2007) and granular dolomitic carbonates (Ionov *et al.*, 1993; Ionov *et al*., 2002). Secondary carbonates cements associated with the eruption, both syn- and post-eruptive, are found coating volcanic pipes or conduits and cementing brecciated basalt (Amundsen *et al.*, 2011; Blake *et al.*, 2011).

During the subglacial eruptions of Sverrefjellet, the degassing of primitive alkali basalts would have yielded substantial quantities of carbon dioxide (CO_2) alongside glacial meltwater. This dynamic subglacial system of the interaction of CO_2-rich fluids and brecciated host rocks facilitated the mineral carbonation.

Mineral carbonation occurs following the interaction of rocks, particularly mafic or ultramafic rocks, and CO_2 bearing fluids (Olajire, 2013). When CO_2 is dissolved in water it can expressed by the chemical reactions:

$$CO_2(g) + H_2O \leftrightarrow H_2CO_3 \leftrightarrow HCO_3^- + H^+ \leftrightarrow CO_3^{2-} + 2H^+ \quad \textbf{(Equation 1)}$$

The interaction of carbonic acid (H_2CO_3), and rocks results in the increased solubility of minerals in the host rock (Xu *et al.*, 2004). Due to this acidification process, ions from the primary silicate phases are released to the aqueous solution as the silicate minerals within host rock starts to dissolve, causing the concentration of ionic species in solution to increase. The interaction of these species with the carbonate ions can result in the formation of secondary carbonate phases (Xu *et al.*, 2004; IPCC, 2005; Benson and Cole, 2008) for example:

$$HCO_3^- + Ca^{2+} = CaCO_3\,(s) + H^+ \quad \textbf{(Equation 2)}$$

$$HCO_3^- + Mg^{2+} = MgCO_3\,(s) + H^+ \quad \textbf{(Equation 3)}$$

The dissolution of common silicate minerals in basalt and peridotite, such as pyroxene (**Equation 4**) or olivine, forsterite, (**Equation 5**) releases cations which are then available to interact with carbonate ions and precipitate secondary carbonate minerals:

$$2H^+ + H_2O + (Ca, Mg, Fe)SiO_3 \leftrightarrow Ca^{2+}, Mg^{2+}, Fe^{2+} + H_4SiO_4 \quad \textbf{(Equation 4)}$$

$$Mg_2SiO_4 + 2CO_2 \rightarrow 2MgCO_3 + SiO_2 \quad \textbf{(Equation 5)}$$

The extent to which carbonation occurs is based on the release of cations into aqueous solutions, which is dependent on the element, pH and temperature (Snæbjörnsdóttir *et al.*, 2020). When dissolved, calcium reacts with carbonate to form calcite and/or aragonite ($CaCO_3$), with precipitation occurring below ~300 °C (Ellis, 1959, 1963). Above ~65 °C dissolved magnesium reacts with carbonate to form magnesite ($MgCO_3$) and dolomite ($CaMg(CO_3)_2$) (Saldi *et al.*, 2009; Gadikota *et al.*, 2014; Johnson *et al.*, 2014). Hydrous Mg-carbonate minerals, such as hydromagnesite ($Mg_5(CO_3)_4(OH)_2{\cdot}4H_2O$), nesquehonite ($MgCO_3{\cdot}3H_2O$) and dypingite ($Mg_5(CO_3)_4(OH)_2{\cdot}5H_2O$) form at lower temperatures, where the formation of magnesite and dolomite is kinetically inhibited (Turvey

et al., 2018). The formation of iron bearing carbonates can be limited depending on the oxidation state. Fe^{2+} often oxidises before it can form siderite ($FeCO_3$), as such there are no known Fe^{3+} carbonates in nature, when Fe^{2+} oxidises it forms Fe oxides and Fe oxyhydroxides instead (Rogers *et al.*, 2006). However, when the pH is low enough to prevent the oxidaion of Fe^{2+} to Fe^{3+} and at ambient to moderate tempaeratures, ankerite ($CaFe(CO_3)_2$) can form (Gysi and Stefánsson, 2012; McGrail *et al.*, 2017).

Carbonate cements have a variety of forms, textures and habits (Dana, 1932; Bathurst, 1972). Carbonate cements can range from blocky spar, to radiaxial fans to acicular needles to finely laminated (Folk, 1964, 1965; Flügel, 2010). Several generations of growth with different textures can be observed within a cement, following transitions of crystal forms and changes in carbonate chemistry. These multigenerational cements offer a fascinating window into the geochemical conditions of carbonate formation, even in cements that are millimetres thick. Textures within carbonate cements can provide insights into the crystal growth, for example, oscillatory zoning results from changes in fluid composition (Reeder, 1991).

Natural carbonation of mafic and ultramafic rocks has been observed in a range of geological settings including basalt-hosted petroleum reservoirs in Western Greenland (Rogers *et al.*, 2006) and the mantle section of the Oman Ophiolite (Kelemen *et al.*, 2011). Flood basalts have been proposed as significant potential repositories for carbon capture and storage (CCS) as an alternative to the conventional sedimentary reservoirs due to several advantages: Their abundance on the Earth's surface, basalts make up ~10% of the continental crust (Schaef et al., 2010; Gislason and Oelkers, 2014); They are highly reactive to CO_2-containing fluids (Rosenbauer et al., 2012; Gislason and Oelkers, 2014); They contain amble amounts of divalent metal cations (roughly 25 wt % calcium, magnesium and iron oxides) to form carbonate minerals (Schaef et al., 2010; Gislason and Oelkers, 2014; Gislason et al., 2014).

The natural carbonation of mafic rocks, as seen at Sverrefjellet, provides a natural analogue for carbon capture and storage via mineralisation projects such as CarbFix, Iceland (Snæbjörnsdóttir *et al.*, 2020). According to Archer (2005) and Snæbjörnsdóttir *et al.* (2014, 2017) offshore basaltic CCS

in the mid-ocean ridges theoretically has the potential to store all the CO_2 from burning of all fossil fuel on Earth (~5000 Gt C).

There has been relatively little previous work on the mineral carbonation and carbonate chemistry of the Sverrefjellet carbonate cements. What little there has been has focused on carbonates as analogues for carbonates on the Martian surface (Amundsen *et al.*, 2011; Blake *et al.*, 2011; Morris *et al.*, 2011). Work to date has predominantly focused on the carbonates found within xenoliths from the Bockfjord Volcanic Complex (BVC) on Spitsbergen, as they provide a terrestrial analogue to the geochemistry of Martian carbonates, such as the carbonate globules found in meteorite ALH84001 (Golden *et al.*, 2000; Treiman *et al.*, 2002; Steele *et al.*, 2007 etc.), as well as localities on Mars including the Comanche outcrops in the Columbia Hills of the Gusev crater (Morris *et al.*, 2010, 2011) and the in the Nili Fossae region (Ehlmann *et al.*, 2008). As such, the Spitsbergen carbonates have been analysed using a range of techniques, such as visible and near-infrared spectra (VNIR) (Morris *et al.*, 2011)**,** electron microprobe (Blake *et al.*, 2011) and oxygen and carbon isotope analysis (Amundsen *et al.*, 2011), in order to provide insight into the origin and formation of the Martian carbonates.

In this study, we present a petrological and geochemical investigation of carbonate-cemented basalts, in order to critically evaluate the evolution and mechanisms of the *in situ* carbonation of alkali basalts as an analogy for basaltic carbon capture and storage. The Sverrefjellet carbonated basalts offer an ideal natural laboratory for this study. We aim to aim to shed some light on the following questions i) How did the carbonate mineralisation evolve? ii) How does the geochemistry of the host basalt influenced the resulting carbonates? iii) What insights can we gather about the formation conditions of the carbonates based on the morphology of the carbonate cement? For this purpose, we have characterised carbonate-bearing basalt samples of Quaternary age from Sverrefjellet (Spitsbergen, Svalbard) using, optical microscopy, high-resolution electron microscopy, including energy dispersive spectroscopy and cathodoluminescence and powder X-ray diffraction. The objective of this research is to characterise the complex geochemistry and mineralogy of the Sverrefjellet

carbonates and infer the mechanisms of formation of the carbonates, as well as the aqueous chemistry and environmental conditions that promoted its formation.

5.3 GEOLOGICAL SETTING

Svalbard is situated on the north-western corner of the Eurasian plate, and represents the subaerial portion of the Barent shelf (Worsley, 2008; Dörr *et al.,* 2019). The lithosphere beneath Svalbard is thinned, ~50 km thick (Vågnes and Amundsen, 1993; Griffin *et al.*, 2012). The geology of Svalbard was heavily influenced by the Caledonian orogeny (400- 500 Ma), having been part of the Laurentian continental margin during the collision with Baltica (Gee and Teben'kov, 2004; Gee *et al.,*, 2006; Griffin *et al.*, 2012). Svalbard's current topography is the result of several periods of uplift and erosion, Karsil'ščikov (1996) proposed eight erosional surfaces, ranging from the pre-Carboniferous to the Holocene. Vågnes and Amundsen (1993) report that the uplift in Svalbard is elongated along the continental margin, resulting from the Cenozoic epeirogenic uplift along the margin of the North Atlantic.

The Bockfjord region (north-western Spitsbergen) is defined by the Breibogen-Bockfjorden Fault (BBF), which bisects the landscape, juxtaposing Proterozoic to Palaeozoic aged basement of the Hekla Hoek formation to the west of the fault and Devonian Old Red Sandstones to the east of the fault. BBF trace denotes the western boundary of the major Devonian graben (Griffin *et al.*, 2012).

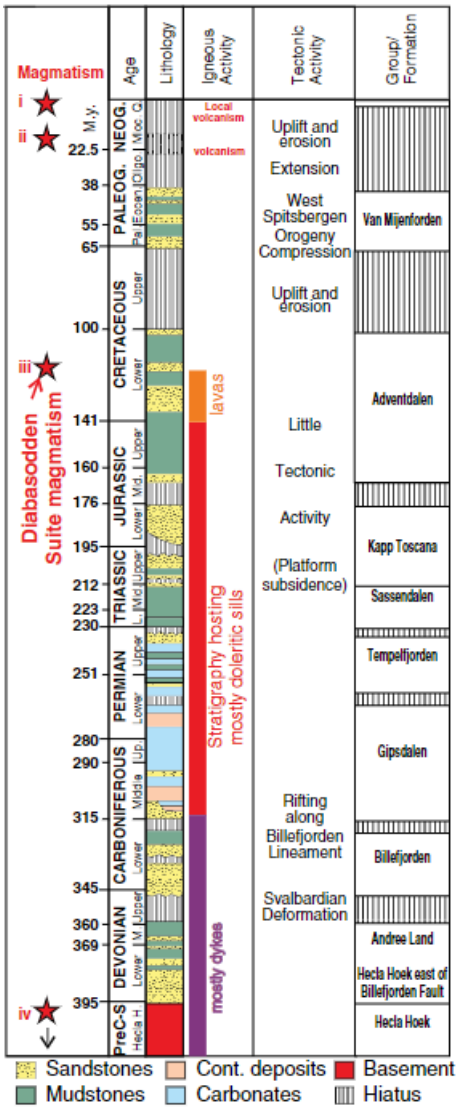

Figure 5.1: Stratigraphic column of Svalbard from Senger et al. (2014), after Nøttvedt et al. (1993). Red stars (★) denote main magmatic events, including i) Quaternary Bockfjorden Volcanic Complex (BVC) ii) plateau basalt lavas of the Seidfjellet Formation, (iii) the Diabasodden Suite and (iv) Caledonian and older events. The intrusive rocks consist predominantly of dikes and sills.

5.3.1 Volcanic activity

Svalbard has experienced several periods of igneous activity throughout its geological record, both intrusive and extrusive, from the Palaeo- Proterozoic through to the Holocene (Figure 5.1). These can be broadly spilt into four main episodes, as described by Prestvik (1977) and Senger *et al.* (2014):

Pre-Mesozoic; Late Mesozoic basaltic intrusive and lavas (Diabasodden Suite dolerites); Cenozoic plateau lavas (Seidfjellet Formation) and the Quaternary Bockfjord Volcanic Complex (BVC). The latter show extensive carbonation reactions which are examined in detail in this paper.

Evidence of Precambrian volcanics on Svalbard include the Palaeo- Proterozoic meta-volcanics, dates to ca. 2500 Ma (Harland and Butterfield, 1997) and extensive granite intrusions, dated to ca. 1700 Ma (Ohta *et al.*, 1996), as well as Ediacaran aged volcanics in western Spitsbergen (Harland *et al.*, 1993). Palaeozoic activity includes acidic plutons and magmatism in Ny-Frieslandian (north-eastern Spitsbergen). Gayer *et al.*, (1966) summarised the radiometric ages, suggesting prolonged silicic magmatism from ca. 420- 340 Ma. This includes the Chydenius granite, linked to the late stages of the Ny-Frieslandian orogeny. There is a shift to basic magmatism in the mid-Carboniferous, with lamprophyre dykes (Gayer *et al.*, 1966). Late Mesozoic basaltic intrusive and lavas, known collectively Diabasodden Suite dolerites, (Dallmann *et al.*, 1999) are geochemically distinctive from other magmatic provinces in Svalbard. They are geochemically similar to the Mesozoic High Artic Large Igneous Province, as discussed by Senger *et al.* (2014), who suggest a common source. The Seidfjellet Formation consists of plateau basalts, covering an area of at least 4000 km^2 , and is up to 275 m thick in places (Hoel and Holtedahl, 1911; Hoel, 1914; Burov and Zagruzina, 1976; Senger *et al.*, 2014) and unconformably overlies Devonian sediments. The formation consists of enriched olivine tholeiites and olivine basalts, which likely originated in the upper mantle at depths of ~ 40- 50 km, whilst the plagioclase phenocrysts crystallised in a mid-crustal chamber <15 km (Tuchschmid and Spillmann, 1992; Harland, 1997; Sushchevskaya *et al.*, 2009).

5.3.2 Quaternary (/Late Cenozoic) Volcanism

The Bockfjord Volcanic Complex (BVC) in north-western Spitsbergen consists of three Quaternary volcanic centres: Sverrefjellet; Sigurdfjell and Halvdanpiggen. The BVC lies on the NNW- SSE trending Breibogen-Bockfjorden Fault zone in the Bockfjorden- Woodfjorden area of north-western Spitsbergen (Figure 5.2 and Figure 5.3), current motion along the fault system is extensional. The

BVC represents off-axis eruptions of the Knipovich mid-ocean ridge (Crane *et al.*, 2001; Sushchevskaya *et al.*, 2008). The fault separates the basement Hekla Hoek formation (gneisses, amphiboles, schists and marbles) to the west and the Devonian aged sediments to the east (Griffin *et al.*, 2012). Hot springs along the trace of the fault were initially noted by Hoel and Holtedahl (1911). The following description of the volcanic centres are based on Skjelkvåle *et al.* (1989) and Harland (1997).

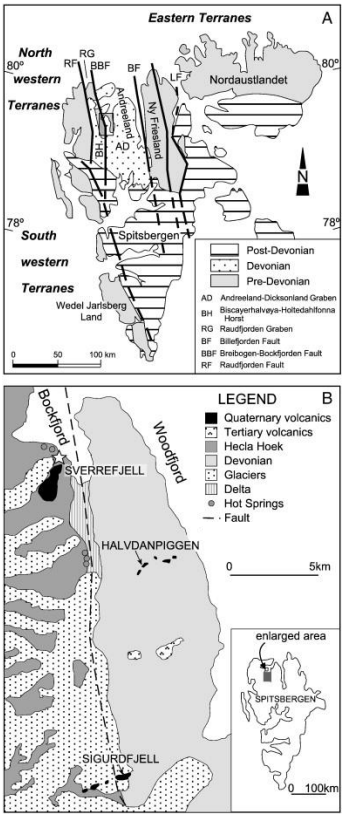

Figure 5.2: Geology of Svalbard, from Griffin et al. (2012). (A) Terrane divisions of Svalbard, showing basic geology after Gee et al. (2006). (B) Close up of the geology of the Breibogen-Bockfjorden Fault zone, with locations of the volcanic centres. The BBF trace denotes the west boundary of the major Devonian graben.

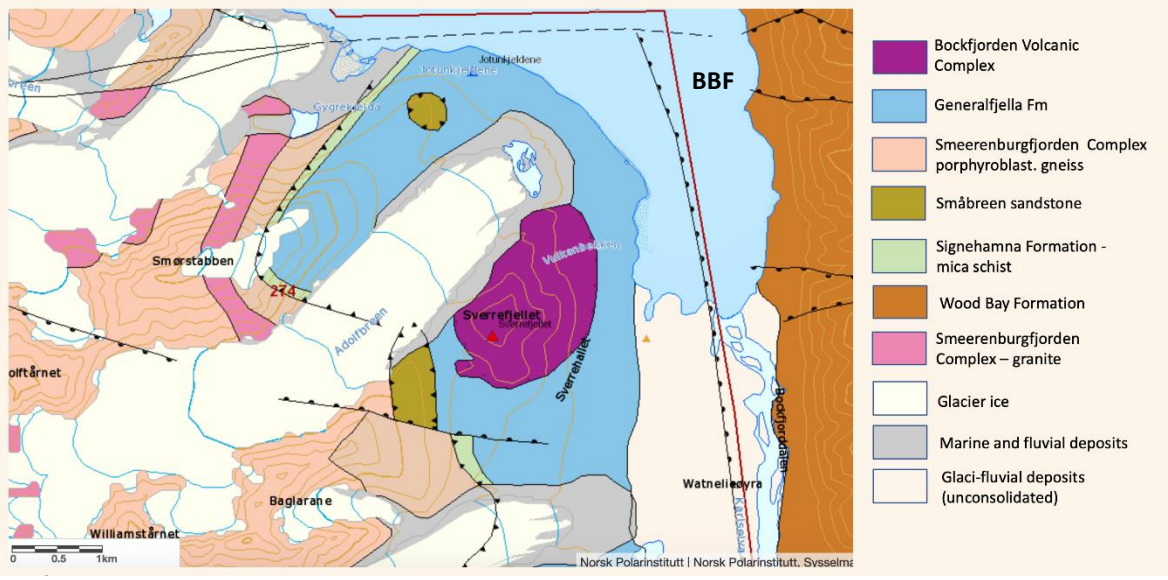

Figure 5.3: Geological map of Bockfjorden area. BBF Breibogen-Bockfjorden Fault. (After Norsk Polarinsitutt).

Sverrefjellet

Sverrefjellet is an eroded stratovolcano, 3 km wide and 506 m high, 79.4318 °N, 13.3058 °E (Treiman, 2012). Skjelkvåle *et al.* (1989) estimated about one-third of the volcanoes' original volume has been removed. There are several marine terraces on the eastern flank of the volcano, consisting of reworked volcanic material, ranging from 5 to 60 m above sea level. The volcano consists of roughly 20 vol.% lava flows, the remaining ~80 vol.% consists of frost weathered fragmented material. It is unusual for a stratovolcano as large as Sverrefjellet to develop from primitive alkali basaltic eruptions, which typically are volumetrically small isolated events (Skjelkvåle *et al.*, 1989).

There are two main lava flow types: Pahoehoe type flows (up to 2 m thick) and pillowed flows (up to 5 m thick). The pillowed flows occur in repetitive sequences, with up to 15 cycles, creating large wall-like edifices, separated by stratified ashfall materials (2-3 cm). Sub-horizontal lava tubes are also present on the eastern flanks. The wall like nature of the pillow flows has been interpreted as arising from sub-aqueous eruption, adjacent/in close proximity to a glacier wall, suggesting that the

volcano developed with the rise of neighbouring glaciers (Skjelkvåle *et al.*, 1989). All the lavas contain large volumes of xenoliths, described below. Published ages of the eruption of Sverrefjellet range from 6000 years to ca. 1 million years, Treiman (2012) dated the eruption as 1.05 ± 0.07 (1σ) My using the Ar-Ar method.

Sigurdfjellet and Halvdanpiggen

Sigurdfjellet is a 4.5 km long ridge, 200-250 m wide, 20 km south of Sverrefjellet, along the same fault line. It is made up of breccias, lapillistone, tuffs, agglomerates and rare flows and resulted from a fissure type eruption. Similar to Sverrefjellet, there are mantle xenoliths, which are entrained in bombs, up to 8 cm across.

Halvdanpiggen lies in between Sverrefjellet and Sigurdfjellet and is 5 km east of the Breibogen Fault. It has been extensively eroded, significantly more so than Sverrefjellet. It's main feature is a 250 m high volcanic neck, containing pyroclastic breccia and basaltic blocks. The pyroclastic breccias are rich (60-70 % by volume) in high pressure xenoliths, which are up to 30 cm across. There are adjacent basaltic volcanic centres near Halvdanpiggen, Olavstårnet and Haraldknattane. Evdokimov *et al.* (1991) reported K-Ar ages for Sigurdfjellet and Halvdanpiggen volcanic centres as ca. 2 and 2.7 My respectively.

5.3.3 Xenoliths

The volcanic complex of Sverrefjell is famous due to its abundance of xenoliths, said to be one of the richest such deposits on Earth, with xenoliths accounting for ~15-20 vol.% of the complex, in certain zones this is as high as 40-60 vol.% **(Figure 4)** (Amundsen, 1987; Skjelkvåle *et al.*, 1989; Ionov *et al.*, 1993, 1996). Conservative estimates by Skjelkvåle *et al.* (1989) accounted for the amount of mantle derived fragments at Sverrefjell as about 0.15- 0.2 km^3.

Amundsen (1987) discussed the xenoliths' petrology and geochemistry, noting the variety of origins including both upper mantle and lower crustal lithologies. Cr-diopside spinel lherzolites represent fragments of upper mantle. Thermobarometry of mantle xenoliths indicate a thin (27km) continental crust and a high geothermal gradient (9 kbar/ 950 °C- 17 kbar/ 1150 °C) (Amundsen *et al.*, 1987). Nikitina *et al.* (2022) reported the high-alumina pyroxenites, spinel and spinel–garnet clinopyroxenites, spinel–garnet websterites, and websterites. The xenoliths' petrology and geochemistry have been well reported in the literature e.g. (Amundsen, 1987; Treiman *et al.*, 2002; Steele *et al.*, 2007).

The other volcanic centres in the BVC are also abundant in xenoliths, which are mineralogically different than the Sverrefjell xenoliths (Skjelkvåle *et al.*, 1989). At Sigurdfjell the upper mantle xenoliths are composed of volatile rich Cr-diopside with interstitial amphibole and garnet pyroxenite. The lower crustal xenoliths are similar to those at Sverrefjell; however, the upper crustal xenoliths consist of Devonian Old Red Sandstone. The Halvdanpiggen xenolith assemblage is similar to Sigurdfjell, though crustal xenoliths are sparse.

5.4 METHODS

5.4.1 SAMPLE COLLECTION

The sample was collected from the Bockfjord Volcanic Complex (BVC), at the Sverrefjell volcanic centre (Figure 5.4), in north-western Spitsbergen, Svalbard, by Dr. Rodriguez-Blanco, during the NASA/ESA Arctic Mars Analogue Svalbard Expedition (AMASE) in 2009, led by Dr. Andrew Steele. The samples were chosen to encompass the range of carbonate cement styles and host rock lithologies. These lithologies included vesicular basalt, mantel derived olivine rich xenoliths and zones of intense carbonate encrusting.

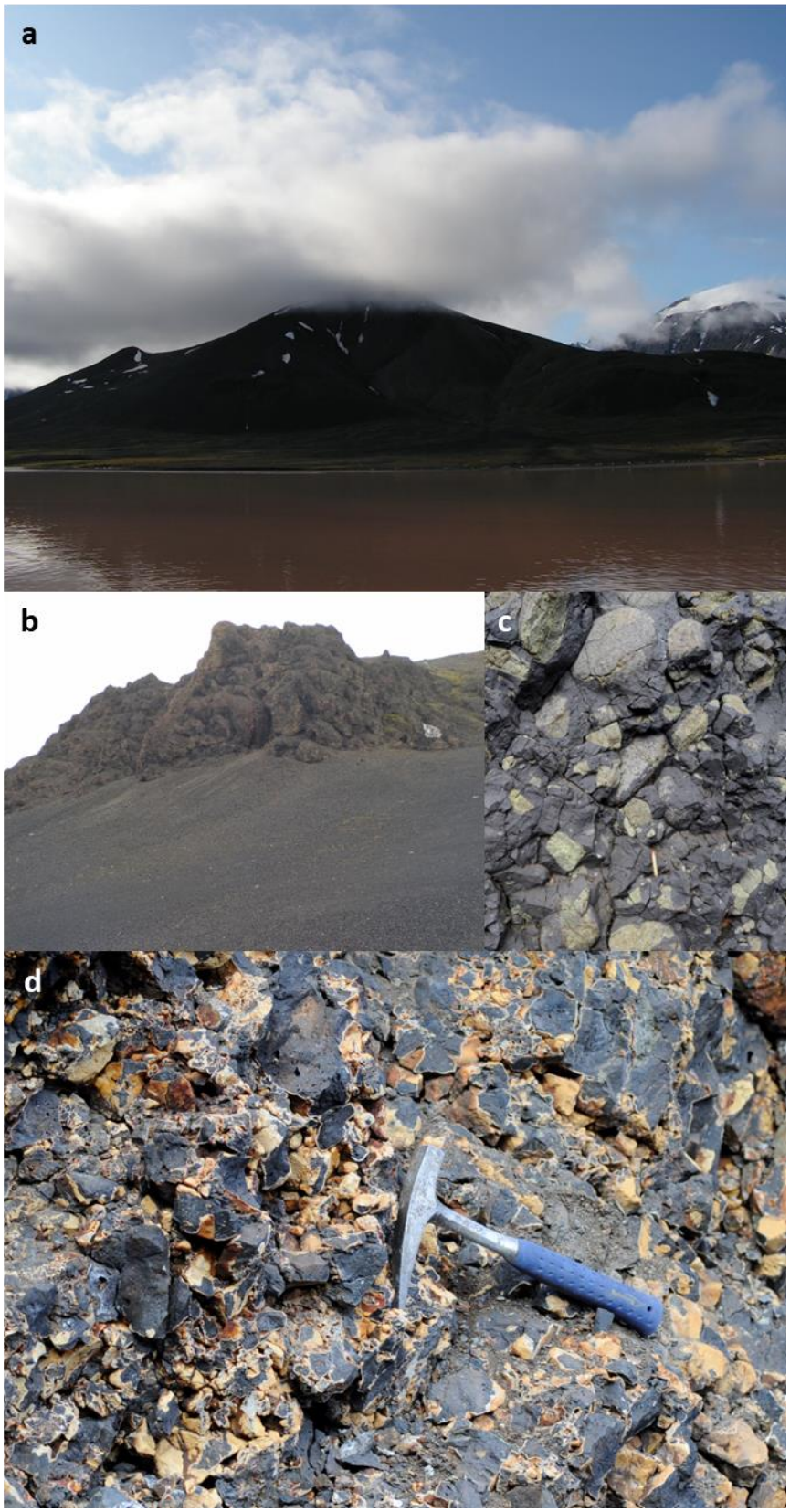

Figure 5.4: Field photos from sampling during the 2009 AMASE trip. a) Sverrefjellet volcano b) c) Sverrefjellet is famous for the abundance of xenoliths (casing for scale ~ 7 cm). d) Brecciated basalt

with extensive carbonate cementation, area where samples here samples where taken from (hammer for scale 34 cm).

5.4.2 ANALYSIS

Samples were prepared for bulk analysis, powder X-ray diffraction (XRD), as well four polished thin sections, set in epoxy resin (dimensions *20 x 40 mm*, thickness *100* μm) were prepared for petrographic analysis and characterisation using optical microscopy, scanning electron microscopy (SEM), including energy dispersive spectroscopy (EDS) and cathodoluminescence (CL). These techniques were used to determine the mineralogical and elemental compositions of the samples and to ascertain any chemical textures within the carbonate cements. All analyses were carried out in the iCRAG Lab and the Unit 7 (Geochemistry Lab) at Trinity Technology and Enterprise Centre at Trinity College Dublin.

Firstly, the thin sections were examined under binocular microscope to obtain composite images of the rocks, as well as examining petrological features and textures within the carbonate cements. Next the thin sections were examined using transmitted light microscopy, under both in plane-polarised light (PPL) and under crossed polars (XP).

5.4.2.1 XRD

Samples from both the carbonate rims/cements and the basalt host rock were prepared for powder XRD to determine i) the carbonate phases present in the cements and ii) the average bulk mineral composition of the basaltic host rock. A total of 16 powders were carefully obtained using a precision micro drill in selected areas of the rocks prepared for XRD, covering the diversity of the Svalbard basalt hosted carbonates, encompassing carbonate cements, basalt and xenoliths. Powders (~0.050 g) were mounted on zero-background silicon single crystal mounts.

The samples were analysed with a Bruker D5000 powder X-ray diffractometer with a Cu tube (λ=1.5406A). The samples were scanned from a 2θ range 5-70 ° at 0.15°/step. The patterns produced

were compared to the standardised Powder Diffraction File (PDF-4) database of the International Centre for Diffraction Data (ICDD, 2018). Rietveld refinement was carried out using TOPAS software (Coelho *et al.*, 2011) to quantify the crystalline phases.

In the carbonate samples, the Mg content was calculated using the equation after Arvidson and Mackenzie (1999):

$$X_{(MgCO_3)} = -3.6393 d_{(10\bar{1}4)} + 11.0405 \quad \textbf{(Equation 6)}$$

Where $X_{(MgCO3)}$ represents the mole percent $MgCO_3$ in the calcite $d_{(10\bar{1}4)}$ represents the d-spacing of the $\{10\bar{1}4\}$ Bragg peak.

5.4.2.2 SEM

Scanning electron microscopy (SEM) combined with energy dispersive X-ray spectroscopy (EDS) and cathodoluminescence (CL) were used to obtain high-resolution images of the whole sample, as well as individual crystals and aggregates. The thin sections were carbon-coated and were examined at micro- and near nanometre resolution using a Tescan Mira4 Field Emission Scanning Electron Microscope fitted with a backscattered electron (BSE) detector and two X-Max 170 mm^2 Oxford Instruments EDS detectors. The SEM was operated at 20 keV accelerating voltage and with a beam current of 300 pA. Qualitative major elemental composition of the sample was obtained by carrying out spot spectra and line spectra analyses and mapping of element distribution. Data evaluation was carried out with AZtecTimed (Oxford Instruments), using AutoPhaseMap to display the spatial distribution and composition of each phase.

5.4.3 GEOCHEMICAL MODELLING

Reaction calculations of basalt host minerals (Forsterite, Enstatite and Anorthite) with CO_2 and carbonate mineral saturation states calculations were performed using PHREEQC (Parkhurst and

Appelo, 1999, 2013) . The CarbFix PHREEQC database (Voigt *et al.*, 2018) was used in the calculations.

5.5 RESULTS

5.5.1 PETROGRAPHY

In hand sample the carbonate cement coating measures approximately 1 millimetre thick or less (maximum of 1.5 mm). Within the cement, there are noticeable, extremely thin opaque bands of varying colours, each measuring just a few micrometres in thickness. These bands exhibit a changing pattern as one moves outward from the basaltic contact. Starting at the innermost region near the basalt contact, the carbonate is rust coloured, followed by a white cement and a beige-tan zone, with the outermost surface a deep tan-orange colour. The surface of the cement has a slightly undulated morphology and follows the topography of the brecciated basalt. The host basalt is vesicular with large xenoliths of granular lherzolite.

Prior to SEM analysis, the optical petrography of the samples was mainly studied using binocular lens microscopy. Figure 5.5 presents a composite image of a thin section. Under binocular lens, the contact of the basalt and the carbonate occurs on a rim (µm thick) of altered basaltic glass. The carbonate cement exhibits a variety of textures as one moves outward from the basalt contact (Figure 5.6). Beginning with an initial opaque orange-brown mottled texture near the basalt contact, it transitions into a translucent grey-white banded or laminated texture. Further outward, it transforms into translucent white fan-like radial cements. Finally, at the outermost rim, the cement is thin, measuring just a few micrometers in thickness and appearing as a rusty dark orange-brown colour. Remarkably, in certain areas, the cements grow directly from the xenolith surface, which consists of large (µm-mm sized) olivine and pyroxene crystals. Inspection under reflected light microscopy revealed similar results. Examining the fan-like radial cement under cross polarisers, it appears to be made up of individual blades that are optical optically continuous. This gives the appearance of the fan going through undulous extinction when the microscope stage is rotated (Appendix C1).

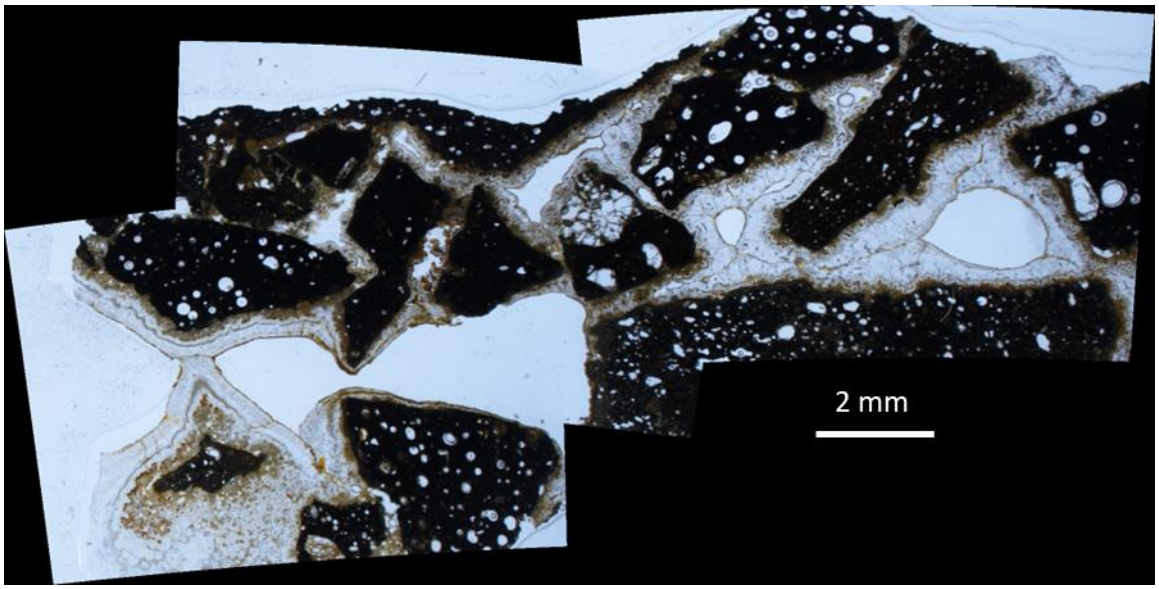

Figure 5.5: Composite optical microscopy image of the brecciated basalt with carbonate cement (binocular lens microscope).

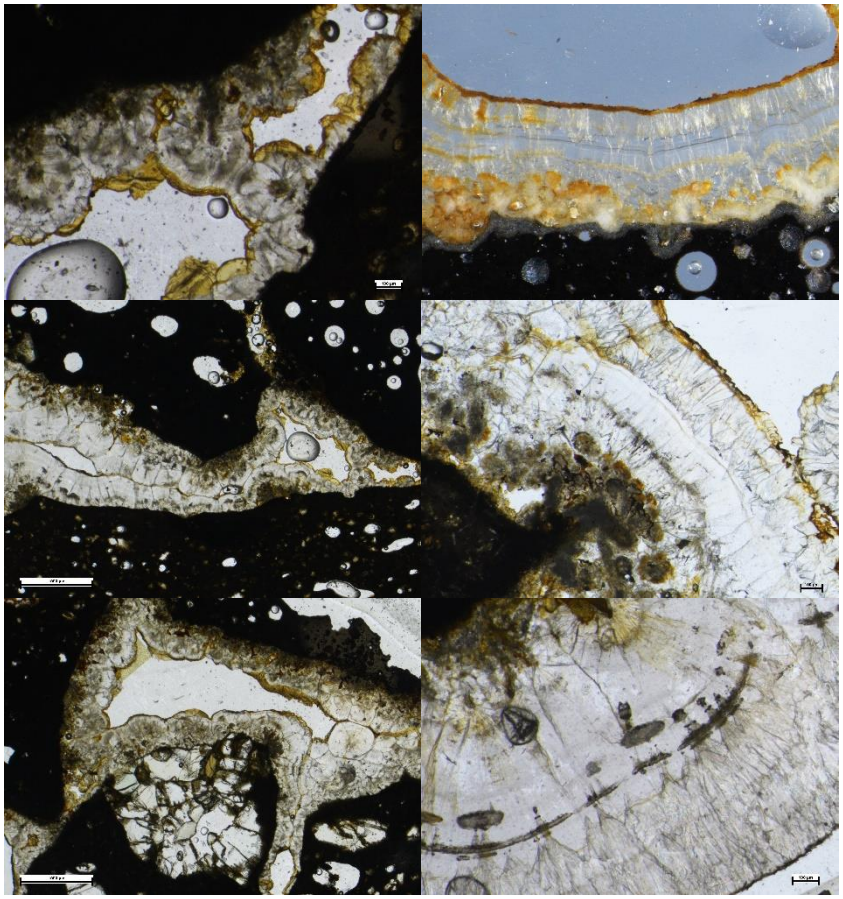

Figure 5.6: Optical microscopy images (binocular lens microscope) showing the variety of carbonate cements from the Sverrefjell volcanic centre samples. Multiple types of carbonate cement on (a -d) basalt (black) with altered rim (grey) with multiple types of carbonate cement on (a -d) basalt (black) with altered rim (grey) with multiple types of carbonate cement (clear/yellow) and final Fe-phase (dark orange); (e) carbonate cement growing directly on olivine xenolith (X). (f) Radiaxial fibrous cement.

5.5.2 XRD

XRD analyses revealed a variety of carbonate and silicate minerals within the Sverrefjellet samples. Mineralogical compositions determined by XRD are presented in Table 5.1 and Table 5.2**.** Results from the basaltic host rock sample includes basaltic glass, plagioclase, pyroxenes and Fe-Ti oxides. Xenoliths hosted in the basalt are compositionally lherzolite, consisting of majority (ferroan) forsterite (up to 92% Mg), ferroan enstatite with diopside (Figure 5.7).

Part of specimen	Phases detected	Formulae	Wt %
Xenolith	Forsterite (ferroan)	$(Mg, Fe)(SiO_4)$	75
	Enstatite	$MgSiO_3$	25
Host basalt with xenolith	Forsterite (ferroan)	$(MgFe)(SiO_4)$	92
	Enstatite	$MgSiO_3$	4
	Albite (calcian)	$(Na,Ca)(Si,Al)_4O_8$	4
Xenolith	Enstatite (ferroan)	$(Mg, Fe)SiO_3$	54
	Forsterite	$(Mg, Fe)(SiO_4)$	36
	Diopside	$MgCaSi_2O_6$	10
Host basalt with xenolith	Forsterite (ferroan)	$(Mg, Fe)(SiO_4)$	55
	Diopside (ferroan)	$(Mg, Fe)CaSi_2O_6$	42
	Ti- phase (titanite?)	$CaTiSiO_5$	3
Xenolith	Diopside (ferroan)	$(Mg, Fe)CaSi_2O_6$	63
	Enstatite (ferroan)	$(Mg, Fe)SiO_3$	20
	Forsterite (ferroan)	$(Mg, Fe)(SiO_4)$	17
Xenolith	Forsterite (ferroan)	$(Mg, Fe)(SiO_4)$	75
	Enstatite (ferroan)	$(Mg, Fe)SiO_3$	25

Table 5.1: Basalt host rock and xenolith mineralogy. Phase identification was carried out using DIFFRAC.EVA software from Bruker in combination with the Powder Data File (PDF-4, The International Centre for Diffraction Data). Quantification was done with TOPAS software (Coelho et al., 2011).

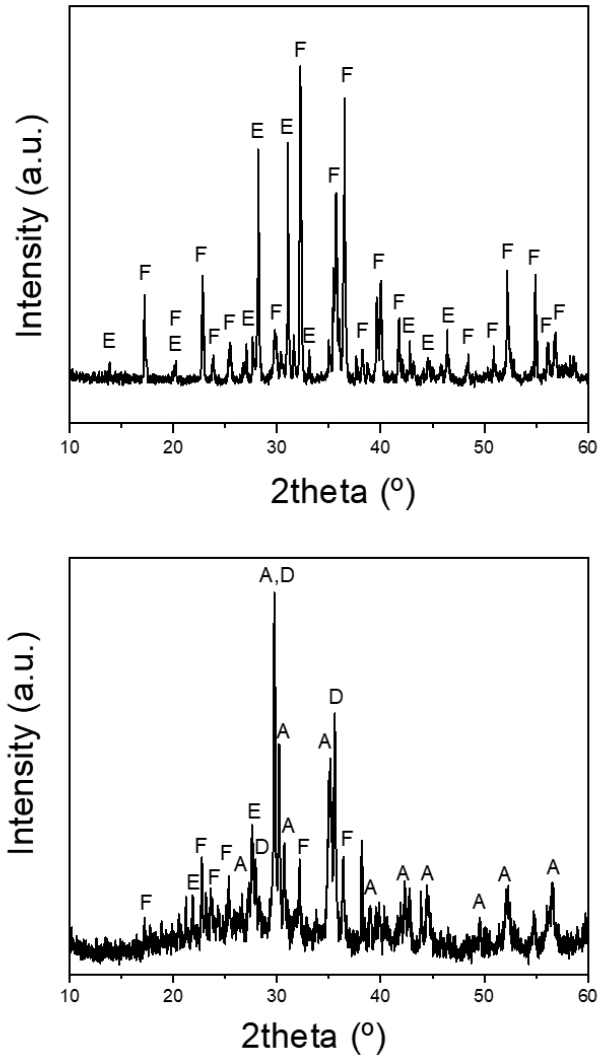

Figure 5.7: powdered XRD patterns obtained from xenolith bearing-basalt host samples. Augite (A); Diopside (D); Enstatite (E) and Forsterite (F).

The characterisation by XRD of selected samples of the carbonate coating revealed the carbonate cement consists of calcite-type carbonates (Figure 5.8**)** within the magnesite-calcite-siderite compositional range. The calcite-type carbonates show compositional variations due to changes in cation content, as demonstrated in the broadness (FWHM) and slight asymmetry of the $\{10\bar{1}4\}$ Bragg peak. The main d-spacings of the $\{10\bar{1}4\}$ peaks are shown in Figure 5.9. The diffraction patterns reveal that some samples contain a small amount of dolomite as well as poorly ordered calcite-type carbonate phases (i.e. siderite, magnesite etc.), as evidenced by the pronounced broadening and shifting to higher 2Θ values of the Bragg peaks. This phenomenon can be attributed to cation-substitution mechanisms in these divalent calcite-type carbonates (Morris *et al.*, 2011). The absence of super-structure Bragg peaks in the dolomite indicates that this phase could consist of proto-dolomite or very-high-magnesium calcite with near-dolomite stoichiometry but showing Ca^{2+}-Mg^{2+} disorder (Gregg *et al.*, 2015).

Phases detected	Mg content[1]
Mg,Mn carbonate	0.84
Dolomite (ferroan)	
Mg,Mn carbonate	0.89
Dolomite	
Dolomite (ferroan)	
Siderite	0.14
Dolomite	0.51
Siderite	0.48
Dolomite (ferroan)	0.79
Dolomite (ferroan)	0.94

Table 5.2: Carbonate cement phase identification carried out using DIFFRAC.EVA software from Bruker in combination with the Powder Data File (PDF-4, The International Centre for Diffraction Data). Powdered carbonate cements were carefully obtained using a precision micro drill, targeting different regions within the cement e.g., the deep rusty tan-orange outermost layer, the beige-tan inner zone.

[1]Mg Content: Where Mg= 1.0 = pure Magnesite ($MgCO_3$) and Mg= 0.5 is dolomite ($Ca,Mg(CO_3)_2$). Mg values were calculated from the d-spacing values of the calcite-type (104) Bragg peak by using the equation by Arvidson and Mackenzie (1999).

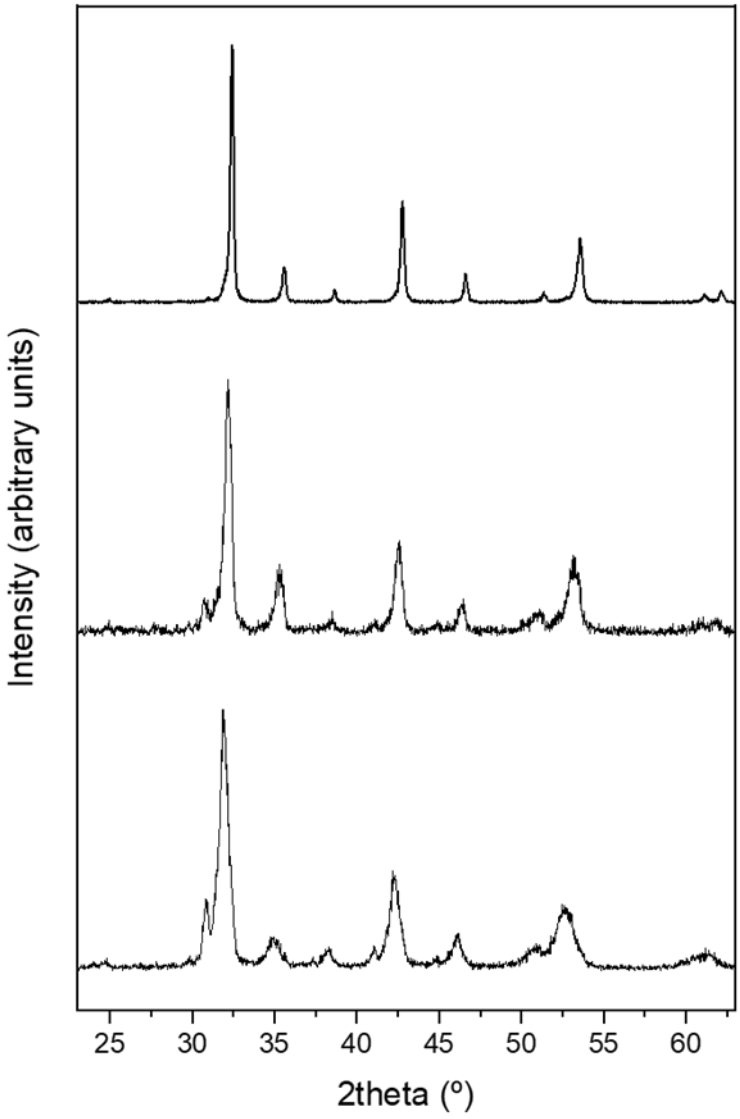

Figure 5.8: powdered XRD patterns obtained from carbonate cement samples. Samples are Mg-rich calcite type solid solutions, with minor dolomite. The sharpest peak refers to the (104) calcite type main XRD peak.

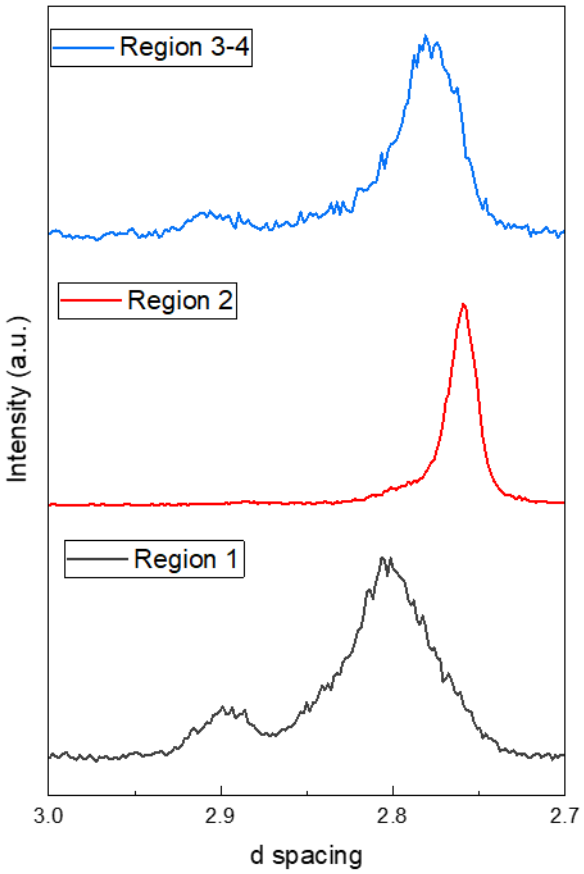

Figure 5.9: d-spacings of the (104) Bragg peaks of the calcite-type carbonates selected from different regions of the carbonate samples. The shift from larger to smaller values indicates a decrease of the unit-cell dimensions due to a decrease of the 2+ cation radius. The broadness and asymmetry of the Bragg peaks indicates are a consequence of compositional variations within the calcite-type solid solutions. As references, the d-spacing of the (104) Bragg peak of stoichiometric ordered dolomite, siderite and magnesite are 2.89, 2.79 and 2.74 Å, respectively.

5.5.3 SCANNING ELECTRON MICROSCOPY BACK SCATTERED ELECTRONS (BSE)

Four main carbonate cement regions were identified in some areas of the thin sections with a variety of microfabrics, which evolve from contact with the basaltic host rock out to the periphery of the encrusting carbonates. Figure 5.12 and Figure 5.13 shows the 4 cement regions:

- Region 1 (up to 275 μm thick): Cement in contact with the host rock, consisting of parallel concentric layers (≤ 25 μm thick) with sawtooth texture (Figure 5.13b). Texture is strongly affected with the local microtopography of host substrate.
- Region 2 (up to 320 μm thick): Cement consisting of alternating light and dark fine parallel laminae (≤ 20 μm thick).
- Region 3 (up to 200 μm thick): Cement composed of radial crystal fans (≤ 140 μm width). Minor parallel banding that overlaps the fans. Crystals grow perpendicular to the substrate and have a transitional contact with region 4 carbonates.
- Region 4 (≤ 50 μm thick): Thin final cement, containing nanocrystalline phases. Bright on BSE images, with localised porosity.

Due to the brecciated nature of the basalt host, the carbonate cements frequently grow into pore spaces, however, pore space is often limited, with not enough space for the development of the full sequence of cementation to occur (Figure 5.10). As such, “Region 2” type cement appears to be the dominant cement type, as it coats most of the carbonate cements almost everywhere in the samples (Figure 5.16**,** Figure 5.19 etc.). Where pore space is limited the finely laminated “Region 2” carbonate cement exhibits a botryoidal habit. Even in cases where the complete sequence may not be fully preserved, a significant portion of the cements appears to be coated by the “Region 4” type microcrystalline cement.

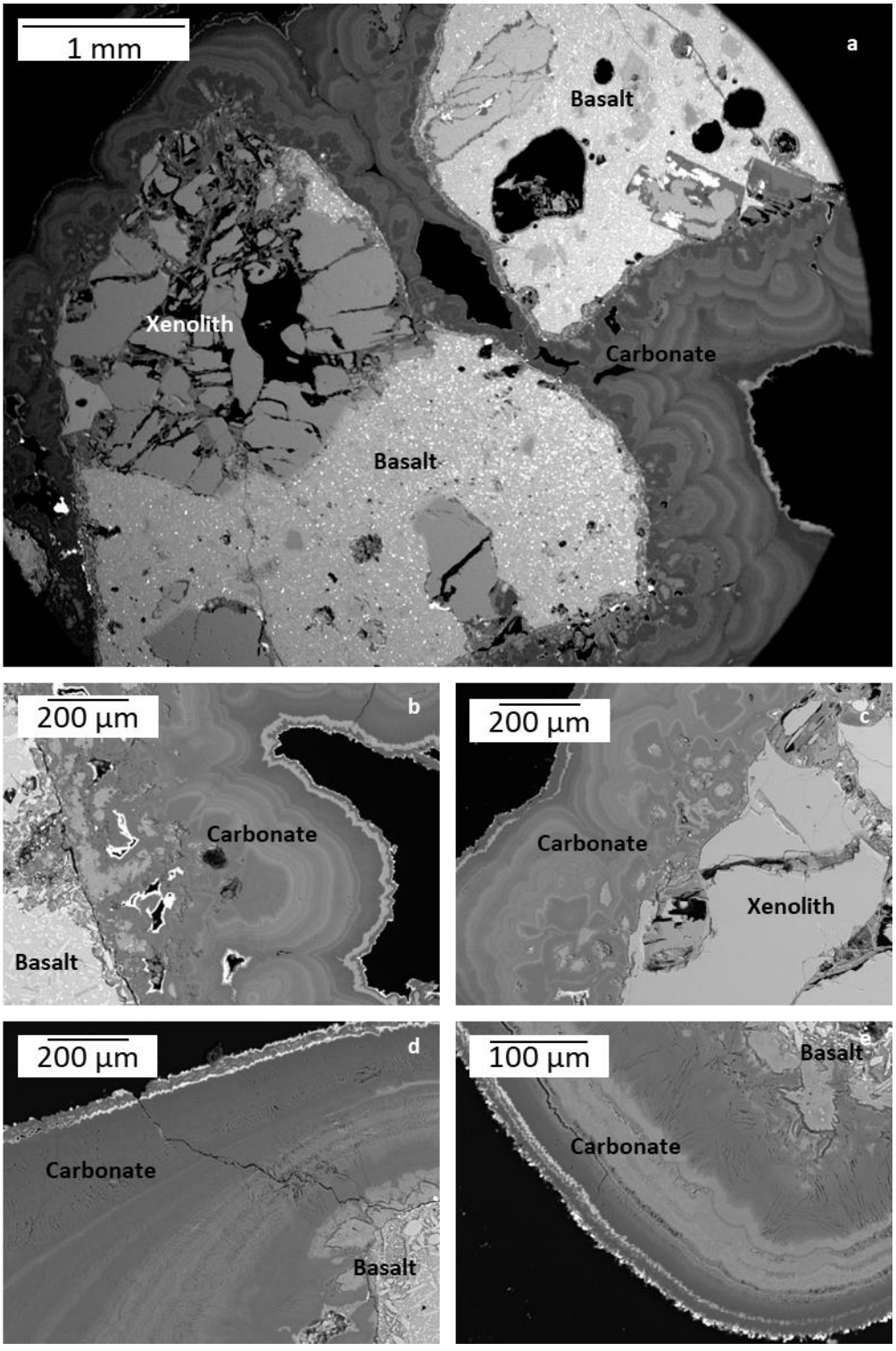

Figure 5.10: SEM-BSE image of carbonated xenolith bearing-basalt. a) Overview of sample with carbonate cement growing on host basalt substrate and on large olivine xenolith. b) Carbonate growing on altered basalt with "region 1" type carbonates (morphology determined by substrate

topography), followed by finely laminated "region 2" type carbonate. c) Carbonate growing from olivine bearing-xenolith. d and e) Carbonate, predominately Mg-rich, growing from altered basalt.

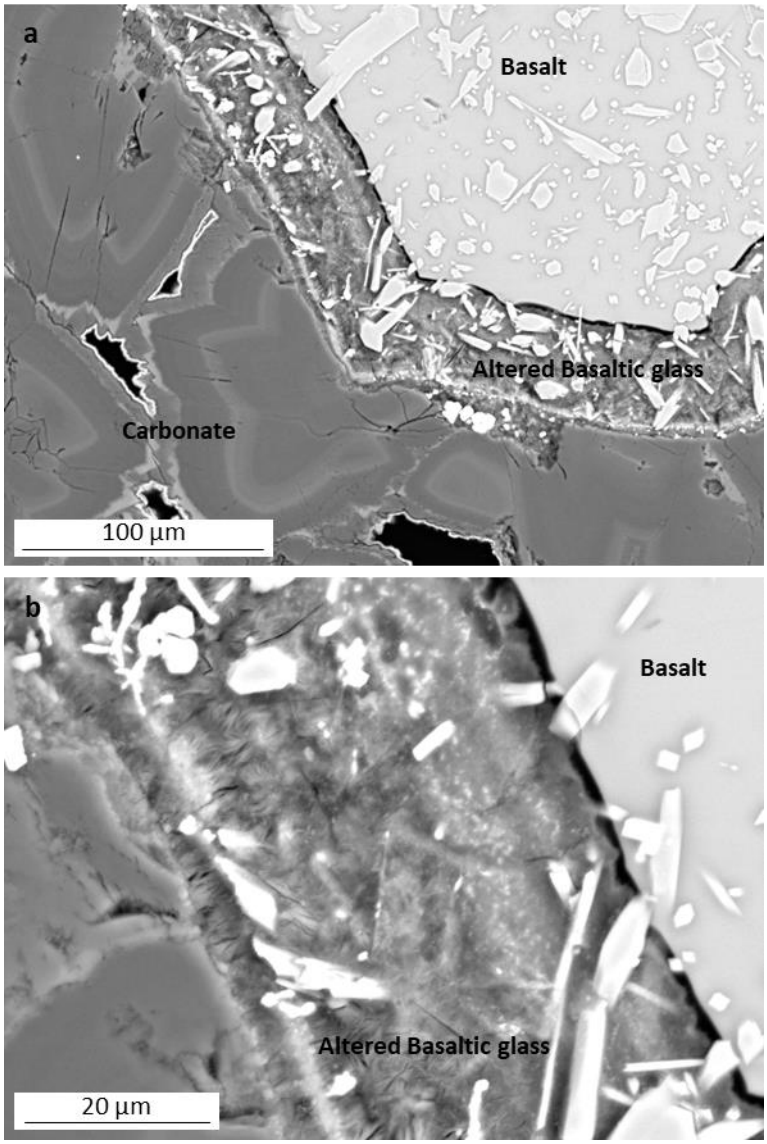

Figure 5.11: SEM-BSE images of a) the basalt host with an altered basaltic rim which is associated with the carbonates. b) close up of altered rim.

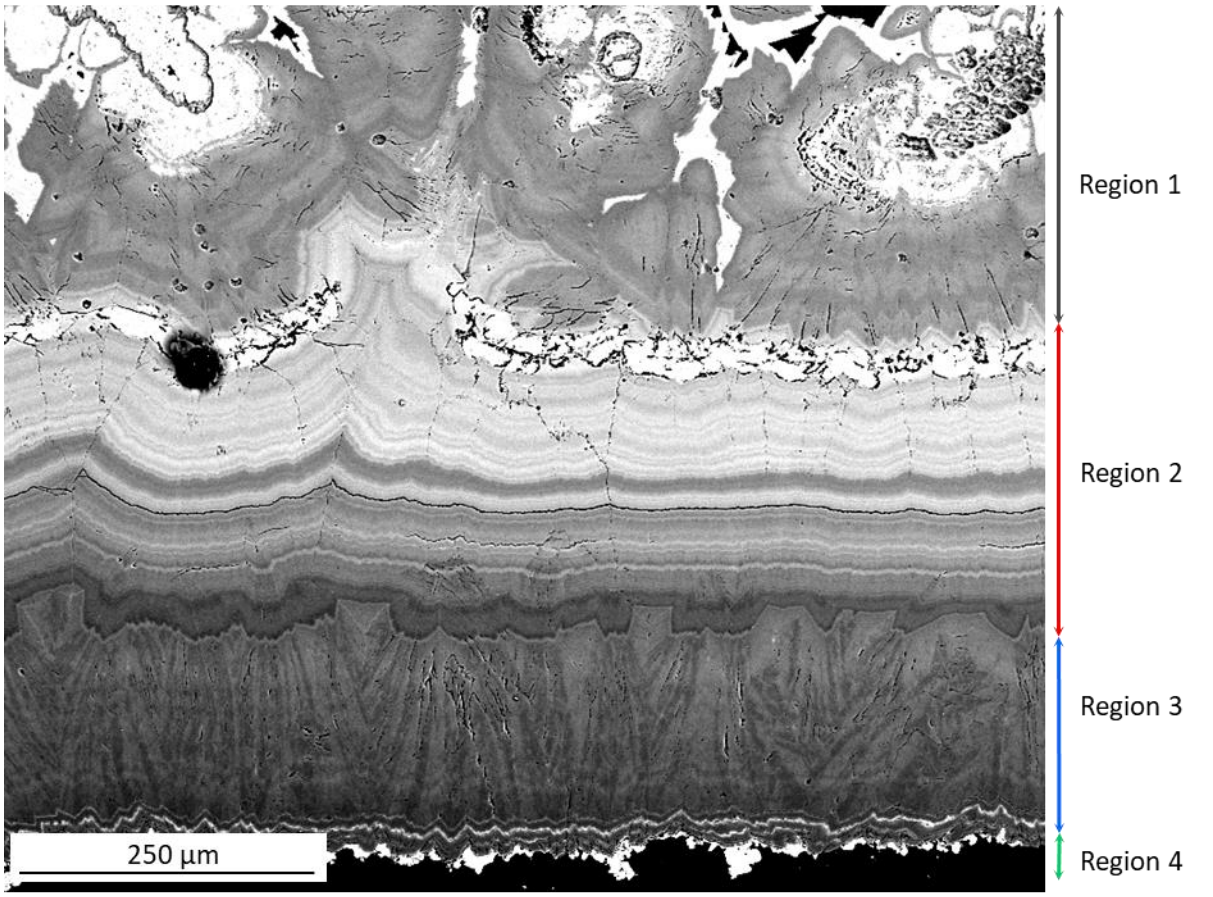

Figure 5.12: SEM-BSE image of sequence of carbonate cements. Carbonate cements evolve outwards from the basalt substrate surface (top) to the edge of the cement (bottom) with four distinctive cement regions. Cation content of cement changes throughout the sequence of cement growth.

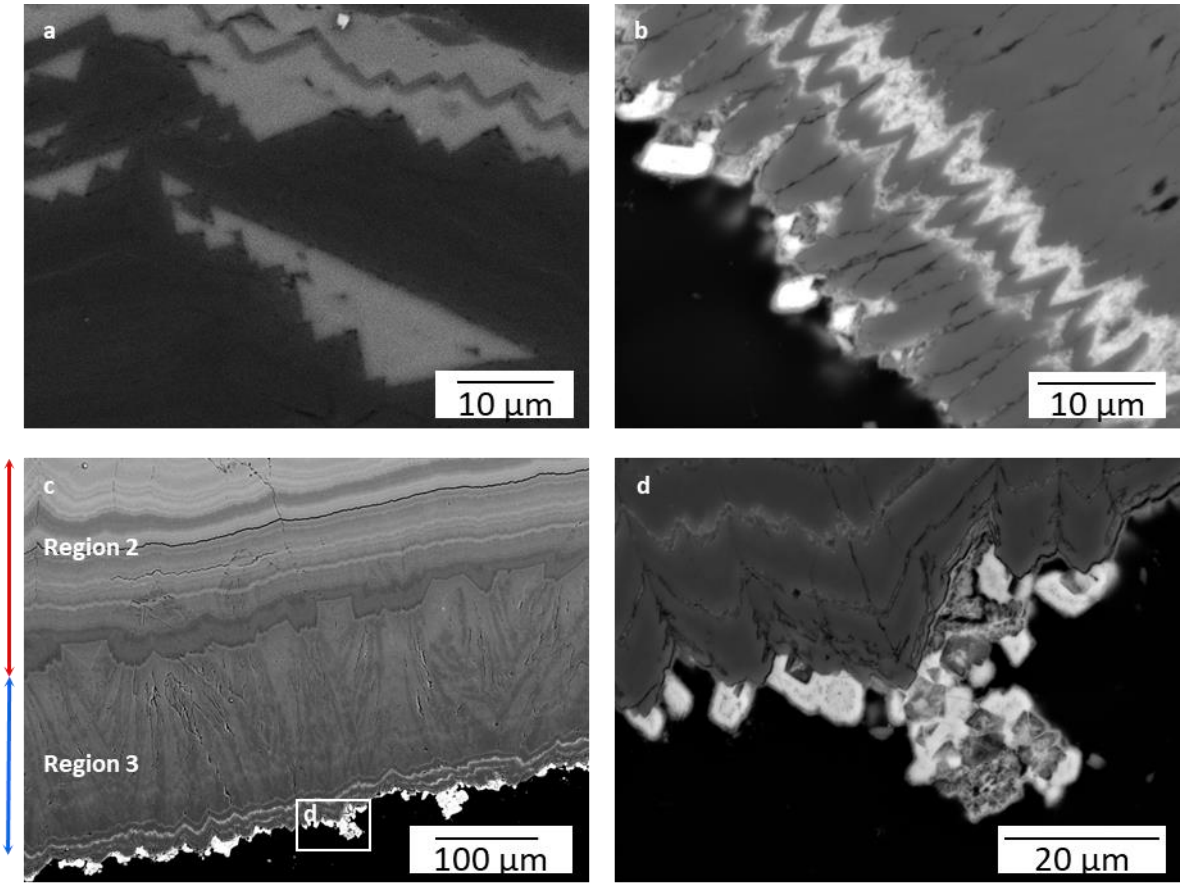

Figure 5.13: SEM-BSE image of selected carbonate cement regions with different textures. a) Sawtooth carbonate formed by the apical section of calcite type carbonate rhombs (pale grey) within carbonate groundmass. b) "Region 1" type carbonate, parallel concentric layers. Sawtooth texture likely a consequence of microtopography of basalt substrate. c) "Region 2" type cement consisting of parallel bands, followed by "Region 3" type radial growth cement. Lastly "Region 4" cements (white box). d) Inset of "Region 4" cement demonstrating individual crystals.

5.5.4 SEM-CL

Scanning electron microscopy cathodoluminescence (SEM-CL) photomicrograph of “Area 5” highlighted the heterogeneity, both inter- and intra-, of the carbonate cement regions (Figure 5.14). Cathodoluminescence photomicrograph showed distinct areas of luminescent blue (dull to bright luminescence) and pink (dull to bright luminescence) within the calcite-type carbonate cement. Cathodoluminescence photomicrographs showed that the majority of the basaltic host rock portion (fine grained groundmass) is dull to non-luminescent, with certain phenocrysts exhibiting dull to bright blue luminescence.

The textural distinctions between different cement types are especially pronounced within the carbonates of 'Region 1' and 'Region 2'. These textural differences are linked to the variations in luminescence levels, particularly the contrasting blue and pink luminescence. In 'Region 1,' the sawtooth texture is characterized by alternating segments of bright to medium luminescence. 'Region 2' carbonates, when subjected to cathodoluminescence, reveal oscillations of luminescent blue and pink within the fine laminae. Moving to 'Region 3,' the carbonates exhibit bright blue luminescence, with the radial texture being notably prominent, especially at the crystal terminations, which display intense bright blue luminescence. Similarly 'Region 4' carbonates also exhibit a bright blue luminescence.

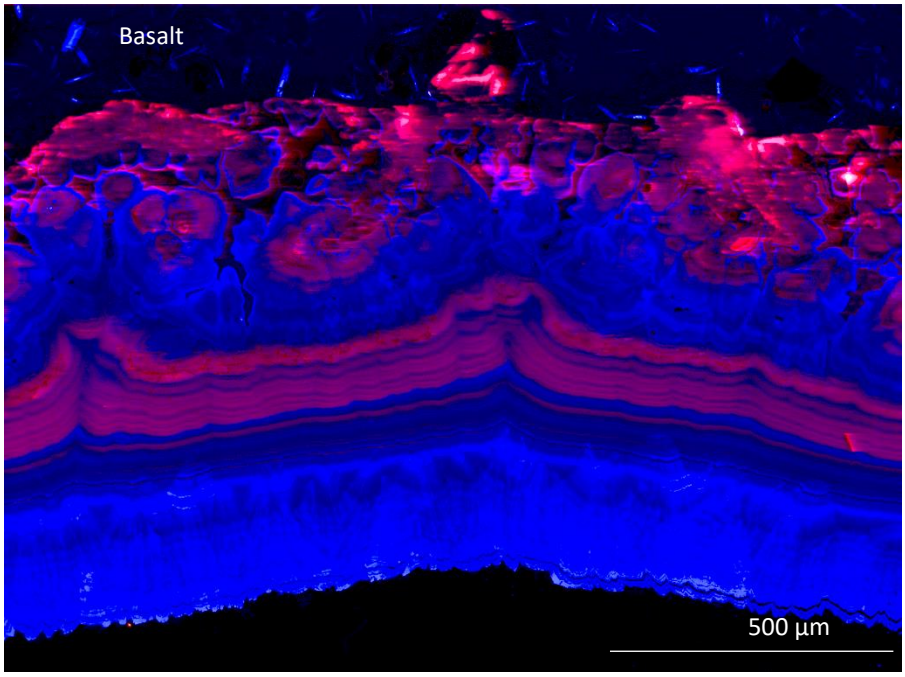

Figure 5.14: SEM-CL image showing compositional zoning and highlighting different textural regions within the cements.

5.5.5 SEM-EDS

EDS compositional maps allowed us to determine the chemical compositions of the i) basalt host rock and xenoliths and ii) carbonate cements. This approach proved especially valuable in cases where minerals could not be definitively identified through XRD alone, especially within the host basalt. In such cases, we relied on the chemical composition to infer the likely presence of specific minerals.

Figure 5.15 represents the chemical distribution within the basaltic host. The fine grained ground mass is rich in Si, K and Na. The presence of P overlapping with Ca is assumed to be a consequence of the presence of apatite, with Ti-Fe oxides also present in the basalt. Within the basalt Ca and Mg appears to be associated with crystalline phases, with the source of Ca likely being anorthite (An: $CaAl_2SiO_8$). Figure 5.16 represents the chemical distribution within the basaltic host, the xenolith and the carbonate cement. The xenoliths exhibit a high Mg content, consistent with the

mineralogical composition (forsterite and enstatite) identified through powder XRD analysis. Table 5.3 demonstrates the average elemental composition of the host basalt and xenoliths.

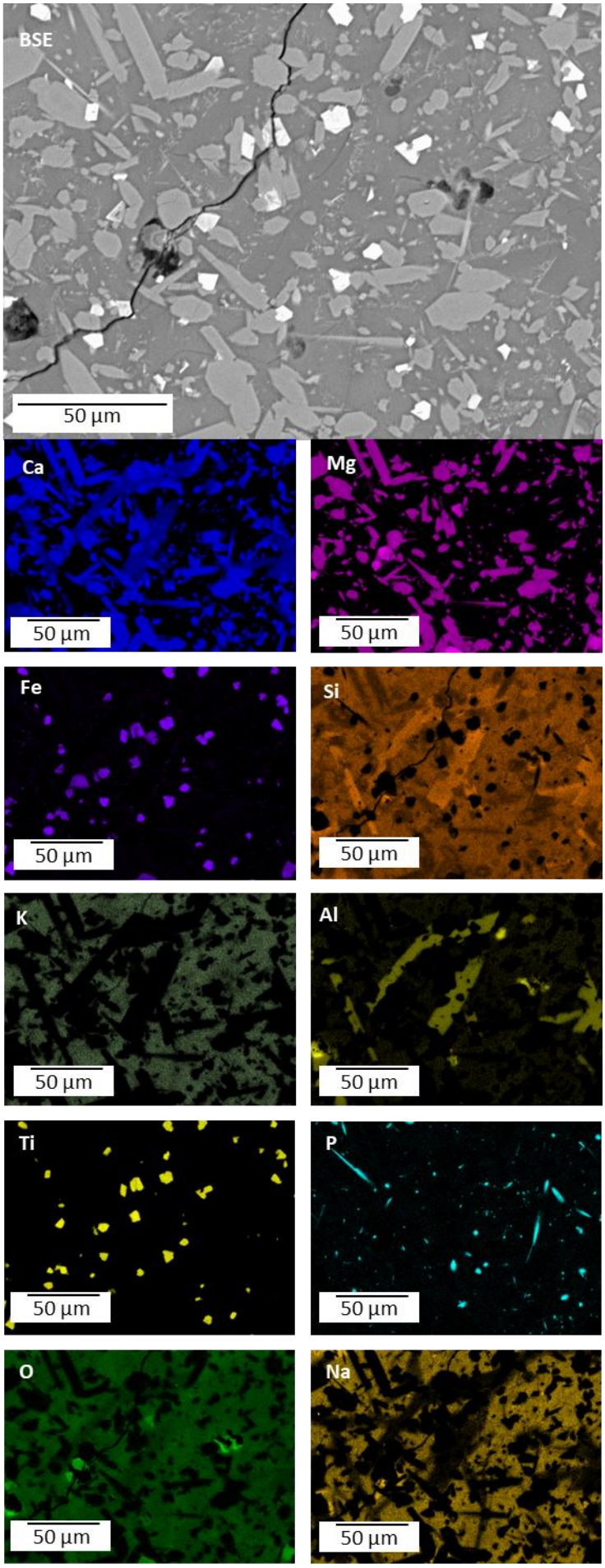
BSE
50 µm
Ca
50 µm
Mg
50 µm
Fe
50 µm
Si
50 µm
K
50 µm
Al
50 µm
Ti
50 µm
P
50 µm
O
50 µm
Na
50 µm

Figure 5.15: SEM-BSE image and EDS compositional maps showing distribution of elements within the basalt host.

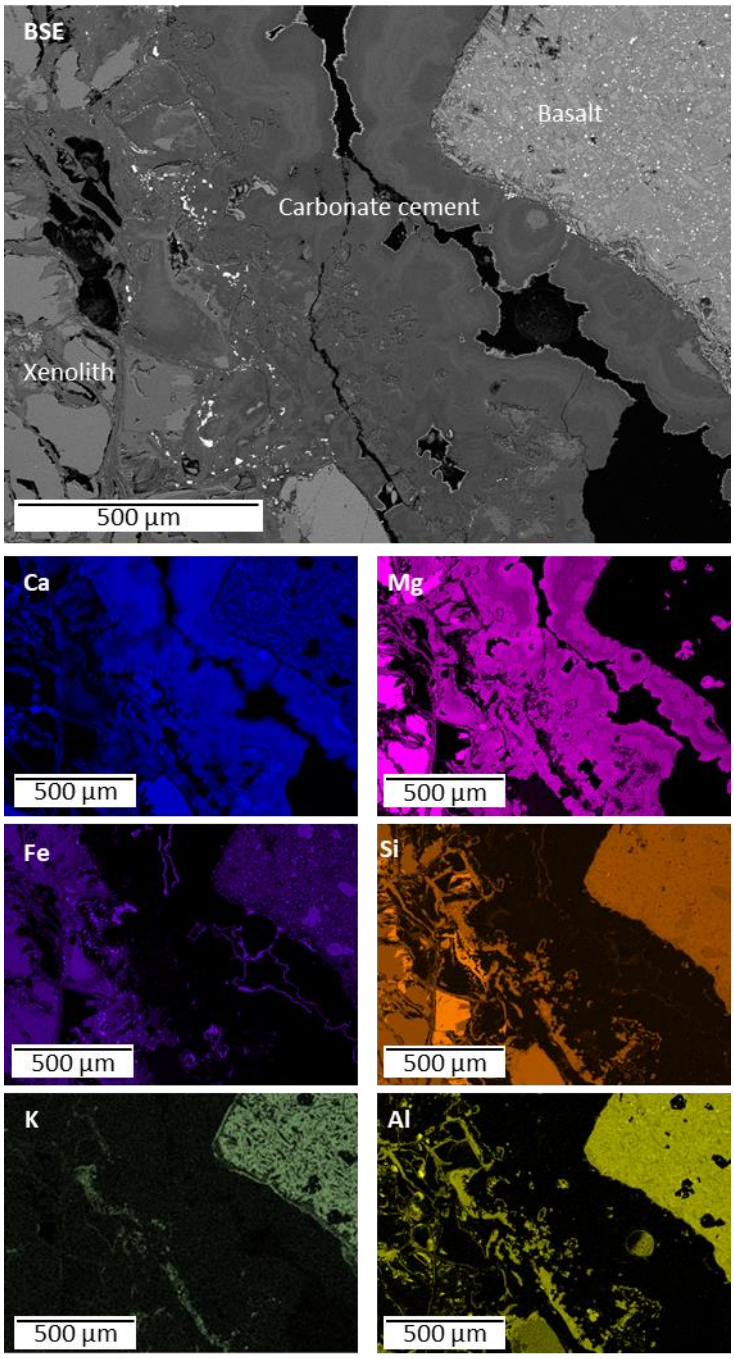

Figure 5.16: SEM-BSE image and EDS compositional maps showing distribution of elements between the basalt host, the xenolith and the carbonate cements.

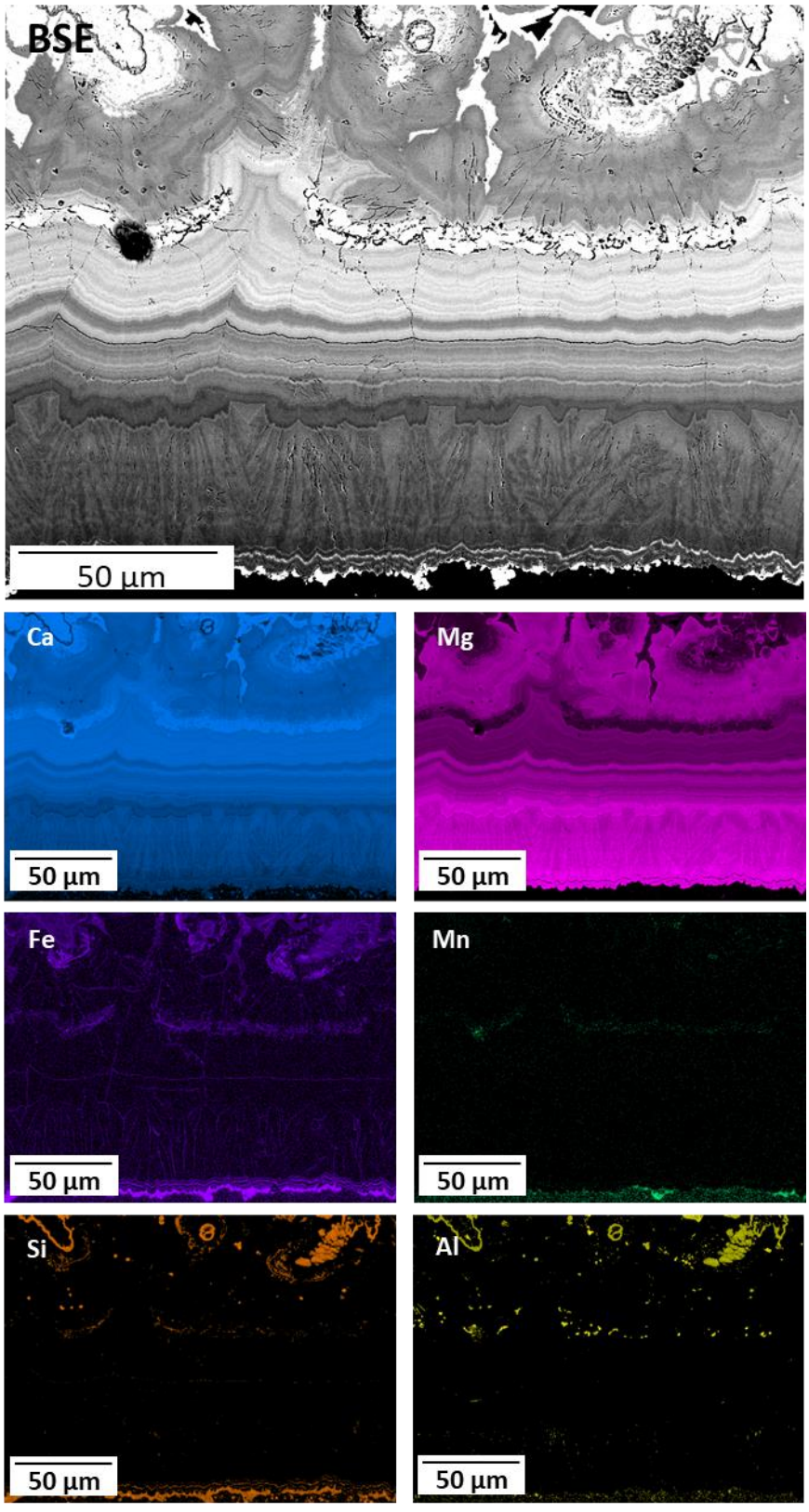

Figure 5.17: SEM-BSE image and EDS compositional maps showing distribution of elements within "Area 5".

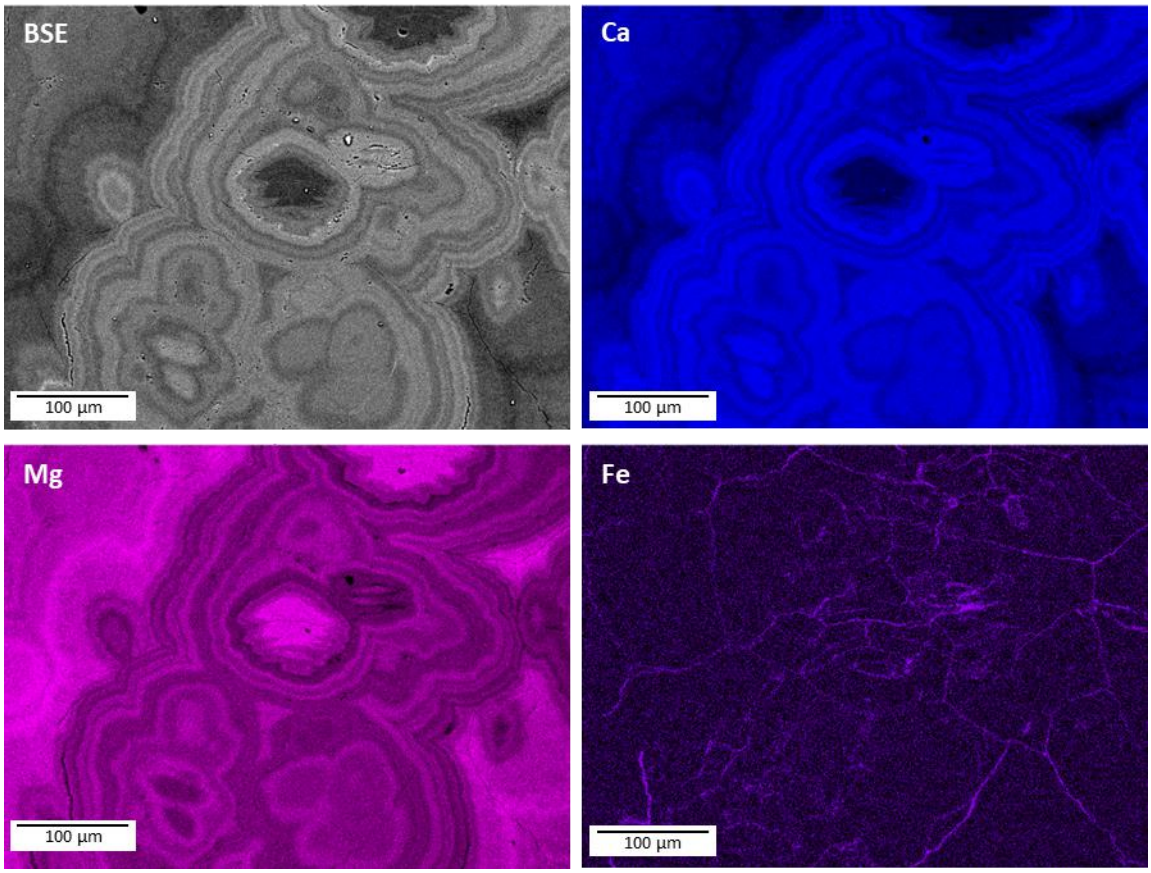

Figure 5.18: SEM-BSE image and EDS compositional maps showing distribution of elements within the finely laminated zoned "region 2" carbonate cement, exhibiting a botryoidal habit due to fluctuations of Ca and Mg. Fe is not a main component of this cement and appears to be present only after fracturing.

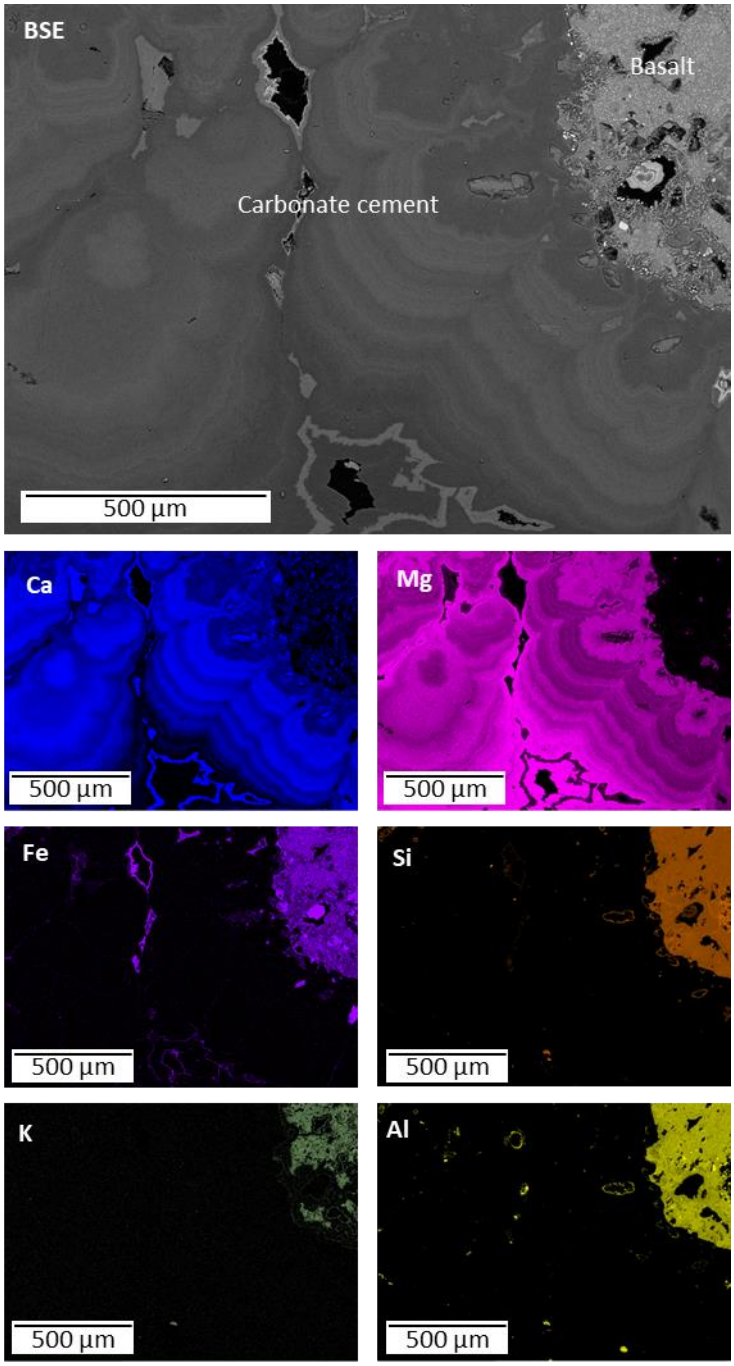

Figure 5.19: SEM-BSE image and EDS compositional maps showing distribution of elements within the "Region 2" carbonates. Carbonates are finely laminated, with some lamination thickness < 50 µm. The zoned carbonate cement exhibits botryoidal habit, due to fluctuations of Ca and Mg.

Element (At%)	Host Basalt	Xenolith
O	62.030	62.287
Na	1.858	BDL
Mg	3.822	25.250
Al	5.802	0.154
Si	13.199	8.6041
P	0.140	0.032
S	0.0967	0.026
Cl	0.0967	0.0167
K	0.430	0.050
Ca	4.561	1.497
Ti	2.084	BDL
Mn	0.112	0.044
Fe	6.758	2.641
Ni	BDL	0.131

Table 5.3 Average Elemental composition (at%) of host basalt and xenoliths determined by SEM-EDS point spectra. BDL (Below detection limit).

EDS compositional maps of the carbonates demonstrate that Ca and Mg are the main cations present in the calcite-type carbonates, with minor Fe. Figure 5.17**,** Figure 5.18 and Figure 5.19 shows that there are oscillations between Ca-rich and Mg-rich zones, these zones were also highlighted with SEM-CL. Traces of Fe and Mn were also detected. For example point spectra analysis within "Region 2" revealed variations of Fe and Mn, which correlates to different luminous zones within "Region 2" as observed with SEM-CL: pink luminous zone (Fe^{2+} 0.027 at%; Mn^{2+} 0.026 at%) and the blue luminous zone (Fe^{2+} 0.081 at%; Mn^{2+} 0.032 at%). The average Ca/Mg ratios within the respective luminous zone in "Region 2" also varies: pink luminous zone (Ca/Mg 0.57) blue luminous zone (Ca/Mg 0.28).

The analysis of major elemental composition through both point spectra and line spectra in all carbonate cements revealed a systematic and progressive change across the various cement regions. Most carbonate cements consist of a binary solid-solution between Ca and Mg calcite-type carbonate, evolving from calcian proto-dolomite to magnesite and progressing towards a ferro-magnesite composition Figure 5.20. A consistent pattern of rising magnesium content was noted, with the Ca/Mg

ratio progressively decreasing as one moves farther away from the host rock, ultimately culminating in the formation of ferro-magnesite.

"Region 1" carbonates oscillate between three compositions: From calcian proto-dolomite ($Mg_{0.35-0.42}$ $Ca_{0.65-0.58}$) and dolomite ($Mg_{0.5-0.61}$ $Ca_{0.5-0.39}$) to calcian-magnesite ($Mg_{0.65-0.84}$ $Ca_{0.35-0.16}$) composition (Figure 5.21). Within "Region 1" the Ca/Mg varies from 1.81 to 0.19. "Region 2" carbonates continue the trend of increasing Mg composition towards magnesite, ranging from dolomitic to magnesitic ($Mg_{0.53-0.92}$ $Ca_{0.47-0.08}$) (Figure 5.22), the Ca/Mg varies from 0.51 0.11 In "Region 3" the carbonate cement has a composition closer to magnesite ($Mg_{0.73-0.96}$ $Ca_{0.27-0.04}$), the Ca/Mg varies from 0.37 to 0.04 (Figure 5.23) . The elemental analyses indicate a notable increase in the proportion of ferro-magnesite towards the border with 'Region 4. Lastly, the final phase of cement, "Region 4", continues the trend from magnesite to siderite (Figure 5.24). It is worth noting that in both "Region 3 and 4" the content of Fe is greater than 50%, likely including μ- to nano- inclusions of non Fe-carbonates (e.g., Fe-oxides or Fe-silicates). For example, within "Region 4" the Fe/Mg ratio varies from 0 to 13.57, the maximum value. It is important to highlight that the μ- to nano- inclusions of non Fe-carbonates likely produces a bias of the Fe/Mg ratios. Also it is worth noting that the SEM revealed that post-carbonate Fe-rich fractures are present throughout the carbonate cement (Figure 5.18). The probed areas were selected to avoid fractures affecting the pre-existing carbonated materials to avoid outliers originating from non-carbonate iron rich nanophases.

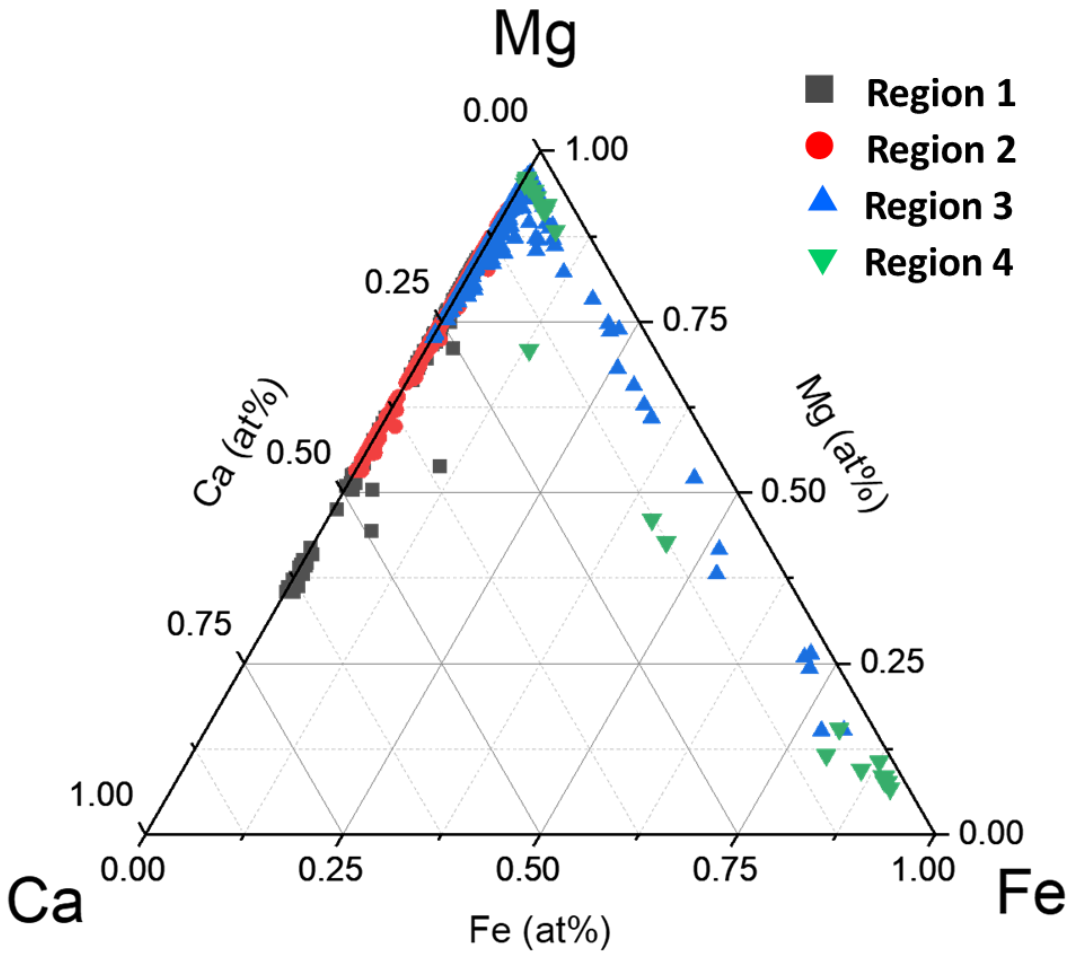

Figure 5.20: Ternary plot of carbonate phase compositions from SEM EDS maps of Area 5 (Thin section 3) demonstrating the evolution of the carbonate cement. Atom proportions of Ca, Fe and Mg normalised to 100% are plotted and show a general increase in the proportion of Ca-magnesite across the carbonate cement regions. Compositions of greater than 50% Fe likely include μ- or nano-inclusions of non Fe-carbonates (e.g. Fe-oxides or Fe-silicates).

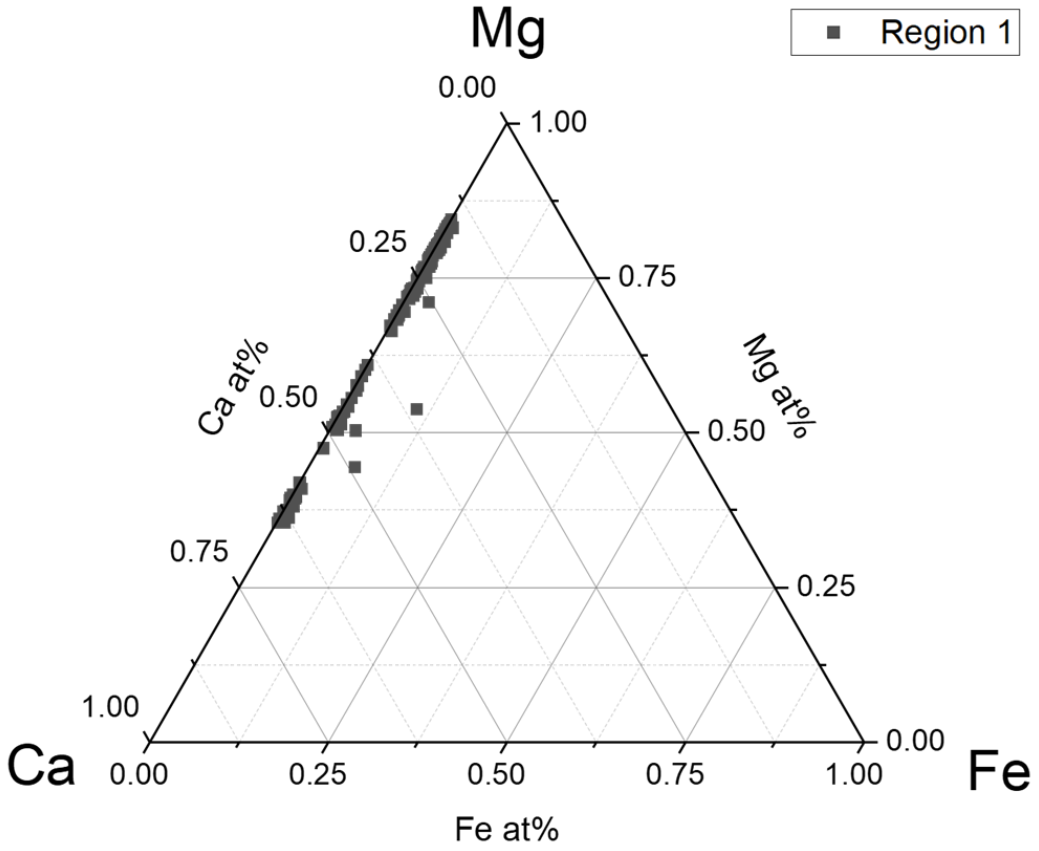

Figure 5.21: Ternary plot of carbonate phase compositions from SEM EDS maps of Area 5 (Thin section 3) demonstrating the composition of "Region 1" type carbonate cement. Region 1 has three distinct compositions, with increasing Mg content. The carbonates oscillated between the three compositions from calcian protodolomite to dolomite to calcian-magnesite composition.

Weight proportions of Ca, Fe and Mg normalised to 100% are plotted and show a general increase in the proportion of Ca-magnesite across the carbonate cement regions.

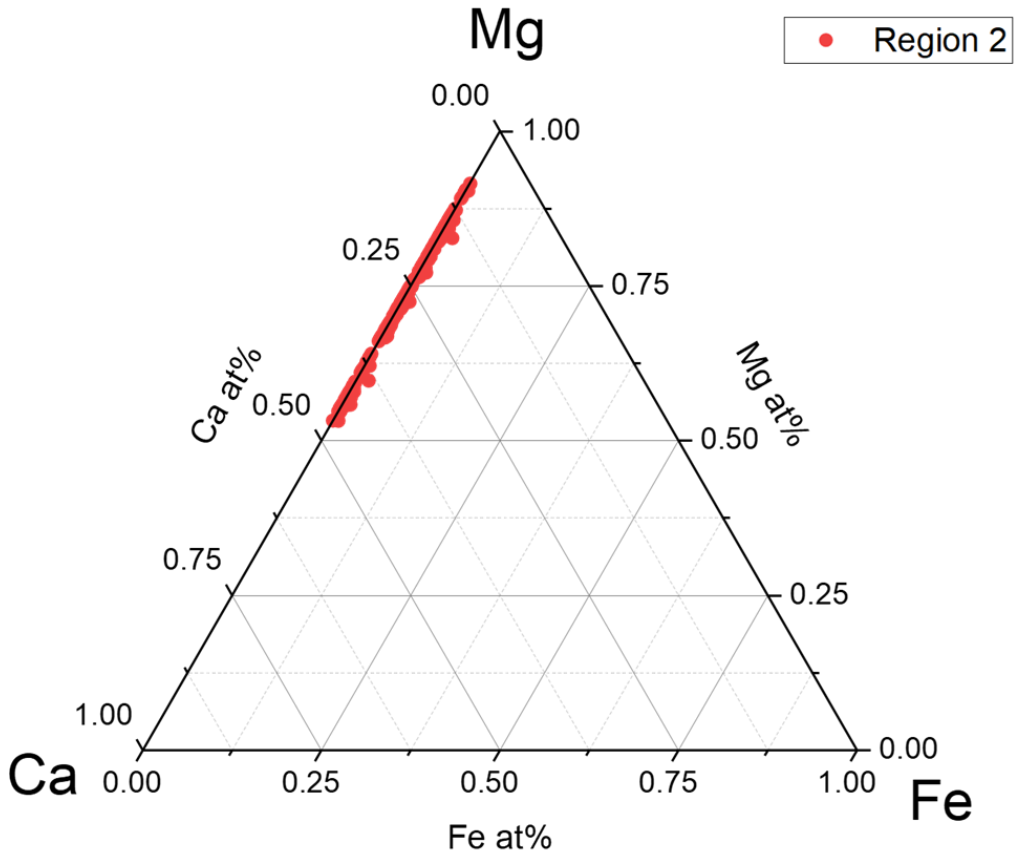

Figure 5.22: Ternary plot of carbonate phase compositions from SEM EDS maps of Area 5 (Thin section 3) demonstrating the composition of "Region 2" type carbonate cement. Region 2 follows the increased Mg content. The carbonates evolve from dolomite to calcian-magnesite composition.

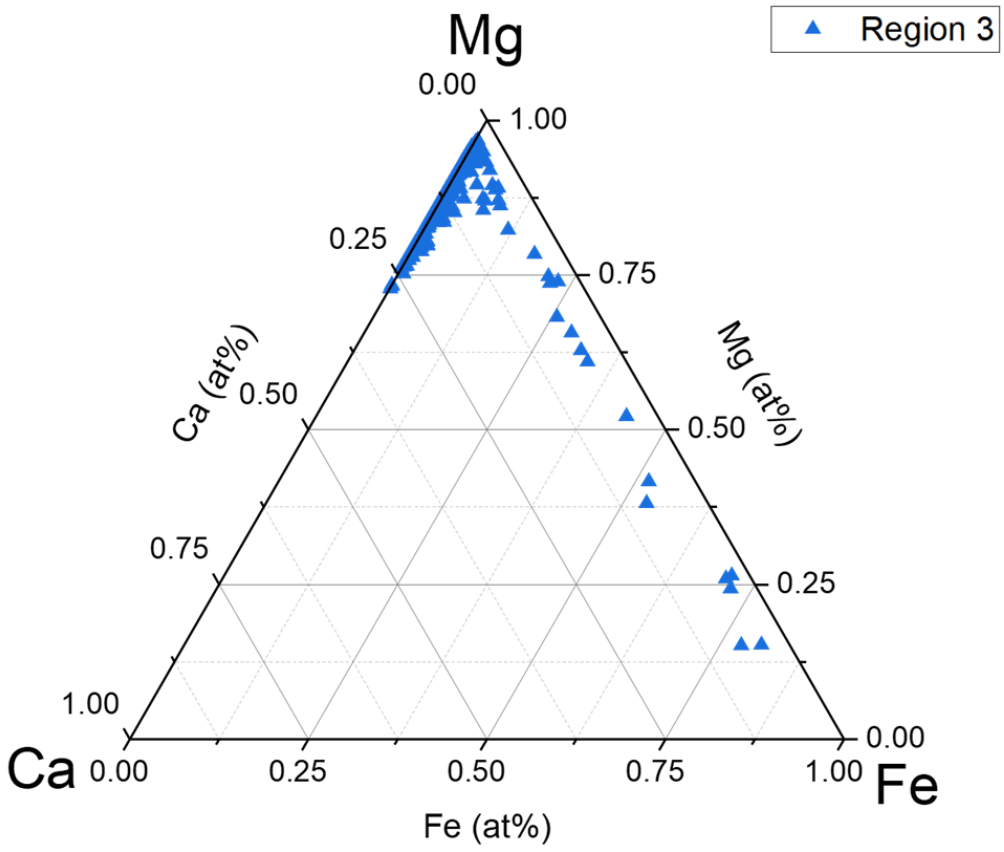

Figure 5.23: Ternary plot of carbonate phase compositions from SEM EDS maps of Area 5 (Thin section 3) demonstrating the composition of "Region 3" type carbonate cement. Region 3 the carbonate cement is magnesite in composition and shows a general increase in the proportion of ferro-magnesite towards the border with Region 4. Weight proportions of Ca, Fe and Mg normalised to 100% are plotted and show a general increase in the proportion of Ca-magnesite across the carbonate cement regions. Compositions of greater than 50% Fe likely include μ- or nano- inclusions of non Fe-carbonates (e.g. Fe-oxides or Fe-silicates).

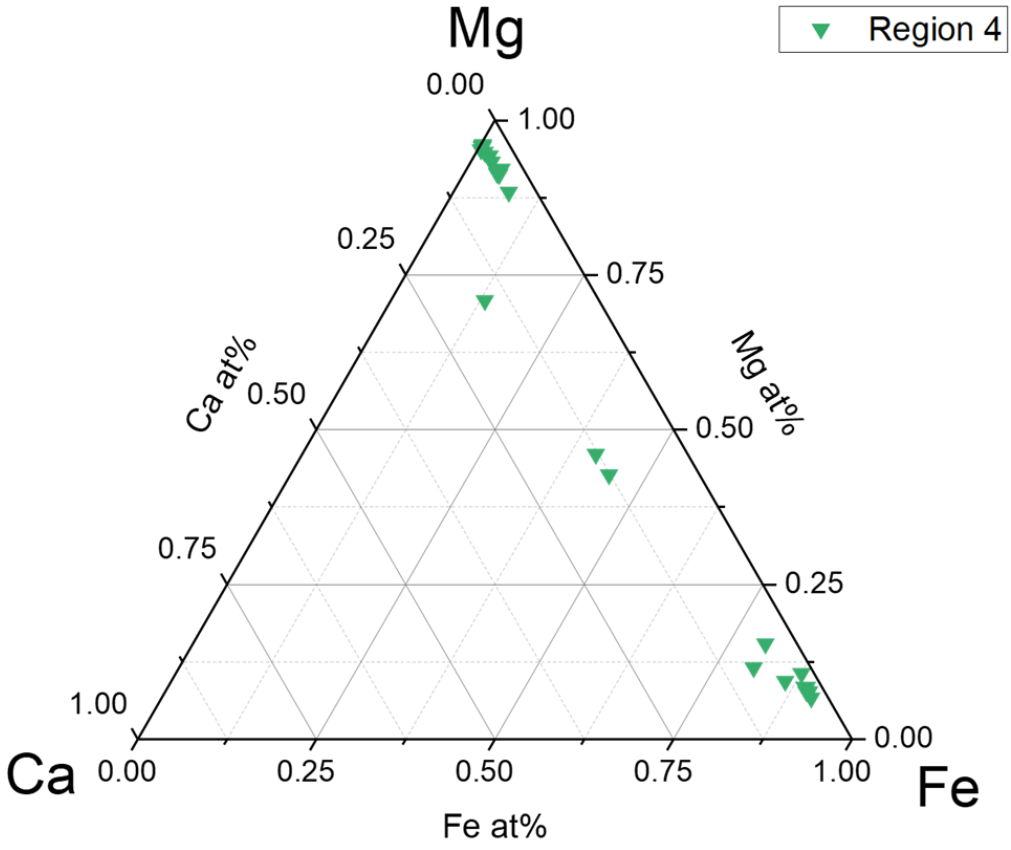

Figure 5.24: Ternary plot of carbonate phase compositions from SEM EDS maps of Area 5 (Thin section 3) demonstrating the composition of "Region 4" type carbonate cement. Region 4 shows a general increase in the proportion of ferro-magnesite. Compositions of greater than 50% Fe likely include μ- or nano- inclusions of non Fe-carbonates (e.g. Fe-oxides or Fe-silicates).

The chemical distribution of Ca, Mg and Fe within the spherical globules/nodules that exhibit zoning was obtained from SEM-EDS line spectra (Figure 5.25). The globules/nodules range in size from 80-170 μm in diameter. The compositional range of the carbonate globules tends to trend from a Ca-rich interior, evolving into an Mg enriched zone, followed by a thin Fe-rich rim (<5 μm). Excluding the rim, the carbonate concentrations consist of a binary solid solution between Ca- and Mg- calcite type carbonate, with reciprocal the Mg and Ca values. The zones within the globules/nodules can be distinguished in the SEM-BSE images due to contrast differences.

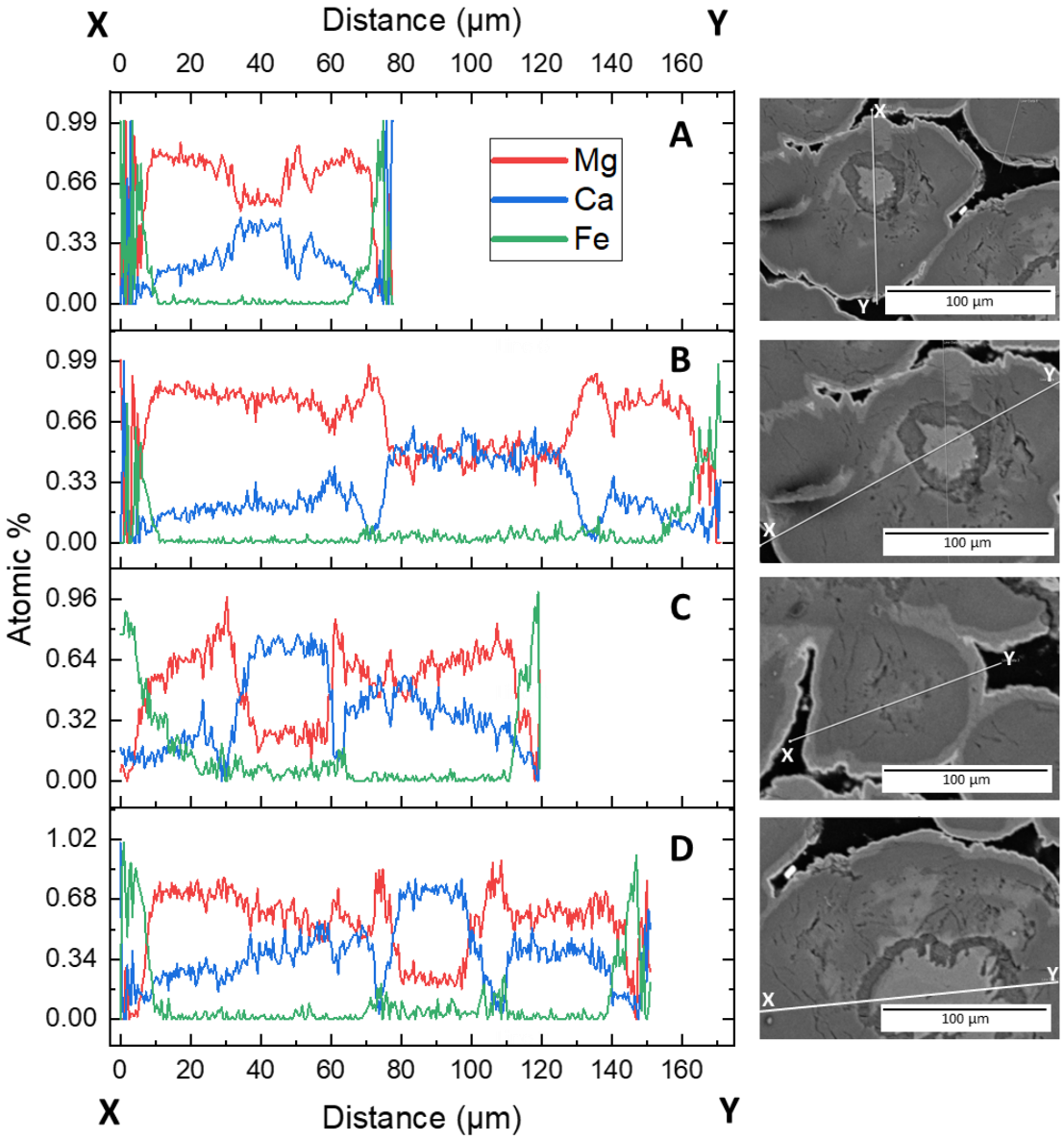

Figure 5.25: SEM-BSE image and EDS line spectra, showing distribution of Mg, Ca and Fe within zoned carbonate nodules.

5.5.6 PHREEQC SIMULATIONS

The saturation indices (SI) values of magnesite, hydromagnesite, nesquehonite, dolomite and calcite with respect to varying levels of pCO_2 (0.004 atm, 1 atm, 10 atm and 100 atm) as a function of temperature (°C) and pH are presented in Appendix C4. These hydrogeochemical simulations offer a deeper understanding of the dynamic interplay between key factors influencing carbonate mineralization, shedding light on the geochemical processes at play that will be discussed below.

5.6 DISCUSSION:

Carbonation of alkali basalts

The carbonate mineralisation at the Sverrefjellet consisted of a fluid-rock interaction that resulted in the release of divalent cations Ca^{2+}, Mg^{2+} and Fe^{2+} from the host basalt (including the xenoliths) to a CO_2-rich aqueous solution at hydrothermal conditions. This CO_2 originated from the degassing of alkali basalts during volcanic activity. As Sverrefjellet erupted subglacially (Skjelkvåle *et al.*, 1989) the combination of meltwater and CO_2 would have resulted in the formation of abundant acidic gas-charged water (*Equation 1*). Basaltic rocks contain roughly 25 wt% Ca, Mg and Fe oxides, as well as ample amounts of other cations, including Al^{3+} and Na^{+}. (Schaef *et al.,* 2010; Gislason and Oelkers, 2014; Gislason *et al.*, 2014) and they are highly reactive to CO_2-containing fluids, even more compared to sedimentary rocks, meaning the cations in the basalt are rapidly available to form carbonate minerals (Rosenbauer *et al.*, 2012; Gislason and Oelkers, 2014).

The resulting carbonates predominantly exhibit a calcite-type structure, within the magnesite-calcite-siderite compositional field, which reflects the underlying chemistry within the system. XRD revealed the presence of calcite-type (rhombohedral) carbonates, and SEM-EDS revealed the absence of Ba^{2+} or Sr^{2+} ions, larger ions compared to Ca^{2+} and Mg^{2+} that in high concentration would have contributed to the crystallisation of aragonite-type carbonates (e.g. strontianite, $SrCO_3$ and witherite, $BaCO_3$).

The chemical composition of the main carbonate constituent divalent ions, Mg^{2+}, Ca^{2+} and Fe^{2+} can be attributed to the origins of the primary minerals of the host basalt (Figure 5.15, Figure 5.16 and Figure 5.19). The dissolved concentration of Mg in these carbonate-bearing fluids would have been greater than that of Ca and Fe, suggesting that the higher abundance of Mg within the system is a consequence of the dissolution of Mg-bearing minerals. SEM-EDS analyses revealed that Mg originates from both the basalt (average Mg content 3.82 at%) and xenoliths (average Mg content 25.25 at%) from minerals like forsterite (Mg_2SiO_4) and enstatite (Mg_2Si2O_6). Ca primarily derives from minerals found in the basalt (average Ca content 4.56 at%), particularly feldspars (anorthite, $CaAl_2Si_2O_8$). Fe is present in the basalt in Fe-oxides and basaltic glass, as well as in the xenoliths (average Fe content 2.64 at%). The resulting carbonates precipitated from an aqueous solution saturated with respect to the magnesite-calcite-siderite compositional field, however there is a variable cation content and mineralogy from the basaltic wall rock outward following a general trend of increasing Mg relative to Ca and Fe towards a magnesite ($MgCO_3$) composition. This change in Mg/Ca content and carbonate mineralogy is reflected in the differences in cement textures (Figure 5.12 and Figure 5.13). When examined in conjunction with SEM and cathodoluminescence (SEM-CL) analysis, the carbonate cement reveals various stages of carbonate mineral crystallization, referred to as cement “Regions”. Some of these textures appear to be strongly influenced by the local topography of the host rock (i.e. Region 1 type cement), as they are in direct contact with it. In contrast, others exhibit a distinct texture characterized by radial crystal fans (i.e. Region 3 type cement) suggesting different growth kinetics and likely distinct growth mechanisms at play. By examining the cement types we can shed light on the changing growth kinetics and mechanisms behind the carbonate formation.

Examining the carbonate textures

By utilising SEM-EDS in combination with SEM-CL and integrating the crystal chemistry data, particularly major element composition, we gain the capability to tightly constrain and elucidate the intricate carbonate history of the Sverrefjellet deposits. This comprehensive analytical approach

enables us to explore the formation, growth, and evolution of these carbonate minerals in a detailed manner, shedding light on their geological context and development.

The carbonate cementation process typically involves multiple types and multiple generations of growth (Bathurst, 1972; Bathurst et al., 1993). Perhaps the most (visually) striking finding in the Sverrefjellet samples was the variety of carbonate textures within the carbonate cements. SEM revealed different generations of carbonate cements with distinct textures, this was reinforced with SEM-CL. Notably "area 5" (thin section 3; see Figure 5.12 and Figure 5.14**)**, offered a full suite of the cement types, highlighting the four different growth "regions" (Figure 5.13). It is worth noting that while "area 5" provides a full sequence of the carbonate cement history, the cements are observed throughout many areas of the samples where the porosity is smaller and the cements infill the porosity (e.g. Figure 5.10**,** Figure 5.19**,** Appendix C2 etc.). Examining the carbonate textures and microfabrics can provide insight into the growth mechanisms of the cements (Bathurst, 1972; Bathurst *et al.*, 1993).

Both "Region 1 and 2" carbonates are similar in that the cement consists of fine laminated parallel bands, of alternating Ca/Mg. The development of a continuous laminated cement structure serves as a valuable reference for understanding the specific growth conditions that prevailed during its formation, as discussed by Reeder (1991). This laminated texture also reveals consistent fluctuations in the calcium-magnesium ratios, reflecting the evolution in the fluid composition during growth. Fluctuations within the Ca/Mg ratio in "Region 1" ranged from 1.81 to 0.19 (average Ca/Mg ratio 0.50); fluctuations within the Ca/Mg ratio in "Region 2" ranged from 0.51 to 0.11 (average Ca/Mg ratio 0.27).

The growth banding observed in 'Regions 1 and 2' reveals that the growth interface, extending outward from the basalt host, aligns in parallel with the compositional interface. This results in a relatively uniform progression of growth across the surface of the cement, a phenomenon previously documented by Reeder in 1991 (Reeder, 1991). The banded nature of "Regions 1 and 2", light and dark bands in BSE, reflects either changing growth conditions or variations in growth mechanisms (Reeder, 1991; Paquette, Ward and Reeder, 1993). As the cement is consistently finely laminated it can be assumed that the banded microfabric arose from changes in fluid compositions, i.e. Ca/Mg

ratio in the fluid, rather than a change in growth mechanism. This textural chemistry suggests a uniform growth rate, implying the growth rate and temperature remained stable when both “Regions 1 and 2” formed as the cement extended away from the host substrate, running parallel to it (Bathurst, 1972; Reeder, 1991; Bathurst et al., 1993; Paquette et al. 1993).

In 'Region 1,' the carbonates exhibit direct growth on the host basalt, occasionally extending onto xenoliths in some instances (Figure 5.16). The growth surface in this region is notably rough and comprises altered basaltic glass. Consequently, the resulting texture of the carbonate cement mirrors the irregular topography of the host substrate, imparting a distinct coarseness and orientation, a phenomenon previously described by Reeder in 1991. This textured appearance is exemplified by the sawtooth texture (Figure 5.13), which is indicative of the orientation of the primary carbonates. This textural profile gradually undergoes a transition as one moves further away from the host contact, leading to the development of 'Region 2' type carbonates. In 'Region 2,' the finely laminated cement grows, forming nearly horizontal parallel bands relative to the substrate. Additionally, there are instances of overlapping growth between 'Region 1' and 'Region 2' type cements in other areas of the rock, where the porous volume is also smaller (Figure 5.19).

In contrast to the gradual growth of 'Region 1' and 'Region 2' cements, 'Region 3' cement seems to have experienced a fast radial growth. The texture of “Region 3” type cements differs distinctly from the laminated carbonates that precede it. Its bladed nature demonstrates a change in growth mechanism. The cement grows perpendicular to the substrate and consists of radial fans of Ca-poor magnesite, similar to the radial fast carbonates described by Shuster *et al.* (2018), which can be attributed to a fast crystallisation kinetics of carbonates. Kendall and Tucker (1973) interpreted radiaxial cement as a replacement of an early diagenetic acicular cement. The radiaxial fans are capped by bipyramidal terminations, the transitional contact with final cement reflects this, with saw-tooth textures observed between the regions. When subjected to cathodoluminescence, the radiaxial magnesite exhibits a uniform bright blue luminescence, effectively accentuating the radiaxial texture of the cement. Notably, the bipyramidal terminations display an intense bright blue luminescence, denoting a transitional path to “Region 4”.

BSE image reveals that there is minor banding within the fans, resulting from fluctuations within the Ca/Mg ratio, ranging from 0.37 to 0.04 (average Ca/Mg ratio 0.13). This cement represents an enrichment of Mg in the system, due to the depletion of Ca following the precipitation of "Regions 1 and 2" type carbonates, resulting in a close composition to magnesite. The radial fan-like nature of the carbonate cements suggests that crystal nucleation and subsequent growth initiated at a few specific nucleation sites and under conditions of high supersaturation. Optical analysis revealed that the blades are optically continuous, indicating that the fans grew as single crystals. We suggest that the formation of these carbonates probably took place at lower temperatures compared to Regions 1 and 2, so their nucleation would have been inhibited by the strong hydration shell of Mg (Berner, 1975; Rodriguez-Blanco *et al.*, 2012; Juan Diego. Rodriguez-Blanco *et al.*, 2014).

The terminal cement, "Region 4" is a heterogeneous cement rich in Fe, consisting of not just carbonates (magnesite, siderite) but also, likely Fe oxides or hydroxides, and Fe silicates. Fe preferentially precipitated as a coating on the carbonate substrate, offering valuable insights into potential changes in redox conditions within the geological system. This potential change in redox conditions would have influenced the mobility of this Fe and promoted its precipitation as Fe-bearing phases, resulting in the formation of Fe carbonate coatings on the Ca-Mg carbonates and Fe oxides. Examination of the cement (Appendix C3) revealed that the Fe-rich layers appear to have grown through the formation of nanophases embedded within the carbonates crystals, suggesting potential pseudomorphic replacement processes where siderite may have, in part, transformed into non-carbonate solids. However, it is essential to approach this data interpretation with caution, primarily due to the limited volume of cement available for analysis (thickness < 50 μm) within 'Region 4,' coupled with the inherent challenges associated with characterizing the Fe-bearing nanophases. Therefore, further investigation of this specific cement type would require nanomaterial characterisation techniques.

Zoning

Composition zonation patterns within the carbonate cements is a distinct feature in the samples, especially in "Region 1 and 2". Zoning can provide abundant information on the changing growth and

conditions and mechanisms, fingerprinting the environmental conditions in which the crystallisation occurs (Reeder, 1991). Zoning within the Sverrefjellet carbonates principally involves variations of Ca and Mg, with minor Fe fluctuations. Comparative microscopy involving SEM-CL and EDS elemental maps, alongside EDS point and line spectra, offers valuable insights into comprehending the growth dynamics and elemental distribution within the carbonate cements. In particular, this methodology is very useful in highlighting the zoning within the samples, and can bring the distribution of Mn^{2+} into consideration (Fraser *et al.*, 1989; Reeder *et al.*, 1990; Reeder, 1991).

The prevailing interpretation of concentric compositional zoning patterns is that they primarily signify temporal changes in the composition of the fluid from which crystallization occurs (Reeder and Paquette, 1989; Reeder *et al*., 1990; Reeder, 1991; Paquette *et al*., 1993). Oscillatory zoning is a phenomenon that occurs during crystal growth and results in alternating zones of different composition within a single crystal (Shore and Fowler, 1996). Our carbonate cements are composed of Ca-Mg-Fe calcite-type carbonates that form an isomorphous series, but they do not exist as individual single crystals. Instead, they exhibit a polycrystalline or granular structure. However, in some Regions like 1 and especially 2, the carbonates show some optical continuity in the polarising microscope. As such, in this chapter, the term ‘oscillatory zoning’ will be used in its broadest sense to refer to alternation in the chemistry (mainly Ca and Mg) within the carbonate cements across micrometres in thickness.

SEM-CL imaging (Figure 5.14) revealed different luminous colours between “Regions 1 and 2” carbonates. The host basalt is dull to nonluminous, within the basaltic glass there are bladed phases that exhibit medium blue luminescence. “Region 1” exhibits two distinct zones of cathodoluminescence. The initially formed carbonate, directly in contact with the host and heavily influenced by the basalt microtopography, displays medium to bright pink luminous zones. This region corresponds to the calcian proto-dolomite, with the highest Ca content within the cements. As carbonates move further away from the host basalt boundary the luminescence changes of alternating bands of dull to medium luminous blue. This mimics the alternating light and dark banding observed with SEM-BSE, indicating fluctuations of the Ca/Mg content.

"Region 2" also exhibits two distinct zones of cathodoluminescence: Firstly, the zone (approx. 120 μm thick) in direct contact with "Region 1" that predominantly consists of bright pink luminous zones with intermittent fine laminate of blue zones. This is followed by a region of dull blue luminescence (approx. 75 μm thick). Comparative microscopy of SEM-CL images with EDS elemental maps reveals that of pink and blue luminescence correspond to areas with high Ca and high Mg content, respectively. According to (Fraser *et al.*, 1989; Reeder *et al*., 1990; Reeder, 1991; Spötl, 1991) fluctuations in the concentration and ratio of Fe^{2+} and Mn^{2+} influence cathodoluminescence. Correlating the Fe^{2+} and Mn^{2+} content obtained from EDS spectra data with the distinct pink and blue luminous zones within 'Region 2' reveals variations between the two zones. The pink luminous zone exhibits a composition of Mn^{2+} of 0.026 at% and Fe^{2+} of 0.027 at%, while the blue luminous zone shows a composition of Mn^{2+} of 0.032 at% and Fe^{2+} of 0.081 at%. Furthermore, the average Ca/Mg ratios in each zone indicate a difference, with 0.57 in the pink zone and 0.28 in the blue zone. These variations may suggest that Mn^{2+} and Fe^{2+} ions preferentially associate with higher Mg carbonate phases. However, in order to investigate this relationship, additional SEM-CL analysis combined with other techniques like LA-ICP-MS would be necessary. "Region 3" has some minor parallel banding overlapping the radial fans, suggesting a decrease in the Ca/Mg ratio due to the gradual depletion of Ca in the fluid. The region exhibits uniform bright blue luminescence. Overall, the pink luminous zones correlate to zones of higher Ca/Mg and blue luminous zones correlate to zones of lower Ca/Mg, highlighting the chemical oscillations throughout the carbonate cements.

In many areas of the thin sections SEM-BSE revealed concentric composition zonation patterns within cement nodules, see (Figure 5.24), and SEM-EDS line spectra disclosed the distribution of Mg, Ca and Fe. Within the concentric nodules, the progression from a Ca-rich interior to an Mg-enriched zone, culminating in a thin Fe-rich rim, accurately encapsulates the broader evolutionary trend in cement chemistry observed within the Sverrefjellet carbonates. Similar concentrically zoned carbonates were examined Steele *et al.* (2007), who observed zoning within carbonate globules in both ALH84001 meteorite and in (spinel lherzolite) xenoliths from Bockfjord Volcanic Complex (BVC). They found that zoning within the BVC globules finely oscillated from Fe-rich magnesite in

the core to almost pure magnesite at the rim, with an outer magnetite rim. They hypothesized that similarities between samples suggest similar formation, via cooling of hydrothermal fluids in a single deposition event.

Chemical evolution of carbonates

Using ternary diagrams to plot the proportions of Ca, Fe, and Mg (normalized to 100%) serves as a valuable tool for gaining insights into the geochemical evolution of the carbonate cements within the magnesite-calcite-siderite compositional range. Ternary plots of carbonate phase compositions from SEM-EDS spectra demonstrate that the differences between these regions is not limited to textural differences, but also changes in Ca, Fe and Mg content.

The intricate interplay between several environmental factors and the evolving geochemical conditions within the system is likely responsible for the observed trends in carbonate chemistry, including the transition towards higher Mg/Ca ratios as the distance from the source increases. Starting from a composition close to a calcian proto-dolomite (in contact with the host basalts), this gradually evolves towards Ca-magnesite as the cement transitions further away from the host contact. The final two regions (3 and 4) exhibit a trend towards ferro-magnesite. This general trend towards magnesite followed by a sharp trend towards ferro-magnesite can be clearly seen in Figure 5.20**.**

Fluctuations in the Ca-Mg content are observed throughout the cements. Quantitative analyses reveal a consistent trend of decreasing calcium concentrations as one moves further away from the host or source. Region 1 has three distinct compositions, with increasing Mg content (Figure 5.21). The carbonates oscillated between three compositions from calcian proto-dolomite to dolomite to calcian-magnesite composition, covering a Mg range from 0.35 to 0.84. While this cement has an overall pattern of increasing magnesite composition, this increasing trend is not linear. The oscillating magnesite composition can be observed in SEM-BSE, demonstrated by the sawtooth texture of apical sections of calcite type carbonate rhombs, light (Ca-rich) within a dark (Mg-rich) carbonate groundmass. SEM-CL also highlights the changing Ca-Mg amounts with varying luminescence

intensity: Higher Mg areas correlate to bright blue luminescence, while lower Mg show a dull blue luminescence. Region 2 carbonates continue this oscillating upward trend towards a magnesite composition (Figure 5.22), evolving from dolomite to calcian-magnesite, covering a Mg range of 0.53 to 0.92 %.

Regions 3 and 4 represent a transition toward ferro-magnesite, as shown in Figure 5.23 and Figure 5.24. It is crucial to keep in mind that compositions exceeding 50% Fe in these regions are likely to contain micro- or nano-sized inclusions of non-Fe carbonates, such as Fe-oxides or Fe-silicates. This observation holds particular significance within the heterogeneous “Region 4”.

The Ca/Mg ratio of “Region 1” type cements is up to 1.81 (average Ca/Mg 0.50), whereas the Ca/Mg ratio of “Region 3” is up max 0.37 (average Ca/Mg 0.13). This suggests a spatial variation in the composition of the carbonates, likely influenced by local geochemical conditions and the availability of Ca ions within the surrounding environment. The fluctuating cationic composition of the carbonates mirrors the changes in the fluid composition, giving rise to episodic crystallization events.

The general increase in the proportion of magnesite composition within the carbonates can be attributed to the higher abundance of Mg within the system. Though siderite is not as abundant as calcium-magnesium carbonates, Fe-bearing minerals are still present within the cement within the fractures and as distinct phases, notably within the “Region 4” cement. This observation suggests that at certain points in time, the concentration of Fe was sufficiently high to facilitate the crystallization of discreet phases, even forming single crystals. The cross-cutting nature of the Fe-bearing fractures suggests a subsequent minor brittle deformation of the cement post-mineralization, accompanied by the mobilization of iron-bearing fluids.

Mg is the dominant cation within this system, as such it is important to understand the behaviour of Mg within the context of basalt carbonation. When examining the influence of Ca in $MgCO_3$ crystallisation, Berninger *et al.* (2016) found that while Ca^{2+} is incorporated into growing

$MgCO_3$ seeds, there is little to no noticeable effect on the growth rate, contrary to the inhibiting influence of Mg^{2+} on $CaCO_3$ growth. This is due to differences in hydration shell. Mg^{2+} inhibits $CaCO_3$ growth due to its dehydration from solution, as Ca^{2+} has a weaker hydration shell it does not influence the $MgCO_3$ growth rate. Other experimental studies and geochemical modelling allow a deeper insight into the role of Mg in CO_2 sequestration via mineralisation. Rosenbauer *et al.*, (2012) coupled high pressure experiments and thermodynamic equilibrium models reacting basalt with CO_2-charged fluids from 50 to 200 °C at 300 bar, as well as geochemical modelling results. They concluded that the Mg content within the basalt plays a pivotal role in determining the amount of CO_2 sequestered by the rock. An average basaltic MgO content of 8% would facilitate the sequestration of approximately $2.6 \cdot 10^8$ metric tons of CO_2 / Km^3 of basalt. However, the formation of Mg-rich clays (i.e. smectites) can inhibit the formation of carbonates, as the cations are consumed. Oelkers *et al.* (2019) studied stable Mg^{2+} isotope signatures to assess the fate of Mg^{2+} during the in situ mineralisation of CO_2 at the CarbFix Project. Their isotope mass balance calculations suggest that more than 70% of the Mg^{2+} liberated from the host rock by the injected gas charged water had precipitated as Mg-clays. They predict that the percentage will increase over the duration of the study period.

Dissolution of host basalt and origin of the carbonates

The supply of Ca, Mg and Fe is directly related to the dissolution of the host basalt and the rates of dissolution are dependent on the fluid temperature and pH (Snæbjörnsdóttir *et al.*, 2020). There are numerous studies examining the dissolution of divalent metal-bearing silicates, including the phases present within the Sverrefjellet samples, e.g. enstatite (Oelkers and Schott, 2001), forsterite (Oelkers *et al.*, 2018) and anorthite (Oelkers and Schott, 1995) as well as volcanic glass (Oelkers and Gislason, 2001; Gislason and Oelkers, 2003, etc.). Recently Heřmanská *et al.* (2022) published a comprehensive database on the mineral dissolution rates of primary silicate minerals and glasses. In turn the dissolution rates of primary silicate minerals and glasses are dependent on the pH of the aqueous

solution, as well as the water composition, the partial pressure of CO_2 (pCO_2) and the temperature of the system (Snæbjörnsdóttir *et al.*, 2020).

The pH of acidic gas-charged water (*Equation 1*) is typically 3–5 (Snæbjörnsdóttir *et al.*, 2020). At lower pH the forsterite is more soluble and its dissolution rate is faster compared to basic pH. However, within the pH range of 6-8, it becomes feasible to dissolve forsterite and release sufficient Mg to create supersaturation conditions conducive to the formation of certain carbonates, such as magnesite. (Oelkers *et al.*, 2018; Snæbjörnsdóttir *et al.*, 2020). For example, while PHREEQC indicates that magnesite is supersaturated at a P_{CO2} of 1 atm (Appendix C4), particularly within the temperature range of 10-180 °C and at pH levels ranging from 6.2 to 9.3, it is important to consider that this phase is kinetically inhibited at temperatures below 60 °C. Therefore, the more realistic range of magnesite supersaturation at that partial pressure is limited to the pH range of 6.2-7.6 within the temperature range of 70-180 °C. This fits within the pH range permitting sufficient dissolution of forsterite and magnesite precipitation.

The assessment of supersaturation conditions, as calculated using PHREEQC, provides saturation indices for minerals such as magnesite, hydromagnesite, nesquehonite, dolomite, and calcite. These indices have been determined across a spectrum of pH and temperature values, encompassing various levels of partial pressure of CO_2 (pCO_2) as shown in Appendix C4. This reveals the feasibility of achieving mineral carbonation processes, particularly for minerals like forsterite and enstatite, resulting in the formation of magnesite or magnesium carbonates. Importantly, this feasibility also extends to relatively low-temperature conditions when a specific range of $CO_{2(g)}$ pressure conditions are applied. Reaction path modelling by Snæbjörnsdóttir *et al.* (2018) of the mineralisation at the CarbFix site revealed a "sweet spot" for CO_2 mineralisation at the pH range ~5.2-6.5 in basalts at low temperature (20-50 °C)". This sheds some light on the potential temperature conditions during the mineralisation of the Sverrefjellet carbonates.

The origin of the Mg-rich carbonates found at the BVC have been interpreted as precipitating from hydrothermal carbonate-bearing fluids associated with volcanic activity (Treiman *et al.*, 2002; Steele *et al.*, 2007; Morris *et al.*, 2010, 2011; Blake *et al.*, 2011). It has also been suggested that the

carbonates are cryogenic in origin (Amundsen *et al.*, 2011). These authors agree with the hydrothermal origin of the carbonates, several factors could contribute to this observation, primarily bases on the abundance of Mg-carbonates. Treiman *et al.* (2002) present several arguments supporting the hydrothermal origins of the carbonates. Firstly the variations in zoning patterns and mineral compositions (e.g., this paper, Amundsen *et al.*, 2011; Blake *et al.*, 2011; Morris *et al.*, 2011) suggest highly local sources of carbonates, rather than an extensive regional reservoir, i.e. seawater. The subglacial erruptive nature of Sverrefjellet is consistent with this localised hydrothermal origin (Skjelkvåle *et al.*, 1989). Stable isotope compositions from Golden *et al.* (2000) suggest a near-surface reservoir for the carbon and oxygen, further supporting the hydrotheraml origin for carbonates. Perhaps the most significant argument for hydrothermal origin is the prevalence of magnesite, which is reported in several studies (e.g. this paper, Amundsen *et al.*, 2011; Blake *et al.*, 2011; Morris *et al.*, 2011 etc.), which indicates above ambient temperatures. The nucleation of these carbonates at low temperature is inhibited by the strong hydration shell of Mg^{2+}. However, it is worth mentioning that these carbonates represent the final stage of crystallisation, intermediate phases may have transformed and undergone diagenesis. Hydrated Ca- and/or Mg-bearing carbonates like monohydrocalcite, hydromagnesite, or nesquehonite can indeed form and remain metastable under low hydrothermal conditions (< 60 ºC) before transforming into more stable anhydrous phases (e.g., Rodriguez-Blanco *et al.*, 2014; 2015 and references therein), While it is plausible these hydrated phases initially formed and subsequently underwent recrystallization into magnesite, powder XRD and SEM revealed no remnants or traces of these hydrated carbonates or discernible replacement textures indicative of such a process in any of the samples. Treiman et al. (2002) also identified the zeolite chabazite amount the carbonates, noting it as a characteristic hydrothermal mineral. The identification of small Al-rich regions in the EDS maps, particularly in proximity to the basaltic glass, raises the possibility of the presence of minerals such as clays, zeolites (e.g., chabazite), or gibbsite. Nonetheless, it is essential to note that none of these minerals have been detected through powder XRD analysis. Additionally, SEM-SE images and maps (Figure 5.11) suggest that these Al-bearing minerals could potentially exist in nanosized forms, a circumstance that would indeed pose challenges in their detection and characterization.

Kinetic determinations

Temperature plays a pivotal role in this hydrothermal system, which originated from a volcanic eruption beneath a layer of blue glacier ice (Skjelkvåle *et al.*, 1989; Amundsen *et al.*, 2011; Blake *et al.*, 2011). As previously discussed, temperature influences the dissolution of host mineral, leading to the release of cations into solution and the resulting carbonation, which did not necessarily need to occur at very high temperatures.

In order for Mg carbonates to crystallise, the kinetic threshold due to Mg^{2+} strong hydration shell must be surpassed, this require temperatures to facilitate dehydration. The temperatures associated with this environment are conducive to the growth of both dolomite and Mg-rich carbonates. At the CarbFix project, Iceland, calcite is the main carbonate phase mineralising, unlike the magnesite-rich carbonates mineralise principally at Sverrefjellet. This could indicate that the Sverrefjellet carbonates formed at higher temperature (compared to the CarbFix site), promoting the dehydration of the Mg^{2+} ions from solution prior to their incorporation into growing crystals. Matter *et al.* (2016) reported the mineral trapping occurs at 20- 50°C at the CarbFix site within 2 years post-injection.

SEM-BSE analysis has unveiled a discernible pattern of episodic crystallization, indicating the occurrence of distinct phases of carbonate growth that are likely associated with different growth mechanisms. Experimental studies have further demonstrated the substantial impact of temperature and chemical composition (Mg/Ca ratios) of the fluids responsible for dolomitization e.g. (Kaczmarek and Thornton, 2017; Zvir *et al.*, 2021; Pina *et al.*, 2022). The presence of calcian proto-dolomite ($Mg_{0.35\text{-}0.42}$ $Ca_{0.58\text{-}0.64}$) within “Region 1” can offer further insight into the initial carbonation. Experimental evidence suggests that the formation of such Ca-rich dolomite often occurs in mild hydrothermal conditions, even at relatively low temperatures, even as low as 60 °C (Rodriguez-Blanco *et al.*, 2015). Proto-dolomite cement typically arises from a poorly-ordered precursor and may undergo a protracted transformation into dolomite over geologic timescales (Pina *et al.*, 2022). Non-

stoichiometric, disordered Ca-rich dolomite typically exhibits small crystallite sizes, resulting in broad Bragg peaks in X-ray diffraction patterns, which aligns with the patterns obtained from our samples Figure 5.9. Note, the Bragg peak of stoichiometric ordered dolomite is 2.89 Å (Zvir *et al.*, 2021; Pina *et al.*, 2022) whereas the Bragg peaks of the non-stoichiometric, disordered Ca-rich dolomite exhibited broadness and asymmetry, indicative of compositional variations within the solid solution (Morris *et al.*, 2011).

Sverrefjellet carbonates as analogues

Basaltic CCS analogue:

The carbonation of the Sverrefjellet basalts provides a natural analogue for *in situ* basaltic carbon capture and storage (CCS), such as the CarbFix Project (e.g. Alfredsson *et al.*, 2008; Matter *et al.*, 2016; Snæbjörnsdóttir *et al.*, 2017, 2018, 2020, etc.). Carbfix involves the injection of CO_2-bearing solutions into a subsurface permeable basaltic reservoir 500-800 at metres depth.

Alfredsson *et al.* (2008, 2013) reported the geology and geochemistry of CarbFix injection site as an olivine tholeiite basalt, comprised of lava flows and hyaloclastite formations. Major element analysis of rock samples revealed that the total concentration of key carbonate forming divalent cations Ca-Mg-Fe (cation oxides CaO, MgO,and FeO), ranged from 25 to 33% of the rocks (Alfredsson et al., 2013). The hyaloclastites have low permeability and act as cap rock during injection and have alterations zones consist of smectite, calcite, Ca-rich zeolites, these alteration zones further reduce the permeability of the hyaloclastites. Alfredsson et al. (2013) found that the water in the target injection zones are supersaturated with respect to non-carbonates: Ca-zeolite, analcime, Ca–Mg–Fe smectite, as well as calcite, and aragonite.

The pilot injections revealed that within two years over 95% of the injected CO_2 was mineralised, with calcite being the primary carbonates formed, (Matter *et al.*, 2016; Snæbjörnsdóttir *et al.*, 2017). Since injection started in 2014 at the Carbfix site in Hellisheiði, Iceland, over 70,000 tons of CO_2 have been successfully stored (Snæbjörnsdóttir *et al.*, 2021).

A key difference between carbonate mineralisation of the alkali basaltic at Sverrefjellet the olivine tholeiite basaltic present at Hellisheiði, Iceland, is the abundance of Mg-rich xenoliths, rich minerals like forsterite (Mg_2SiO_4) and enstatite (Mg_2Si2O_6), present in the Sverrefjellet, which is in places high as 40-60 vol.% (Amundsen, 1987; Skjelkvåle et al., 1989; Ionov et al., 1993, 1996). The high amounts of Mg drives the mineralisation of Mg-rich carbonates at Sverrefjellet, whereas the CarbFix carbonates are Mg-poor "the cation concentration of the precipitates consisted mostly of calcium (>94%) with some iron (<3%), silica (<2%) and magnesium (<1%)" (Snæbjörnsdóttir *et al.*, 2017).

Snæbjörnsdóttir *et al.* (2017, 2018) calculated the saturation indices of calcite, magnesite and siderite using PHREEQC, as well as continuous monitoring of the solution saturation states throughout injection. They found that calcite became supersaturated approximately 100 days after the start of each injection, resulting in the fixation of the CO_2 into precipitated calcite. Unlike the Sverrefjellet carbonates, neither magnesite nor dolomite were identified, despite monitoring of the fluids revealed the saturation states was similar to calcite; Snæbjörnsdóttir *et al.* (2017) suggest that the lack of magnesite and dolomite precipitation could be attributed to temperature induced kinetic inhibition. As previously stated, during the mineralisation of the Sverrefjellet carbonates temperatures associated with this environment would have to be high enough conducive for the growth of both dolomite and Mg-rich carbonates.

Martian carbonate analogue

Sverrefjellet samples have been discussed as terrestrial analogues for Martian carbonates due to chemical similarities and the carbonate globules hosted in the ALH 84001 Martian meteorite. As such, the Sverrefjellet carbonates provide insight into the potential carbonate formation conditions on Mars.

Martian paleolakes, such as Jezero, Gale and Gustav, are (proposed) sites of carbonate deposition, as such they have been areas of interest and discovery by Mars Exploration Rover (MER)

Spirit, the Mars Science Laboratory (MSL) *Curiosity*, and the *Perseverance* rover (McLennan *et al.*, 2019). Data from the MER *Spirit* at the Columbia Hills of Gusev crater revealed that carbonates found at the Comanche outcrops (Comanche and Comanche Spur) are abundant through the outcrops and have a Mg-Fe rich bulk chemical composition, consisting of 16 to 34 weight percent, which is similar to the ALH84001 meteorite carbonate weight percent (Morris *et al.*, 2010, 2011). MER *Spirit*'s Mössbauer spectrometer (MIMOS II) was used for quantitative mineralogical analysis of Fe-bearing materials (Klingelhöfer *et al.*, 2003) and it revealed that the Comanche Spur is an assemblage of Fe^{2+}-bearing olivine and Fe^{2+}-bearing carbonate (Morris *et al.*, 2010). The carbonates are low in Ca, and Mn, as revealed by *Spirit*'s Alpha Particle X-Ray Spectrometer (APXS). Morris *et al.* (2010) calculated the chemical composition of the Comanche carbonates, reporting "Mg-Fe carbonate ($Mc_{0.62}Sd_{0.25}Cc_{0.11}Rh_{0.02}$, where Mc = magnesite, Sd = siderite, Cc = calcite, and Rh = rhodochrosite) and a forsteritic olivine ($Fo_{0.72}Fa_{0.28}$,where Fo = forsterite and Fa = fayalite)". Morris *et al.* (2011) carried out Mössbauer spectroscopy on the Spitsbergen carbonates, as terrestrial analogue for the Comanche carbonates, fortifying their earlier interpretation of the origin of the Comanche carbonates. Morris *et al.* (2010) speculates that the Gusev carbonates are secondary and precipitated from hydrothermal carbonate-bearing fluids at near neutral pH, associated with volcanic activity during the Noachian era (4.1- 3.7 Ba). Previous studies evaluating the origin of Martian carbonates have drawn parallels to the Mg-rich carbonates found at the BVC, interpreting precipitation from hydrothermal carbonate-bearing fluids associated with volcanic activity (Treiman *et al.*, 2002; Steele *et al.*, 2007; Morris *et al.*, 2010, 2011; Blake *et al.*, 2011).

Limitations:

While the results demonstrated in this chapter provide insight into the geochemical conditions during basalt carbonation, it is important to note that there presents some limitations.

Regarding the ternary plots that show a final trend towards ferro-magnesite (Region 3: Figure 5.23 and Region 4: Figure 5.24), these data must be interpreted with caution because the presence of non-carbonate iron bearing phases. Due to the heterogeneous nature of "Region 4" type cement, there is potential for bias towards siderite composition due to inflated Fe content, compositions of greater

than 50% Fe likely include μ- or nano- inclusions of non Fe-carbonates (e.g. Fe-oxides or Fe-silicates). While we made careful efforts to selectively sample specific areas using a precision micro drill, it is important to exercise caution when interpreting the results, especially for 'Region 4' where the cement is exceedingly thin (< 50 μm thickness). Contamination of samples is a distinct possibility and should be taken into account.

5.7 CONCLUSIONS

We carried out a study of the geochemistry of the carbonate cements that precipitated *in situ* following the eruption of the Sverrefjellet volcano in Svalbard. Samples represent *in situ* carbonation of basalt, a natural analogue of carbon capture and storage via basaltic mineralisation projects, such as CarbFix, Iceland. This study demonstrated the influence of the geochemistry of the host basaltic rock during the carbonation process.

The correlation of petrography, XRD results, SEM, cathodoluminescence, elemental compositional data provides insight into the mechanisms behind the carbonation sequence, allowing a better understanding of the chemical texture of the cements, the influence of the basaltic host rock and the evolution of the sample.

Carbonation occurs due to the interplay of temperature, pressure, pH, the dissolution of the basalt host and the availability of CO_2. The carbonate cements consist of calcite-type carbonates within the magnesite-calcite-siderite compositional range. Textural differences within cements, reveals several stages of carbonation, during which the minerals evolve from a composition close to a calcian proto-dolomite, this gradually evolves towards Ca-magnesite as the cement transitions further away from the host contact, the carbonate cement further evolves towards ferro-magnesite and is ultimately followed by a terminal iron rich carbonate and non-carbonate cement. These observed textural and compositional changes in the carbonate cement align with variations in the kinetics and mechanisms of carbonate precipitation. These variations are driven by the shifting Ca/Mg ratios as the cement progresses away from the host rock.

Through an examination of the geochemistry and texture of the Sverrefjellet carbonates, these formations offer a natural analogue for the mineralization of basalts from multicomponent solutions in the context of carbon capture and storage. The chemistry of the host basalt directly influenced the resulting carbonate cements. The dissolution of Mg-rich silicate phases, such as forsterite and enstatite, result in Mg as the most abundant cation forming carbonates in the system. The carbonation conditions (e.g., basalt dissolution following the interaction with CO_2-rich fluids) at Sverrefjellet provide a natural analogue for CCS via mineralisation. Calcite is the main carbonate phase mineralising at CarbFix (Iceland) whereas magnesite-rich carbonates mineralise principally at Sverrefjellet, indicating that the Sverrefjellet carbonates likely formed at higher temperature compared to the CarbFix site, allowing Mg^{2+} dehydration from solution prior to incorporation into growing crystals. These findings significantly enhance our comprehension of mineral-fluid interactions and the subsequent carbonation processes within basaltic reservoirs.

5.8 REFERENCES

Alfredsson, H. A. et al. (2008) ‘CO2 sequestration in basaltic rock at the Hellisheidi site in SW Iceland: stratigraphy and chemical composition of the rocks at the injection site’, Mineralogical Magazine. GeoScienceWorld, 72(1), pp. 1–5. doi: 10.1180/MINMAG.2008.072.1.1.

Alfredsson, H. A. et al. (2013) ‘The geology and water chemistry of the Hellisheidi, SW-Iceland carbon storage site’, International Journal of Greenhouse Gas Control, 12, pp. 399–418. doi: 10.1016/j.ijggc.2012.11.019.

Amundsen, H. E. F. (1987) ‘Evidence for liquid immiscibility in the upper mantle’, Nature . Nature Publishing Group, 327(6124), pp. 692–695. doi: 10.1038/327692a0.

Amundsen, H. E. F. et al. (2011) ‘Cryogenic Origin for Mars Analog Carbonates in the Bockfjord Volcanic Complex Svalbard (Norway)’.

Amundsen, H. E. F., Griffin, W. L. and O’reilly, S. Y. (1987) ‘The lower crust and upper mantle beneath northwestern Spitsbergen: evidence from xenoliths and geophysics’, Tectonophysics. Elsevier, 139(3–4), pp. 169–185. doi: 10.1016/0040-1951(87)90095-3.

Archer, D. (2005) ‘Fate of fossil fuel CO2 in geologic time’, Journal of Geophysical Research C: Oceans. doi: 10.1029/2004JC002625.

Arvidson, R. S. and Mackenzie, F. T. (1999) ‘The dolomite problem; control of precipitation kinetics by temperature and saturation state’, American Journal of Science. American Journal of Science, 299(4), pp. 257–288. doi: 10.2475/AJS.299.4.257.

Bathurst, R. G. C. (1972) Carbonate Sediments and Their Diagenesis. 2nd edn. Elsevier.

Bathurst, R. G. C., Rezak, R. and Lavoie, D. L. (1993) Carbonate Microfabrics. Edited by R. Rezak and D. L. Lavoie. New York, NY: Springer New York (Frontiers in Sedimentary Geology). doi: 10.1007/978-1-4684-9421-1.

Berner, R. A. (1975) ‘The role of magnesium in the crystal growth of calcite and aragonite from sea water’, Geochimica et Cosmochimica Acta. Pergamon, 39(4), pp. 489–504. doi: 10.1016/0016-7037(75)90102-7.

Berninger, U. N. et al. (2016) ‘On the effect of aqueous Ca on magnesite growth – Insight into trace element inhibition of carbonate mineral precipitation’, Geochimica et Cosmochimica Acta. Pergamon, 178, pp. 195–209. doi: 10.1016/J.GCA.2016.01.019.

Blake, D. F. et al. (2011) ‘Carbonate cements from the Sverrefjell and Sigurdfjell volcanoes, Svalbard Norway: analogues for Martian carbonates’, in 42nd Lunar and Planetary Science Conference.

Burov, Y. P. and Zagruzina, I. A. (1976) ‘Results of a determination of the absolute age of Cenozoic basic rocks of the northern part of the island of Spitsbergen (translated from Russian)’, Geologija Sval’barda, pp. 139–140.

Coelho, A. A. et al. (2011) ‘The TOPAS symbolic computation system’, Powder Diffraction. Cambridge University Press, 26(S1), pp. S22–S25. doi: 10.1154/1.3661087.

Crane, K. et al. (2001) ‘The role of the Spitsbergen shear zone in determining morphology, segmentation and evolution of the Knipovich Ridge’, Marine Geophysical Research. Springer Netherlands, 22(3), pp. 153–205. doi: 10.1023/A:1012288309435/METRICS.

Dallmann, W. . et al. (1999) ‘Lithostratigraphic Lexicon of Svalbard. Review and Recommendations for Nomenclature Use. Upper Paleozoic to Quaternary Bedrock.’, Norsk Polarinstitut, p. 325.

Dana, E. S. (1932) Dana’s Textbook of Mineralogy . 4th edn. Edited by W. . Ford. New York: John Wiley and Sons.

Dörr, N. et al. (2019) ‘Cenozoic development of northern Svalbard based on thermochronological data’, Terra Nova. John Wiley & Sons, Ltd, 31(3), pp. 306–315. doi: 10.1111/TER.12402.

Ehlmann, B. L. et al. (2008) ‘Orbital identification of carbonate-bearing rocks on Mars’, Science. American Association for the Advancement of Science , 322(5909), pp. 1828–1832. doi: 10.1126/SCIENCE.1164759/SUPPL_FILE/EHLMANN-SOM.PDF.

Ellis, A. J. (1959) ‘The solubility of calcite in carbon dioxide solutions’, American Journal of Science. American Journal of Science, 257(5), pp. 354–365. doi: 10.2475/AJS.257.5.354.

Ellis, A. J. (1963) ‘The solubility of calcite in sodium chloride solutions at high temperatures’, American Journal of Science. American Journal of Science, 261(3), pp. 259–267. doi: 10.2475/AJS.261.3.259.

Elvevold, S., Dallmann, W. and Blomeier, D. (2007) Geology of Svalbard. Edited by S. Elvevold. Norsk Polarinstitutt. Available at: https://brage.npolar.no/npolar-xmlui/handle/11250/173141 (Accessed: 13 February 2023).

Evdokimov, A. . et al. (1991) ‘Kajnozojskij magmatizm, gidrotermal’naja dejatel’nost’ i perspektivy rudonosnosti zony razlomov Ekman-fiord–Vud-fiord, ostrov Zapadnyj Špicbergen. (Cenozoic magmatism, hydrothermal activity and ore potential of Ekmanfjorden and Woodfjorden fault zone, Spi’, PGO Sevmorgeologija.

Flügel, E. (2010) ‘Microfacies of Carbonate Rocks’, Microfacies of Carbonate Rocks. Springer Berlin Heidelberg. doi: 10.1007/978-3-642-03796-2.

Folk, R. L. (1964) ‘Recrystallisation of ancient limestones’, AAPG Bulletin. GeoScienceWorld, 48(4), pp. 525–526. doi: 10.1306/BC743C61-16BE-11D7-8645000102C1865D.

Folk, R. L. (1965) ‘Some Aspects of Recrystallization in Ancient Limestones’, Dolomitization and Limestone Diagenesis. SEPM Society for Sedimentary Geology. doi: 10.2110/PEC.65.07.0014.

Fraser, D. G., Feltham, D. and Whiteman, M. (1989) ‘High-resolution scanning proton microprobe studies of micron-scale trace element zoning in a secondary dolomite: implications for studies of redox behaviour in dolomites’, Sedimentary Geology. Elsevier, 65(3–4), pp. 223–232. doi: 10.1016/0037-0738(89)90024-9.

Gadikota, G. et al. (2014) ‘Chemical and morphological changes during olivine carbonation for CO 2 storage in the presence of NaCl and NaHCO 3’, Physical Chemistry Chemical Physics. Royal Society of Chemistry, 16(10), pp. 4679–4693. doi: 10.1039/C3CP54903H.

Gayer, R. . et al. (1966) ‘Radiometric age determinations on rocks from Spitsbergen’. Oslo.

Gee, D. G., Bogolepova, O. K. and Lorenz, H. (2006) ‘The Timanide, Caledonide and Uralide orogens in the Eurasian high Arctic, and relationships to the palaeo-continents Laurentia, Baltica and Siberia’, Geological Society Memoir, 32, pp. 507–520. doi: 10.1144/GSL.MEM.2006.032.01.31.

Gee, D. G. and Teben’kov, A. M. (2004) ‘Svalbard: a fragment of the Laurentian margin’, in The Neoproterozoic Timanide Orogen of Eastern Baltica. London: Geological Society of London, pp. 191–206. doi: 10.1144/GSL.MEM.2004.030.01.16.

Gislason, S. and Oelkers, E. (2014) ‘Carbon Storage in Basalt’, Science, 334, pp. 373–374.

Gislason, S. R. et al. (2014) ‘Rapid solubility and mineral storage of CO2 in basalt’, in Energy Procedia. Elsevier Ltd, pp. 4561–4574. doi: 10.1016/j.egypro.2014.11.489.

Gislason, S. R. and Oelkers, E. H. (2003) ‘Mechanism, rates, and consequences of basaltic glass dissolution: II. An experimental study of the dissolution rates of basaltic glass as a function of pH and temperature’, Geochimica et Cosmochimica Acta. Pergamon, 67(20), pp. 3817–3832. doi: 10.1016/S0016-7037(03)00176-5.

Golden, D. C. et al. (2000) ‘An experimental study on kinetically-driven precipitation of calcium-magnesium-iron carbonates from solution: Implications for the low-temperature formation of carbonates in martian meteorite Allan Hills 84001’, Meteoritics & Planetary Science. John Wiley & Sons, Ltd, 35(3), pp. 457–465. doi: 10.1111/J.1945-5100.2000.TB01428.X.

Gregg, J. M. et al. (2015) ‘Mineralogy, nucleation and growth of dolomite in the laboratory and sedimentary environment: A review’, Sedimentology. John Wiley & Sons, Ltd, 62(6), pp. 1749–1769. doi: 10.1111/SED.12202.

Griffin, W. L. et al. (2012) ‘Coupling, decoupling and metasomatism: Evolution of crust–mantle relationships beneath NW Spitsbergen’, Lithos. Elsevier, 149, pp. 115–135. doi: 10.1016/J.LITHOS.2012.03.003.

Gysi, A. P. and Stefánsson, A. (2012) ‘CO2-water–basalt interaction. Low temperature experiments and implications for CO2 sequestration into basalts’, Geochimica et Cosmochimica Acta. Pergamon, 81, pp. 129–152. doi: 10.1016/J.GCA.2011.12.012.

Harland, W. B. (1997) The Geology of Svalbard. Edited by W. B. Harland. Geological Society, London.

Harland, W. B. and Butterfield, N. J. (1997) ‘Chapter 12: Pre-Vendian history’, in Harland, W. B. (ed.) The Geology of Svalbard, Geological Society Memoir 17. London : Geological Society, London, pp. 227–243. doi: 10.1144/GSL.MEM.1997.017.01.12.

Harland, W. B., Hambrey, M. L. and Waddams, P. (1993) Vendian Geology of Svalbard. Oslo: NORSK POLARINSTITUTT.

Heřmanská, M. et al. (2022) ‘A comprehensive and internally consistent mineral dissolution rate database: Part I: Primary silicate minerals and glasses’, Chemical Geology. Elsevier, 597, p. 120807. doi: 10.1016/J.CHEMGEO.2022.120807.

Hoel, A. (1914) ‘Nouvelles observations sur le district volcanique du Spitsberg du Nord.’, Skrifter udgivne af Videnskabssekskabet i Kristiania. Mat.-Natuurv,t., K1, pp. 1–33.

Hoel, A. and Holtedahl, O. (1911) ‘Les nappes de lave, les volcans et les sources thermales dans les environs de la Baie Wood au Spitsberg’, Vid. Selsk. Skr. I. Nat. kl. , 8.

Ionov, D. A. et al. (1993) ‘Carbonated peridotite xenoliths from Spitsbergen: implications for trace element signature of mantle carbonate metasomatism’, Earth and Planetary Science Letters. Elsevier, 119(3), pp. 283–297. doi: 10.1016/0012-821X(93)90139-Z.

Ionov, D. A. et al. (1996) ‘Carbonate-bearing mantle peridotite xenoliths from Spitsbergen: Phase relationships, mineral compositions and trace-element residence’, Contributions to Mineralogy and Petrology. Springer Verlag, 125(4), pp. 375–392. doi: 10.1007/S004100050229/METRICS.

Ionov, D. A., Mukasa, S. B. and Bodinier, J. L. (2002) ‘Sr–Nd–Pb Isotopic Compositions of Peridotite Xenoliths from Spitsbergen: Numerical Modelling Indicates Sr–Nd Decoupling in the Mantle by Melt

Percolation Metasomatism', Journal of Petrology. Oxford Academic, 43(12), pp. 2261–2278. doi: 10.1093/PETROLOGY/43.12.2261.

Johnson, N. C. et al. (2014) 'Olivine dissolution and carbonation under conditions relevant for in situ carbon storage', Chemical Geology. Elsevier, 373, pp. 93–105. doi: 10.1016/J.CHEMGEO.2014.02.026.

Kaczmarek, S. E. and Thornton, B. P. (2017) 'The effect of temperature on stoichiometry, cation ordering, and reaction rate in high-temperature dolomitization experiments', Chemical Geology. Elsevier, 468, pp. 32–41. doi: 10.1016/J.CHEMGEO.2017.08.004.

Karsil'ščikov, A. A. (1996) Soviet geological research in Svalbard 1962-1992 : extended abstracts of unpublished reports, 105. Norsk polarinstitutt.

Kelemen, P. B. et al. (2011) 'Rates and Mechanisms of Mineral Carbonation in Peridotite: Natural Processes and Recipes for Enhanced, in situ CO2 Capture and Storage', https://doi.org/10.1146/annurev-earth-092010-152509. Annual Reviews , 39, pp. 545–576. doi: 10.1146/ANNUREV-EARTH-092010-152509.

Kendall, A. C. and Tucker, M. E. (1973) 'Radiaxial fibrous calcite: a replacement after acicular carbonate', Sedimentology. John Wiley & Sons, Ltd, 20(3), pp. 365–389. doi: 10.1111/J.1365-3091.1973.TB01616.X.

Klingelhöfer, G. et al. (2003) 'Athena MIMOS II Mössbauer spectrometer investigation', Journal of Geophysical Research: Planets. John Wiley & Sons, Ltd, 108(E12), p. 8067. doi: 10.1029/2003JE002138.

Matter, J. M. et al. (2016) 'Rapid carbon mineralization for permanent disposal of anthropogenic carbon dioxide emissions', Science. American Association for the Advancement of Science, 352(6291), pp. 1312–1314. doi: 10.1126/science.aad8132.

McGrail, B. P. et al. (2017) 'Field validation of supercritical CO2 reactivity with basalts', Environmental Science and Technology Letters, 4(1). doi: 10.1021/acs.estlett.6b00387.

McLennan, S. M. et al. (2019) ‘The sedimentary cycle on early mars’, Annual Review of Earth and Planetary Sciences. Annual Reviews Inc., 47, pp. 91–118. doi: 10.1146/ANNUREV-EARTH-053018-060332.

Morris, R. V. et al. (2010) ‘Identification of carbonate-rich outcrops on Mars by the spirit rover’, Science. American Association for the Advancement of Science, 329(5990), pp. 421–424. doi: 10.1126/SCIENCE.1189667/SUPPL_FILE/MORRIS.SOM.PDF.

Morris, R. V et al. (2011) ‘A Terrestrial Analogue from Spitsbergen (Svalbard, Norway) for the Comanche Carbonate at Gusev Crater, Mars’, in 42nd Lunar and Planetary Science Conference. Woodlands.

Nikitina, L. P. et al. (2022) ‘Xenoliths of High-Alumina Pyroxenites in the Basalts of the Sigurd Volcano, Spitsbergen Island (Svalbard Archipelago), as Indicators of the Paleozoic Geodynamics of the Regional Lithosphere’, Russian Geology and Geophysics. GeoScienceWorld, 63(10), pp. 1093–1110. doi: 10.2113/RGG20214389.

Nøttvedt, A. et al. (1993) ‘Svalbard-Barents Sea correlation: A short review’, Norwegian Petroleum Society Special Publications, 2(C), pp. 363–375. doi: 10.1016/B978-0-444-88943-0.50027-7.

Oelkers, E. H. et al. (2018) ‘Olivine dissolution rates: A critical review’, Chemical Geology. Elsevier, 500, pp. 1–19. doi: 10.1016/J.CHEMGEO.2018.10.008.

Oelkers, E. H. et al. (2019) ‘Using stable Mg isotope signatures to assess the fate of magnesium during the in situ mineralisation of CO2 and H2S at the CarbFix site in SW-Iceland’, Geochimica et Cosmochimica Acta, 245. doi: 10.1016/j.gca.2018.11.011.

Oelkers, E. H. and Gislason, S. R. (2001) ‘The mechanism, rates and consequences of basaltic glass dissolution: I. An experimental study of the dissolution rates of basaltic glass as a function of aqueous Al, Si and oxalic acid concentration at 25°C and pH = 3 and 11’, Geochimica et Cosmochimica Acta. Pergamon, 65(21), pp. 3671–3681. doi: 10.1016/S0016-7037(01)00664-0.

Oelkers, E. H. and Schott, J. (1995) ‘Experimental study of anorthite dissolution and the relative mechanism of feldspar hydrolysis’, Geochimica et Cosmochimica Acta. Pergamon, 59(24), pp. 5039–5053. doi: 10.1016/0016-7037(95)00326-6.

Oelkers, E. H. and Schott, J. (2001) ‘An experimental study of enstatite dissolution rates as a function of pH, temperature, and aqueous Mg and Si concentration, and the mechanism of pyroxene/pyroxenoid dissolution’, Geochimica et Cosmochimica Acta. Pergamon, 65(8), pp. 1219–1231. doi: 10.1016/S0016-7037(00)00564-0.

Ohta, Y. et al. (1996) ‘Precambrian and Caledonian events in Svalbard, northewestern edge of the Eurasian plate’, in 30th International Geological Congress, Bejing, China, 1996. Bejing: Swedish Polar Research Secretariat.

Olajire, A. A. (2013) ‘A review of mineral carbonation technology in sequestration of CO2’, Journal of Petroleum Science and Engineering. Elsevier, 109, pp. 364–392. doi: 10.1016/J.PETROL.2013.03.013.

Paquette, J., Ward, W. B. and Reeder, R. J. (1993) ‘Compositional Zoning and Crystal Growth Mechanisms in Carbonates: A New Look at Microfabrics Imaged by Cathodoluminescence Microscopy’. Springer, New York, NY, pp. 243–252. doi: 10.1007/978-1-4684-9421-1_18.

Parkhurst, D. and Appelo, C. (2013) Description of input and examples for PHREEQC version 3: a computer program for speciation, batch-reaction, one-dimensional transport, and inverse geochemical calculations.

Parkhurst, D. L. and Appelo, C. A. J. (1999) ‘User’s guide to PHREEQC (Version 2): A computer program for speciation, batch-reaction, one-dimensional transport, and inverse geochemical calculations’, Water-Resources Investigations Report. doi: 10.3133/WRI994259.

Pina, C. M., Pimentel, C. and Crespo, A. (2022) ‘The Dolomite Problem: A Matter of Time’, ACS Earth and Space Chemistry. American Chemical Society, 6(6), pp. 1468–1471. doi: 10.1021/ACSEARTHSPACECHEM.2C00078/ASSET/IMAGES/MEDIUM/SP2C00078_M002.GIF.

Prestvik, T. (1977) ‘Cenozoic plateaulavas of Spitsbergen-a geochemical study’, Norsk Polarinstituitt, pp. 129–143.

Reeder, R. J. (1991) ‘An Overview of Zoning in Carbonate Minerals’, Luminescence Microscopy and Spectroscopy<subtitle>Qualitative and Quantitative Applications</subtitle>. SEPM Society for Sedimentary Geology. doi: 10.2110/SCN.91.25.0077.

Reeder, R. J., Fagioli, R. O. and Meyers, W. J. (1990) ‘Oscillatory zoning of Mn in solution-grown calcite crystals’, Earth-Science Reviews. Elsevier, 29(1–4), pp. 39–46. doi: 10.1016/0012-8252(0)90026-R.

Reeder, R. J. and Paquette, J. (1989) ‘Sector zoning in natural and synthetic calcites’, Sedimentary Geology. Elsevier, 65(3–4), pp. 239–247. doi: 10.1016/0037-0738(89)90026-2.

Rodriguez-Blanco, J. D. et al. (2012) ‘The role of pH and Mg on the stability and crystallization of amorphous calcium carbonate’, in Journal of Alloys and Compounds. doi: 10.1016/j.jallcom.2011.11.057.

Rodriguez-Blanco, J. D. et al. (2014) ‘The role of Mg in the crystallization of monohydrocalcite’, Geochimica et Cosmochimica Acta. Pergamon, 127, pp. 204–220.

Rodriguez-Blanco, J. D., Shaw, S. and Benning, L. G. (2015) ‘A route for the direct crystallization of dolomite’, American Mineralogist. Walter de Gruyter GmbH, 100(5–6), pp. 1172–1181. doi: 10.2138/am-2015-4963.

Rogers, K. L. et al. (2006) ‘CO2 metasomatism in a basalt-hosted petroleum reservoir, Nuussuaq, West Greenland’, Lithos. Elsevier, 92(1–2), pp. 55–82. doi: 10.1016/J.LITHOS.2006.04.002.

Rosenbauer, R. J. et al. (2012) ‘Carbon sequestration via reaction with basaltic rocks: Geochemical modeling and experimental results’, Geochimica et Cosmochimica Acta, 89, pp. 116–133. doi: 10.1016/j.gca.2012.04.042.

Saldi, G. D. et al. (2009) ‘Magnesite growth rates as a function of temperature and saturation state’, Geochimica et Cosmochimica Acta. Pergamon, 73(19), pp. 5646–5657. doi: 10.1016/J.GCA.2009.06.035.

Schaef, H. T., McGrail, B. P. and Owen, A. T. (2010) ‘Carbonate mineralization of volcanic province basalts’, International Journal of Greenhouse Gas Control, 4(2), pp. 249–261. doi: 10.1016/j.ijggc.2009.10.009.

Senger, K. et al. (2014) ‘Late Mesozoic magmatism in Svalbard: A review’, Earth-Science Reviews. Elsevier, 139, pp. 123–144. doi: 10.1016/J.EARSCIREV.2014.09.002.

Shore, M. and Fowler, A. D. (1996) ‘Oscillatory zoning in minerals; a common phenomenon’, The Canadian Mineralogist, 34(6), pp. 1111–1126.

Shuster, A. M. et al. (2018) ‘The Tonian Beck Spring Dolomite: Marine dolomitization in a shallow, anoxic sea’, Sedimentary Geology. Elsevier, 368, pp. 83–104. doi: 10.1016/J.SEDGEO.2018.03.003.

Skjelkvåle, B. L. et al. (1989) ‘A primitive alkali basaltic stratovolcano and associated eruptive centres, Northwestern Spitsbergen: Volcanology and tectonic significance’, Journal of Volcanology and Geothermal Research. Elsevier, 37(1), pp. 1–19. doi: 10.1016/0377-0273(89)90110-8.

Snæbjörnsdóttir, S. et al. (2014) ‘CO 2 storage potential of basaltic rocks in Iceland and the oceanic Ridges’, in Energy Procedia. Elsevier Ltd, pp. 4585–4600. doi: 10.1016/j.egypro.2014.11.491.

Snæbjörnsdóttir, S. et al. (2017) ‘The chemistry and saturation states of subsurface fluids during the in situ mineralisation of CO2 and H2S at the CarbFix site in SW-Iceland’, International Journal of Greenhouse Gas Control. Elsevier Ltd, 58, pp. 87–102. doi: 10.1016/j.ijggc.2017.01.007.

Snæbjörnsdóttir, S. et al. (2018) ‘Reaction path modelling of in-situ mineralisation of CO2 at the CarbFix site at Hellisheidi, SW-Iceland’, Geochimica et Cosmochimica Acta, 220. doi: 10.1016/j.gca.2017.09.053.

Snæbjörnsdóttir, S. Ó. et al. (2020) ‘Carbon dioxide storage through mineral carbonation’, Nature Reviews Earth & Environment. Springer Science and Business Media LLC, 1(2), pp. 90–102. doi: 10.1038/s43017-019-0011-8.

Snæbjörnsdóttir, S. Ó. et al. (2021) ‘Protecting Our Climate by Turning CO2 Into Stone’, Frontiers for Young Minds. Frontiers Media SA, 9. doi: 10.3389/FRYM.2021.579895.

Spötl, C. (1991) ‘Cathodoluminescence of magnesite: Examples from the Eastern Alp’, Geology, 19(1), pp. 52–55.

Steele, A. et al. (2007) ‘Comprehensive imaging and Raman spectroscopy of carbonate globules from Martian meteorite ALH 84001 and a terrestrial analogue from Svalbard’, Meteoritics & Planetary Science. John Wiley & Sons, Ltd, 42(9), pp. 1549–1566. doi: 10.1111/J.1945-5100.2007.TB00590.X.

Sushchevskaya, N. M. et al. (2008) ‘Conditions of Quaternary magmatism at Spitsbergen Island’, Geochemistry International. Maik Nauka-Interperiodica Publishing, 46(1), pp. 1–16. doi: 10.1134/S0016702908010011/METRICS.

Sushchevskaya, N. M. et al. (2009) ‘Geochemistry of Neogene magmatism at Spitsbergen Island’, Geochemistry International. Springer, 47(10), pp. 966–978. doi: 10.1134/S0016702909100024/METRICS.

Treiman, A. H. et al. (2002) ‘Hydrothermal origin for carbonate globules in Martian meteorite ALH84001: a terrestrial analogue from Spitsbergen (Norway)’, Earth and Planetary Science Letters. Elsevier, 204(3–4), pp. 323–332. doi: 10.1016/S0012-821X(02)00998-6.

Treiman, A. H. (2012) ‘Eruption age of the Sverrefjellet volcano, Spitsbergen Island, Norway’, Polar Research. Norwegian Polar Institute, 31(SUPPL.). doi: 10.3402/POLAR.V31I0.17320/SUPPL_FILE/ZPOR_A_11818773_SM0001.XLS.

Tuchschmid, M. and Spillmann, P. (1992) ‘Neogene and Quaternary volcanism on Spitsbergen : the revival of an Arctic Hot Spot Neogene and Quaternary volcanism on Spitsbergen-the revival of an Arctic Hot Spot’, Swiss Journal of Geosciences, 72(2), pp. 251–270.

Turvey, C. C. et al. (2018) ‘Hydrotalcites and hydrated Mg-carbonates as carbon sinks in serpentinite mineral wastes from the Woodsreef chrysotile mine, New South Wales, Australia: Controls on carbonate mineralogy and efficiency of CO2 air capture in mine tailings’, International Journal of Greenhouse Gas Control. Elsevier, 79, pp. 38–60. doi: 10.1016/J.IJGGC.2018.09.015.

Vågnes, E. and Amundsen, H. E. F. (1993) ‘Late Cenozoic uplift and volcanism on Spitsbergen: Caused by mantle convection?’, Geology, 21(3), pp. 258–254.

Voigt, M. et al. (2018) ‘Evaluation and refinement of thermodynamic databases for mineral carbonation’, Energy Procedia. Elsevier, 146, pp. 81–91. doi: 10.1016/J.EGYPRO.2018.07.012.

Worsley, D. (2008) ‘The post-Caledonian development of Svalbard and the western Barents Sea’, Polar Research. Norwegian Polar Institute, 27(3), pp. 298–317. doi: 10.3402/POLAR.V27I3.6197.

Zvir, Y., Pimentel, C. and Pina, C. M. (2021) ‘The effect of stoichiometry, mg-ca distribution, and iron, manganese, and zinc impurities on the dolomite order degree: A theoretical study’, Minerals. MDPI AG, 11(7), p. 702. doi: 10.3390/MIN11070702/S1.

Chapter 6.

CONCLUSIONS

This thesis presents two experimental studies on factors influencing the mechanisms and kinetics of carbonate crystallisation and a detailed case study of the *in situ* carbonation of basaltic host rock from the Sverrefjellet volcano in Svalbard. This final section will seek to draw them together and present some broader conclusions on the nature and magnitude of mineral carbonation in carbon capture and storage processes.

Chapter 3 "Synergistic effects of Mg^{2+}, SO_4^{2-} and citrate ions on $CaCO_3$ crystallisation inhibition":

This study demonstrates the complexity of $CaCO_3$ formation pathways from multicomponent solutions containing common inorganics (Mg^{2+} and SO_4^{2-}) and organics (citrate ions, CIT). The key findings from Chapter 3 are:

- Minor changes in solution chemistry (ions and concentrations) significantly affect $CaCO_3$ formation mechanisms, kinetics and crystallisation pathways.
- The effects of each ion are not uniform, with Mg^{2+} having greater influence over SO_4^{2-}. The individual effects are often overridden by the more potent ones when combined, e.g. $MgSO_4$ or SO_4^{2-} + CIT.
- Concentration of inhibitors influences the kinetics of $CaCO_3$ crystallisation, with nucleation inhibited and an overall negative correlation between ion concentration and crystallisation rate.
- The polymorph selection and crystal morphologies of the resulting $CaCO_3$ crystals are also influenced by the multicomponent solutions. For example, aragonite crystallisation is

predominantly promoted, and morphological influences include spherulitic nanoaggregates in aragonite and elongation along the *c*-axis in calcite.

Chapter 4 "Mechanistic insights into the formation of aragonite-type carbonates: the role of Ca^{2+} in the crystallisation of strontianite and witherite":

This study demonstrates that the transformation of calcite-type to aragonite-type carbonates can take place at ambient to low hydrothermal conditions (21- 80 °C) via the interaction of calcite and Ba/Sr-bearing aqueous solutions. The key findings from Chapter 4 are:

- Transformation extent depends on solution composition, calcite grain size, temperature, and pH of the aqueous solution.
- Replacement of calcite to Ca-bearing strontianite and witherite occurs through dissolution-precipitation mediated by the solution and oriented overgrowth, with grain size affecting the extent and kinetics of replacement.
- The kinetics of the replacement reactions by aragonite-type carbonate are also dictated by the ionic radii and molar volume, with strontianite crystallising faster than witherite.
- Nucleation from solution experiments also revealed that strontianite crystallises faster than witherite. However, the influence of Ca^{2+} on the formation of $BaCO_3$ and $SrCO_3$ is represented by inhibiting crystallization kinetics, due to its dehydration in solution before incorporating into the crystal. The change of coordination number of Ca between aqueous solution (VI) and aragonite-type carbonates (IX) carbonates can further explain the slow down of the crystallisation kinetics of the two aragonite-type carbonates.

Chapter 5 "New insights into the textural and chemical evolution during natural carbonation processes at Sverrefjellet volcano, Svalbard":

This study demonstrated the influence of the geochemistry of the host rock during the carbonation of basalt and that the resulting carbonate cements evolved in response to changing Ca/Mg ratios as the cement progressed away from the host rock. The key findings from Chapter 5 are:

- The chemistry of the host basalt directly influenced the resulting carbonate cements. The dissolution of Mg-rich phases, such as forsterite and enstatite, result in Mg as the most abundant cation forming carbonates in the system.
- The carbonate cements consist of calcite-type carbonates within the magnesite-calcite-siderite compositional range. Changes in cations (Ca^{2+}/ Mg^{2+}/ Fe^{2+}) ratio are reflected in the chemical evolution of the calcite-type carbonate.
- Different stages of carbonation are observed in the cements, overlapping with a crystal chemistry evolution from calcian proto-dolomite to magnesite-rich compositions and ultimately to iron-rich carbonates and non-carbonate cements.
- The carbonation conditions (e.g. basalt dissolution following the interaction with CO_2 charged fluids) at Sverrefjellet provide a natural analogue for CCS via mineralisation (e.g., CarbFix project, Iceland). Calcite is the main carbonate phase mineralising at CarbFix, whereas magnesite-rich carbonates mineralise principally at Sverrefjellet, indicating that the Sverrefjellet carbonates likely formed at higher temperature, allowing the dehydration of the Mg^{2+} ion from solution prior to incorporation into the growing carbonate crystals.

General conclusions

The goal of this thesis was to examine the effects of multi-component solutions on the crystallization of common divalent carbonates experimentally and within natural systems, in both synthetic and natural polymineralic systems. Prior to this study, the influence of ions on carbonate

formation was predominantly limited to single ions. In chapters 3 and 4, we carried out a comprehensive exploration of the impact of foreign ions on the kinetics and mechanisms governing divalent (Ca, Sr, Ba) carbonates, leveraging in situ experiments. Moving forward to chapter 5, we focused on the intriguing evolution of a complex divalent (Ca, Mg, Fe) carbonate cement crystallised via an *in situ* basalt carbonate mineralization.

Throughout this investigation, we have expanded our knowledge regarding the kinetic and mechanistic factors associated with carbonate formation. The synergistic influence of ions significantly diverges from their individual effects, thereby offering profound insights into the impacts of multi-component solutions on natural and synthetic carbonate crystallisation. These main variables taken into consideration include: i) ions ratio and concentration in solution; ii) the saturation state within aqueous solutions; iii) the dehydration of divalent (e.g, Ca^{2+}, Mg^{2+}, Sr^{2+}, Ba^{2+}) ions; iv) variations in the ionic radii of these divalent cations; v) the effects of the differing coordination numbers of these divalent cations among carbonate types. This research significantly advances our comprehension of the intricate factors governing divalent carbonate crystallization, carbonate mineral replacement reactions, and the corresponding processes in natural basaltic CCS analogues. By seamlessly integrating homogeneous nucleation experiments, mineral replacement reactions, and meticulous (high-resolution) examinations of naturally carbonated basalts, alongside geochemical modelling, we have achieved a profound mechanistic insight into carbonate formation. This comprehensive approach elucidates how various factors such as the presence of foreign ions, supersaturation levels, and temperature intricately impact the kinetics and mechanisms of carbonate formation. The contributions made here have wide applicability: The goal of this research was to extend our understanding about the factors affecting carbonate crystallisation in relation to CO_2 sequestration, as well as biomineralisation process, industrial applications and wider carbonate geochemistry. In turn, this works contributes to a better understanding of the processes, mechanisms, and variables affecting the nucleation and growth of carbonates within natural systems or industrial applications, ultimately paving the way for enhanced control and optimization of carbonate crystallization in diverse settings.

By unravelling the multifaceted impact of multicomponent solutions on the crystallization of divalent carbonates in both natural and synthetic settings, deciphering the underlying mechanisms governing carbonate formation, and comprehending the kinetics involved, we are poised to exert precise control over metastable and stable carbonate formation. This newfound knowledge holds the key to regulating the kinetics and mechanisms of carbonate formation, whether in the context of field-based geological processes or industrial carbon capture and storage (CCS) applications

APPENDICES

Appendix A

Supplements to Chapter 3

A1 Comparisons between this study and Montanari *et al*. (2017) and Nielsen *et al*. (2016).

As there are a number of similarities, as well as differences, between and this paper, Montanari *et al.* (2017) and Nielsen *et al.* (2016) the following provides a brief description of both papers and summaries the experimental conditions, notably the concentrations.

Montanari *et al*. (2017) investigated the effect of citrate (CIT) on $CaCO_3$ as a function of increasing mol % CIT/Ca. They also examined the influence on crystallization rates and crystal polymorph, size, and morphology, using UV-Vis spectrophotometry to examine changes in solution absorbance, i.e., turbidity, following methods detailed in Tobler *et al.* (2014, 2015). Experiments were carried out at 22 °C. Equal volumes of 4 mM $CaCl_2$ solution and 4 mM Na_2CO_3 solution (± CIT) were mixed. CIT concentrations varied from 0 to 4 mM, so the mol % CIT/Ca ranged from 0-100% CIT/Ca. Full range of concentrations listed in Table A1.1. Complementary batch experiments (total volume 500 mL) were carried out to characterize the final crystallisation products with SEM and XRD, as well as XPS (X-ray photoelectron spectroscopy) and TGA (Thermogravimetric analysis).

Nielsen *et al*. (2016) investigated the inhibiting effect of Mg^{2+} and SO_4^{2-}, both individually and together, on calcite growth rates. Calcite seed (30 ± 4 mg) was added to a solution of a reaction vessel containing 4 mM $CaCl_2$, 4 mM $NaHCO_3$ and 0.1 M NaCl, after a adjusting the change in pH of the solution to the initial solution (pH 8.3 ± 00.2) and allowing the undisturbed growth of calcite, inhibitors (solutions of $MgCl_2$, Na_2SO_4 or $MgSO_4$) were introduced to the sample cell. Inhibitor concentrations varied from 0.70 mM to 40.0 mM, full range of concentrations listed in Table A1.2.

Ca/CIT %	Ca Concentration (mM)	CIT Concentration (mM)	JMAK model fit	
			t_{ind} (min)[a]	k (x10^{-3} s^{-1})
0	4	-	0.8	842
2.5	4	0.1	1.3	702
5	4	0.2	1.0	587
10	4	0.4	1.5	413
20	4	0.8	2.2	333
25	4	1	2.2	227
50	4	2	3.9	101
75	4	3	10.0	44
100	4	4	27.0	16

Table A1.1: Inhibitor concentrations and data collected from turbidity experiments from Montanari et al. (2017). Note the crystallisation rate (k) values are x10^{-3} s^{-1}, whereas the results in this paper are ***x10^{-6} s^{-1}****, highlighting the drastic drop in crystallisation rates with the combination of CIT and ions. For example, the Montanari et al. (2017) experiment where Ca/CIT 25% (4 mM $CaCl_2$ with 1 mM CIT) the k value is 227 x 10^{-3} s^{-1}, compared to the same Ca/CIT ratio with the addition of 10 mM Mg^{2+} is* ***25 x 10^{-6} s^{-1}***

Mg^{2+} concentrations (mM)	$MgSO_4$ concentrations (mM)	SO_4^{2-} concentrations (mM)
1.8	0.14	0.70
2.1	2.2	1.1
3.2	3.0	2.6
3.3	3.9	4.0
4.1	4.1	7.0
5.3	8.0	7.1
5.8	10	9.1
6.2	12.6	12.5
6.3	12.7	13.0
9.3		20.5
10		40.0
12.3		
13.3		

Table A1.2: Inhibitor concentrations from Nielsen et al. (2016)

A2 The influence of fluid saturation state

The kinetics of $CaCO_3$ crystallisation from aqueous solution depend on the fluid saturation state. This was demonstrated in turbidity experiments by Montanari *et al.* (2017), (taken from the supporting information, figure S1) by lowering the saturation index (SI) by reducing initial $[Ca^{2+}]$ from 2 to 0.375 mM, while keeping $[CO_3^{2-}]$ constant at 2. Measuring the SI from 2.2 to 1.6 demonstrates the negative correlation/inverse relationship between SI and solution turbidity to reach a plateau.

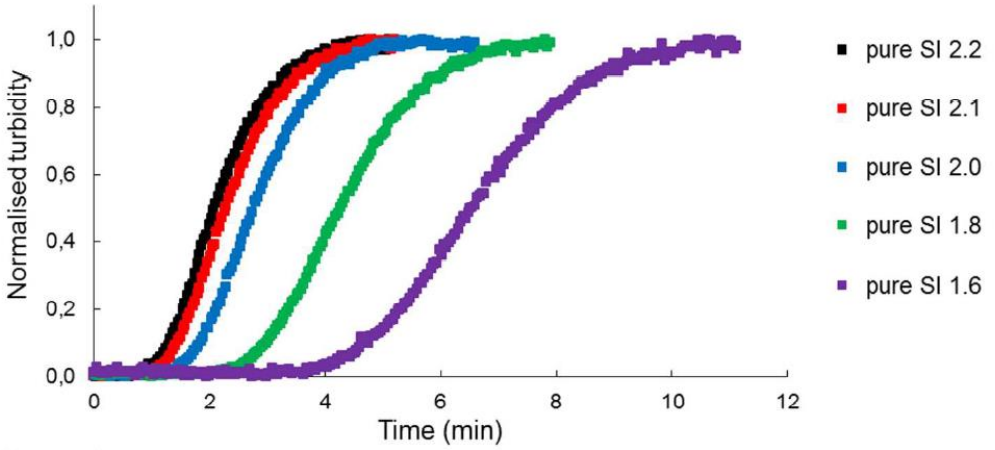

Figure A2.1 :Normalised turbidity profile of $CaCO_3$ crystallisation experiments as function of time and saturation index (SI) in pure $CaCO_3$ experiments carried out by Montanari et al. (2017).

A3 Description of Turbidity experiments sample cell

Turbidity experimental set up (Figure A3) is configured in the following method, a Deuterium-Halogen Light Source, connected to an optical fiber to illuminate the sample cell, held in a cuvette holder and another fiber to return the signal to the spectrometer; linked to the computer via a USB cord. The experiment is setup on the computer via the OceanView Spectrometer Operating Software. Changes in absorbance at 450 nm was measured for a minimum of 1 second, after methods of Rodriguez-Blanco *et al.*, (2014); Tobler *et al.*, (2015); Montanari *et al.*, (2017). The experimental system is only suitable for measuring at ambient temperatures.

The sample cell consists of a disposable plastic 1 cm pathway cuvette (volume 3.0 mL) with Z dimension 15 mm. Z dimension is defined as "the distance from the base of the cell to the centre of the sample compartment window or aperture (i.e. the area through which the light passes)" (StarnaScientific, no date). 1 mL of the $NaCO_3$ (± additives) bearing solution is pipetted (Eppendorf™ variable volume pipette, 1 mL) into cuvette, followed by 1 mL of the $CaCl_2$ (± additives) bearing solution (cuvettes were open to the atmosphere). The cuvette

holder is placed on a magnetic stirrer (800 rpm) to ensure consistent mixing of the solutions. The precipitates were vacuum filtered, washed in isopropanol and dried following the methods of Rodriguez-Blanco *et al.* (2008). The ensure scalability the filter papers were examined using the SEM and the $CaCO_3$ polymorphs and morphologies were the same as those observed in the batch experiments.

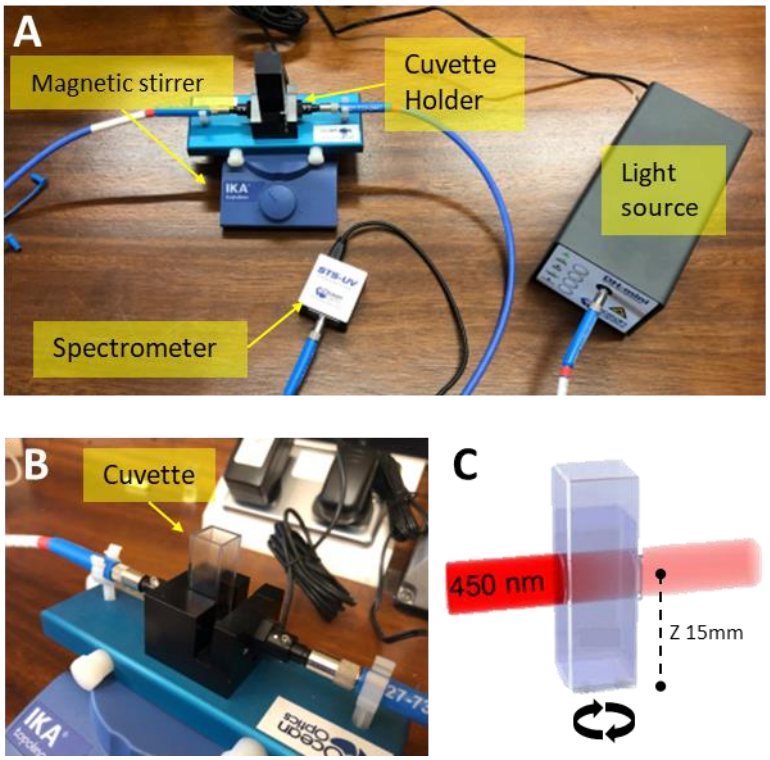

Figure A3.1: Turbidity experimental set up A and B) Sampling set up, consisting of Light source (OceanOptics, DH-mini UV-Vis-NIR Deuterium-Halogen Light Source with Shutter), cuvette in cuvette holder (Ocean Optics, CUV-UV Cuvette Holder) on a magnetic stirrer and a spectrometer (OceanOptics, STS-UV Microspectrometer) linked to the computer with OceanView operating software. C) Schematic of sample cell, cuvette with light source at 450 nm, with Z dimension of 15 mm.

A4 Batch experiment

Batch experiments (1 L total volume, covered with parafilm), using the same solutions as the turbidity experiments, to complement the turbidity experiments were set up in the following. Solutions were mixed in a graduated beaker (Pyrex®, capacity 1000 mL heavy duty). 500 mL of the $NaCO_3$ (± additives) bearing solution is poured into the graduated beaker, followed by 500 mL of the $CaCl_2$ (± additives) bearing solution. The beaker is placed on a magnetic stirrer (800 rpm), prior to the addition of the solutions, to ensure consistent mixing of the solutions. The precipitates were vacuum filtered, washed in isopropanol and dried following the methods of Rodriguez-Blanco *et al.* (2008).

A5 XRD detection and quantification limits

LOD: 0.1%

LOQ: 1%

A6 Species distribution and saturation indices predicted with PHREEQC

Mg^{2+} concentration (mM)	Total Mg Available	Log a (Mg^{2+})	Log a ($MgCO_3$)	Saturation Index		
				Calcite	Aragonite	Vaterite
-	-	-	-	2.16	2.01	1.58
1	5.00×10^{-4}	-3.614	-3.988	2.13	1.98	1.55
5	2.50×10^{-3}	-2.702	-3.408	2.02	1.87	1.44
10	5.00×10^{-3}	-2.625	-3.223	1.92	1.77	1.34
15	7.50×10^{-3}	-2.464	-3.139	1.83	1.68	1.25
20	1.00×10^{-2}	-2.354	-3.09	1.76	1.61	1.18

Table A6.1: Magnesium species distribution and saturation indices predicted with PHREEQC using concentrations from round 1 experiments with Mg. (Mg^{2+} and $MgCO_3$ distribution values in Log activity).

$MgSO_4$ concentration (mM)	Total Ca	Log a (Ca^{2+})	Log a ($CaSO_4$)	Total Mg	Log a (Mg^{2+})	Log a ($MgSO_4$)	Saturation Index		
							Calcite	Aragonite	Vaterite
-	2.00×10^{-3}	-3.070	-	-	-	-	2.16	2.01	1.58
1		-3.078	-4.275	5.00×10^{-4}	-3.628	-4.923	2.12	1.97	1.54
5		-3.111	-3.673	2.50×10^{-3}	-2.968	-3.628	1.99	1.84	1.41
10		-3.149	-3.466	5.00×10^{-3}	-2.708	-3.123	1.87	1.72	1.29
15		-3.181	-3.365	7.50×10^{-3}	-2.565	-2.847	1.78	1.63	1.20
20		-3.209	-3.303	1.00×10^{-2}	-2.469	-2.660	1.70	1.55	1.12

Table A6.2: Calcium and magnesium species distribution and saturation indices predicted with PHREEQC using concentrations from round 1 experiments with $MgSO_4$ (Ca^{2+}, $CaSO_4$, Mg^{2+}, $MgSO_4$ and $MgCO_3$ distribution values in Log activity).

SO_4^{2-} concentration (mM)	Total Ca Available	Log a (Ca^{2+})	Log a ($CaSO_4$)	Saturation Index		
				Calcite	Aragonite	Vaterite
-	2.00×10^{-3}	-3.070	-	2.16	2.01	1.58
1		-3.088	-4.274	2.14	1.99	1.56
5		-3.147	-3.666	2.07	1.92	1.49
10		-3.200	-3.452	2.00	1.85	1.42
15		-3.241	-3.345	1.94	1.79	1.36
20		-3.275	-3.278	1.89	1.74	1.31

Table A6.3: Calcium species distribution and saturation indices predicted with PHREEQC using concentrations from round 1 experiments with SO_4 (Ca^{2+} and $CaSO_4$ distribution values in Log activity).

Mg (mM)	CIT concentration (mM)	Total Mg available	Log a (Mg^{2+})	Log a ($MgCO_3$)	Total CIT Available	Mg^{2+}-(CIT)	Ca^{2+} -(CIT)	Saturation Index		
								Calcite	Aragonite	Vaterite
10	-	5.00×10^{-3}	-2.625	-3.223	-	-	-	1.92	1.77	1.34
	0.1		-2.628	-3.225	5.00×10^{-5}	-4.521	-4.944	1.91	1.76	1.33
	0.5		-2.640	-3.233	2.50×10^{-4}	-3.822	-4.245	1.90	1.75	1.33
	1.0		-2.656	-3.243	5.00×10^{-4}	-3.520	-3.944	1.89	1.74	1.32

Table A6.4: Magnesium and CIT species distribution and saturation indices predicted with PHREEQC using concentrations from round 2 experiments with Mg + CIT (Distribution values in Log activity).

$MgSO_4$ (mM)	Total Mg	Log a (Mg^{2+})	Log a ($MgSO_4$)	Log a ($MgCO_3$)	Total Ca	Log a (Ca^{2+})	Log a ($CaSO_4$)	Total CIT Available	Mg^{2+} - (CIT)	Ca^{2+}- (CIT)	Saturation Index		
											Calcite	Aragonite	Vaterite
10	5.00 x 10^{-3}	-2.708	-3.123	-3.255	2.00 x 10^{-3}	-3.149	-3.466	-	-	-	1.87	1.72	1.29
		-2.711	-3.125	-3.257		-3.152	-3.468	5.00 x 10^{-3}	-4.520	-4.957	1.87	1.72	1.29
		-2.724	-3.135	-3.266		-3.165	-3.478	2.50 x 10^{-4}	-3.821	-4.257	1.86	1.71	1.28
		-2.740	-3.148	-3.278		-3.181	-3.490	5.00 x 10^{-4}	-3.520	-3.956	1.85	1.70	1.27

Table A6.5: Magnesium, calcium and CIT species distribution predicted with PHREEQC using concentrations from round 2 experiments with $MgSO_4$ + CIT (Distribution values in Log activity).

SO_4^{2-} concentration (mM)	CIT concentration (mM)	Total Ca	Log a (Ca^{2+})	Log a ($CaSO_4$)	Total CIT Available	Ca^{2+} - (CIT)	Saturation Index		
							Calcite	Aragonite	Vaterite
10	-	2.00×10^{-3}	-3.200	-3.452	-	-	2.00	1.85	1.42
	0.1		-3.211	-3.462	5.00×10^{-5}	-4.407	1.99	1.84	1.41
	0.5		-3.257	-3.505	2.50×10^{-4}	-3.711	1.96	1.81	1.38
	1.0		-3.32	-3.565	5.00×10^{-4}	-3.415	1.90	1.75	1.32

Table A6.6: Calcium and CIT species distribution and saturation indices predicted with PHREEQC using concentrations from round 2 experiments with SO_4 + CIT (Distribution values in Log activity).

A7 Changes to induction time (t_{ind})

The addition of inhibitors resulted in delays to the induction time (t_{ind}), though the extent of the delay is not uniform, it is dependent on i) inhibitor and ii) concentration. Box plot and percentage change values for *round 1* experiments are provided in Figure A7.1 and Table A7.1; *round 2* experiments are presented in Figure A7.2 and Table A7.2.

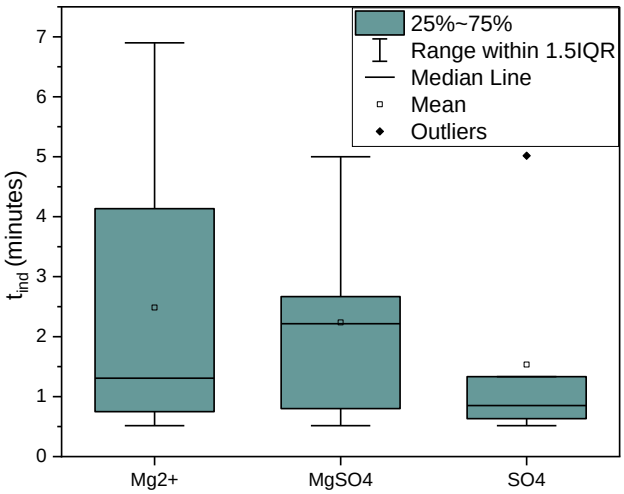

Figure A7.1: Round 1 induction time (t_{ind}). The Mg^{2+} system has the widest range of t_{ind} values, followed by $MgSO_4$ then SO_4^{2-}.

	Percentage change (%)		
Concentration (mM)	**Mg^{2+}**	**$MgSO_4$**	**SO_4^{2-}**
1	45	55	23
5	174	416	158
10	132	274	81
15	700	384	48
20	1235	868	871

Table A7.1: Percentage change values of Round 1 induction time (t_{ind}) relative to the pure system experiment following addition of inhibitors. Induction time increased in all experiments. The average % increase of Mg^{2+} = 457%; SO_4^{2-} = 77% (average excludes the outlier value from + 20 mM SO_4^{2-} experiment); $MgSO_4$ = 399%.

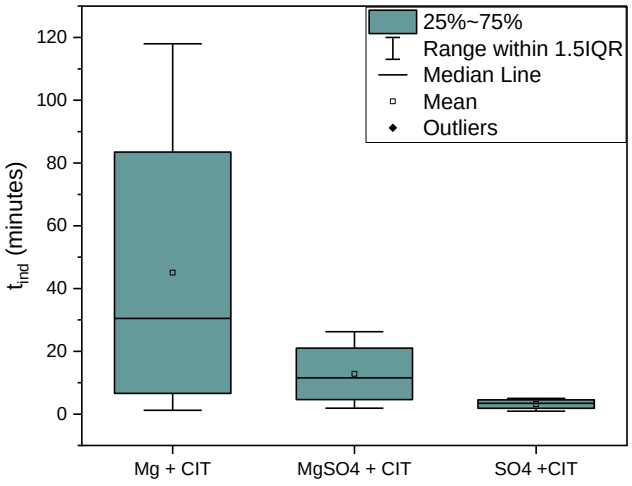

Figure A7.2: Round 2 induction time (t_{ind}), displaying a similar pattern of results to round 1 experiments, the CIT + Mg^{2+} system has the widest range of t_{ind} values, followed by CIT + $MgSO_4$ then CIT + SO_4^2.

	Percentage change (%)		
CIT Concentration (mM)	**Mg^{2+}**	**$MgSO_4$**	**SO_4^{2-}**
0.1	900	729	194
0.5	3983	1282	438
1.0	9733	287	341

Table A7.2: Percentage change values of Round 2 induction time (t_{ind}) relative to the 10 mM Round 1 experiment following addition of inhibitors. Induction time increased in all experiments. The average % increase of CIT + Mg^{2+} = 4872 %; CIT + SO_4^{2-} = 324%; CIT + $MgSO_4$ = 766%.

A8 Representative examples of experimental repetition

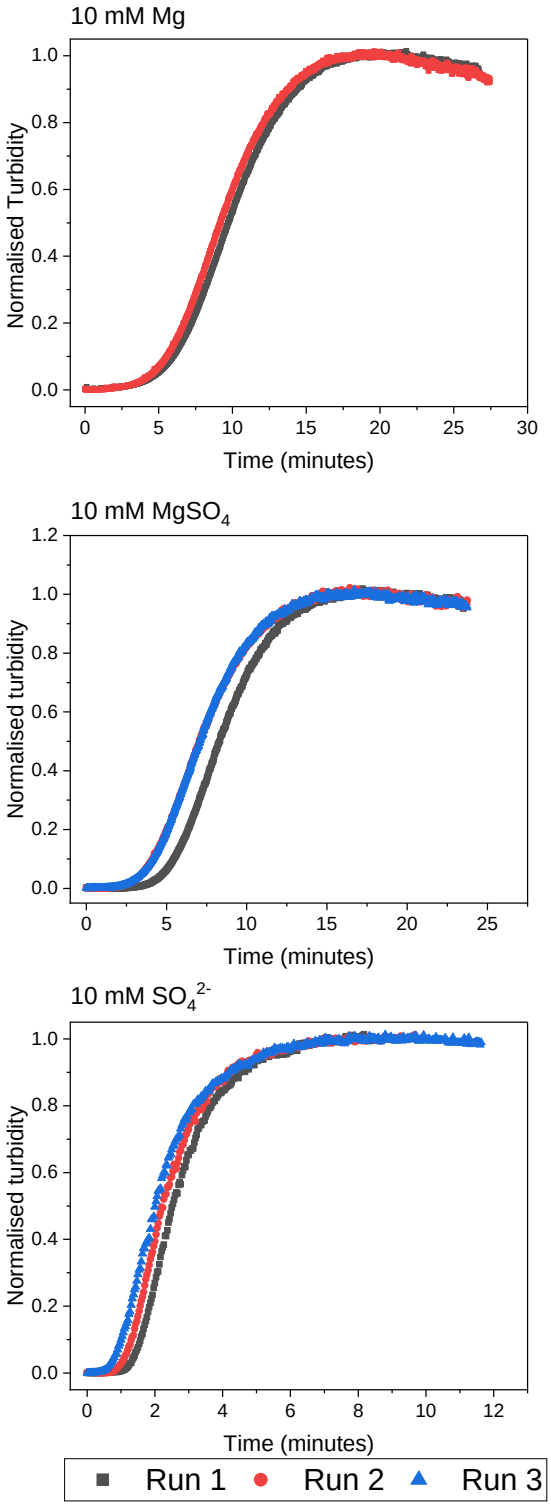

Figure A8.1: Repetitions of Round 1 turbidity experiments with 10 mM of inhibitor.

	Crystallisation rate k (x 10^{-3} s^{-1})			Induction time (t_{ind})		
	Mean	**RSD**	**RSE**	**Mean**	**RSD**	**RSE**
10 mM Mg^{2+}	1.59	± 5%	± 4%	1.06	± 19%	± 13%
10 mM $MgSO_4$	2.00	± 8%	± 4%	2.14	± 20%	± 11%
10 mM SO_4	1.27	± 10%	± 7%	0.11	± 27%	± 16%

Table A8.1: Corresponding Error values for repetitions of the Round 1 normalized turbidity experiments shown in Figure A8.1. Error values presented are the average from all the experiments, the relative standard deviation (RSD) and the relative standard error (RSE) values. Induction time, t_{ind}, minutes.

	k rate percentage change (%)		
Concentration (mM)	**Mg^{2+}**	**$MgSO_4$**	**SO_4^{2-}**
1	-32	-30	-10
5	-72	-69	-36
10	-77	-70	-13
15	-87	-70	-20
20	-99	-86	-88

Table A8.2: Percentage change values of Round 1 crystallisation rates (k) relative the pure system following addition of inhibitors. Crystallisation rate reduced in all experiments. The average % reduction of Mg^{2+} = -74%; SO_4^{2-} = -33%; $MgSO_4$ = -65%.

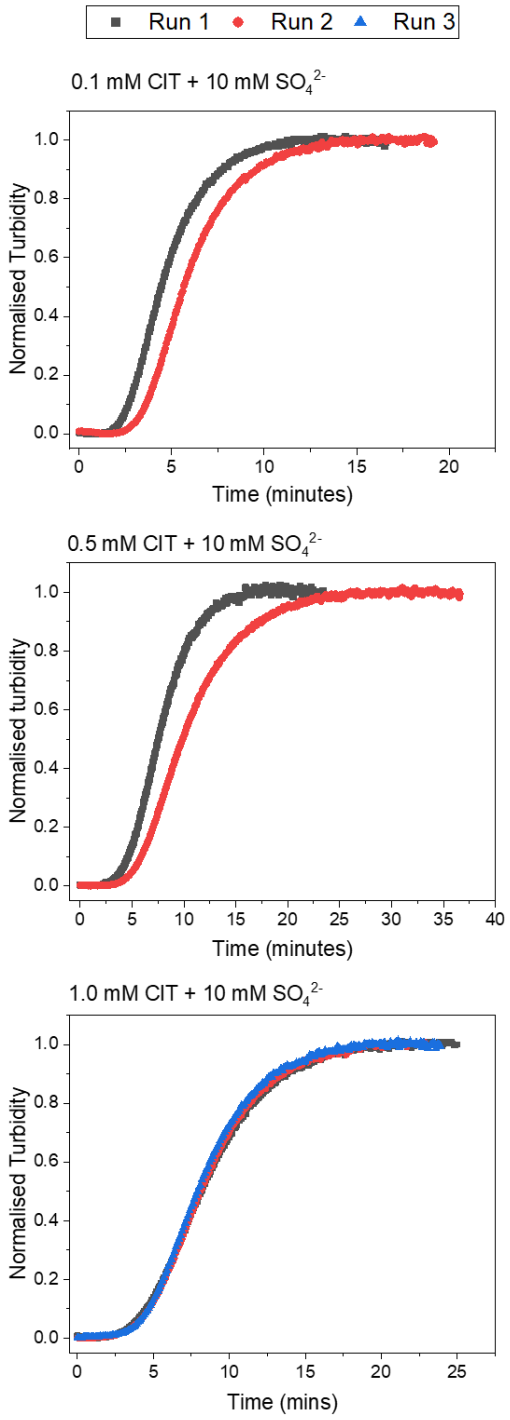

Figure A8.2: Repetitions of Round 2 from the SO_4^{2-} + CIT experiments.

	Crystallisation rate *k* (x 10^{-3} s^{-1})			Induction time (t_{ind})		
	Mean	**RSD**	**RSE**	**Mean**	**RSD**	**RSE**
0.1 mM CIT	2.98	17%	12%	2.50	13%	9%
0.5 mM CIT	1.73	19%	13%	2.47	8%	5%
1.0 mM CIT	1.80	2%	1%	1.97	8%	4%

Table A8.2: Corresponding Error values for repetitions of the Round 2 normalised turbidity experiments (10 mM SO_4 + CIT) shown in Figure A8.2. Error values presented are the average from all the experiments, the relative standard deviation (RSD) and the relative standard error (RSE) values. t_{ind} minutes.

	***k* rate percentage change (%)**		
CIT Concentration (mM)	**Mg^{2+}**	**$MgSO_4$**	**SO_4^{2-}**
0.1	-71	-84	-56
0.5	-90	-95	-75
1.0	-98	-98	-71

Table A8.3: Percentage change values of Round 2 crystallisation rate (k) relative the 10 mM Round 1 experiment following addition of inhibitors. Crystallisation rate reduced in all experiments. The average % reduction of CIT + Mg^{2+} = 87%; CIT + SO_4^{2-} = 67%; CIT + $MgSO_4$ = 92%.

A9 Representative fits of normalized Turbidity data.

The reaction with kinetics that conform to this equation give a straight line when $-ln\ ln(1-y)$ is plotted against $ln\ t$ (Putnis, 1992; Xia *et al.*, 2009). The intercept on the y axis gives the value of n *ln* k, by which the crystallization rate (*k*) value can be determined. The empirical parameter n value is given by the value of the slope, which is used to compare reaction mechanisms. The initial stages of crystallisation fit the JMAK model where n ~ 4 (α = 0-0.8). The Avrami constant is *n* = d + 1, where d is the growth dimensionality (Gránásy *et al.*, 2005; Zemenová *et al.*, 2020). In the case of spherulitic growth, which occurs in 3 dimensions the d=3, therefore resulting in *n*= 3 + 1 value.

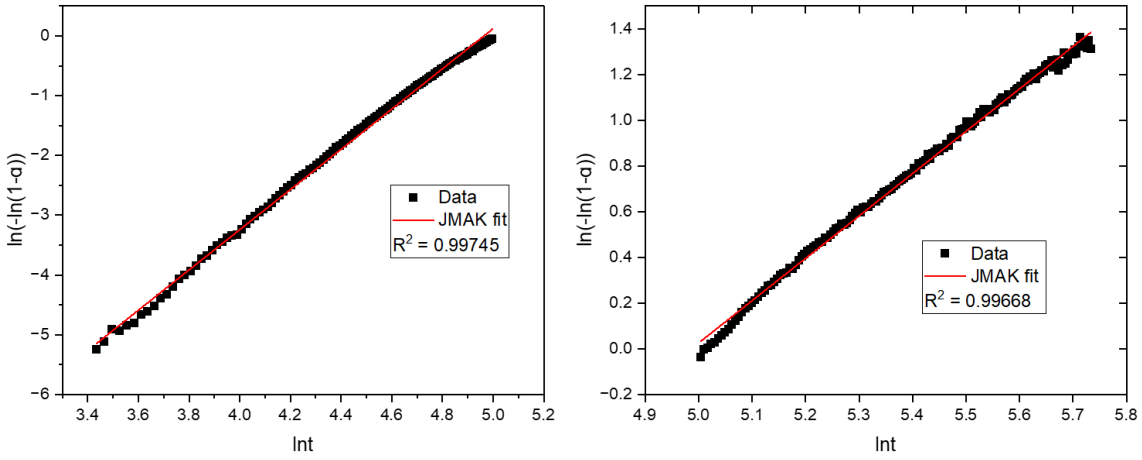

Figure A9.1: Representative fits of normalized UV–Vis data collected from the pure $CaCO_3$ system (no additives) experiment. The plot on the left shows the fit of the data collected during the initial part of the turbidity experiment and the fit is used to calculate the induction time (t_{ind}). The plot on the right shows the fit of the data collected during the latter part of the turbidity experiment, the fit on the right is used to determine the rate constant (k).

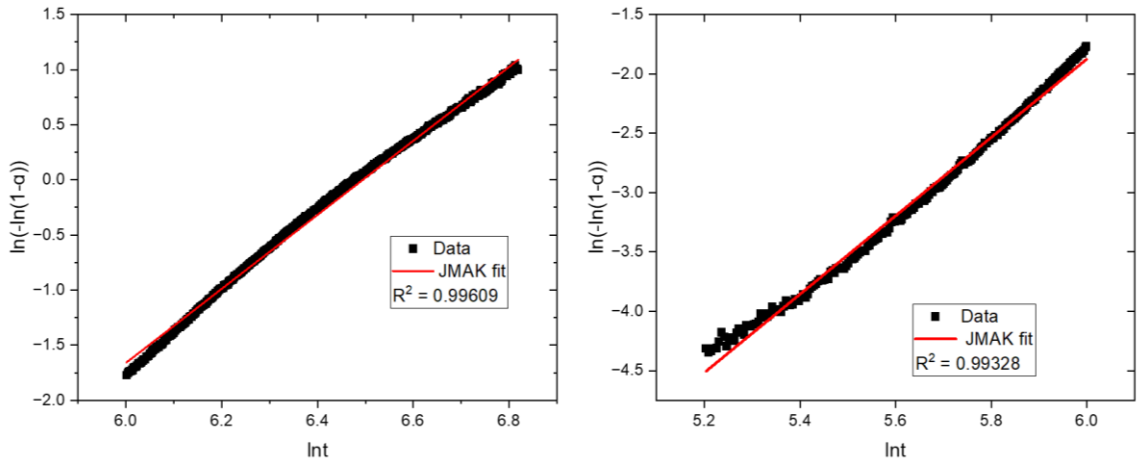

Figure A9.2: Representative fits of normalized UV–Vis data collected from Round 1 experiment, with 10 mM Mg^{2+}. The plot on the left shows the fit of the data collected during the initial part of the turbidity experiment and the fit (n ~4) is used to calculate the induction time (t_{ind}). The plot on the right shows the fit (n ~1) of the data collected during the latter part of the turbidity experiment, the fit on the right is used to determine the rate constant (k).

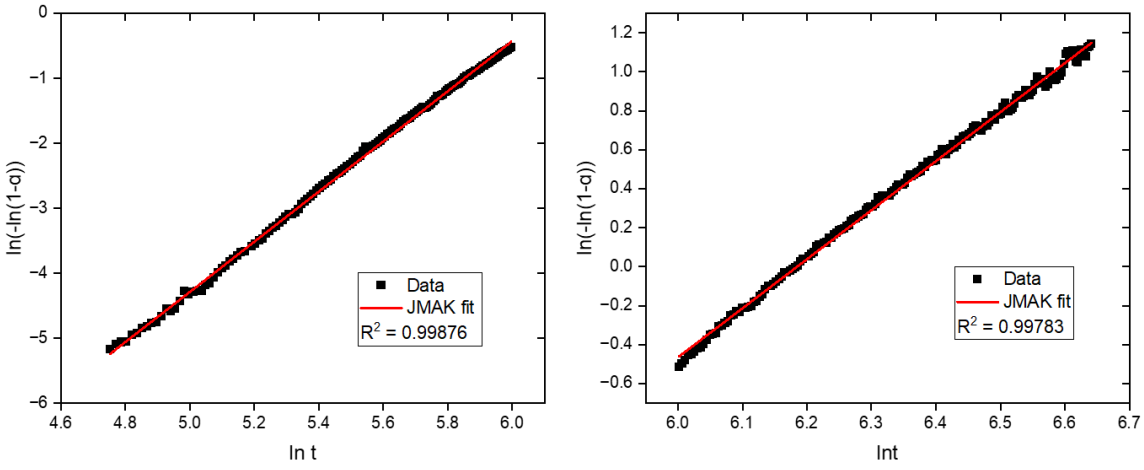

Figure A9.3: Representative fits of normalized UV–Vis data collected from Round 1 experiment, with 10 mM $MgSO_4$. The plot on the left shows the fit of the data collected during the initial part of the turbidity experiment and the fit (n ~4) is used to calculate the induction time (t_{ind}). The plot on the right shows the fit (n ~1) of the data collected during the latter part of the turbidity experiment, the fit on the right is used to determine the rate constant (k).

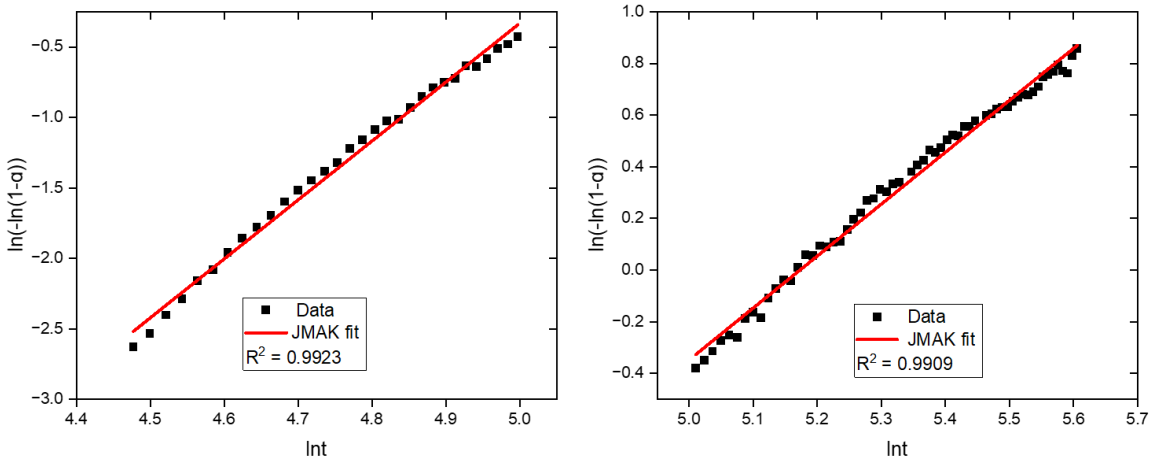

Figure A9.4: Representative fits of normalized UV–Vis data collected from Round 1 experiment, with 10 mM SO_4^{2-}. The plot on the left shows the fit of the data collected during the initial part of the turbidity experiment and the fit (n ~4) is used to calculate the induction time (t_{ind}). The plot on the right shows the fit (n ~1) of the data collected during the latter part of the turbidity experiment, the fit on the right is used to determine the rate constant (k).

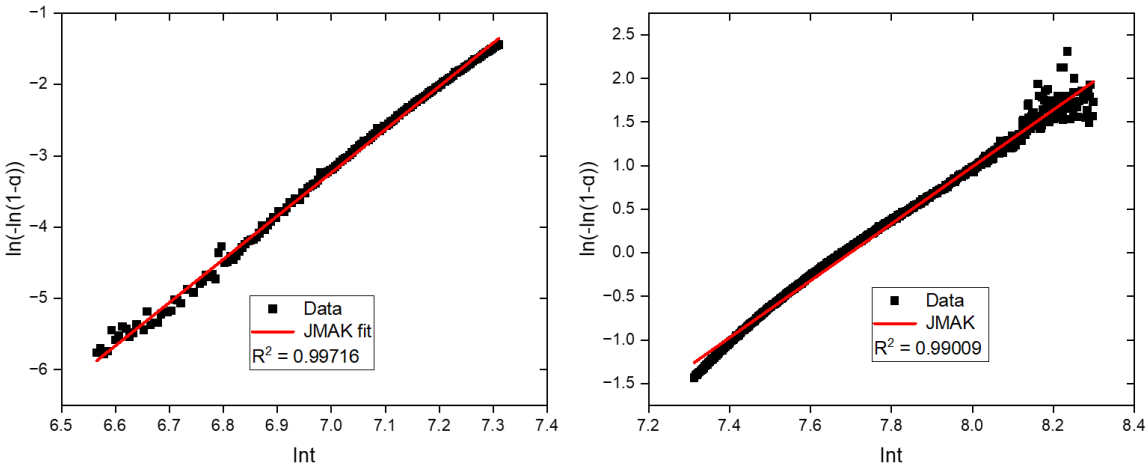

Figure A9.5: Representative fits of normalized UV–Vis data collected from Round 2 experiment, with 10 mM Mg + 0.1 mM CIT. The plot on the left shows the fit of the data collected during the initial part of the turbidity experiment and the fit (n ~4) is used to calculate the induction time (t_{ind}). The plot on the right shows the fit (n ~1) of the data collected during the latter part of the turbidity experiment, the fit on the right is used to determine the rate constant (k).

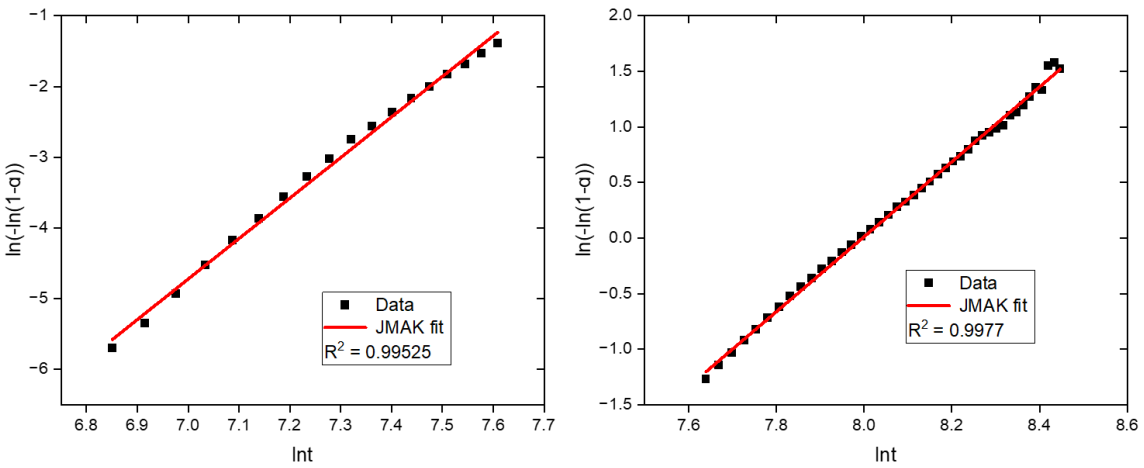

Figure A9.6: Representative fits of normalized UV–Vis data collected from Round 2 experiment, with 10 mM $MgSO_4$ + 0.1 mM CIT. The plot on the left shows the fit of the data collected during the initial part of the turbidity experiment and the fit (n ~4) is used to calculate the induction time (t_{ind}). The plot on the right shows the fit (n ~1) of the data collected during the latter part of the turbidity experiment, the fit on the right is used to determine the rate constant (k).

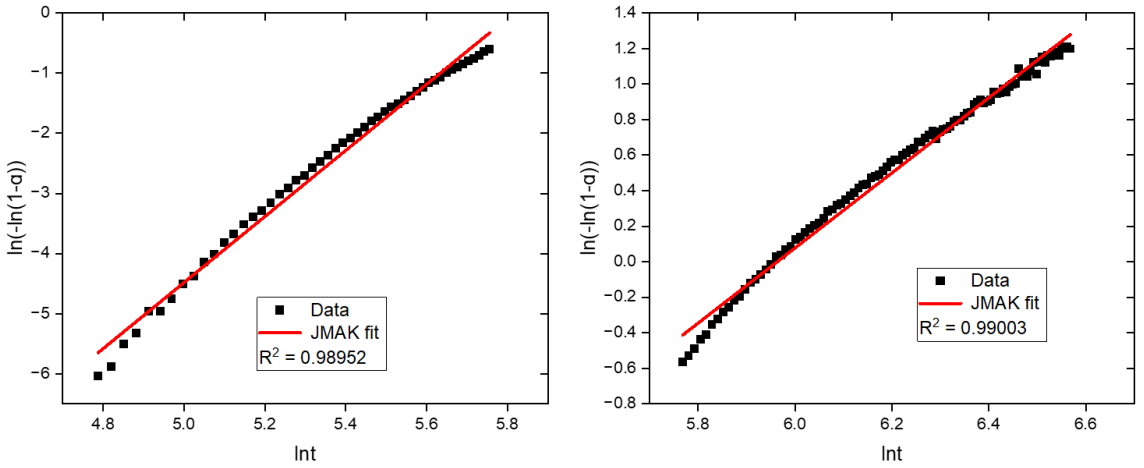

Figure A9.7: Representative fits of normalized UV–Vis data collected from Round 2 experiment, with 10 mM SO_4 + 0.1 mM CIT. The plot on the left shows the fit of the data collected during the initial part of the turbidity experiment and the fit (n ~4) is used to calculate the induction time (t_{ind}). The plot on the right shows the fit (n ~1) of the data collected during the latter part of the turbidity experiment, the fit on the right is used to determine the rate constant (k).

Appendix B

Supplements to Chapter 4

B1 Changes to induction time (t_{ind})

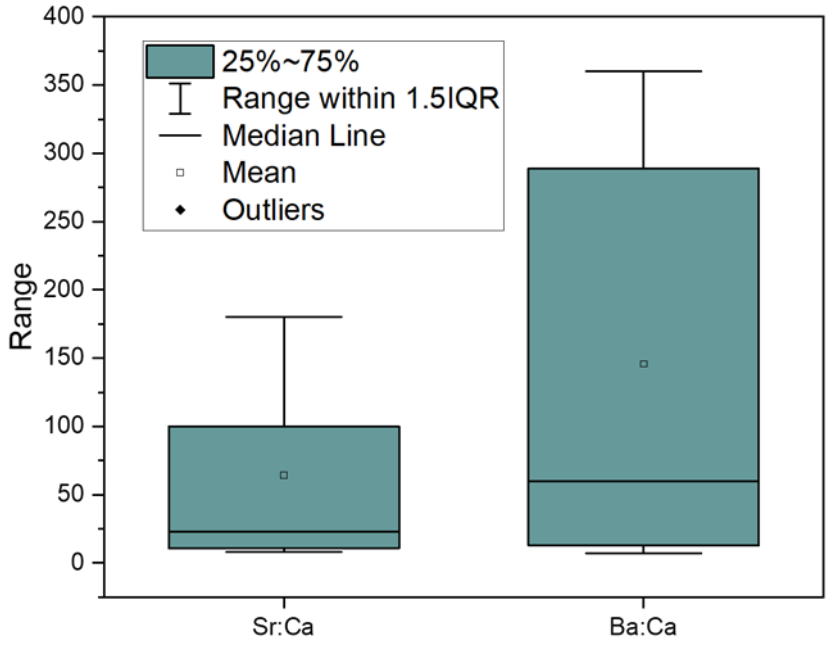

Figure B1.1: Induction time box plots: $SrCO_3$ system experiments (left) and $BaCO_3$ system experiments (right). The inhibiting effect is more pronounced in the $BaCO_3$ experiments, despite the lower molarities of Ca^{2+}.

Effect of Ca^{2+} on $SrCO_3$ t_{ind}	
Ca^{2+} Concentration (mM)	**Percentage change (%)**
1	188
2	38
3	1150
4	2150
Effect of Ca^{2+} on $BaCO_3$ t_{ind}	
Ca^{2+} Concentration (mM)	**Percentage change (%)**
0.1	86
0.25	757
0.5	4029
1.0	5043

Table B1.1: Percentage change values of induction time (t_{ind}) relative to the pure system experiments (no added Ca^{2+}) following addition of Ca^{2+}. Induction time increased in all experiments. The average % increase of the $SrCO_3$ experiments is 881%. The average % increase of the $BaCO_3$ experiments is 2479%.

B2 Changes to crystallisation rate (*k*)

Effect of Ca^{2+} on $SrCO_3$ *k*	
Ca^{2+} Concentration (mM)	**Percentage change (%)**
1	-73
2	-95
3	-84
4	-88
Effect of Ca^{2+} on $BaCO_3$ *k*	
Ca^{2+} Concentration (mM)	**Percentage change (%)**
0.1	-42
0.25	-93
0.5	-95
1.0	-96

Table B2.1: Percentage change values of crystallisation rate (k) relative to the pure system experiments (no added Ca^{2+}) following addition of Ca^{2+}. crystallisation rate decreased in all experiments. The average % decrease of the $SrCO_3$ experiments is -86%%. The average % decrease of the $BaCO_3$ experiments is -81%.

B3 Representative fits of normalized Turbidity data- $BaCO_3$ experiments

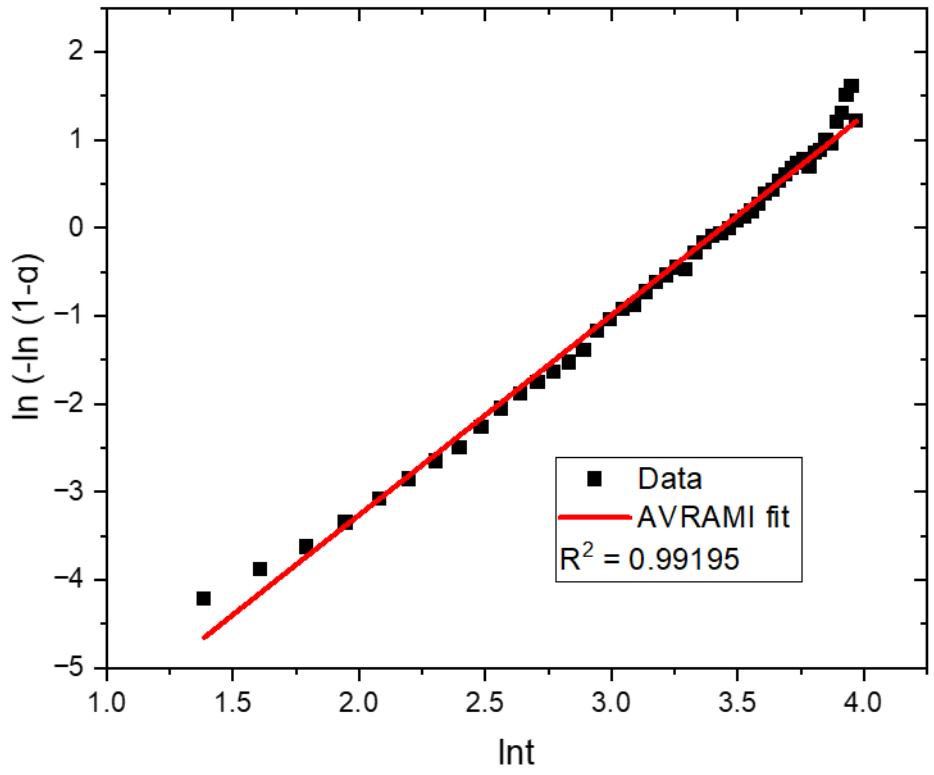

Figure B3.1: Representative fits of normalized UV–Vis data collected from the pure $BaCO_3$ system (no additives) experiment., the fit is used to determine the rate constant (k).

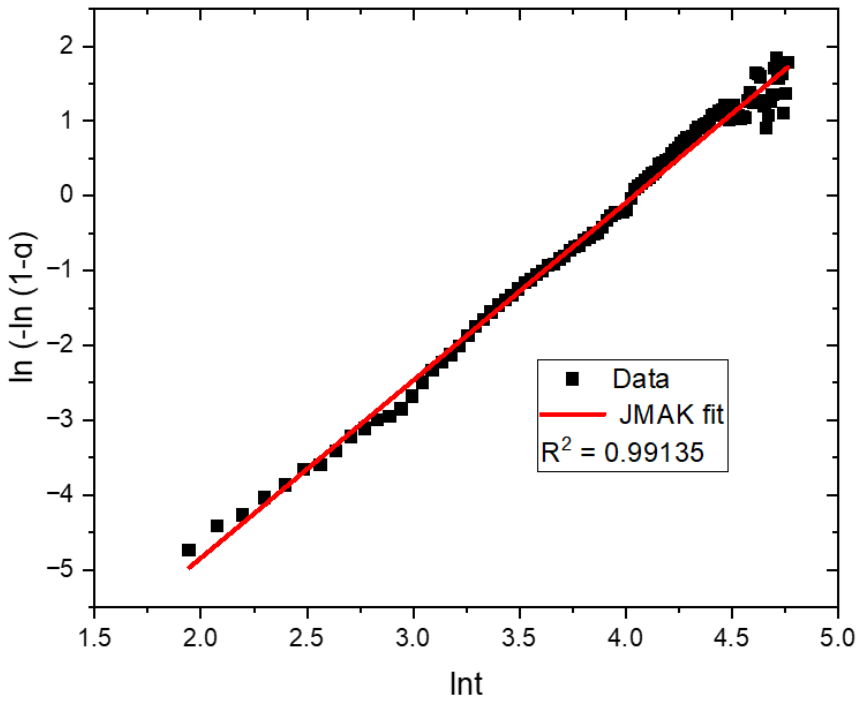

Figure B3.2: Representative fits of normalized UV–Vis data collected from the $BaCO_3$ + 0.1 mM Ca experiment. the fit is used to determine the rate constant (k).

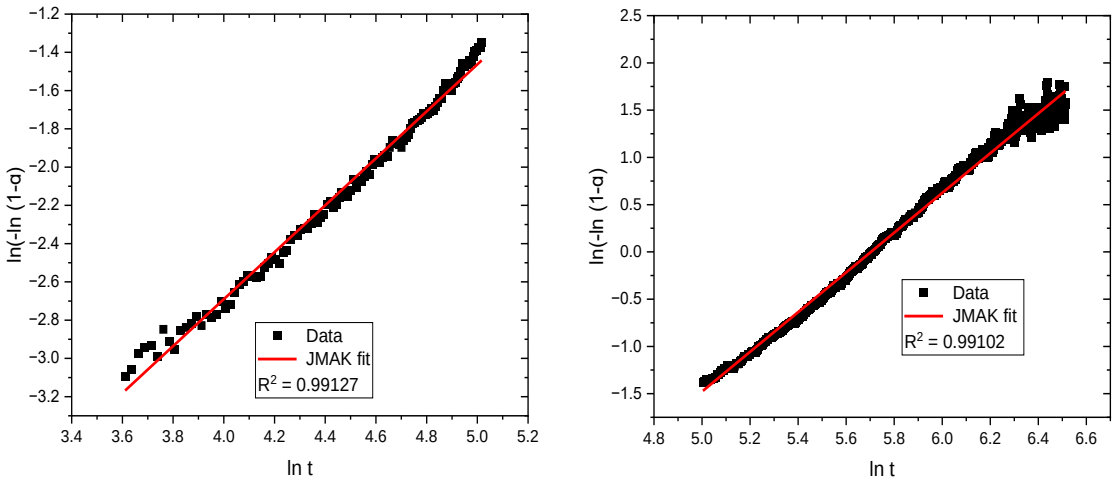

Figure B3.3: Representative fits of normalized UV–Vis data collected from the $BaCO_3$ + 0.25 mM Ca experiment. the fit is used to determine the rate constant (k).

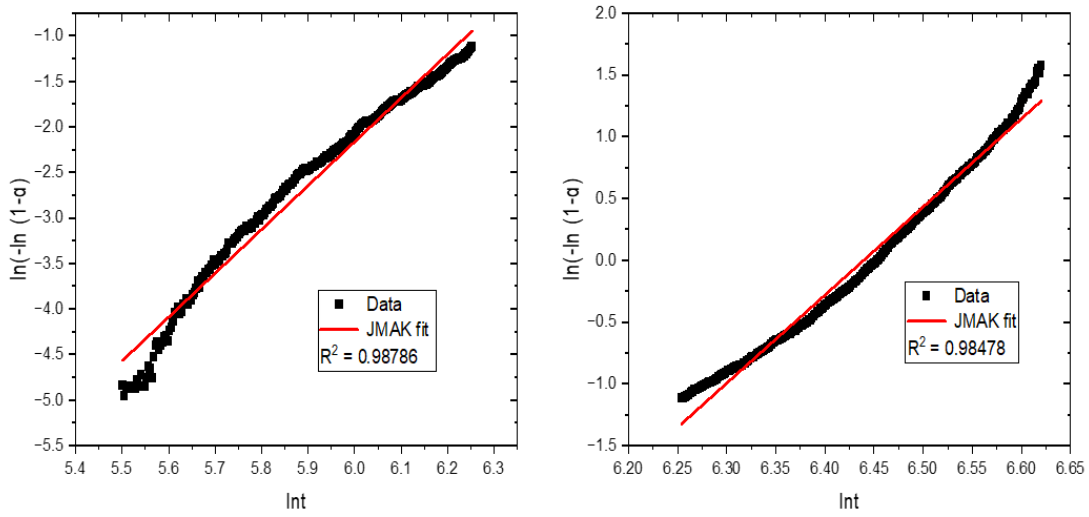

Figure B3.4: Representative fits of normalized UV–Vis data collected from the $BaCO_3$ + 0.5 mM Ca experiment. the fit is used to determine the rate constant (k).

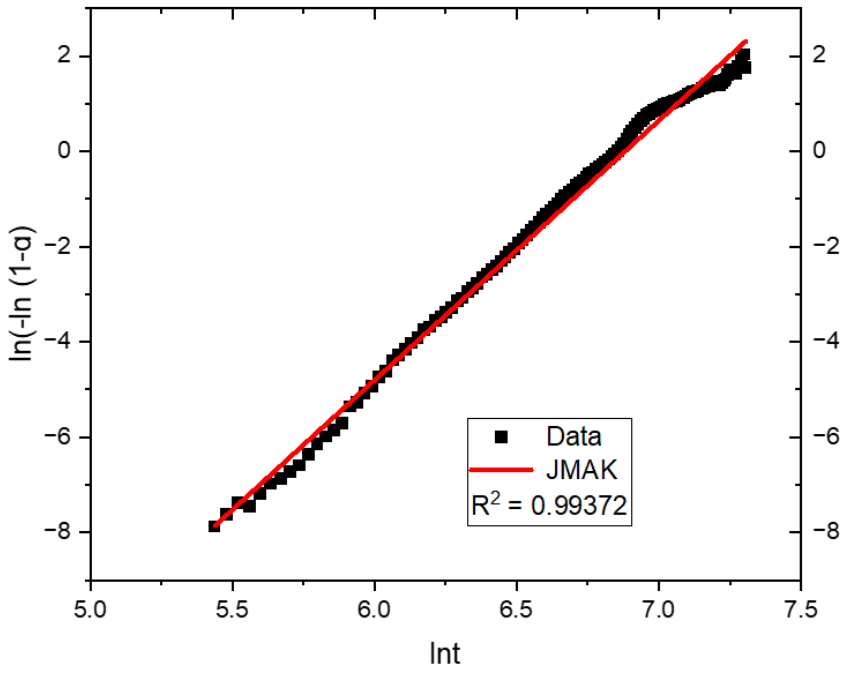

Figure B3.5: Representative fits of normalized UV–Vis data collected from the $BaCO_3$ + 1.0 mM Ca experiment. the fit is used to determine the rate constant (k).

B4 Representative fits of normalized Turbidity data- $SrCO_3$ experiments

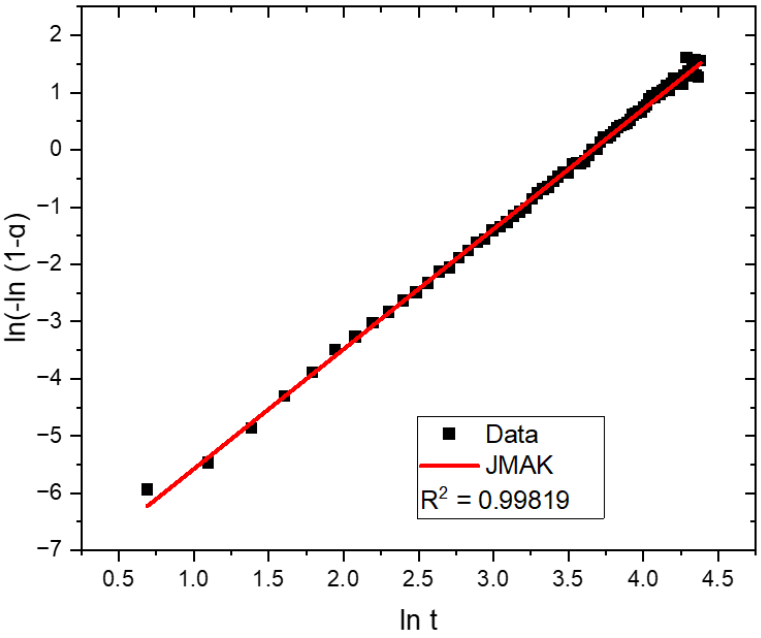

Figure B4.1: Representative fits of normalized UV–Vis data collected from the pure $SrCO_3$ system (no additives) experiment., the fit is used to determine the rate constant (k).

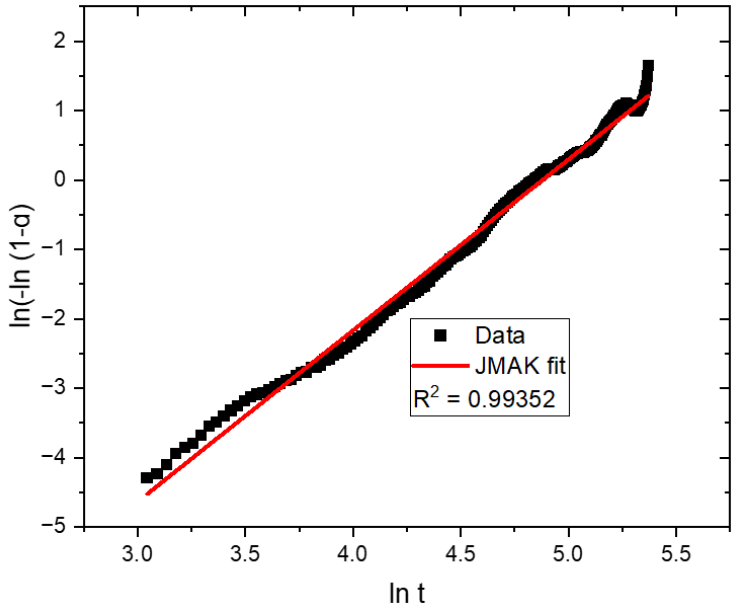

Figure B4.2: Representative fits of normalized UV–Vis data collected from the $SrCO_3$ + 1.0 mM Ca experiment. the fit is used to determine the rate constant (k).

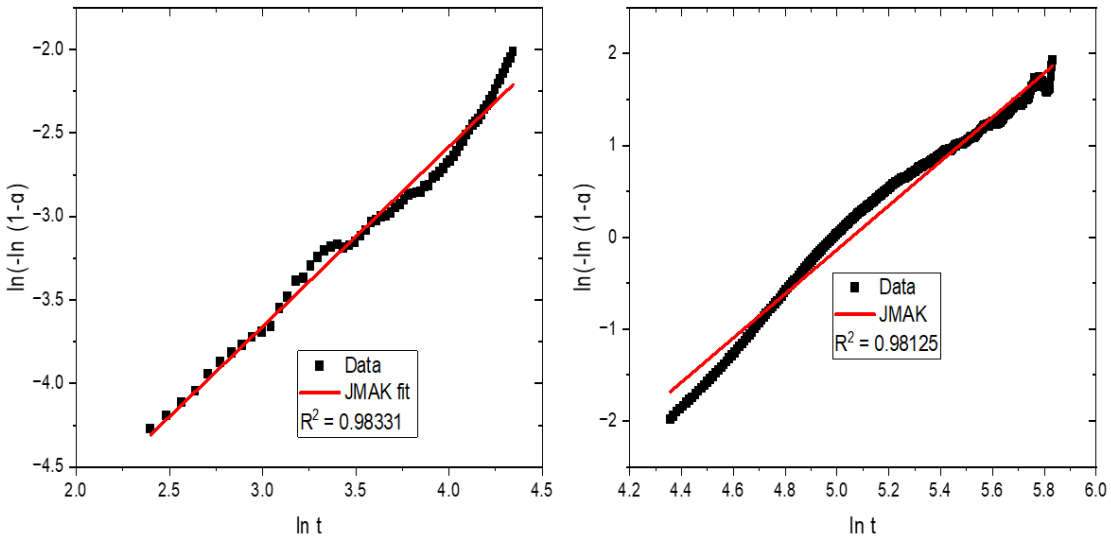

Figure B4.3: Representative fits of normalized UV–Vis data collected from the $SrCO_3$ + 2.0 mM Ca experiment. the fit is used to determine the rate constant (k).

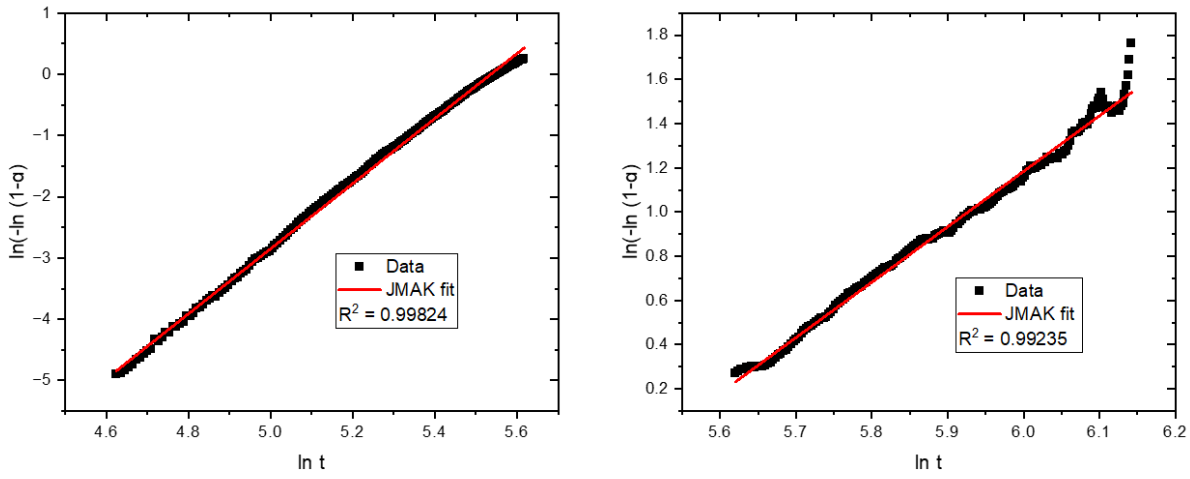

Figure B4.4: Representative fits of normalized UV–Vis data collected from the $SrCO_3$ + 3.0 mM Ca experiment. the fit is used to determine the rate constant (k).

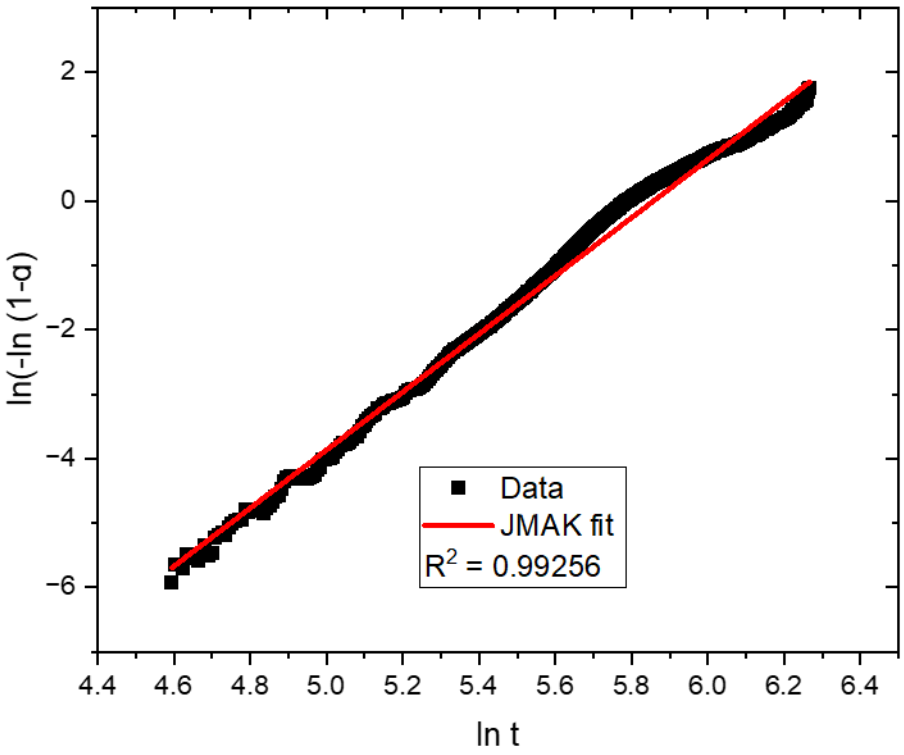

Figure B4.5: Representative fits of normalized UV–Vis data collected from the $SrCO_3$ + 4.0 mM Ca experiment. the fit is used to determine the rate constant (k).

B5 SEM-EDS Spectrum images $SrCO_3$ homogeneous nucleation experiments

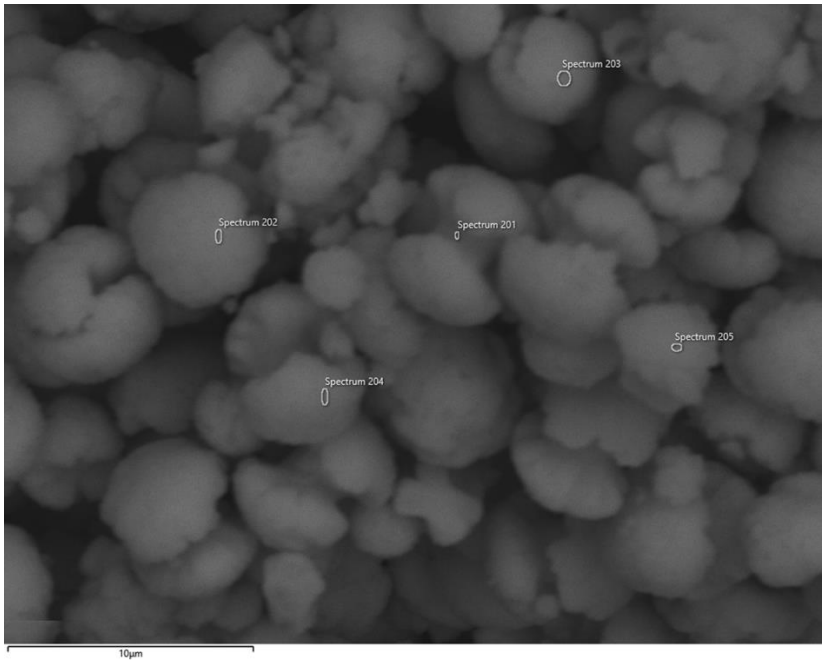

Figure B5.1: Element content (atom %) in $SrCO_3$ determined with energy dispersive spectroscopy (EDS) analysis.

	$SrCO_3$ + 1.0 mM Ca Spectrum 201- 205			
	O	**Ca**	**Sr**	**Ba**
Max	80.67	16.95	12.13	0.07
Min	76.48	10.07	6.56	0.01
Mean	78.74	12.34	8.89	0.03
Standard Deviation	1.82	2.72	2.16	0.03
RSD	2.31%	22.04%	24.30%	100.00%
Standard Error	0.81	1.22	0.97	0.01
RSE	1.03%	9.86%	10.87%	44.72%

Table B5.1: Element content (atom %) in $SrCO_3$ determined with energy dispersive spectroscopy (EDS) analysis. Error values presented are the average from all the point spectra, the relative standard deviation (RSD) and the relative standard error (RSE).

B6 The influence of fluid saturation state for Replacement reactions

For the replacement reaction experiments we examined the calcite saturation index (SI) across a range of values (SI from -3 to 0). This is to account for the dissolution of $CaCO_3$ the calcite, as initially the solution would not be in equilibrium with calcite (SI = 0) reaching a saturation index of zero is not instantaneous.

Temperature (°C)	**Initial Calcite Saturation Index**	**$BaCO_3$ Saturation Index**	**$SrCO_3$ Saturation Index**
21 °C	0	7.23	4.42
	-1	6.69	2.54
	-2	6.13	1.99
	-3	5.55	1.41
40 °C	0	6.75	4.18
	-1	1.66	2.40
	-2	1.08	1.83
	-3	0.48	1.23
60 °C	0	6.32	2.84
	-1	1.53	2.28
	-2	0.93	1.69
	-3	0.31	1.08
90 °C	0	5.77	3.72
	-1	1.35	2.14
	-2	0.72	1.52
	-3	0.07	0.89

Table B6.1: Calcite saturation index (SI) across a range of values (SI from -3 to 0).

B7 Calcite seeds

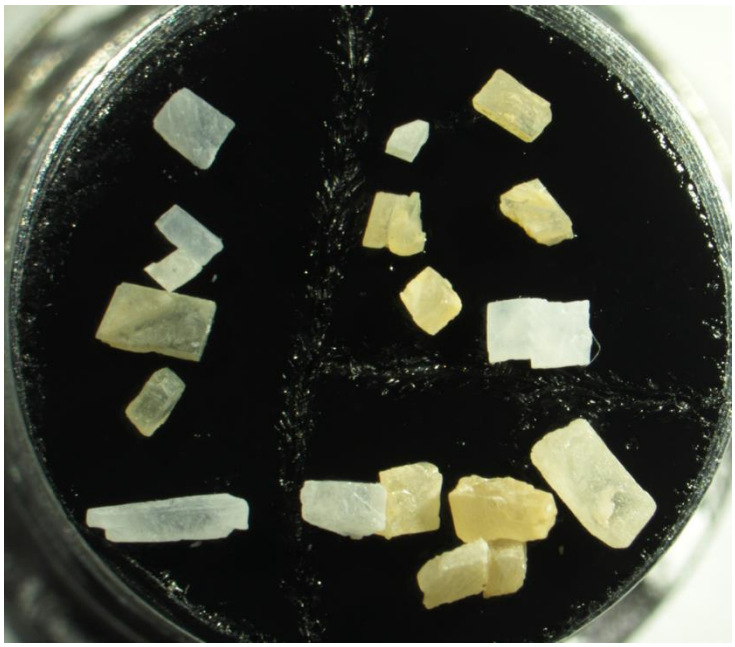

Figure B7.1: Calcite seeds post reaction with Sr-bearing solutions display (puck diameter 12 mm)

Appendix C

Supplements to Chapter 5

C1 Reflected light micrographs

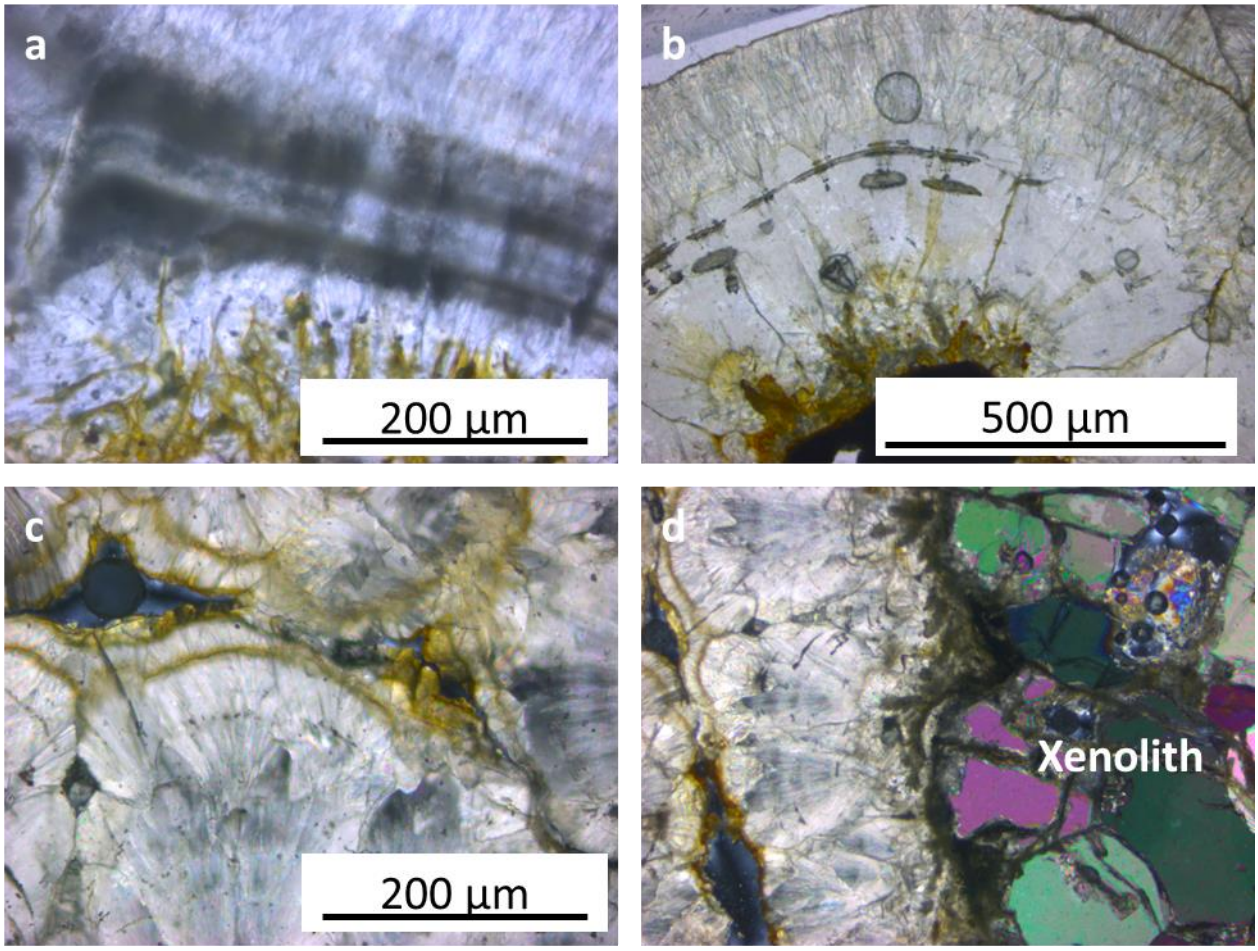

Figure C1.1: Reflected light microscope images of carbonate cement displaying a range of microtextures., including banded/laminated (a). Fan like radial cement under cross polars (c), with cement growing from xenolith (d).

C2 SEM-EDS data for “area 1”

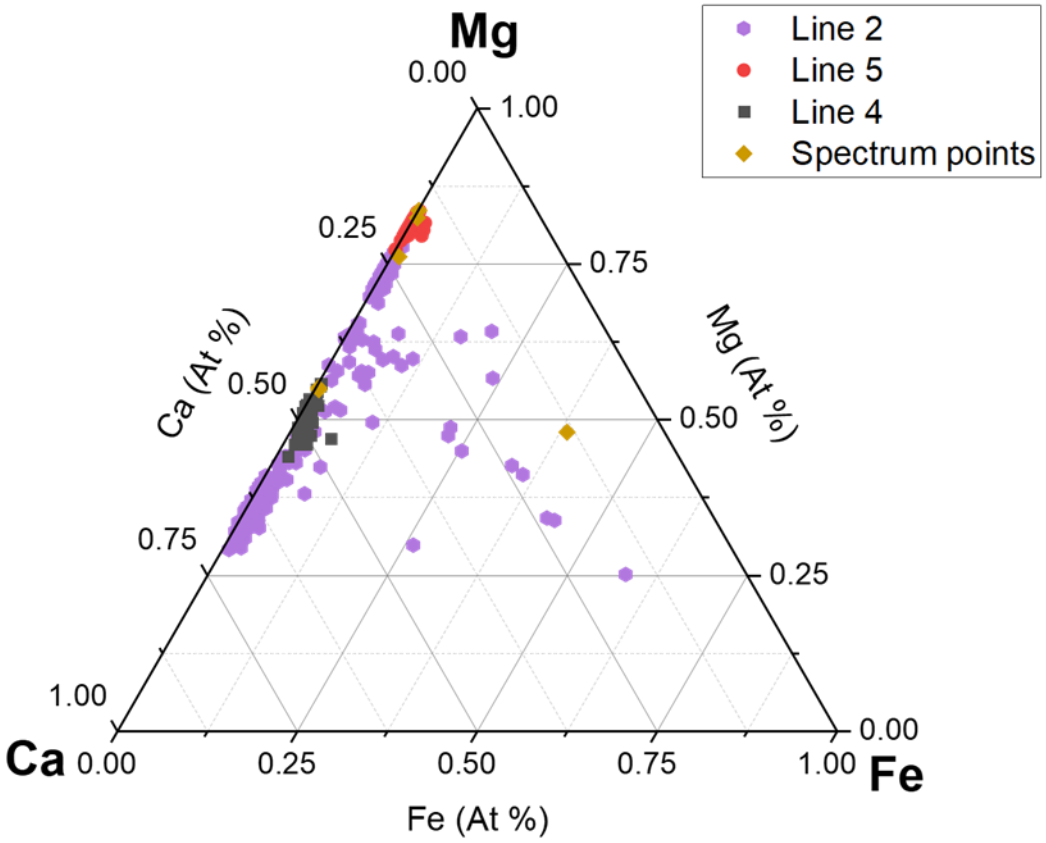

Figure C2.1: Ternary plot of carbonate phase compositions from SEM EDS maps of Area 1 demonstrating the evolution of the carbonate cement from “Region 1” (Line 4 ■) to “Region 2” (Line 2 ●). Weight proportions of Ca, Fe and Mg normalised to 100% are plotted and show a general increase in the proportion of Ca-magnesite across the carbonate cement regions. Compositions of greater than 50% Fe likely include μ- or nano- inclusions of non Fe-carbonates (e.g. Fe-oxides or Fe-silicates).

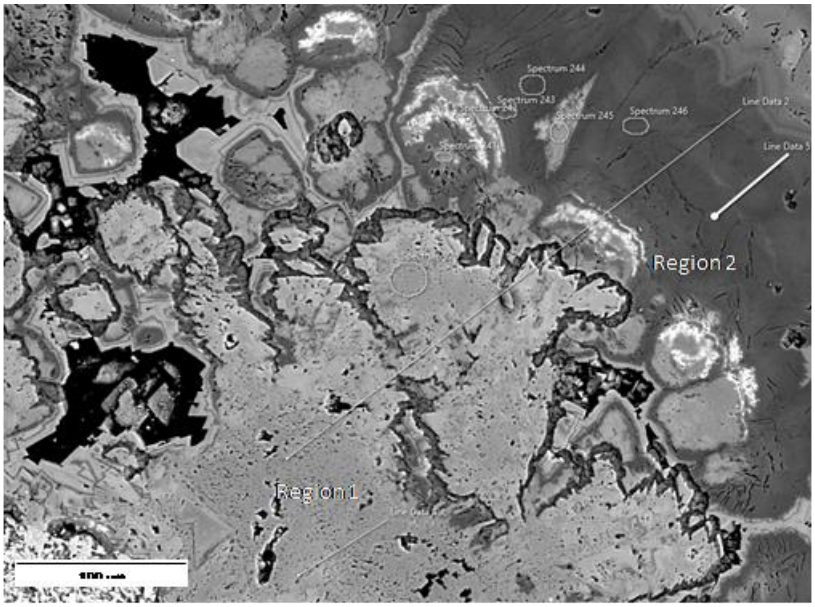

Figure C2.2: SEM EDS line and point analysis locations across region 1 and Region 2 type carbonate cements in "area 1".

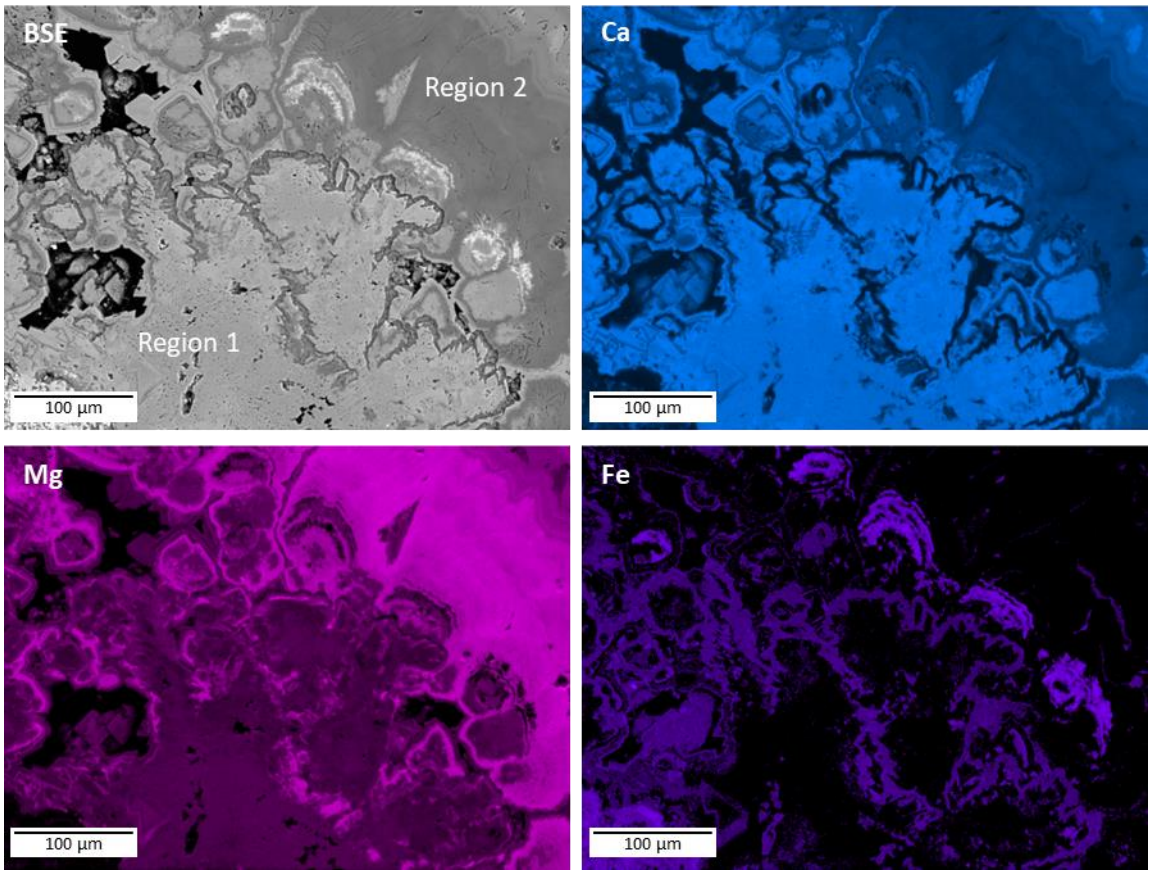

Figure0.1: SEM-BSE image and EDS compositional maps showing distribution of elements (Ca. Mg and Fe) between "Region 1" and "Region 2" type carbonate cements in "area 1".

C3 EDS Analysis points

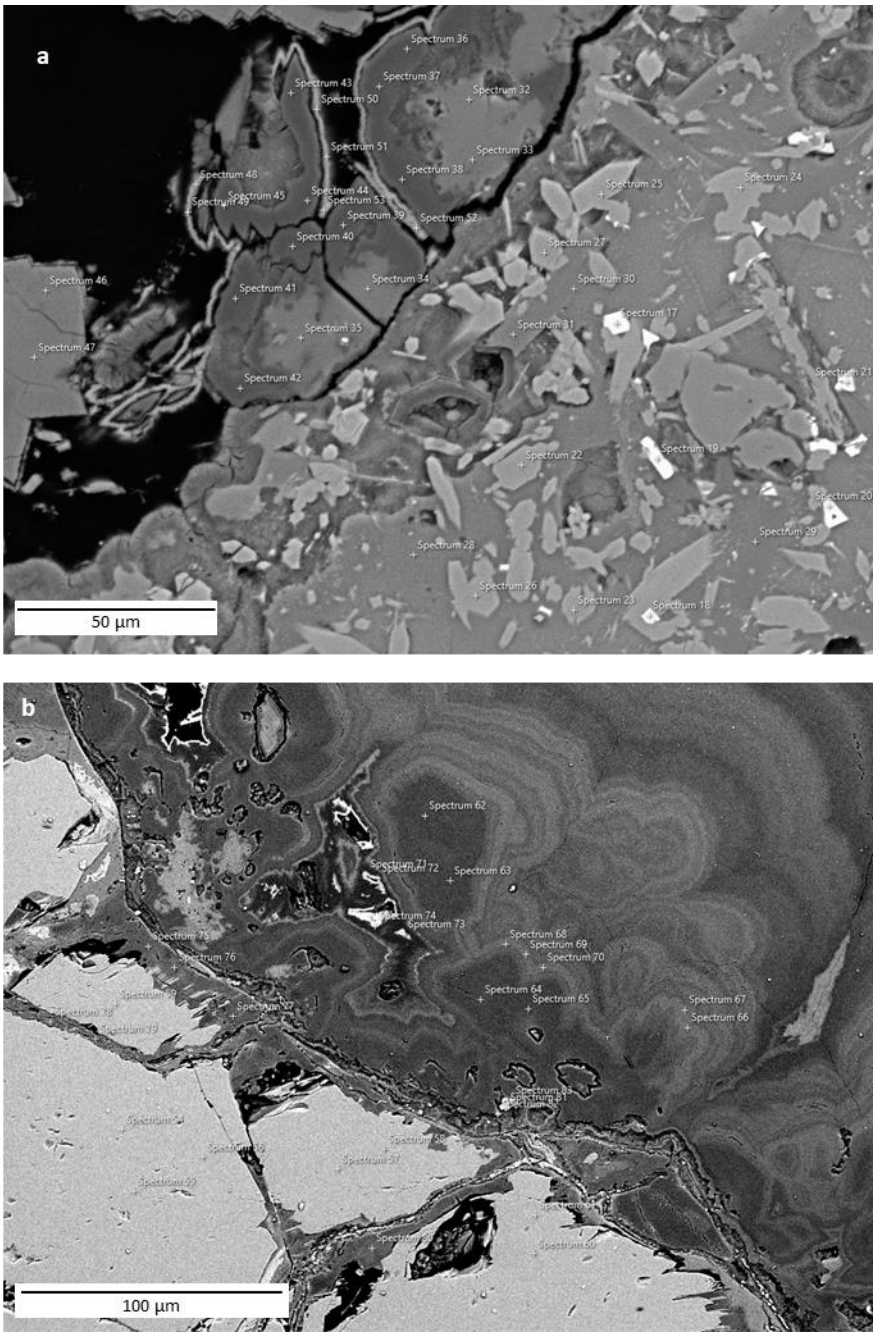

Figure C3.1: SEM-BSE image and EDS compositional spectra point analysis for a) host basalt and b) xenolith.

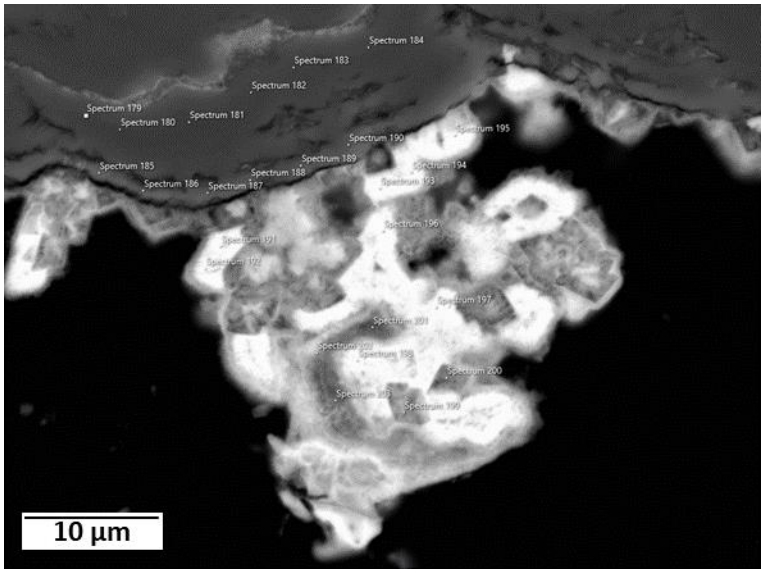

Figure C0.2: SEM-BSE image and EDS compositional spectra point analysis for "Region 4" cement.

C4 PHREEQC SIMULATION

PHREEQC geochemical code for calculating the Saturation Indices (SI) of magnesite, hydromagnesite, nesquehonite, dolomite and calcite as a function of temperature and pH with respect to varying levels of pCO_2.

```
SOLUTION 1
    temp      25
    pH        7
    pe        4
    redox     pe
    units     mmol/kgw
    density   1
    -water    1 # kg

EQUILIBRIUM_PHASES 1  #See note below
    CO2(g)    -3.5 10
    Enstatite 0 10
    Forsterite 0 10
    Anorthite 0 10

REACTION_TEMPERATURE 1
    10 200 in 20 steps

SELECTED_OUTPUT 1
    -file                 NiamhSvalbard_1.txt
    -reset                false
    -pH                   true
    -temperature          true
    -saturation_indices    Magnesite   Hydromagnesite
Nesquehonite  Dolomite Calcite
```

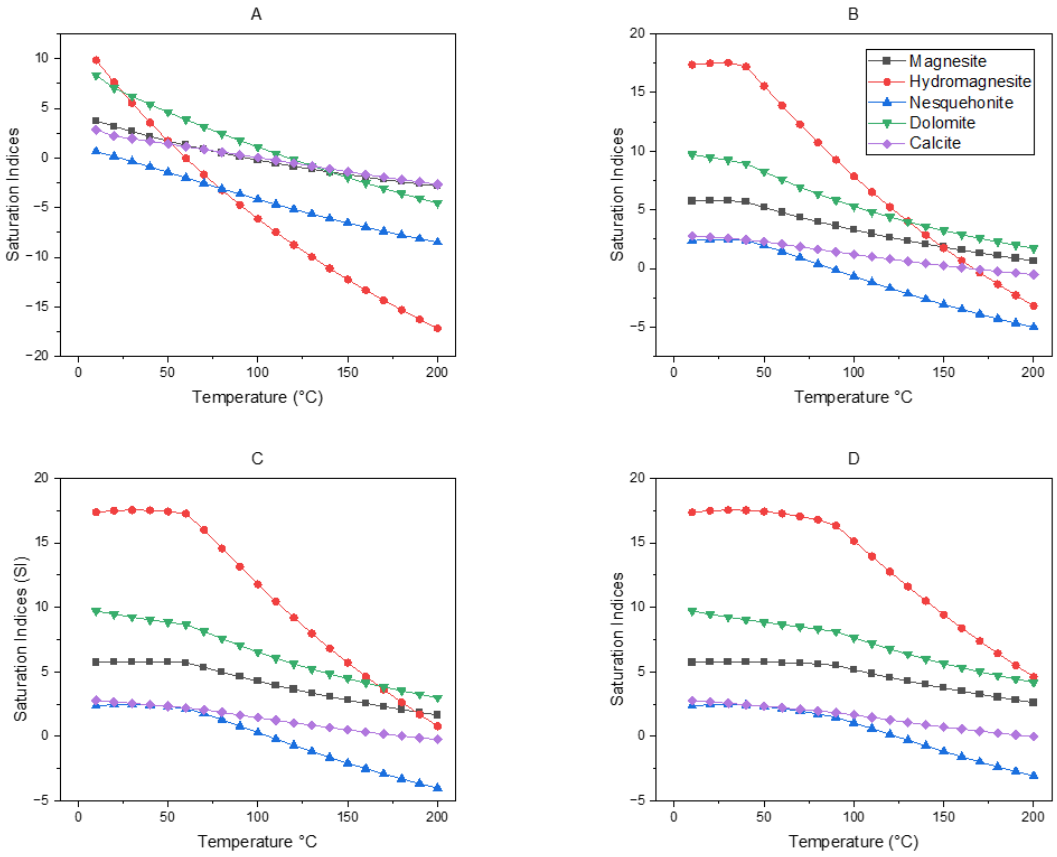

Figure C4.1: Saturation Indices (SI) of magnesite, hydromagnesite, nesquehonite, dolomite and calcite as a function of temperature (°C) with respect to varying levels of pCO_2 ***A****) 0.004 atm,* ***B****) 1 atm,* ***C****) 10 atm and* ***D****) 100 atm.*

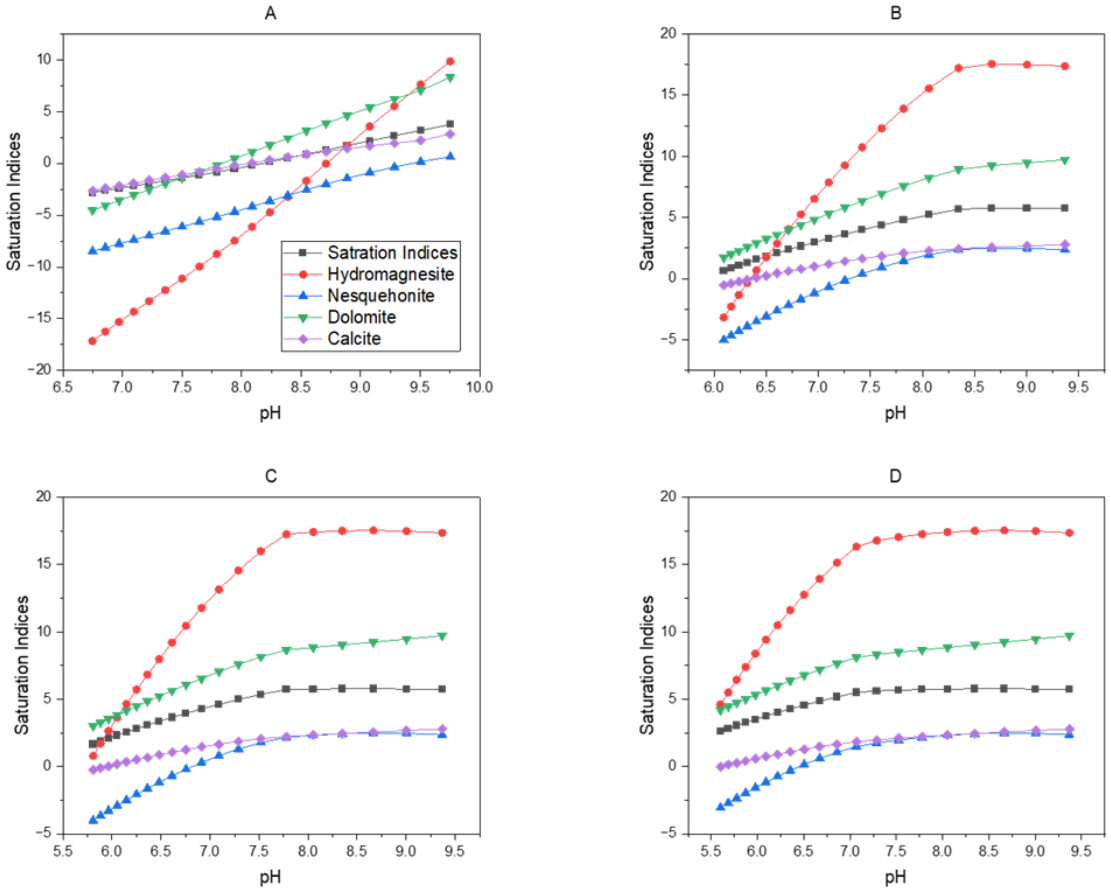

Figure C4.2: Saturation Indices (SI) of magnesite, hydromagnesite, nesquehonite, dolomite and calcite as a function of pH with respect to varying levels of pCO_2 ***A****) 0.004 atm,* ***B****) 1 atm,* ***C****) 10 atm and* ***D****) 100 atm.*